Geodetic monitoring of complex shaped infrastructures using Ground-Based InSAR

Zur Erlangung des akademischen Grades eines
DOKTOR DER INGENIEURWISSENSCHAFTEN (Dr.-Ing.)
bei der KIT-Fakultät
für Bauingenieur-, Geo-, und Umweltwissenschaften
des Karlsruher Instituts für Technologie (KIT)

genehmigte

DISSERTATION

von

Dipl.-Ing. Matthieu Rebmeister
aus Strasbourg, Frankreich

Tag der mündlichen Prüfung:	04.12.2023
Referent:	Prof. Dr.-Ing. Stefan Hinz
Korreferent:	Prof. Dr. Michael Eineder

Abstract

In the context of climate change, alternatives to fossil energies need to be used as much as possible to produce electricity. Hydroelectric power generation through the utilisation of dams stands out as an exemplar of highly effective methodologies in this endeavour. Various monitoring sensors can be installed with different characteristics w.r.t. spatial resolution, temporal resolution and accuracy to assess their safe usage. Among the array of techniques available, it is noteworthy that ground-based synthetic aperture radar (GB-SAR) has not yet been widely adopted for this purpose. Despite its remarkable equilibrium between the aforementioned attributes, its sensitivity to atmospheric disruptions, specific acquisition geometry, and the requisite for phase unwrapping collectively contribute to constraining its usage. Several processing strategies are developed in this thesis to capitalise on all the opportunities of GB-SAR systems, such as continuous, flexible and autonomous observation combined with high resolutions and accuracy.

The first challenge that needs to be solved is to accurately localise and estimate the azimuth of the GB-SAR to improve the geocoding of the image in the subsequent step. A ray tracing algorithm and tomographic techniques are used to recover these external parameters of the sensors. The introduction of corner reflectors for validation purposes confirms a significant error reduction. However, for the subsequent geocoding, challenges persist in scenarios involving vertical structures due to foreshortening and layover, which notably compromise the geocoding quality of the observed points. These issues arise when multiple points at varying elevations are encapsulated within a singular resolution cell, posing difficulties in pinpointing the precise location of the scattering point responsible for signal return. To surmount these hurdles, a Bayesian approach grounded in intensity models is formulated, offering a tool to enhance the accuracy of the geocoding process. The validation is assessed on a dam in the black forest in Germany, characterised by a very specific structure.

The second part of this thesis is focused on the feasibility of using GB-SAR systems for long-term geodetic monitoring of large structures. A first assessment is made by testing large temporal baselines between acquisitions for epoch-wise monitoring. Due to large displacements, the phase unwrapping can not recover all the information. An improvement is made by adapting the geometry of the signal processing with the principal component analysis. The main case study consists of several campaigns from different stations at Enguri Dam in Georgia. The consistency of the estimated displacement map is assessed by comparing it to a numerical model calibrated on the plumblines data. It exhibits a strong agreement between the two results and comforts the usage of GB-SAR for epoch-wise monitoring, as it can measure several thousand points on the dam. It also exhibits the possibility of detecting local anomalies in the numerical model. Finally, the instrument has

been installed for continuous monitoring for over two years at Enguri Dam. An adequate flowchart is developed to eliminate the drift happening with classical interferometric algorithms to achieve the accuracy required for geodetic monitoring. The analysis of the obtained time series confirms a very plausible result with classical parametric models of dam deformations. Moreover, the results of this processing strategy are also confronted with the numerical model and demonstrate a high consistency. The final comforting result is the comparison of the GB-SAR time series with the output from four GNSS stations installed on the dam crest.

The developed algorithms and methods increase the capabilities of the GB-SAR for dam monitoring in different configurations. It can be a valuable and precious supplement to other classical sensors for long-term geodetic observation purposes as well as short-term monitoring in cases of particular dam operations.

Zusammenfassung

In einem Kontext des Klimawandels ist es erforderlich, so weit wie möglich auf Alternativen zu fossilen Energien zurückzugreifen, um Strom zu erzeugen. Die Stromerzeugung durch Wasserkraftnutzung über Staudämme zeichnet sich als ein Beispiel für äußerst effektive Methoden in diesem Unternehmen aus. Zur Bewertung ihrer sicheren Verwendung können verschiedene Überwachungssensoren mit unterschiedlichen Merkmalen hinsichtlich räumlicher Auflösung, zeitlicher Auflösung und Genauigkeit installiert werden. Unter den verfügbaren Techniken ist bemerkenswert, dass die bodengestützte synthetische apertur radar (engl. *ground-based synthetic aperture radar*, GB-SAR) noch keine verbreitete Anwendung für diesen Zweck gefunden hat. Trotz ihres bemerkenswerten Gleichgewichts zwischen den oben genannten Eigenschaften, trägt ihre Anfälligkeit für atmosphärische Störungen, spezifische Erfassungsgeometrie und die Notwendigkeit des Phasenabwicklung (engl. *phase unwrapping*) zusammen dazu bei, ihre Verwendung einzuschränken. Um alle Gelegenheiten von GB-SAR Systemen zu nutzen, wie kontinuierliche, flexible und autonome Beobachtung in Kombination mit hoher Auflösung und Genauigkeit, werden in dieser Arbeit verschiedene Verarbeitungsstrategien entwickelt.

Die Notwendigkeit, den GB-SAR genau zu lokalisieren und seine Ausrichtung zu kennen, ist eine erste Herausforderung, die gelöst werden muss, um die spätere Geokodierung des Bildes zu verbessern. Ein *ray tracing* Algorithmus in Kombination mit tomographischen Algorithmen werden verwendet, um diese externen Parameter der Sensoren wiederherzustellen. Die Einführung von *corner reflectors* zu Validierungszwecken bestätigt eine signifikante Fehlerreduktion. Es bestehen jedoch weiterhin Herausforderungen in Szenarien mit vertikalen Strukturen aufgrund von *foreshortening* und *layover*, die die Geokodierungsqualität der beobachteten Punkte erheblich verschlechtern. Diese Probleme treten auf, wenn mehrere Punkte in unterschiedlichen Höhen in einer einzigen Auflösungszelle erfasst werden und Schwierigkeiten bei der genauen Lokalisierung des Streupunkts auftreten, der für das beobachtete Signal verantwortlich ist. Um diese Hindernisse zu mildern, wird ein Bayesian Ansatz basierend auf ein Intensitätsmodelle formuliert, der eine Möglichkeit zur Verbesserung der Genauigkeit des Geokodierungsprozesses bietet. Die Validierung erfolgt an einem Staudamm in Deutschland, der durch eine sehr spezifische Struktur gekennzeichnet ist.

Ein zweiter Teil der Arbeit konzentriert sich auf die Machbarkeit der Verwendung von GB-SAR-Systemen für die geodätische Langzeitüberwachung großer Strukturen. Eine erste Bewertung erfolgt durch Testen großer zeitlicher Basislinien zwischen den Erfassungen für eine epochenweise Überwachung. Aufgrund großer Verschiebungen kann die Phasenabwicklung nicht alle Informationen wiederherstellen, und eine Verbesserung wird durch Anpassung der Signalverarbeitungsgeome-

trie mit der Hauptkomponentenanalyse erreicht. Die Hauptfallstudie besteht aus mehreren Kampagnen von verschiedenen Stationen am Enguri Damm in Georgien. Die Konsistenz der geschätzten Verschiebungskarte wird durch den Vergleich mit an den Lotlinienkalibrierten numerische Modellen überprüft. Es zeigt eine starke Übereinstimmung zwischen den beiden Ergebnissen und bestätigt die Verwendung von GB-SAR für die epochenweise Überwachung, da es mehrere tausend Punkte am Damm messen kann. Dieser Vergleich hat auch gezeigt, dass der GB-SAR lokale Anomalien im Modell detektieren kann. Schließlich wurde das Instrument auch für eine kontinuierliche Überwachung von zwei Jahren am Enguri Damm installiert. Ein geeigneter Flussdiagramm wurde entwickelt, um die bei klassischen interferometrischen Algorithmen auftretende Drift zu beseitigen und die für die geodätische Überwachung erforderliche Genauigkeit zu erreichen. Die Analyse der erhaltenen Zeitreihen bestätigt ein sehr plausibles Ergebnis mit klassischen parametrischen Modellen der Deformationen des Damms. Darüber hinaus werden die Ergebnisse dieser Verarbeitungsstrategie auch mit dem numerischen Modell in Bezug gesetzt und zeigen eine hohe Übereinstimmung. Das abschließende ermutigende Ergebnis ist der Vergleich der Zeitreihen des GB-SAR mit den Ausgaben von vier GNSS-Stationen, die auf dem Damm Kronne installiert sind.

Die entwickelten Algorithmen und Methoden haben die Fähigkeiten des GB-SAR für die Überwachung von Staudämmen in verschiedenen Konfigurationen erweitert. Es kann eine wertvolle Ergänzung zu anderen klassische Sensoren für langfristige geodätische Beobachtungszwecke sowie für kurzfristige Überwachung bei besonderen Dammoperationen sein.

Résumé

Dans un contexte de changement climatique, il est nécessaire d'utiliser autant que possible des alternatives aux énergies fossiles pour produire de l'électricité. La production d'énergie hydroélectrique par le biais de barrages se distingue comme un exemple de méthodologies très efficace dans cette perspective. Pour assurer leur opération en toute sécurité, un large éventail de capteurs de surveillance est à disposition, avec différentes caractéristiques en ce qui concerne la résolution spatiale, la résolution temporelle et la précision. Parmi la gamme de techniques disponibles, la surveillance par radar à synthèse d'ouverture terrestre (RSOT, angl. *ground-based synthetic aperture radar*) n'a pas encore été adoptée comme système de mesure établi et fiable. Malgré son équilibre remarquable entre les attributs susmentionnés, sa susceptibilité aux perturbations atmosphériques, sa géométrie d'acquisition spécifique et la nécessité du dépliage de phase (angl. *phase unwrapping*) contribuent à restreindre son utilisation. Afin de capitaliser toutes les opportunités des systèmes RSOT, telles que l'observation continue, flexible et autonome combinée à de hautes résolutions et précisions, plusieurs stratégies de traitement sont développées dans cette thèse.

La nécessité de géoréférencer avec exactitude le RSOT est un premier défi à résoudre afin d'améliorer le géocodage ultérieur de l'image. Un algorithme de *ray tracing* ainsi que des méthodes tomographiques sont utilisés pour estimer ces paramètres externes du RSOT. L'introduction de *corner reflectors* à des fins de validation confirme une réduction significative des erreurs. Cependant, des défis persistent dans les scénarios impliquant des structures verticales en raison du *foreshortening* et du *layover*, compromettant notablement la qualité du géocodage des points observés. Ces problèmes surviennent lorsque plusieurs points à des altitudes variables sont projetés dans un unique pixel, ce qui pose des difficultés pour localiser précisément le point responsable du signal. Pour surmonter ces obstacles, une approche bayésienne basée sur des modèles d'intensité est formulée, offrant un moyen d'améliorer la précision du processus de géocodage. La validation est éffectuée sur un barrage en Allemagne, caractérisé par une structure très spécifique et complexe.

Une deuxième partie de cette thèse est axée sur la faisabilité d'utiliser des systèmes RSOT pour la surveillance géodésique de grandes structures à long terme. Une première évaluation est réalisée en testant des mesures espacées de plusieurs mois. En raison de grands déplacements, le dépliage de phase présente de nombreuses erreurs lorsqu'il est appliqué dans la géométrie classique. Une amélioration est apportée en adaptant cette dernière par le biais de l'analyse en composantes principales. L'étude de cas consiste en plusieurs campagnes menées depuis différentes stations au barrage d'Enguri en Géorgie. La cohérence des déplacements estimés est évaluée en les comparant

à deux modèles numériques calibrés sur les données des pendules. Elle présente un fort accord entre les deux résultats et confirme l'intérêt d'utiliser le RSOT pour la surveillance par campagnes, car il peut mesurer plusieurs milliers de points sur le barrage. Cette comparaison a également mis en évidence la possibilité de détecter des anomalies locales dans le modèle numérique. Enfin, l'instrument a également été installé pour une surveillance continue de deux ans au barrage d'Enguri. Un algorithme adéquat est développé pour éliminer la dérive survenant avec les algorithmes interférométriques classiques afin d'atteindre l'exactitude et la précision requises pour une surveillance géodésique. L'analyse des séries temporelles obtenues confirme un résultat très plausible avec des modèles paramétriques classiques des déformations d'un barrage. À nouveau, la comparaison avec le modèle numérique permet de valider la consistance et la stabilité de la chaîne de traitement proposée. Enfin, les résultats de l'interférométrie radar ont été comparés aux données des antennes GNSS installées sur la crête du barrage, comme ultime validation de la méthode proposée.

Les algorithmes et méthodes développés ont augmenté les capacités du RSOT pour la surveillance des barrages dans différentes configurations. Il peut être un complément précieux à d'autres capteurs géodésiques pour des observations à long terme ainsi que pour la surveillance à court terme, lors d'opérations particulières sur les barrages.

Abbreviations

1D	one dimensional
2D	two dimensional
3D	three dimensional
APS	atmospheric phase screen
BW-SBAS	block-wise SBAS
BW-SM	block-wise single master
CI	confidence interval
CS	compressive sensing
CR	corner reflector
DAMAST	Dams and Induced Seismicity —Technology for Risk Reduction
DBAS	daily baseline subset
DBSCAN	density-based spatial clustering of applications with noise
DEM	digital elevation model
FDA	functional data analysis
FFT	fast Fourier transform
GB-SAR	ground-based synthetic aperture radar
GNSS	Global Navigation Satellite System
GUI	graphical user interface
HST	Hydrostatic-Season-Time
ICP	iterative closest point
IBIS-FM	Image By Interferometric Survey - Frequency Modulated
IDS	Ingegneria Dei Sistemi
InSAR	interferometric synthetic aperture radar
LAD	least absolute deviations
LOS	line-of-sight
LS	least squares
MAP	maximum a posteriori
MCF	minimum cost flow

MIAS	multi-temporal interferometry based on amplitude similarity
ML	maximum likelihood
NCC	normalised cross-correlation
NN	nearest neighbour
NRCS	normalised radar cross section
NRT	near real-time
OLS	ordinary least squares
OMP	orthogonal matching pursuit
PCA	principal component analysis
PDF	probability density function
PS	persistent scatterer
PSC	persistent scatterer candidate
PSI	persistent scatterer interferometry
radar	radio detection and ranging
RCS	radar cross section
RSS	residual sum of squares
SAR	synthetic aperture radar
SBAS	small baseline subsets
SL1MMER	Scale-down by L1-minimisation, Model selection and Estimation Reconstruction
SLC	single look complex
SNAPHU	Statistical-cost, Network-flow Algorithm for Phase Unwrapping
SNR	signal-to-noise ratio
StaMPS	Stanford method for persistent scatterers
TLS	terrestrial laser scanner
TomoSAR	tomographic synthetic aperture radar
TRI	terrestrial radar interferometer
TSVD	truncated singular value decomposition
UAV	unmanned aerial vehicle
WLS	weighted least squares

List of Symbols

Physical generalities

σ	Radar cross section
σ_0	Normalised radar cross section
c	Speed of light in vacuum
F	Doppler frequency
H	Humidity
h	Water level
N	Refractivity index
N_{dry}	Dry part of the refractivity index
N_{wet}	Wet part of the refractivity index
P	Pressure
T	Temperature

Mathematical generalities

$\mathbb{Z}$	Integer numbers
$\mathbb{R}$	Real numbers
$\mathbb{C}$	Complex numbers
i	Imaginary unit
$\mathbb{E}$	Expectation
σ	Standard deviation
V	Circular variance
W	Spatial or temporal window
med	Median

tr	trace operator
rk	rank operator
∇	gradient operator
$\langle ., . \rangle$	Scalar product
$\lvert . \rvert$	Absolute values for numbers or cardinal for sets
$\lVert . \rVert_p$	L_p-norm
$\mathcal{C}^0$	Space of continuous functions
$\mathcal{W}$	Wrapping operator
$\mathcal{U}$	Unwrapping operator
$\mathcal{U}(a, b)$	Uniform distribution between a and b
$\mathcal{N}(\boldsymbol{\mu}, \boldsymbol{\Sigma})$	Normal distribution with mean $\boldsymbol{\mu}$ and covariance $\boldsymbol{\Sigma}$
(α, β)	Horizontal and vertical angles
J_1	Bessel function of first kind of order one
$\hat{s}^2$	Error variance of least squares fit
$\boldsymbol{\Lambda}$, $\mathbf{V}$	PCA matrices of eigenvalues and eigenvectors
$\mathbf{V}_{2\mathrm{D}}$	Matrix of principal plane transformation
CEV	Cumulative explained variance

IBIS-FM parameters

λ	Wavelength
k	Wavenumber
ρ_r	Range resolution
ρ_θ	Cross-range resolution
B_r	Bandwith of the signal in range
Δt	Temporal sampling
L	Length of the linear scanner
G	Antenna gain
P_t	Transmitted power
P_r	Received power
N_p	Number of pulses

Functional data analysis

$\mathbf{y}$	Observation time series
x	Smooth function to estimate
$\hat{\mathbf{y}}$	Estimated smooth time series

$\mathbf{\Sigma}_{\hat{\mathbf{y}}\hat{\mathbf{y}}}$	Covariance matrix of the estimated smooth time series
D^n	Derivative operator to order n
$\mathbf{\Upsilon}$	Matrix of basis functions
$\mathbf{c}$	Basis function coefficients
$\mathbf{\Sigma}_{\hat{\mathbf{c}}\hat{\mathbf{c}}}$	Covariance matrix of the estimated coefficients
$\mathbf{R}$	Roughness penalty matrix
λ_{PEN}	Penalty parameter
L	Penalty operator
$\mathbf{H}$	Hat matrix
ν	Degree of freedom

Geocoding

(X, Y, Z)	Global reference frame axis
$(\tilde{X}, \tilde{Y}, \tilde{Z})$	Reduced reference frame to GB-SAR position and orientation
(x, y)	SAR Cartesian coordinates
(r, θ)	SAR polar coordinates
Ψ	GB-SAR orientation
$\mathcal{X}$	Set of parameters for GB-SAR positioning
δ	Offset
σ	Uncertainty
$\gamma_{\mathcal{I}}^{\text{os}}$	Normalised cross-correlation function
$\gamma_{\mathcal{I}_{xy}}^{\text{os}}$	Normalised cross-correlation function in (x, y) geometry
$\boldsymbol{L}$	Line-of-sight vector
$\boldsymbol{N}$	Surface normal vector
η	Relative elevation angle
$\eta_{\text{GB-SAR}}$	Elevation angle of the GB-SAR
θ_i	Incidence angle
κ	Ratio specular diffuse reflection coefficient
$\mathcal{P}_{\text{2D}}^{\text{tomo}}$	Point cloud from tomographic inversion in 2D geometry
$\mathcal{P}_{\text{3D}}^{\text{tomo}}$	Point cloud from tomographic inversion
$\mathcal{P}_{\text{3D}}^{\text{ray}}$	Point cloud from single signal reflection
$\mathcal{T}$	Translation between point clouds
$f_{\text{2D,3D}}$	A priori geocoding function
$f_{\text{3D,2D}}$	A posteriori geocoding function
f_{3D}	Likelihood geocoding function

f_{AP}	Likelihood Antenna pattern function
f_{LOS}	Likelihood LOS function
$P_{\max}$	Maximum probability value in a resolution cell
T	Threshold for multiple geocoding

Interferometry

z	Single look complex value
A	Signal amplitude
μ_A	Mean amplitude
σ_A	Standard deviation on the amplitude
D_A	Amplitude dispersion
φ	Signal phase
ϕ	Interferometric phase
ϕ_f	Filtered phase
ϕ_c	Complement to filtered phase
ϕ_r	Linear range component of the phase
ϕ_{res}	Residual signal
ψ	Unwrapped interferometric phase
ψ_{disp}	Displacement phase component
ψ_{atmo}	Atmospheric phase component
ψ_{repo}	Repositioning phase component
ψ_{spa}	Spatially correlated disturbing phase
ψ_{cor}	Unwrapped phase corrected from spatial model
ψ_{noise}	Phase noise component
ψ_z	Phase due to the elevation of the point w.r.t. the GB-SAR
γ	Coherence
γ_t	Temporal coherence
$\mathcal{S}_p$	Set of similar points to point p
$\boldsymbol{\psi}$	Vector of integrated phases
$\boldsymbol{\psi}_{\mathbf{sbas}}$	Vector of SBAS phases
$\mathbf{G}$	SBAS integration matrix
$\mathbf{A}$	Design matrix
$\mathbf{W}$	Weight matrix
$\mathbf{x}$	Matrix of PSC coordinates in 2D GB-SAR Cartesian system
$\mathbf{x}_{\mathrm{pca}}$	Matrix of PSC coordinates in 2D PCA system

$\mathbf{X}_{\text{PSC}}$	Matrix of PSC coordinates in 3D
$\mathbf{S}$	Structure tensor of the PSC
C_i	i^{th} coefficient of the correction model
N_{PSC}	Number of PSC
$\mathcal{S}_{\text{ini}}$	Initial set of PSC
$\mathcal{S}_k$	Set of PSC for the block k
$\mathcal{T}_k$	Temporal segment covered by the block k
N_{min}	Minimum block size
N_{max}	Maximum block size
N_{ov}	Number of SLC in the overlap of blocks
$\mathbf{d}_{\text{GB-SAR}}$	Displacement map between two epochs from the GB-SAR
$\mathbf{d}_{\text{NM}}$	Displacement map between two epochs from the numerical model
$\Delta\mathbf{d}$	Difference between the GB-SAR and the numerical model
$\Delta\mathbf{d}_r$	Relative difference between the GB-SAR and the numerical model

Tomography

ρ_s	Rayleigh elevation resolution
ρ_s°	Angular elevation resolution
h	Elevation of scattering points w.r.t. the GB-SAR
γ	Reflectivity profile
$b_\perp$	Orthogonal baseline
$\mathbf{g}$	Observation vector
$\mathbf{L}$	Steering matrix
$\mathbf{V}_q$, $\mathbf{\Sigma}_q$, $\mathbf{U}_q$	TSVD matrices of $\mathbf{L}$ truncated at rank q
Q	Number of dominant points in the resolution cell
σ_b	Orthogonal antenna spread
σ_ε	Data noise
σ_{CR}	Cramér-Rao lower bound
λ_{opt}	Lagrange multiplier

Contents

CHAPTER 1

General introduction

1.1 Scientific context

Dams are essential in water resource management, flood control, and hydroelectric power generation. They contribute to 15 % of the total worldwide electricity production [IEA, 2019], representing the first green source of energy. More than 800 000 dams are constructed in the world, with more than 61 000 considered as large dams, with a height over 15 meters [ICOLD, 2020]. The main advantage of dams for electricity production is their great flexibility. This green energy resource is independent of wind and solar enlightenment compared to wind turbines and photovoltaic installations. It is also easier to turn on and off than nuclear power plants. Their ability to quickly respond to peaks in electricity demand makes them a valuable asset in maintaining a stable power grid. This flexibility not only supports energy supply during peak periods but also contributes to grid stability and reliability. Dams also serve as reservoirs, effectively storing water resources for various purposes [Schmutz and Moog, 2018]. In addition to supplying water for agriculture, they provide a source of drinking water for communities, help regulate the continuous water flow for irrigation, and support industrial processes. Furthermore, the controlled release of water from dams can mitigate the impact of downstream flooding events, offering protection to vulnerable regions. Due to their noticeable advantages, the number of dams has been growing impressively fast since 1950, as visible in [Adamo et al., 2020]. However, it is essential to consider that while dams offer numerous benefits, they also have specific environmental and societal impacts. The construction of dams interrupts the river continuity and can alter natural river ecosystems, impacting aquatic habitats, migratory patterns of fishes, and sediment transport downstream [Schmutz and Moog, 2018]. Additionally, sediment accumulation behind dams can reduce their storage capacity over time, necessitating ongoing maintenance.

Monitoring dams is crucial for ensuring public safety, environmental protection, and the long-term integrity of these critical infrastructure systems. With all the collected monitoring data, engineers and experts can detect early warning signs of potential issues such as structural instability, seepage, or erosion. Regular monitoring enables the identification of maintenance and repair needs, ensuring the continuous functionality and safety of dams. Moreover, it helps to safeguard downstream communities and ecosystems by assessing the potential risks of dam failure or the alteration of water flow

patterns. Through diligent monitoring, authorities can take proactive measures, implement appropriate risk mitigation strategies, and ensure the sustainable and reliable operation of dams. Seismic areas are also of major interest for concerned dams, as studies on arch dams exhibited that the dynamic stresses can reach the same magnitude order as those induced by the hydrostatic pressure [Maeso and Dominguez, 1993]. Therefore, the safety precautions and monitoring strategies should not underestimate the effects of earthquakes on dams.

The main contribution of this thesis is to study the added value of ground-based synthetic aperture radar (GB-SAR) monitoring in dam surveillance. Currently, dams are monitored with several geodetic sensors. According to [Scaioni et al., 2018], the main possible monitoring sensors are collimators, geodetic network with total stations and levelling, Global Navigation Satellite System (GNSS) antennas, terrestrial laser scanners (TLSs), GB-SAR and satellite synthetic aperture radar (SAR). Moreover, a classical geotechnical measurement tool for dam displacements is the pendulum, as described in [Wieland and Kirchen, 2012]. Each instrument has advantages and disadvantages, and a concise and efficient summary is available in [Chrzanowski et al., 2011].

Method	T. reso.	S. reso.	Accuracy	Dimension	Readiness level
Geodetic net.	low	medium	high	1D-3D	operational
Plumblines	high	low	highest	3D	operational
GNSS	highest	low	high	3D	additional
Satellite SAR	medium	high	medium	1D-2D	additional
TLS	low	highest	medium	3D	experimental
GB-SAR	high	very high	high	1D-3D	experimental

Table 1.1: Qualitative evaluation of geodetic measurement systems for dam monitoring. T. reso. and S. reso. are the temporal and spatial resolutions, respectively.

Table 1.1 presents a qualitative overview of the different methods for dam monitoring. The purpose is not to give an exact review of the characteristics of the different sensors but to understand the strengths and weaknesses of each one. The most used techniques are the geodetic networks and the plumblines. While they present a significant lack of temporal and/or spatial resolution, their outstanding reliability ensures their usage for long-term monitoring. GNSS emerges as a novel tool for dam monitoring, but its characteristics are very similar to plumblines. The main drawbacks are the lower accuracy and measurements only feasible on the dam crest, moreover requiring elaborate processing to reach the millimetre accuracy. As a benefit, GNSS provides an absolute displacement, which is valuable knowledge. Satellite SAR is the most varying system, depending on the satellites available. While Sentinel-1 offers free data with a resolution of $2\,\mathrm{m} \times 13\,\mathrm{m}$, with TerraSAR-X, it is possible to achieve a resolution of $0.5\,\mathrm{m} \times 1\,\mathrm{m}$ [Mittermayer et al., 2012], which is higher than the one achieved with traditional GB-SAR. Only the line-of-sight (LOS) displacement can be estimated if only one orbit is available. If ascending and descending orbits are processed, the 2D displacement can be recovered in the *east-up* plane. Over other techniques, the GB-SAR is known for its high spatial and temporal coverage, combined with a high accuracy over short periods. However, its main drawbacks rely on the one dimensional (1D) displacement measurement, coupled with an accuracy over a long period of observations that still needs to be assessed due to potential phase unwrapping errors and atmospheric disturbances. The three dimensional (3D) displacement vector can only be achieved when multiple measurements (with a single or multiple instrument(s)) from different points of view are available.

The main potential of the GB-SAR is currently exploited for open-pit mine and landslide monitoring. The aforementioned disadvantages are less relevant in the case of detecting unexpected, fast, and

strong displacement at specific locations. Even if it has already been used, GB-SAR has not yet achieved widespread usage for dam monitoring, mainly because of constraints induced by the nature of the measurements. According to [Pieraccini and Miccinesi, 2019], more than half of the papers published in the domain of the GB-SAR concerns open-pit mine or landslides, and only five per cent deal with dams.

The initial application of the GB-SAR technique for monitoring dams was pioneered by [Tarchi et al., 1999]. In their study, measurements were conducted biweekly over three months, using the GB-SAR system presented in [Rudolf et al., 1999]. Although no explicit details regarding the specific processing steps employed were provided, the results obtained over the three months were consistent with the data obtained from pendulum-based measurements. To explore the potential for continuous monitoring, [Alba et al., 2008] and [Di Pasquale et al., 2013] further investigated the application of the GB-SAR technique. Their studies demonstrated a consistent correlation between GB-SAR results and measurements obtained using conventional instruments. However, these investigations focused on short-term monitoring, with measurement duration of 37 hours and 3 days, respectively. More recent developments in dam monitoring using GB-SAR were presented in [Wang et al., 2020a], [Qiu et al., 2020], and [Xiang et al., 2019]. These studies showcased the capability of GB-SAR to measure even micro deformations accurately. However, similar to previous works, the measurement duration in these studies did not exceed ten days. [Talich, 2016] conducted the continuous monitoring of a dam over one month, showing a strong correlation between the dam's displacement and the water level.

For epoch-wise monitoring of dams, [Mascolo et al., 2014] and [Jenkins et al., 2012] showed that the coherence remains high over multiple months between terrestrial radar interferometer (TRI)[1] acquisitions and displacement maps are extractable. The work of [Jacquemart and Meier, 2014] and [Wieser et al., 2020] are considered as a reference for this thesis as their studies show a lot of potential regarding the usage of TRI for dam monitoring, but also a lot of challenges that are not yet solved for further and intensive use of these systems. Therefore, the ability of GB-SAR for epoch-wise or continuous monitoring over several weeks was already demonstrated. However, dam monitoring needs to be developed and reliably conducted for years. Indeed, according to [Chouinard and Roy, 2006], a hydro-power dam is affected by three main causes of deformation: the water load, the air temperature, and time (also called irreversible effect). The first two have an approximate period of one year, while the third one is only noticeable after a longer time. The previously mentioned study also showed that a frequency sampling greater than six times a year does not help to have a better regression of classical dam displacement models. However, an additional value of the GB-SAR about dam monitoring is for the safety assessment, as it will help to detect quick and unexpected movements. Indeed, many large dams are located on active seismic faults. Moreover, they can themselves induce seismicity, as well explained in [Simpson et al., 1988]. The GB-SAR can be a valuable tool to understand the induced deformation due to the availability of acquisitions shortly before and after an induced earthquake.

The main case study used throughout this thesis is the Enguri Dam in Georgia. Indeed, the work realised is a part of the Dams and Induced Seismicity —Technology for Risk Reduction (DAMAST) project. It is an interdisciplinary project combining various measurement tools for dam safety assessment. The Institute of Photogrammetry and Remote Sensing from the Karlsruhe Institute of Technology (KIT) is responsible for the local deformation monitoring via a GB-SAR system. Other institutions from the KIT are responsible for sedimentation assessment, regional deformation, and seismic monitoring to assess faults and stress. More information about the project can be found in

[1] Terrestrial radar interferometer is the most general class of instruments. GB-SAR is part of the TRI sensors, but other TRI exist based on real antennas or multiple input multiple output (MIMO) antennas. [Caduff et al., 2015]

[Mueller and Strauss, 2019]. The GB-SAR system was installed in April 2021 and is still acquiring data at the time of writing this thesis.

1.2 Thesis objectives

The main objective of this thesis is to optimise the possibilities offered by a GB-SAR system for infrastructure monitoring through advanced processing. The measurements lead at Enguri Dam in Georgia exposes a lot of challenges that need to be overcome to take advantage of the full potential offered by GB-SAR measurements. This thesis presents innovative approaches and methods in various domains to provide a solution for each challenge. The main aspects treated are the following:

- To develop an autonomous algorithm to localise and orientate the GB-SAR system precisely. Currently, the system is positioned via an exterior measurement tool, as GNSS or total station, on the external 3D model of the observed scenario. However, external devices can generally not provide an accuracy high enough to orientate the GB-SAR system. Sometimes, none of these measurement tools are available, and the operator needs to visually estimate the system's location on the 3D model. Enhancing the accuracy of the orientation and location of the system is the first step required for further processing.
- Due to the complex geometry of dams and the particular distortions induced by SAR observations, especially the layover and the foreshortening, the estimation of the real-world position of the scatterers is sometimes ambiguous. A solution to estimate their position is required to fully understand deformation maps in complex scenarios.
- Improving the processing of epoch-wise GB-SAR monitoring in complex scenarios is also of major interest. Indeed, due to the valley in front of the dams, choosing an ideal station for monitoring is not always possible. In the case of non-optimal views on the monitored object, new algorithms must be developed to enhance the system's coverage.
- The robustness of the interferometric processing chain for long-term geodetic monitoring is the major lack in current GB-SAR processing strategies. For long-term monitoring, more than several hundred thousand images are available. Therefore, the probability of one or several unwrapping errors is very high and ways to reduce them as much as possible must be developed and implemented. Due to a large amount of the processed data and the signal processing, the drift of the estimated time series w.r.t. the raw measurement should also be minimised.
- The GB-SAR results should be compared to other methods for both epoch-wise and long-term monitoring. For this assessment, numerical models and GNSS antennas installed on the dam crest provide valuable information.

1.3 Outline

This thesis is organised into three main parts, each one containing two chapters:

- **Part 1: GB-SAR and data presentation**

  Chapter 2 is dedicated to the presentation of the GB-SAR system, the information contained in the observed signal, as well as the main processing chains and algorithms currently existing for GB-SAR data analysis. Following the state of the art, possible optimisation directions are also presented at the end of the chapter.

  Chapter 3 presents the main case study used in this thesis: the Enguri Dam. Moreover, some concepts about dams' deformation mechanisms are also evoked. The measurement concept with different GB-SAR observation stations is shortly presented to give an overview of the available dataset.

- **Part 2: Geometry**

  Chapter 4 contains the development of a new method to automatically estimate the external parameters of the system, i.e. its location and orientation w.r.t. a georeferenced 3D model. This step is significant, especially when the targets are far from the sensor. It is based on a new ray tracing algorithm and tomographic acquisitions. Corner reflectors are used to assess the validity of the method.

  Chapter 5 deals with a new geocoding algorithm developed to improve the interpretation of the deformation results. Considering the incidence angle and the antenna pattern, this method is based on a Bayesian model to search for the most plausible 3D position of the observed image pixels. If tomographic data are available, the geocoding model considers the output to enhance the model.

- **Part 3: Interferometry**

  Chapter 6 is dedicated to methods for analysing epoch-wise monitoring from diverse points of view. New approaches are presented to propose the recovery of very complex signals due to distorted acquisition geometries. The results are compared to two numerical models calibrated on the plumblines data to assess the validity of the methodology.

  Chapter 7 presents two strategies based on continuous observations with the system. The first method enables slow deformation monitoring based on daily averaged observations. The emphasis is made on minimising long-term drifts to be able to use the GB-SAR as a geodetic sensor. The results of this method are compared to one numerical model and GNSS data. The second method ensures near real-time monitoring, with access to the integrated time series, at the cost of the number of reliable points observed.

Part 1 is an essential step to understand the context of the following work through a comprehensive portrayal of the system and the main test site, avoiding excessive intricacy. Part 2 focuses on the system's geometry and the interpretation of GB-SAR results. The reader more interested in the interferometric processing part of the thesis can directly continue with Part 3, assuming a precise georeferencing and geocoding of the processed data. Finally, Chapter 8 provides a conclusion of the research by highlighting the advancements of the proposed approaches, addressing remaining deficiencies and offering insights into potential avenues for future investigations.

CHAPTER 2

Ground-based SAR and InSAR principle

Contents

2.1 Introduction

This chapter presents a general overview of the SAR technique, focusing on ground-based systems. The main subject of this thesis is the application of the GB-SAR within a specific context rather than proposing improvements to the system itself. Consequently, only the necessary concepts and results valuable for the comprehension of this work are explained. For a more extensive exploration of SAR systems, a thorough presentation can be found in [Curlander and McDonough, 1991] or [Oliver and Quegan, 2004]. A detailed examination of the SAR image formation is presented in [Cumming and Wong, 2005].

The first section provides a concise summary of the history of the system and its imaging concept. Following that, the radio detection and ranging (radar) equation and the radiometric properties of the radar image are summarised, as these properties play a crucial role in future chapters, particularly in the simulation of GB-SAR images. The third part focuses on the geometric properties of GB-SAR images by presenting the link between the 2D image and the 3D world. The fourth section emphasises the properties of interferometric synthetic aperture radar (InSAR) and its utility in monitoring applications. Notably, the statistical properties of the observed signal are presented. Finally, a brief overview of the recent advances in GB-SAR processing concepts is delivered. The chapter concludes by recapitulating the key parameters of the system used in the case studies: the Image By Interferometric Survey - Frequency Modulated (IBIS-FM) sensor from the company Ingegneria Dei Sistemi (IDS) Georadar.

2.2 GB-SAR principle

2.2.1 History and concept

The history of SAR systems can be traced back to the invention of the radar in 1904, as noted in [Griffiths et al., 2019]. Yet, it was during the Second World War that its full potential emerged, exploited for military purposes to anticipate the movements of adversaries. The primary objective of this technology is to measure the distance between an emitter and an object or target. It operates by sending out an electromagnetic wave in a specific direction, which gets reflected by the object. By measuring the temporal delay between the transmission and reception of the signal, it is possible to estimate the desired distance precisely. For example, considering a system that emits a signal with the speed of light c at time $t = t_0$, reaches the target at time $t = t_1$, and detects the reflected signal at $t = t_2$, the distance r between the emitter and the object can be determined using the subsequent formula:

$$r = \frac{c\,(t_2 - t_0)}{2} \tag{2.1}$$

The presence of the factor two in the denominator arises from the two-way path of the electromagnetic signal. This equation is illustrated in Figure 2.1.

The fundamental radar principle enables the retrieval of responses in a single dimension, resulting in a range profile as measurement output. The SAR is a particular type of radar invented in 1954 [Wiley, 1985]. The main characteristic of this tool lies in its moving transmitter along an orthogonal trajectory relative to the observed scene, thereby synthesising an augmented antenna size. Initially conceived for satellite systems to avoid the very small resolution in azimuth, arising from the too small ratio between mechanic antennas and range to the observed scenario, the concept has been

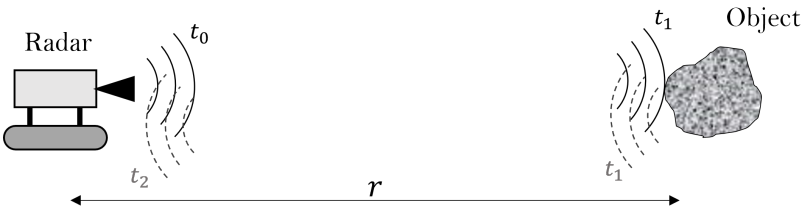

Figure 2.1: Schema of the radar principle. Full waves indicate the emitted signal, and dashed waves indicate the reflected signal.

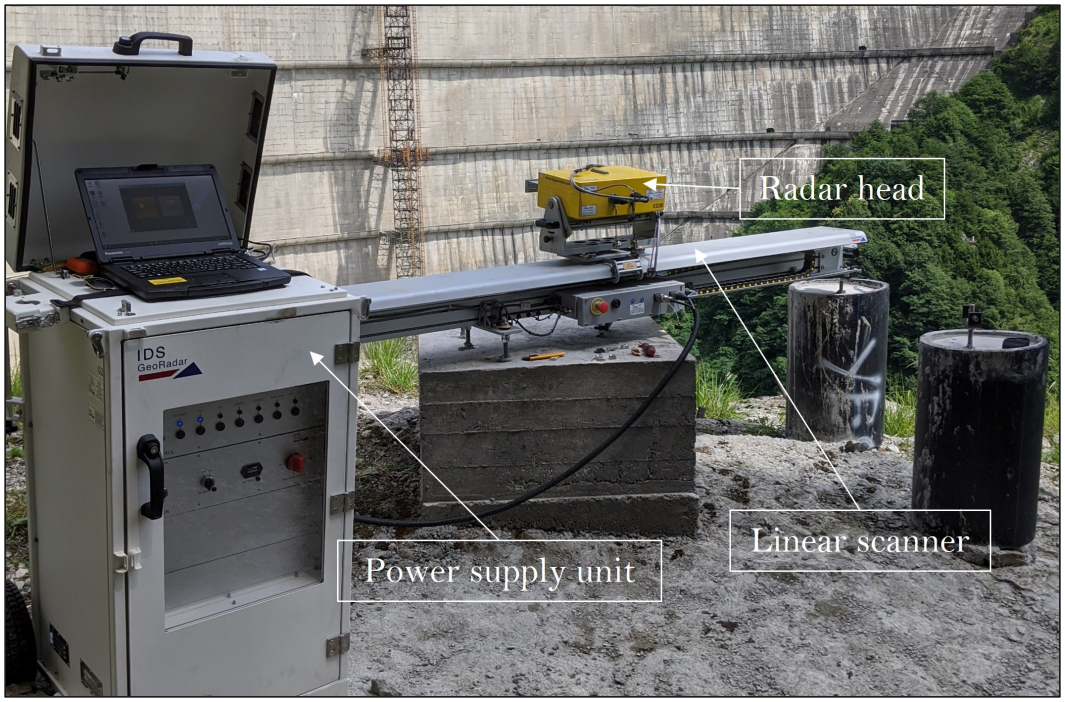

Figure 2.2: Three main components of a GB-SAR system: the radar head, the linear scanner and the power supply unit.

adapted to ground-based platforms. This extension enables the monitoring of local scenarios with very high-resolution radar systems.

A GB-SAR is a specific instrument in the family of the terrestrial radar interferometer (TRI), and not all of the possible terrestrial sensors are based on the SAR technology, as described in [Pieraccini and Miccinesi, 2019]. Although mechanical and electrical characteristics may diverge, the core concept of the TRI systems centres around obtaining a radar image. In this work, our focus remains exclusively on GB-SAR systems. These instruments are grounded on three primary components, as depicted in Figure 2.2. The radar head functions as a sensor, managing signal transmission and reception and moves along the linear scanner to synthesise the larger antenna. The power supply unit encompasses various logistical elements, including batteries and a controller notebook. Additionally, it is crucial to install the instrument on a stable concrete foundation for long-term monitoring purposes. This configuration ensures the proper operation and stability of the GB-SAR system, allowing for accurate data acquisition and reliable monitoring over extended periods.

Band	Frequency [GHz]	Wavelength [cm]	Typical application
W	75 - 110	0.3 - 0.4	Short range GB-SAR
V	40 - 75	0.4 - 0.8	Short range GB-SAR
Ka	27 - 40	0.8 - 1.1	Rarely used for SAR
K	18 - 27	1.1 - 1.7	Rarely used for SAR
Ku	12 - 18	1.7 - 2.4	Satellite altimetry or GB-SAR
X	8 - 12	2.4 - 3.8	High resolution SAR (urban monitoring)
C	4 - 8	3.8 - 7.5	Global deformation mapping
S	2 - 4	7.5 - 15	Little but increasingly use
L	1 - 2	15 - 30	Geophysical monitoring - biomass mapping
P	0,3 - 1	30 - 100	Experimental

Table 2.1: SAR bands used in remote sensing and their corresponding applications.

Radar instruments operate within the microwave domain, with various frequency bands available. A summary of commonly employed frequency bands in radar remote sensing is provided in Table 2.1, as documented in [Flores-Anderson et al., 2019]. GB-SAR systems typically operate within the Ku or X band, as highlighted by [Crosetto et al., 2013]. This choice implies a smaller wavelength than satellite SAR, resulting in heightened sensitivity to displacement phenomena. However, it also increases the sensitivity of GB-SAR systems to atmospheric changes, as shown in [Zebker et al., 1997], which decreases the measurement accuracy.

2.2.2 Resolution of a GB-SAR system

In the case of the SAR, the transmitting unit emits a chirp signal characterised by a continuous and linear frequency modulation. The ability of the system to separate two targets lying on different distances is defined by the range resolution ρ_r, which is inversely proportional to the bandwidth of the emitted signal B_r. This relationship can be expressed as follows:

$$\rho_r = \frac{c}{2\,B_r} \tag{2.2}$$

A larger bandwidth implies a smaller value for ρ_r and, therefore, a higher resolution. Through the acquisition of data from different positions on the linear scanner, the system also discerns distinct targets along the cross-range direction. This process synthesises an acquisition, as it would have been done by a system with a real antenna of length $2L$. The angular resolution of the system called cross-range resolution ρ_θ, sending a signal with the wavelength λ is given with:

$$\rho_\theta = \frac{\lambda}{2\,L} \tag{2.3}$$

To obtain the final image, it is necessary to focus all the acquisitions made on the rail. The concept of focusing is extensively explained for satellite SAR in [Hein, 2010] and is illustrated for the GB-SAR case in [Rödelsperger, 2011]. Generally, the algorithms used for focusing entail advanced algorithms like match filtering or chirp scaling. Following this step, a complex number $Ae^{i\varphi}$ is stored in each pixel, providing two exploitable observations: the amplitude A and the phase φ. The amplitude provides more information about the nature of the scatterer [Monserrat et al., 2014], while the phase

is more relevant for geodetic tasks, as it contains the distance information. The obtained acquisition is denoted as a single look complex (SLC) image.

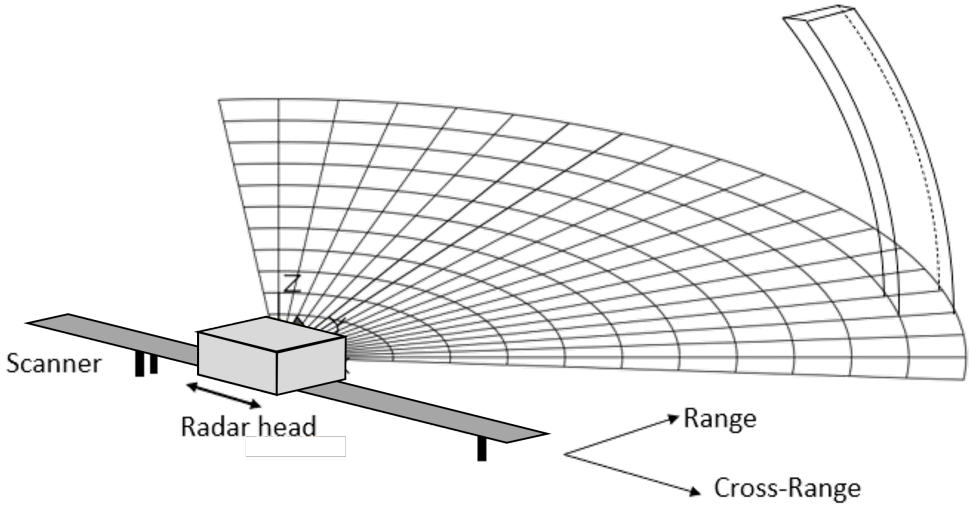

Figure 2.3: Imaging concept of the GB-SAR. The 2D grid represents the geometry of the received image. The 3D shape represents all the information of the 3D world projected in a pixel.

Figure 2.3 illustrates the acquisition grid of the GB-SAR. Compared to conventional optical imaging systems, the 3D volume depicted over one pixel is a distinctive characteristic of GB-SAR images. Section 2.4 delves into this topic, specifically exploring the volume formed by the intersections of geometrical shapes to create it. All scatterers within this volume contribute to the observed signal in the pixel.

2.3 Radiometry of GB-SAR images

As the amplitude plays a secondary role in displacement monitoring, only a short introduction about the *radar equation* suffices to understand the interferometric process. However, some concepts developed in this work are also based on the amplitude received by the radar system, especially the development of a GB-SAR image simulator presented in Chapter 4, requiring a more extended presentation of the radiometry. The first part of the section is focused on the *radar equation*, and the second part introduces the radar cross section (RCS) more extensively.

2.3.1 Radar equation

This well-known equation establishes the relationship between the power transmitted by the system P_t and the received power P_r after interacting with a scatterer. The latter is influenced by various factors, including the wavelength λ, the antenna gain G, the distance to the target r, and the RCS of the target σ. The antenna gain represents the antenna's ability to convert input power into radio waves directed in a specified direction. For a single-pulse radar, the simplified form of the *radar equation*, as stated in [Barton, 2013], is given by:

$$P_r = P_t \frac{G^2 \lambda^2 \sigma}{(4\pi)^3 r^4} \tag{2.4}$$

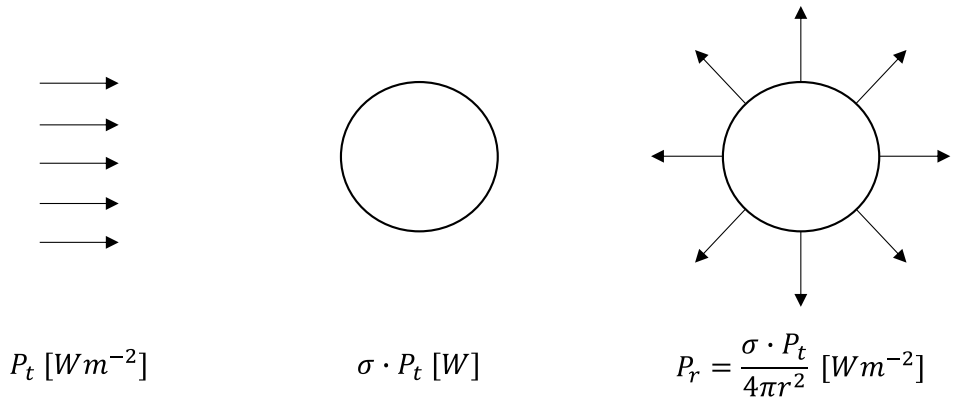

Figure 2.4: Intuitive derivation of the RCS from [Knott et al., 2004].

Equation 2.4 is the simplified version, assuming that the sending and receiving antenna is the same. Additionally, it presupposes an absence of signal loss along the radar-target path. In the case of the SAR, the same target is illuminated by N_p pulses, resulting in a higher received power compared to a conventional radar system, expressed as follows:

$$P_{r,\text{SAR}} = P_r N_p \tag{2.5}$$

Only two variables remain independent of the system's design in this equation: the distance r and the RCS σ. The former is extracted from the coordinates on the radar image, while the latter is subject to many parameters and requires a more extensive presentation.

2.3.2 Radar cross section

The RCS σ plays a critical role in Equation 2.4. A comprehensive explanation of this quantity can be found in [Knott et al., 2004]. The primary definition of the RCS is given by the following limit:

$$\sigma = \lim_{r \to \infty} 4\pi r^2 \frac{P_t}{P_r} \tag{2.6}$$

This equation can be intuitively understood from the interpretation illustrated in Figure 2.4. The radar transmits an initial signal with power P_t that illuminates an object with a certain cross-sectional area, thereby accumulating an energy of σP_t. Subsequently, the target re-radiates this energy isotropically, explaining the factor $4\pi r^2$, which corresponds to the surface area of a sphere. While the isotropic reflection assumption might not hold for all objects, the definition is grounded on it. Moreover, the limit is often negligible to simplify the understanding of the equation. Indeed, in most cases, the target is considered in a far-field position w.r.t. the transmitter and receiver. Yet, with this assumption, we have $P_r \propto r^2$ such that the limit disappears.

The RCS depends on different factors such as:

- the position of the sensor relative to the target
- the target geometry
- the target material composition

- the frequency and wavelength of the signal
- the polarisation

Depending on the wavelength, three scattering regimes can be defined based on the relative size of the object L_0 w.r.t. the wavelength λ. The Rayleigh region corresponds to the case where $\lambda \gg L_0$, the resonant region represents the case where $\lambda \sim L_0$, and the optics region applies when $\lambda \ll L_0$. Since we are considering monitoring large infrastructures using a Ku-band system with $\lambda \approx 1.7\,\text{cm}$, we will briefly focus exclusively on the optics region.

Determining the RCS for complex shapes is challenging, as it requires solving Maxwell's equations, and analytical solutions are only conceivable for simple shapes. Further details and some examples are developed in [Knott et al., 2004].

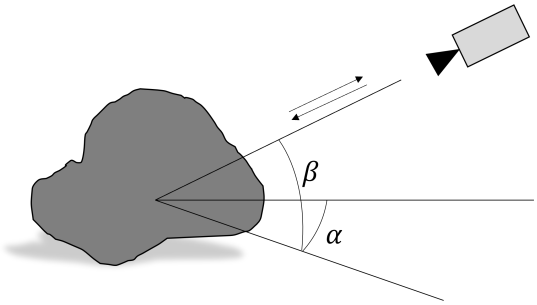

Figure 2.5: Horizontal and vertical angles for the RCS. The reference is the direction yielding the highest RCS.

In Table 2.2, the values of the maximal RCS for the sphere, cylinder, plate and triangular corner reflector (CR) are presented. Those values correspond to the maximal RCS for smooth, perfectly conducting objects (e.g. metallic objects) and with the optimal viewing direction. The decrease of the RCS w.r.t. horizontal and vertical angles given in Figure 2.5 is also provided.

Shape	Max. RCS $\sigma_{\max}$	Vert. angular response β	Hz. angular response α
Sphere	πR^2	independent	independent
Cylinder	$\frac{2\pi ab^2}{\lambda}$	$\left(13\frac{\lambda}{b}\right)^\circ$ for $\sigma = \frac{1}{2}\sigma_{\max}$	independent
Plate	$\frac{4\pi a^2 b^2}{\lambda^2}$	$\left(13\frac{\lambda}{b}\right)^\circ$ for $\sigma = \frac{1}{2}\sigma_{\max}$	$\left(13\frac{\lambda}{b}\right)^\circ$ for $\sigma = \frac{1}{2}\sigma_{\max}$
Triangular CR	$\frac{4\pi a^4}{3\lambda^2}$	Approx. 40° for $\sigma = \frac{1}{2}\sigma_{\max}$	Approx. 40° for $\sigma = \frac{1}{2}\sigma_{\max}$

Table 2.2: Summary of the RCS of different elementary shapes. For the sphere, R corresponds to its radius. For the cylinder, a is the radius of the main disk, and b is the height. For the plate, a and b correspond to the rectangle's length and width. For the triangular CR, a is the length of a side. In the two left columns, the values give the first angle for which the RCS equals half its maximal value. From [Ralph, 2012].

These analytical solutions are not tractable for more complex shapes such as cars, flights or infrastructures. In [Skolnik, 2008], several approximate methods are presented, and the two most famous are the geometric optics and the physical optics (PO). The first theory is based on energy conservation within a virtual tube called a ray. Under several assumptions, the RCS of a body surface at a

specular point (a point on the surface where the angle of reflection equals the angle of incidence) is given by:

$$\sigma = \pi a_1 a_2 \tag{2.7}$$

with a_1 and a_2 the radii of curvature of the body surface at the specular point. Nonetheless, this approximation does not hold for flat surfaces, where the radii of curvature are infinite, consequently rendering the RCS infinite as well.

The observed object can take on either a flat or singly curved shape in employing the PO approximation. This approach relies on two key assumptions: the far-field assumption and the tangential plane approximation. With these hypotheses, the RCS of a circular metal disk can be expressed as:

$$\sigma = 16\pi \left| \frac{A\cos(\theta)}{\lambda} \frac{J_1(kd\sin(\theta))}{kd\sin(\theta)} \right|^2 \tag{2.8}$$

where A is the surface of the disk, d is its diameter, k is the wavenumber, and J_1 is the Bessel function of the first kind of order 1.

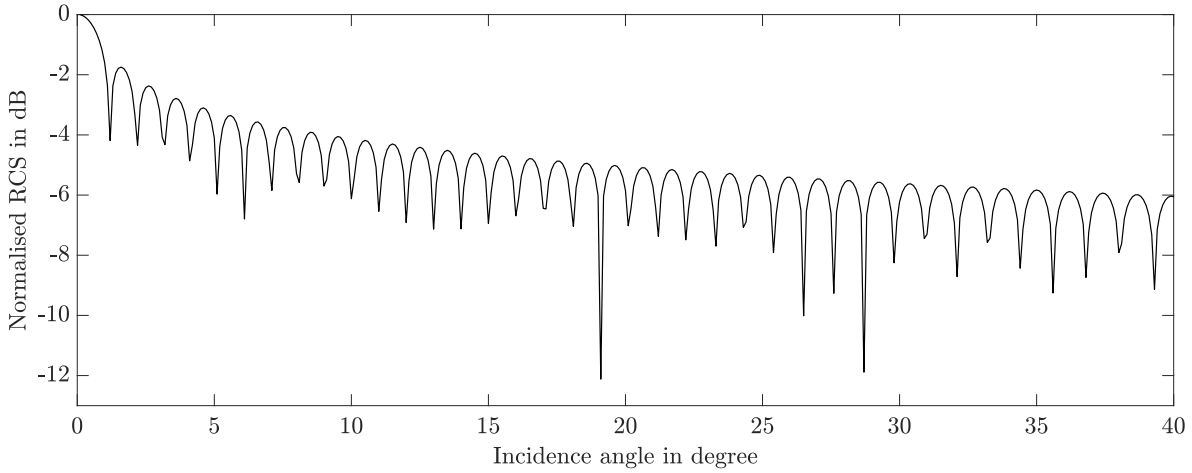

Figure 2.6: RCS of a metallic disk as a function of the incidence angle.

Figure 2.6 displays the RCS of the metallic disk as a function of the incidence angle. One noticeable trend is the general decrease in RCS as the incidence angle increases. A recurring pattern featuring pronounced negative peaks is also discernible due to the zeroes of the Bessel function and is a typical diffraction phenomenon. This highlights the complexity of RCS computation and underscores the challenges that persist within radar signal processing.

Thus far, we have focused solely on the geometric aspects of the observed object. Nevertheless, its material composition holds equal significance in influencing scattering phenomena. For instance, metallic structures exhibit notably stronger reflective characteristics than vegetation or bare soil. As outlined in [Knott et al., 2004], the reflectivity coefficient captures this relationship by expressing it as a function of the material's relative permeability and permittivity. However, it is essential to note that establishing a precise and comprehensive relationship between the material properties and RCS falls beyond the scope of this thesis.

2.4 Geometry of linear GB-SAR images

The specific geometry of GB-SAR images can be distinguished in two main facets. The first encompasses the projection of a point in the 3D world into the two dimensional (2D) radar image. The second aspect expresses the distortions induced by this particular geometry. These two aspects are subsequently illustrated in this section.

2.4.1 Demonstration of the particular GB-SAR geometry

The geometry of GB-SAR images exposes specific properties. As a SAR system, the pixel coordinates are derived through time-delay measurements for the range component and via Doppler frequency measurements for the cross-range part. The Doppler frequency contributes to the formation of isocones with the GB-SAR position as their apexes and the linear scanner as the principal axis.

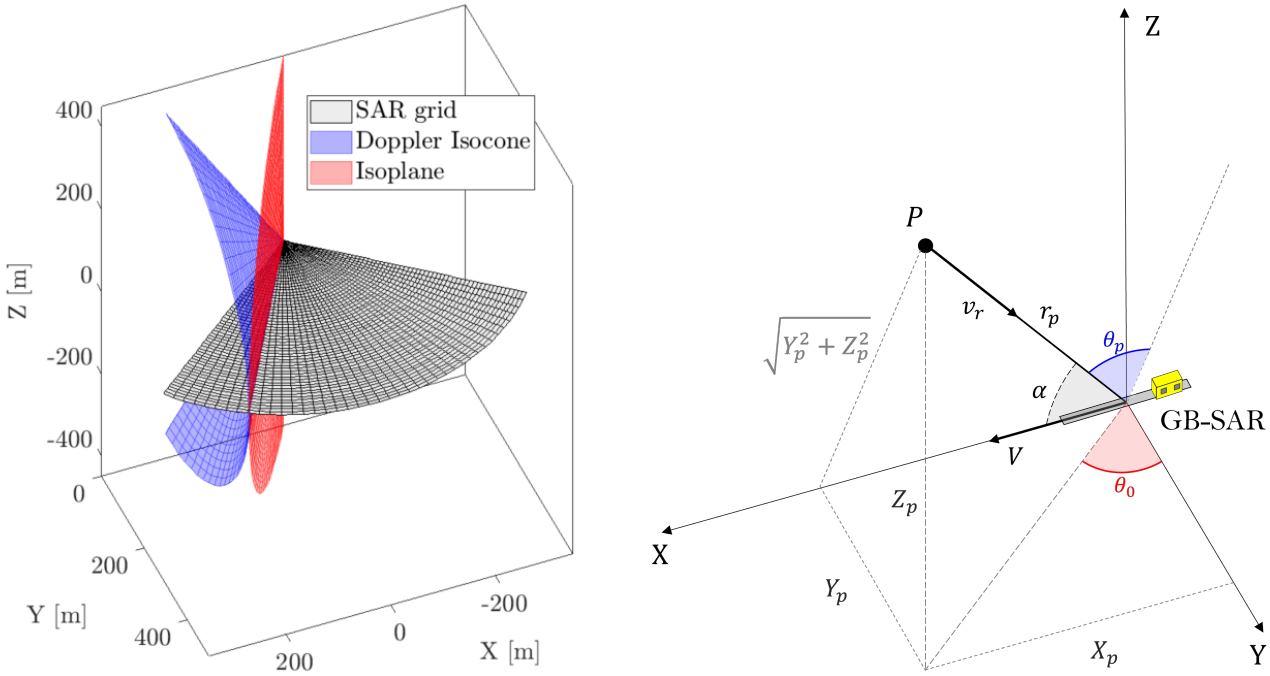

(a) Isocone and isoplane of a cross-range profile

(b) Projection geometry of a GB-SAR

Figure 2.7: Projection geometry of the GB-SAR images. (a) represents the planar approximation and the true cone projection. (b) is a schema to explain the physical reason leading to this projection.

For the description of this paragraph, all the mathematical quantities refer to Figure 2.7b.

In many cases in the literature, as in [Monserrat Hernández, 2012] or in [Cai et al., 2021], the link between the 3D coordinates (X_p, Y_p, Z_p) of a point P and its radar coordinates (r_p, θ_0) is established through the following expressions:

$$\begin{cases} r_p &= \sqrt{X_p^2 + Y_p^2 + Z_p^2} \\ \theta_0 &= \arctan\left(\frac{X_p}{Y_p}\right) \end{cases} \tag{2.9}$$

However, the formation of the SAR image is achieved via Doppler measurements. The Doppler frequency F for a point P in the scanned scene depends on its observed radial velocity v_r. Assuming that the point is stationary in the scene, its velocity is a function of the radar head velocity V, the transmitted wavelength λ, and the direction of the LOS vector. The Doppler frequency F is given by Equation 2.10, as mentioned in [Hein, 2010]:

$$F = -2\frac{v_r}{\lambda} = 2\frac{V\cos(\alpha)}{\lambda} \tag{2.10}$$

This frequency is crucial in determining the cross-range resolution, as highlighted in [Méric et al., 2009]. The latter work concentrates on satellite SAR with the approximation of the satellite path as a local linear trajectory. Therefore, the results can be applied to the linear GB-SAR, given the identical measurement concept. Since both V and λ are constant, the frequency depends solely on α, which is the angle between the X-axis and the LOS vector to point P. It can be calculated as:

$$\alpha = \arctan\left(\frac{\sqrt{Y_p^2 + Z_p^2}}{X_p}\right) \tag{2.11}$$

Equation 2.11 defines a cone with the apex at $(0, 0, 0)$ and the X-axis as the main axis. This indicates that the GB-SAR resolution cells are obtained with the intersection of isospheres from the range measurements and isocones from the Doppler measurements. The final functions which are used in this manuscript to link 3D world coordinates (X, Y, Z) with radar coordinates (r, θ) are given by:

$$\begin{cases} r_p &= \sqrt{X_p^2 + Y_p^2 + Z_p^2} \\ \theta_p &= \arcsin\left(\frac{X_p}{r_p}\right) \end{cases} \tag{2.12}$$

Figure 2.7a depicts a Doppler isocone and a vertical isoplane. All the points in blue have the same Doppler frequency, meaning that they belong to the same cross-range resolution cell. In contrast, the red plane represents the points belonging to the same cross-range plane with $\theta_0 = const.$ according to Equation 2.9.

The last coordinate system consists in the transformation of the (r_p, θ_p) coordinates into Cartesian coordinates (x_p, y_p) via:

$$\begin{cases} x_p = r_p \sin(\theta_p) \\ y_p = r_p \cos(\theta_p) \end{cases} \tag{2.13}$$

This relation also highlights that $x_p = X_p$ and therefore $y_p = \sqrt{Y_p^2 + Z_p^2}$.

2.4.2 Distortion on the GB-SAR image

A GB-SAR image undergoes the influence of three primary distortion effects, namely layover, foreshortening, and shadowing, all of which are well-known phenomena. The significance of these effects is illustrated through a simulation study presented by [Cigna et al., 2014]. Figure 2.8 depicts these three effects. Starting from the left, the first effect portrayed is the foreshortening. In this representation, the elongated distance on the terrain is compressed into a single range bin on the GB-SAR

image plane. The second effect reveals how three distinct areas of the terrain can coincide within the same resolution cell, resulting in the most influential distortion during the interferometric process. This effect mixes the signals from two or more areas within a single resolution cell, making the signal's interpretation challenging. Finally, the shadowing, which corresponds to parts of the terrain not visible by the GB-SAR, is represented in the right part of the figure. No signal is acquired in the corresponding resolution cells, and only the thermal noise of the system is stored.

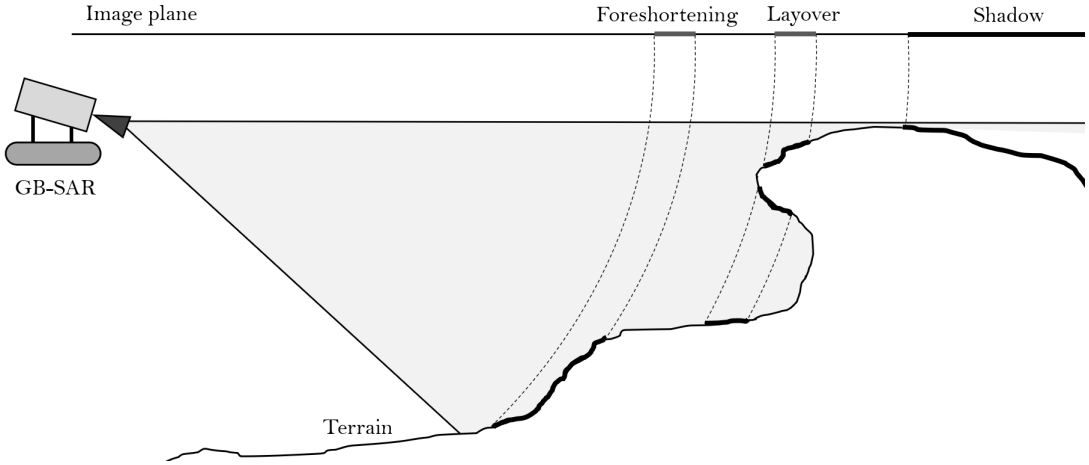

Figure 2.8: Representation of the three imaging distortions of the GB-SAR acquisition. The cross-range is constant, as these effects are only range-dependent.

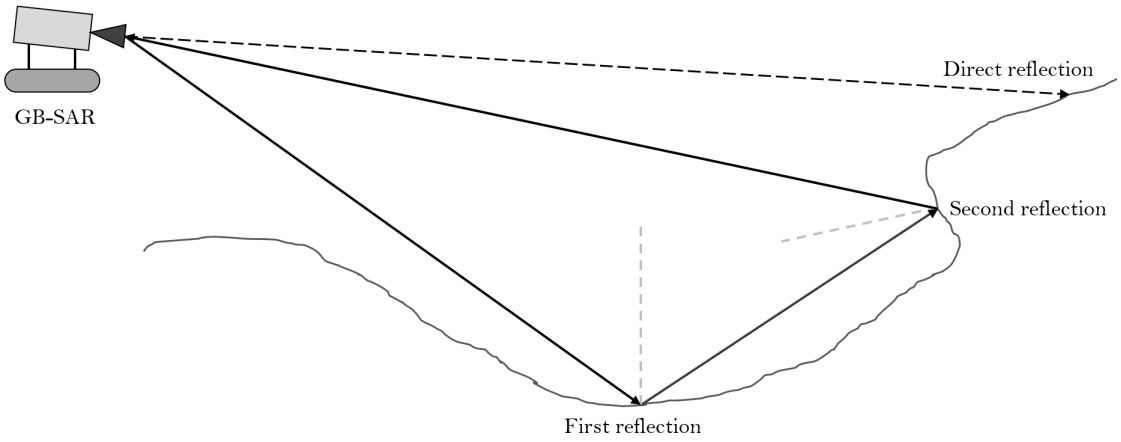

Figure 2.9: Representation of the multiple signal reflection effect in a GB-SAR monitoring scenario. The full line corresponds to a multipath of the electromagnetic wave, while the pointed line corresponds to a single-path trajectory.

Another disturbing effect in the GB-SAR image is the multiple signal reflections. In complex scenarios, the electromagnetic wave may deviate from the direct path *radar-target-radar* and follow a different trajectory within the observed scenario, reflecting on several targets before returning to the sensor. Consequently, Equation 2.1 no longer holds valid. Furthermore, describing a single target within the resolution cell becomes unfeasible, and the phase information can be considerably distorted. The multiple signal reflections occur as demonstrated in the geometry depicted in Figure 2.9.

In the presented scheme, the solid black lines represent the path of a signal undergoing multiple reflections. This signal will be focused in the same pixel as the direct response coming from the black dashed line, as the total path length remains equal. The complex numbers associated with each signal are summed up, rendering their differentiation nearly impossible without supplementary information. This phenomenon arises especially when a lake or other bodies of water are located between the monitored object and the instrument, resulting in the direct specular reflection of the electromagnetic wave. Similarly, in the presence of man-made infrastructures with specific angular structures, multiple reflection signals can be induced, giving rise to this phenomenon. A strong influence of multipath effects on TRI monitoring is presented in [Lucas et al., 2017].

2.5 InSAR principle

InSAR has emerged as a powerful technique with broad applications in remote sensing and geodetic analysis. One of the first employments of InSAR in the literature is the presentation made in [Graham, 1974], first based on airborne systems. This section is dedicated to a brief presentation of the core principles of InSAR and its diverse possibilities. The second part delves briefly into the statistics of the observed signal. Finally, the last part outlines the analysis of several interferograms in a single processing chain to extract relevant information.

2.5.1 Interferometric phase

Originally developed with airborne and spatial sensors, InSAR has evolved to various sensors (car, UAV, terrestrial). The most common configuration is a satellite acquiring an image of an area and coming back several days after, making another acquisition over the same place. Then, two complex images are available for the same region. The concept is similar for ground-based systems, with a considerably higher temporal resolution.

The interferogram formation from the two images is achieved with pixel-wise complex conjugate multiplication. For two complex numbers $z_1 = A_1 e^{i\varphi_1}$ and $z_2 = A_2 e^{i\varphi_2}$, the interferometric phase ϕ is derived as:

$$z = Ae^{i\phi} = z_1\, z_2^* = A_1 e^{i\varphi_1}\, \left(A_2 e^{i\varphi_2}\right)^* = A_1 A_2 e^{i(\varphi_1 - \varphi_2)} \tag{2.14}$$

In satellite InSAR, ϕ contains a lot of contributions, and a clear presentation about it is available in [Bamler and Hartl, 1998]. The phase acquired by GB-SAR systems is simpler due to fewer contributing factors. It has a different representation depending on how the GB-SAR is used. According to [Crosetto et al., 2017], two main configurations can be distinguished:

- **Continuous monitoring**: In this case, the GB-SAR is installed for a long period without being moved and acquires images for several days, weeks, months or years.
- **Discontinuous monitoring**: In this configuration, the GB-SAR is installed to carry out some measurements for one campaign, is removed, and reinstalled at the same place several days, weeks or months after. The accuracy of the repositioning has a strong impact on the observed phase.

The computed signal z is a circular quantity, meaning that the interferometric phase ϕ can only take values in $[-\pi\,;\pi]$ and is defined as wrapped. Therefore, the true phase containing the full

information is the unwrapped phase ψ. The following relation establishes the link between the two quantities:

$$\psi = \phi + 2k\pi \quad k \in \mathbb{Z} \tag{2.15}$$

where k is a whole number and is called the integer ambiguity. Figure 2.10 provides a visualisation of the relation between the wrapped and the unwrapped phase. A complete simulated *sinus* signal is represented with the black curve. Due to the intrinsic properties of the sensor, the acquired phase is wrapped, leading to the observation of the blue curve. The research in the unwrapping topic is currently of major interest and will be further expounded upon in Section 2.6.2.

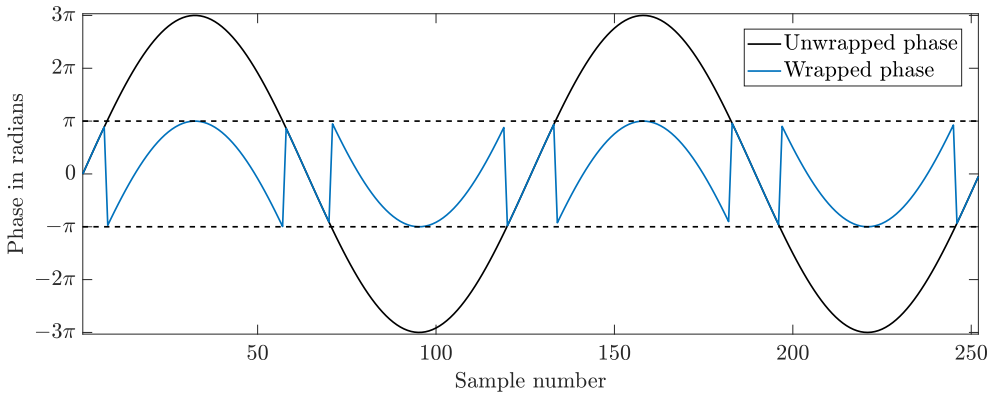

Figure 2.10: Difference between the unwrapped phase in black and its corresponding wrapped phase in blue.

2.5.1.1 Continuous ground-based interferometry

In the case of continuous ground-based interferometry, only three main terms are contained in the observed phase: the displacement component, the atmospheric component and the noise component:

$$\phi = \mathcal{W}\left(\psi_{\text{disp}} + \psi_{\text{atmo}} + \psi_{\text{noise}}\right) \tag{2.16}$$

where $\mathcal{W}$ is the wrapping operator, ψ_{disp} is the phase induced by a displacement, ψ_{atmo} is the phase induced by the change of the atmospheric conditions and ψ_{noise} is the phase noise. The signal of primary interest is denoted by the displacement term, which may exhibit linearity w.r.t. a parameter, e.g. time, or possess a non-specific behaviour.

The atmospheric phase reflects the temporal delay in the electromagnetic wave path between two acquisitions, resulting from variations in atmospheric conditions. The key parameters contributing to this phase component are the temperature (T), the relative humidity (H), and the pressure (P). Then, the model of the atmospheric phase is available in [Iannini and Guarnieri, 2010] and defined by:

$$\psi_{\text{atmo}} = \frac{4\pi}{\lambda} 10^{-6} \int_0^R N(r, t_1) - N(r, t_2) dr \tag{2.17}$$

where R is the range between the radar and the observed point. N is the refractivity index and t_k is the time of the acquisition of image number k. N depends on both time t and location r, and its integration is performed along the *radar-target* trajectory. The relation between the refractivity index N and the usual index of refraction n is $N = (n-1)10^6$. The reference model for the refractivity index is defined in [Iglesias et al., 2013]:

$$N(r,t) = N_{\text{dry}}(T,H,P) + N_{\text{wet}}(T,H,P) \tag{2.18}$$

T, H and P are spatio-temporal functions depending on r and t. The components N_{dry} and N_{wet} represent respectively the dry and wet parts of the refractivity index. According to [Liebe, 1981], the refractivity index N of the atmosphere varies in function of these parameters as the following empirical model:

$$N(P,T,H) = 0.2589\frac{P-e(T,H)}{T} + \left(71.7 + \frac{3.744\cdot 10^5}{T}\right)\frac{e(T,H)}{T} \tag{2.19}$$

with e defined as:

$$e(T,H) = \frac{H}{100}\cdot 6.1016\cdot 10^{\frac{7.5T}{T+237.3}} \tag{2.20}$$

In these equations, T is in °C, P in mbar and H in %. The complexity of the atmospheric phase depends on the variations of these three parameters in the scenario. In the simplest case, the atmospheric parameters vary uniformly on the whole scenario, such that the refractivity index difference ΔN becomes independent of the spatial variable. Consequently, Equation 2.17 can be simplified as:

$$\psi_{\text{atmo}} = \frac{4\pi}{\lambda}10^{-6}\int_0^R \Delta N(t_1,t_2)dr = \frac{4\pi}{\lambda}10^{-6}R\Delta N(t_1,t_2) \tag{2.21}$$

In this case, the atmospheric phase solely depends on the range of the observed point. Section 2.6.3 is dedicated to the existing methods for the correction of the atmospheric signal.

2.5.1.2 Discontinuous GB-SAR interferometry

When a GB-SAR is moved between two measurements, the difference in position and orientation of the sensor contributes to an acquired signal containing more complexity. A coregistration becomes necessary if the movement is significant, exceeding 1/10 of a resolution cell. A comprehensive study outlining the coregistration procedure is provided in [Li et al., 2008], but is not required in this work due to the installation of concrete foundations with anchoring rods.

Secondly, these offsets imply a phase ramp on the whole image. It can be added as an additional phase term ψ_{repo} and increases the complexity of the interferometric phase.

$$\phi = \mathcal{W}\left(\psi_{\text{disp}} + \psi_{\text{atmo}} + \psi_{\text{repo}} + \psi_{\text{noise}}\right) \tag{2.22}$$

A deep investigation into the impacts of various rotation and translation errors is extensively covered in [Hu et al., 2021]. According to this study, the phase term ψ_{repo} at an observed point $P = (X,Y,Z)$ can be approximated as a linear model, as follows:

$$\psi_{\text{repo}} = \frac{X}{r}\varepsilon_X + \frac{Y}{r}\varepsilon_Y + \frac{Z}{r}\varepsilon_Z \tag{2.23}$$

where $\varepsilon_X, \varepsilon_Y, \varepsilon_Z$ are the unknowns disturbing parameters and r is the range of the point. The combination of the repositioning error and the atmospheric component of the phase is responsible for a spatial pattern that can be modelled through various atmospheric models. The regression with least squares over stable areas is the common estimation method.

2.5.1.3 Interferometric phase for height determination

By introducing a known vertical baseline $b_\perp$ between two acquisitions, the height of the scatterers within the resolution cell contributes to the interferometric phase equation [Noferini et al., 2007]. For the following small derivation, we assume no noise, atmospheric change or displacement of the observed point. Then, according to Figure 2.11, it is possible to use the three following relations to derive the expression of the interferometric phase: $\psi_z = 4\pi/\lambda(r_1 - r_2)$, $Z = r_1 \sin(\alpha)$ and the law of cosine $r_2^2 = r_1^2 + b_\perp^2 - 2r_1 b_\perp \sin\alpha$. Using the series expansion of the square root and assuming that $b_\perp \ll r_1$, it is possible to write that:

$$\psi_z = \frac{4\pi}{\lambda}\frac{b_\perp}{r}Z \tag{2.24}$$

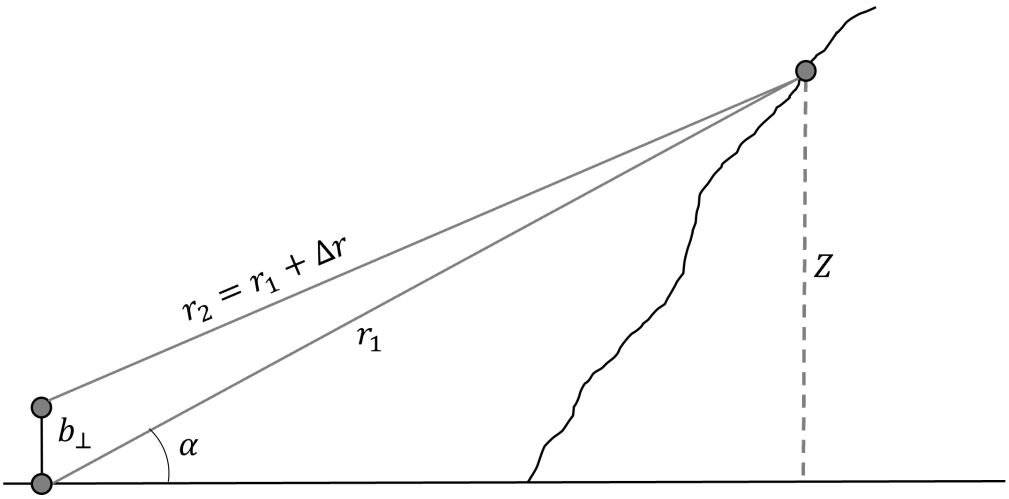

Figure 2.11: Configuration of two GB-SAR acquisitions with a vertical baseline.

The result is derived in detail in [Martinez-Vazquez and Fortuny-Guasch, 2008]. As a linear relation, it could offer a straightforward solution. However, as the measured phase is wrapped, the resolution of Equation 2.24 needs either a very small baseline to avoid phase wraps as in [Pieraccini et al., 2001] or the application of a spatial phase unwrapping. Imposing small baselines reduces the sensitivity while imposing the phase unwrapping requires several conditions, including a spatially continuous field of coherent phases, a smooth topography with a bounded topographic gradient ∇Z and only one main scattering point in the resolution cell. These constraints are not always fulfilled, especially in the case of large infrastructure monitoring. For the condition $|\nabla\psi_z| < \pi$ to be satisfied, Equation 2.24 implies that the maximum gradient in elevation can be computed as:

$$|\nabla Z| < \frac{\lambda}{4}\frac{r}{b_\perp} \tag{2.25}$$

The precision of the estimated elevation σ_z as a function of the wavelength and perpendicular baseline is derived in [Nico et al., 2004]. Using Equation 2.24 and considering that the main sources of error are the phase noise σ_{ψ_z} and the baseline measurement accuracy $\sigma_{b_\perp}$, the propagation error law of [Niemeier, 2008] can be applied to obtain:

$$\sigma_z^2 = \left(\frac{\lambda r}{4\pi b_\perp}\sigma_{\psi_z}\right)^2 + \left(\frac{\psi_z \lambda r}{4\pi b_\perp^2}\sigma_{b_\perp}\right)^2 \tag{2.26}$$

For example, with the following typical parameters $r = 800\,\text{m}$, $\lambda = 17\,\text{mm}$, $b_\perp = 10\,\text{cm}$, $\psi_z = 1\,\text{rad.}$, $\sigma_{\psi_z} = 0.3\,\text{rad.}$ and $\sigma_{b_\perp} = 0.1\,\text{mm}$, the uncertainty in height is about $\sigma_z = 3.3\,\text{m}$. This is consistent with the study of [Martinez-Vazquez and Fortuny-Guasch, 2008], where the standard deviation of the differences between the GB-SAR model and the ground-truth digital elevation model (DEM) is reduced from 5 m to 3 m through advanced processing strategies. The same accuracy is attained in [Strozzi et al., 2011] by averaging ten filtered interferograms. A deeper analysis of GB-SAR results for DEM generation is available in [Tian et al., 2019]. The results highlighted in these studies demonstrate that the technique is not well-suited for precise DEM generation but holds value in understanding the origin of scattered signals.

An alternative to overcome phase unwrapping challenges is to acquire multiple GB-SAR images with varying baselines and apply tomographic algorithms to solve the tomographic synthetic aperture radar (TomoSAR) problem. Detailed explanations of these methods are provided in Chapter 4 as an essential tool for the work presented in this thesis.

2.5.2 InSAR statistics

Computing the interferometric phase ϕ is relatively straightforward. However, it becomes more intricate from a statistical perspective and relies on the complex Gaussian model initially proposed in [Goodman, 1963]. According to this model, a single SAR image generates a complex number, with its real and imaginary components following a Gaussian distribution. To fully understand the probability density function (PDF) of the interferometric phase, the concept of coherence and signal-to-noise ratio (SNR) are first expounded.

2.5.2.1 Coherence and SNR

To evaluate the quality of the interferometric phase, a commonly used metric is the coherence, represented by the complex correlation coefficient γ. A study on the sources of decorrelation in InSAR signals is presented in [Zebker et al., 1992]. Letting z_1 and z_2 the complex values of respectively the first and the second image, the coherence is defined as follows:

$$\gamma = \frac{\mathbb{E}(z_1 z_2^*)}{\mathbb{E}(|z_1|^2)\mathbb{E}(|z_2|^2)} = |\gamma| e^{i\phi_0} \tag{2.27}$$

where $\mathbb{E}$ is the expectation operator. The magnitude of the coherence $|\gamma|$ is a quantity taking values between 0 and 1. A value of 0 indicates no correlation between the first and second acquisition for the considering pixel, implying that the observed phase contains only noise. Conversely, a value

of 1 means a maximum correlation and no uncorrelated noise in the measurements. The quantity ϕ_0 represents the true interferometric phase value. Estimating the coherence can be achieved using various estimators. The theoretical value is determined by considering the temporal mean of the complex numbers. However, computing a reliable mean value is challenging when working with only two acquisitions. The ergodic assumption addresses this limitation, and the mean is calculated using a window W centred around the pixel of interest.

$$\hat{\gamma} = \frac{\sum_{p\in W} z_1(p) z_2(p)^*}{\sqrt{\sum_{p\in W} |z_1^2(p)| \sum_{p\in W} |z_2^2(p)|}} \tag{2.28}$$

The choice of the window shape varies, ranging from the most straightforward forms, like the Boxcar window, to more advanced options, like non-local techniques, as presented in [Deledalle et al., 2010]. The latter work demonstrated that the non-local filter corresponds to the maximum likelihood (ML) estimate of the coherence between a pair of SLC images. However, non-local methods can be computationally demanding due to their iterative nature. In this thesis, the coherence estimation is primarily based on the multi-temporal interferometry based on amplitude similarity (MIAS) method, introduced in [Wang et al., 2018b]. It is a balanced compromise between the quality of non-local techniques and the computational speed of a Boxcar estimator. The MIAS method requires a stack of SLC images, which is always available for ground-based systems due to their acquisition speed. For each pixel p, similar points in a surrounding 15×15 window W are identified using an amplitude similarity quantity S.

$$S(q_1, q_2) = 1 - \frac{|\overline{A}(q_1) - \overline{A}(q_2)|}{\overline{A}(q_1) + \overline{A}(q_2)} \in [0; 1] \tag{2.29}$$

with $\overline{A}(q_1)$ and $\overline{A}(q_2)$ the mean amplitude of the respective pixels over the stack of SLC images. Subsequently, a threshold S_{th} is used to select the neighbouring points similar to the reference point p. The set of such similar points is denoted as $\mathcal{S}_p$:

$$\mathcal{S}_p = \{q \in W \,|\, S(p, q) > S_{\text{th}}\} \tag{2.30}$$

The initial estimate of the coherence $\hat{\gamma}^{(0)}$ is calculated as follows:

$$\hat{\gamma}^{(0)}(p) = \frac{\sum_{q\in\mathcal{S}_p} z_1(q) z_2^*(q)}{\sqrt{\sum_{q\in\mathcal{S}_p} |z_1^2(q)| \sum_{q\in\mathcal{S}_p} |z_2^2(q)|}} \tag{2.31}$$

The final estimate of the coherence at point p is based on the geometrical mean and is computed using the following equation:

$$\hat{\gamma} = \left(\prod_{q\in\mathcal{S}_p} \hat{\gamma}^{(0)}(q) \right)^{\frac{1}{|\mathcal{S}_p|}} \tag{2.32}$$

with $|\mathcal{S}_p|$ the cardinality of the set $\mathcal{S}_p$.

As a measure of signal quality, the coherence is strongly related to the SNR. The SNR is a measure comparing the level of the noiseless signal to the unexpected noise level. The original definition of the SNR is given by:

$$\mathrm{SNR} = \frac{P_{\mathrm{signal}}}{P_{\mathrm{noise}}} \tag{2.33}$$

where P_{signal} and P_{noise} are respectively the power of the signal and the power of the noise. The link between the two quantities for $|\gamma| \in]0,1[$ is given in [Hanssen, 2001]:

$$\mathrm{SNR} = \frac{1}{\frac{1}{|\gamma|} - 1} \tag{2.34}$$

This relation is very useful to compute the SNR of the signal, as the coherence can be easily estimated from a single interferogram.

2.5.2.2 PDF of the interferometric phase and phase noise

The complete derivation of the PDF $\mathcal{P}(\phi)$ is available in [Lee et al., 1994], and only the final result is summarised in this part. Considering two SAR pixels containing respectively the complex numbers z_1 and z_2 that follow a 2D symmetrical Gaussian distribution, the marginal PDF of the interferometric phase $\mathcal{P}(\phi|\gamma,\phi_0)$ is expressed by:

$$\mathcal{P}(\phi|\gamma,\phi_0) = \frac{1-|\gamma|^2}{2\pi}\frac{1}{1-|\gamma|^2\cos^2(\phi-\phi_0)}\left(1+\frac{|\gamma|\cos(\phi-\phi_0)\arccos(-|\gamma|\cos(\phi-\phi_0))}{\sqrt{1-|\gamma|^2\cos^2(\phi-\phi_0)}}\right) \tag{2.35}$$

This PDF is symmetrical around the expected value ϕ_0. If the magnitude of the coherence $|\gamma| = 0$, then $\phi \sim \mathcal{U}([-\pi\,;\pi])$.

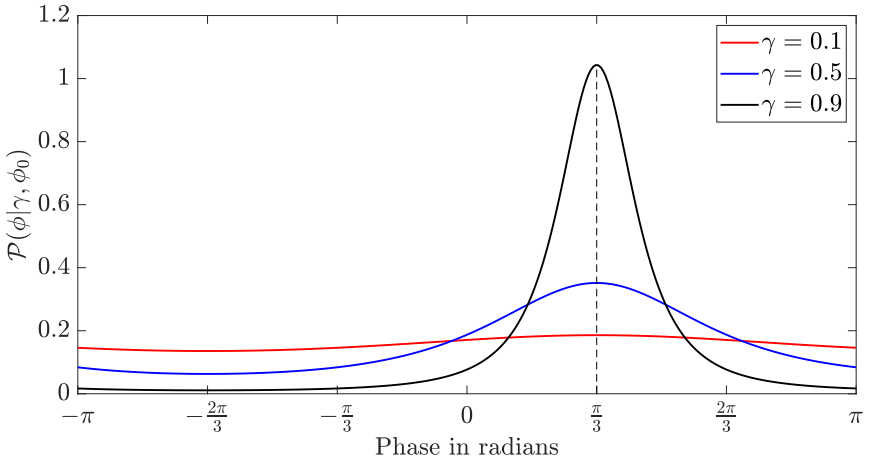

Figure 2.12: Probability density function of the interferometric phase ϕ for an expected value $\phi_0 = \frac{\pi}{3}$ and three different coherence levels.

The last aspect to explore in this brief presentation is the relationship between the variance of the interferometric phase and the coherence. The variance can be calculated as the second moment of Equation 2.35. For point-like targets, the relationship is relatively more straightforward. In contrast to distributed targets, this assumption implies that the received signal within the resolution cell

arises primarily from a single dominant scatterer. A detailed exploration of this relationship is available in [Hanssen, 2001]. For the dominant scatterer case, the variance of the interferometric phase σ_ϕ^2 is given by:

$$\sigma_\phi^2 = \frac{1 - |\gamma|^2}{2|\gamma|^2} \tag{2.36}$$

This equation holds only for coherence magnitude $|\gamma|$ close to 1, as pointed out by [Just and Bamler, 1994].

2.5.3 Multi-temporal InSAR

The concept of multi-temporal InSAR has been pioneered by the permanent scatterer interferometry, introduced by [Ferretti et al., 2001]. The concept is to analyse the interferometric phase of stable scatterers on several SAR images. These stable scatterers, often referred to persistent scatterer (PS), are points characterised by constant scattering properties and affected by minimal phase noise σ_ϕ. A comprehensive overview of the phase noise properties of PS points is presented in [Schenk, 2015]. Identifying PS points is a crucial step in permanent scatterer interferometry to ensure the quality and reliability of deformation measurements. The amplitude dispersion D_A is a key metric used to rapidly identify these points within a SAR image stack and is defined as:

$$D_A = \frac{\sigma_A}{\mu_A} \tag{2.37}$$

where σ_A and μ_A represent respectively the pixel-wise standard deviation and mean of the amplitude on the SAR image stack. As observed in [Ferretti et al., 2001], the close correspondence between σ_ϕ and D_A when both are below 0.25 highlights the effectiveness of D_A as an indicator for identifying PS points. This efficient identification process contributes to the accuracy and reliability of deformation measurements in persistent scatterer interferometry (PSI) applications.

When working with multiple SAR images, the configuration of interferograms is critical. Two prominent families exist, which are the PSI [Hooper et al., 2004] and the small baseline subsets (SBAS) [Berardino et al., 2002] methods. Considering N images, the first approach selects an ideal scene, called Master, and computes the $N-1$ interferograms with all the other scenes. A method to choose the best Master in satellite InSAR is available in [Hooper et al., 2007]. The SBAS methods work with all the interferograms having a temporal baseline[1] below a certain threshold and results generally with more than $N-1$ interferograms, building a redundant network. A least squares inversion via singular value decomposition is achieved to effectively access the integrated time series of the deformation.

One advantage of SBAS is that it builds a network of interferograms with small phase variations, which can aid in phase unwrapping and improve accuracy. However, when phase unwrapping errors occur, they are integrated into the network and can affect the final phase integration. According to [Li et al., 2022], the PSI avoids significant atmospheric and orbital errors. GB-SAR methods are unaffected by the second type of error, meaning that an SBAS system has more advantages.

The main steps of a multi-temporal analysis vary depending on the software used, but the core steps remain constant. The process can be summarised based on the Stanford method for persistent scatterers (StaMPS) manual [Hooper et al., 2010] or the review of [Wang et al., 2020b], as follows:

[1] SBAS methods were initially implemented for the satellite InSAR and also consider the spatial baseline between the satellite repeat-passes to build the interferograms.

- **Coarse pixel selection**: This step involves the removal of pixels that are too noisy or exhibit poor data quality based on predefined criteria such as D_A or SNR. The goal is to retain only reliable pixels for further analysis.
- **Wrapped parameter estimation**: In some cases, specific parameters, such as linear displacement rates, can be estimated using the wrapped phase. These estimates provide initial information about the deformation behaviour of the observed scene.
- **Phase filtering**: Phase filtering is applied to reduce the noise in the interferometric phase. This step is essential for improving the data quality and preparing it for subsequent processing.
- **Phase unwrapping**: Phase unwrapping is a critical step in the InSAR analysis, aiming to resolve the phase ambiguities present in the wrapped phase data, allowing for the reconstruction of the true displacement time series.
- **Atmospheric filtering**: The atmospheric component in the interferometric phase introduces errors in displacement estimation. Several assumptions, especially spatial correlation, are used to carry out this step.
- **Geocoding**: Geocoding involves associating the 2D coordinates of the SAR pixels with corresponding 3D points on the external model of the scenario.

In the next section, mathematical and physical models as well as the algorithms used behind these steps are presented. However, we will neither focus on wrapped parameter estimation nor phase filtering, as they play a subordinate role in satellite GB-SAR.

2.6 GB-SAR state of the art

GB-SAR has already been studied in several ways, and many strategies to process its measurement data have already been proposed. This section is dedicated to the presentation of the main existing and developed algorithms used to process GB-SAR data.

2.6.1 Pixel selection

As previously presented, the initial criterion used in [Ferretti et al., 2001] or in [Hooper et al., 2007] is to process pixels having an amplitude dispersion lower than a given threshold, called persistent scatterer candidate (PSC). The higher the threshold, the higher the number of detected pixels, at the cost of increased noise level in the selected data.

An approach in the GB-SAR case is proposed in [Wang et al., 2018a], where a combination of coherence and amplitude dispersion is used over an SBAS interferogram network. In [Deng et al., 2021], an exploration of the distributed scatterer identification technique, developed in [Ferretti et al., 2011], is proposed for the GB-SAR case. The work in this thesis emphasises on infrastructure monitoring, with observed pixels having a higher quality than natural scenarios and will not consider these enhanced processing strategies.

In long-term continuous monitoring, the most employed solution is to process block-wise. Indeed, a study by [Dörr et al., 2022b] has indicated that the number of identified PSC may decrease as the time series lengthens. Moreover, given that GB-SAR systems are frequently used for real-time

processing, the option to wait until the monitoring period is finished is not feasible. An example is presented in [Wang et al., 2019a], with a near real-time processing chain organised into blocks. This approach involves creating blocks of a defined size and iteratively conducts the pixel selection for each new block.

2.6.2 Phase unwrapping

The challenge of phase unwrapping arises from its intractability. As presented in Equation 2.15, the unwrapped phase is equal to the wrapped phase modulo 2π. Determining the integer ambiguity without any additional information or assumptions remains impossible.

2.6.2.1 1D phase unwrapping

A method developed for 1D signals is introduced in [Tribolet, 1977]. The algorithm is grounded on integrating the phase gradient to recover the original signal. The main assumption is based on the phase derivative $\Delta\phi$, which can not exceed a threshold. For N phase samples and computing $\forall\, k \in [|2\,;N|]$, $\Delta\phi(k-1) = \phi(k) - \phi(k-1)$, the unwrapped phase is given $\forall\, k \in [2;N]$ by:

$$\psi(k) = \begin{cases} \psi(k-1) + \Delta\phi(k-1) + 2\pi & \text{if } \Delta\phi(k-1) < \pi \\ \psi(k-1) + \Delta\phi(k-1) - 2\pi & \text{if } \Delta\phi(k-1) > \pi \\ \psi(k-1) + \Delta\phi(k-1) & \text{otherwise} \end{cases} \tag{2.38}$$

The initialisation of the first sample of the unwrapped phase is achieved simply with $\psi(1) = \phi(1)$. This formulation reflects the Nyquist sampling frequency assumption, which stipulates that neighbouring points can not exhibit phase differences greater than π.

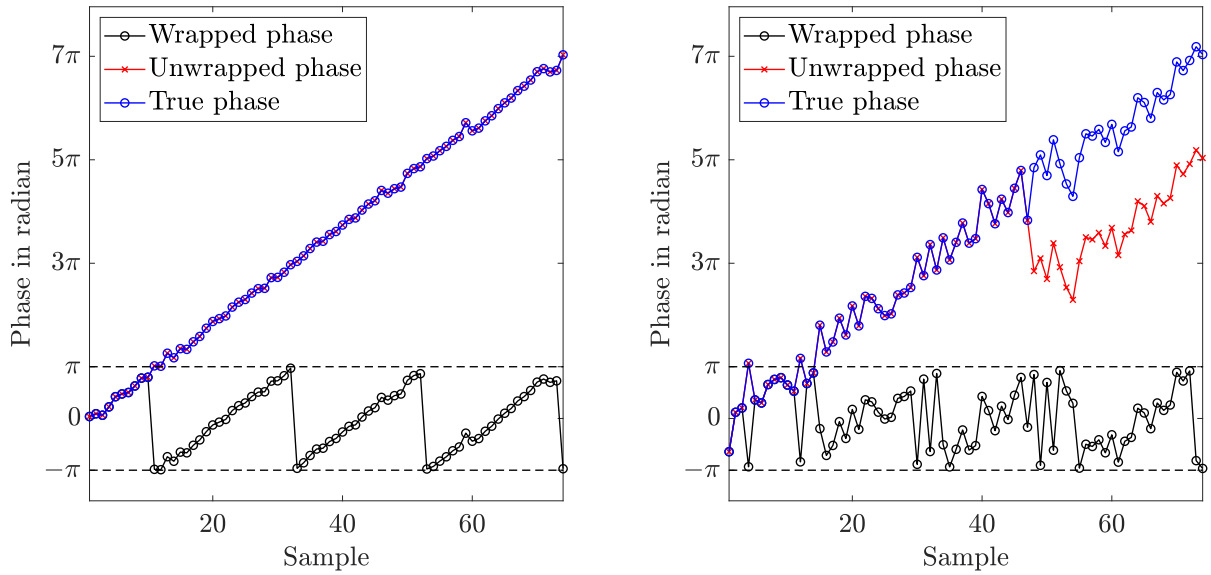

(a) Low noise

(b) High noise

Figure 2.13: Phase unwrapping on simulated signal. A linear phase ramp is simulated with noise added. (a) $\sigma_\phi = 0.2$ and (b) $\sigma_\phi = 1$.

Figure 2.13a represents the processing of the 1D phase unwrapping. The true phase in blue is the quantity to be determined. The GB-SAR can only measure the wrapped phase, represented in black. In the case of low noise, the recovery of the signal works well. However, this assumption is not always enough to recover the true signal. Figure 2.13b represents an example where the unwrapping algorithm fails to estimate the true signal due to a too low SNR.

2.6.2.2 2D phase unwrapping

The phase unwrapping in 2D is a more challenging problem but can also take advantage of more information available. A review of the existing methods is presented in [Yu et al., 2019].

If the assumption about the phase gradient held for the whole interferogram, then the unwrapped phase can be obtained through an arbitrary path [Carballo and Fieguth, 2000]. However, this never happens in a real configuration due to phase noise, atmospheric signal or steep topography. The first development of 2D phase unwrapping for SAR interferograms is presented in [Goldstein et al., 1988]. The concept developed by the latter work proposes a method to identify paths to avoid, using the redundancy of the 2D gradients. Another approach, developed in [Ghiglia and Romero, 1994] and [Ghiglia and Romero, 1996], is based on a global norm minimisation over the whole interferogram. The main drawback of this technique is that it does not enforce the congruence between the wrapped and unwrapped phases.

The first proposition of a network flow formulation for InSAR phase unwrapping has been introduced in [Costantini, 1998]. This algorithmic formulation enables a fast and robust way to optimise the previously defined cost function and is known as the minimum cost flow (MCF) technique. The work of [Chen, 2001] is mainly based on the MCF algorithm but with adaptive cost functions on the interferogram. The famous algorithm is known as Statistical-cost, Network-flow Algorithm for Phase Unwrapping (SNAPHU).

2.6.2.3 3D phase unwrapping

The 3D phase unwrapping is useful when the data to process comes from a stack of SAR images and not only a single interferogram. [Costantini et al., 2002] showed that using a full 3D framework leads to more reliable results than using a series of 2D unwrapping algorithms. The phase gradient is computable along three directions, which gives a higher redundancy than in a 2D-case. A significant contribution in this case has been developed in [Hooper and Zebker, 2007]. The central concept is to use SNAPHU as a starting point. However, the costs are computed from the time series of the points using a linear displacement assumption. Then, the 2D phase unwrapping is conducted with these costs for each interferogram.

Related to GB-SAR data, the unwrapping method developed by [Rödelsperger, 2011] is based on a Kalman filter of the wrapped sequential time series of images. Several models for the Kalman filter are implemented and evaluated, and the one with the highest probability w.r.t. to the integer ambiguity is selected.

Another development of pseudo 3D phase unwrapping is done in [Monserrat et al., 2009] and applied to GB-SAR data in [Monserrat Hernández, 2012]. The ground idea is first to use a 2D spatial unwrapping on a SBAS configuration. Subsequently, the phase is integrated, and the residues are analysed. Iteratively, the interferogram with the largest residue is removed if the network's redundancy remains high enough and the unwrapping and phase integration are led again.

2.6.3 Atmospheric correction

The atmospheric signal has been presented in Section 2.5.1.1. An overview of existing methods to correct the atmospheric phase screen (APS) is presented in [Chao et al., 2019], and they can be categorised in the following groups:

- parametrical methods, which mainly rely on spatial equation models.
- non-parametrical methods, which rely on stable areas or signal properties assumption.
- meteorological methods, using measured data to create a meteorological model and convert it into an APS.

The majority of these methods are applied to unwrapped interferograms. It will be specifically written when the technique is applied to wrapped interferograms.

2.6.3.1 Parametrical methods

The beginning of atmospheric corrections started with the parametrical methods. In [Noferini et al., 2005], one of the first models is proposed using the linear range model to estimate the global uniform atmospheric change through the whole scenario denoted by ψ^r_{atmo}. This component is described on the interferogram via the following model:

$$\psi^r_{\text{atmo}} = C_0 + C_1 r \tag{2.39}$$

The coefficient r is the range of the PS point and the unknown parameters C_0 and C_1 are the estimated parameters with classical least squares (LS) inversion on a set of PS points of the interferogram. In [Yang et al., 2020], the same model is used but on wrapped interferograms. The inversion is led using phase differences of points with different range values. A more complex model, also developed in [Noferini et al., 2005], fits the APS with a second-degree polynomial in range to consider linearly changing atmospheric conditions along this direction.

The current most applied model considers the range and height of the PS points and is introduced in [Iglesias et al., 2013]. The model takes into account the exponential decrease of the pressure and humidity. For limited elevation differences, a linear approximation can be used, leading to the following model:

$$\psi^{rz}_{\text{atmo}} = C_0 + C_1 r + C_2 r Z \tag{2.40}$$

The estimation applied in this methodology also considers the residues of the PS points' phase values to analyse the regression quality. Indeed, the LS estimation is first achieved over all the M PS in the scenes. Denoting with $\boldsymbol{\psi} \in \mathbb{R}^M$ the vector of unwrapped interferometric phase and $\mathbf{A} \in \mathbb{R}^{M\times 3}$, the observation matrix of the quantity $[1\ r\ rZ]$ for each PS, the estimator of the variance error $\hat{s}^2$ is given by:

$$\hat{s}^2 = \frac{\boldsymbol{\psi}^\mathsf{T}\left(1 + \mathbf{A}(\mathbf{A}^\mathsf{T}\mathbf{A})^{-1}\mathbf{A}^\mathsf{T}\right)\boldsymbol{\psi}}{M-3} \tag{2.41}$$

All the PS points satisfying $|\psi - \psi_{\text{atmo}}| > 2\hat{s}$ are considered as outliers, and the estimation is conducted a second time without those PS points, as they may be affected by a strong deformation or other effects. It is also shown in [Wang, 2019] that this atmospheric model corresponds to the best linear model for APS compensation. Different extensions of the atmospheric model are presented in other works such as in [Izumi et al., 2020], [Dematteis et al., 2017] or [Liu et al., 2021]. A different polynomial model using the points' coordinates is used in each situation to better fit the phase values in the non-moving areas.

2.6.3.2 Non-parametrical methods

The first way to correct the atmospheric influence on the interferograms without spatial models is by knowing spatial stable areas. The APS is estimated at these locations and fitted on the whole interferogram using different methods. In [Rödelsperger, 2011], an interpolation is applied and shows better results than a polynomial of first and second order in range, at the cost of precisely knowing stable areas. [Monserrat Hernández, 2012] also uses the stable areas to first estimate the APS at these locations. Finally, the APS is predicted over non-stable areas via a 2D spatial polynomial. Because of this spatial prediction, the ideal scenario happens when stable areas completely surround the moving areas.

Another method developed for wrapped interferograms is presented in [Falabella et al., 2021]. The estimation of the atmospheric phase is based on the adaptive short-term fast Fourier transform. It enables the recovery of a chirp signal in different range directions, similar to a polynomial of second order, but without any preliminary unwrapping or PS point coordinates. Thus, this technique can be applied to raw interferograms, which is a significant improvement.

The developed model in [Deng et al., 2022] can be interpreted as a tomographic processing. Indeed, after the PS selection, the 2D GB-SAR image is decomposed in a grid with a given cell size. Afterwards, the path between each PS and the GB-SAR is reconstructed. A tomographic inversion is applied using the phase values of the PS and Equation 2.17. Moreover, boundary and smooth constraints are added to the equation system to avoid jumps in the final map of the refractivity index.

2.6.3.3 Meteorological methods

The methods using meteorological models need additional sensors to measure the temperature, the humidity and the pressure installed over the monitored area. Then, the refractivity index N is calculated at the locations of the sensors using Equations 2.19 and 2.20. The conversion into phase delays is achieved through the model of Equation 2.17. Finally, an interpolation grid is computed over the whole observed scenario to estimate the atmospheric phase at all the PS locations. The quality of the results depends highly on the density of the meteorological sensors network.

As shown in this part, many different APS correction methods were developed in the past two decades. The most applied methods are parametrical models. However, they assume that a significant part of the interferogram contains stable points, such that the measured signal is only the sum of atmospheric phase and noise. In the case of dam monitoring, the major part of the interferogram undergoes displacements, and it is more challenging to apply these methods.

2.6.4 Geocoding

The geocoding part presents less work in the literature than the unwrapping or the atmospheric correction. Indeed, the challenges of correct geocoding appear only when the observed scenario is complex, i.e. with substantial variations in elevation in a single resolution cell. These scenarios rarely occur as GB-SAR systems are mainly used for landslides and open-pit mines.

The geocoding task can be separated into two main parts: the absolute referencing of the system in the observed scenario and the 3D position estimation of the scatterer inside the resolution cell from the 2D image coordinates.

For the first part, the usual method is to measure the position and orientation of the system via an external measurement tool, for example, a total station or GNSS. However, even using the latter method, the accuracy is not high enough, especially for the orientation of the system. The prominent technique in the literature is to find common structures in the radar image and the observed scenario to estimate the external parameters of the sensor, as in [Lingua et al., 2008], [Marambio et al., 2009], [Tapete et al., 2013] or [Wieser et al., 2020]. In [Caduff and Rieke-Zapp, 2014], artificial corner reflectors were installed to alleviate the identification of similar structures. More recently, [Dematteis et al., 2018] proposed to compute the correlation between the visible part of the DEM and the projected radar image to estimate the orientation of the sensor without any external installation or manual structure identification.

Once the sensor is referenced in the external model, the basic approach to associate a set of 3D coordinates to each 2D image pixel is the so-called back geocoding, detailed in [Monserrat Hernández, 2012]. Each point of the 3D model or DEM is projected onto the GB-SAR geometry via Equation 2.12. Afterwards, to recover the 3D coordinates of one GB-SAR pixel, an interpolation is applied to find the best corresponding 3D points. One of the latest approaches has been developed by [Cai et al., 2021]. It is based on a 3D search window on the world coordinates to find the closest point to the radar for each resolution cell. However, these techniques do not consider strong layover, as it happens on infrastructure monitoring.

2.7 GB-SAR properties for infrastructure monitoring

2.7.1 Instrument characteristics

The measurements used to evaluate the new methodologies developed in this work are acquired with the IBIS-FM system from *IDS Georadar*. This section aims to recap the main parameters of this instrument, with their corresponding values.

Parameter	Notation	Value
Wavelength	λ	17.4 mm
Central frequency	f	17.2 GHz
Signal bandwidth	B_r	200 MHz
Linear scanner length	L	2 m
Range resolution	ρ_r	0.75 m
Cross-range resolution	ρ_θ	4.36 mrad
Maximum range	$r_{\max}$	4 km
Repeat-pass delay	Δt	1 min. 53 sec.

Table 2.3: Main parameters of the IBIS-FM.

2.7.2 Opportunities and challenges using GB-SAR for infrastructure monitoring

The analysis of the advantages and disadvantages of TRI/GB-SAR is already presented in [Rödelsperger, 2011], [Monserrat et al., 2014], [Caduff et al., 2015] and [Wieser et al., 2020]. In our context, we focus especially on the infrastructure monitoring.

2.7.2.1 Opportunities

- **Very high sampling rate**: In seismically active regions, the high sampling rate of GB-SAR proves high benefits. Swift assessment of post-earthquake damage to structures, such as dams, becomes possible, aiding in fast response and recovery.
- **High spatial covering**: As a complement of the very high temporal sampling, the spatial density of the observed structure is a significant advantage of GB-SAR systems. Even at about 1 km of the target, the system can track thousands of points on the structure.
- **Measurement accuracy**: The manufacturer provides an accuracy up to 0.1 mm for the phase measurement, which is higher than other geodetic measurement tools. However, this only mentions the measurement accuracy without considering the atmospheric influence.
- **Autonomous system**: Once installed, the instrument can monitor continuously for several years with minimal maintenance every 3-6 months. Coupled with streamlined data transfer, collecting the SLC images regularly is easy.
- **Measurements every time**: As an active remote sensing technique, the GB-SAR can measure independently from daylight and lead acquisitions during fog or rain.

2.7.2.2 Challenges

- **1D LOS measurement**: The interferometric process enables to compute the displacement of a point between the acquisitions only along the LOS of the instrument. No displacement would be apparent if the LOS and the displacement vectors are orthogonal due to the station location.
- **Phase unwrapping**: Noisy signals at specific locations can lead to unwrapping errors, distorting displacement maps or time series, as presented in Figure 2.13.

- **Relative deformation measurement**: The methodology inherently captures relative displacements, requiring a meticulously chosen reference point or area, assumed to be affected by no deformation process for accurate interpretation.
- **Sensitivity to weather changes**: With its relatively small wavelength, GB-SAR is sensitive to atmospheric variations. Accurate correction over time, especially during substantial structural motion, remains challenging.
- **No choice of the observed points**: The GB-SAR measurements can be interpreted on coherent targets, which means metallic, concrete or rock targets. The number of observation points can easily reach several thousand. However, choosing which points are coherent is impossible, except by installing corner reflectors.
- **Complex geometry**: As detailed in Section 2.4, the acquisition geometry can be intricate, leading to issues like severe layover and foreshortening during monitoring tall vertical structures, potentially skewing observations.

In light of these opportunities and challenges, the forthcoming chapters of this thesis introduce novel methodologies designed to alleviate the limitations of GB-SAR. These advancements aim to establish GB-SAR as a reliable and robust tool for monitoring large infrastructures.

CHAPTER 3

Presentation of the Enguri Dam and measurements

Contents

3.1 Introduction

The main goal of this thesis is the improvement of GB-SAR techniques for infrastructure monitoring. The principal test site, where almost all the measurements were acquired, is the Enguri Dam in the Caucasus. The monitoring with a GB-SAR is a part of the DAMAST project [Mueller and Strauss, 2019]. The Enguri Dam belongs to the family of arch dams, presenting a double curvature, both planimetric and in elevation.

Each methodological chapter introduces novel tools, and their assessment and validation using real data are predominantly applied to this dataset. The whole installation and the data acquisition are presented in the following sections. Firstly, the dam is presented, with the employed monitoring and modelling strategies. Subsequently, the new measurement concept and the GB-SAR stations are exposed. Finally, the presentation extends to the external data and installation required for georeferencing and geocoding.

Figure 3.1: Enguri Dam presentation: (a) Satellite image mapped on the globe ©Google Earth. The white rectangle represents the localisation of the dam and the reservoir. (b) Aerial view of the Enguri Dam and its reservoir ©Georgia Travel Guide.

3.2 The Enguri Dam

3.2.1 General informations

The Enguri Dam is located in the Caucasus, near the village of Jvari. Its construction began in 1961, and the production of electricity was initiated in 1978. Currently, it stands as the world's fifth-largest active arch dam, with a height of 272 m [ICOLD, 2020]. The length of the dam crest is about 800 m, and the reservoir contains approximately a billion cubic meters of water. The water level exhibits specific periodic fluctuations, reaching as much as 100 m within a few months. Located in the Abkhazia region, the hydroelectric power station is linked to the dam through a 14.5 km high-pressure tunnel with a maximum power generation of 1.3 GW. The station annually produces around 4.5 TWh of energy, constituting about 40 % of Georgia's total electricity production. The area surrounding the Enguri Dam is characterised by a high seismic activity [Chelidze et al., 2021], which can have substantial impacts on the concrete structure. Beyond its significance as a critical

energy infrastructure, the Enguri Dam also holds cultural significance and has been standing on Georgia's cultural heritage list since 2015. Figure 3.1 gives a visual insight into the Enguri Dam's location and an aerial perspective of its imposing presence.

3.2.2 Loadings

An extended explanation of loading effects affecting arch dams is presented in [CFBR, 2021], and only a brief summary is presented in this part. The primary loadings can be separated as follows:

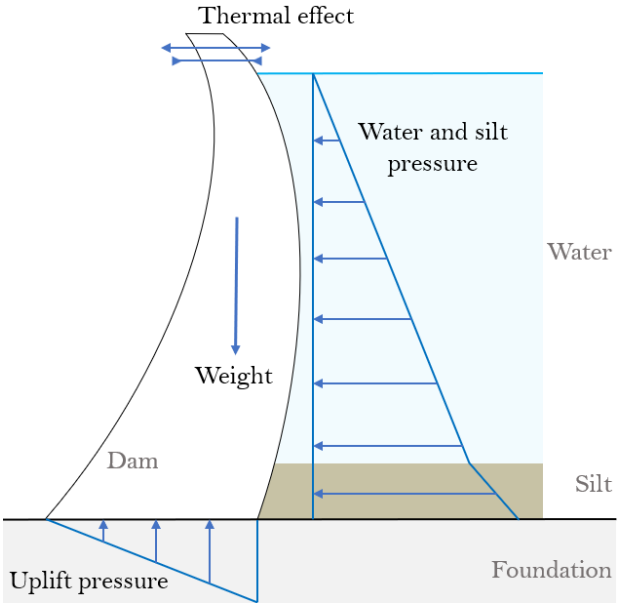

Figure 3.2: Schematic representation of the primary loadings affecting an arch dam.

- Self-dam weight: The dam's structure is exposed to gravity due to its weight.
- Hydrostatic water pressure: The water in the reservoir exerts a horizontal pressure.
- Uplift pressure: Water infiltrates in all possible cracks and joints, especially the ones occurring between the dam and its foundation, resulting in an uplift pressure due to the weight of the upstream water.
- Seismic interactions such as induced hydrodynamic water pressure.
- Thermal changes: Variations of the temperature affect materials which move w.r.t. to their thermal coefficient.

Figure 3.2 is a schematic representation of the major effects inducing the displacement of the dam. The forces represented are not scaled between each other. An explanation and study case of the uplift pressure on a high arch dam is available in [Lin et al., 2016].

3.2.3 Current monitoring strategies

As outlined by [Perner and Obernhuber, 2010], the deformation of an arch dam primarily arises from water level changes in the reservoir and the temperature fluctuations of the concrete. This section introduces the prevailing monitoring strategies implemented at the Enguri Dam, with their specific features. While seismic stations are not discussed here, further insights can be found in [Adamo et al., 2021].

3.2.3.1 Plumblines and numerical modelling

The construction of arch dams is grounded on vertical slices called cantilevers [Ghanaat, 1993]. Each cantilever is classically monitored by installing a chain of plumblines that enables the monitoring of the horizontal displacements with an accuracy under 0.1 mm. For arch dams, the periodic safety assessment often relies on numerical models for stress-strain analysis. A detailed description of the

deformation processes occurring is described in [Bourdarot and Robbe, 2012]. However, determining the elastic properties such as Young's modulus and Poisson's ratio and the coefficient of thermal expansion of the dam materials through laboratory tests is challenging due to the scale difference between laboratory samples and the actual dam size. French guidelines [CFBR, 2021] recommend an alternative approach by calibrating the mechanical properties in numerical models to accurately mirror the observed behaviour of the physical structure. In this regard, the collected pendulum data over the years provide valuable assistance. The Enguri Dam comprises 38 pendulums, arranged to form eight complete lines capable of measuring the relative horizontal displacement between two points at the end of each line with an accuracy of approximately 0.1 mm. Figure 3.3 provides an overview of the plumbline layout. The lines are marked with blue boxes, with five reaching the crest. The number of pendulums constituting the lines is given under the boxes.

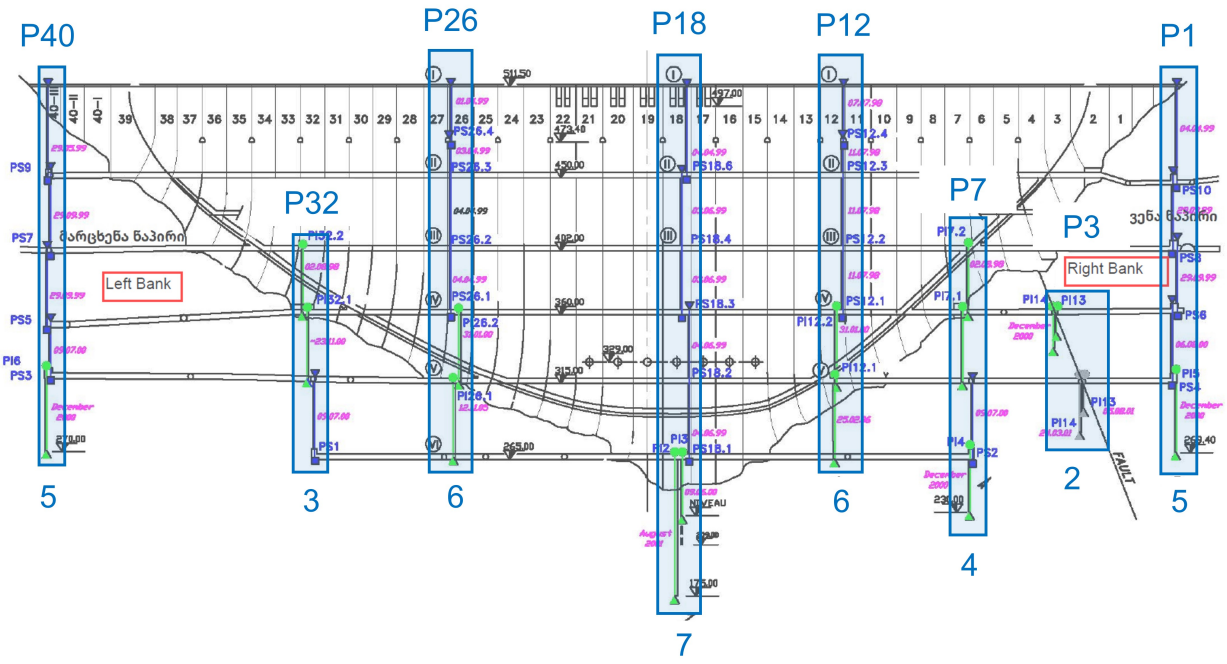

Figure 3.3: Plumbline layout at Enguri Dam.

The data from the pendulums are processed using the Hydrostatic-Season-Time (HST) method [Willm and Beaujoint, 1967]. This statistical model assumes that the displacement d may be separated into the sum of three primary contributions, i.e. $d = F_1 + F_2 + F_3$, with

- F_1: the hydrostatic contribution accounting for water level fluctuations
- F_2: the seasonal part that contains many contributions such as temperature variations
- F_3: the time effect including the irreversible evolution of dam ageing

The original equations of the HST model are defined as follows:

$$F_1(h) = \sum_{k=0}^{4} a_k h^k \tag{3.1}$$

$$F_2(s) = a_5 \cos(s) + a_6 \sin(s) + a_7 \sin^2(s) + a_8 \sin(s)\cos(s) \tag{3.2}$$

$$F_3(t) = a_9 \log(t) + a_{10} e^t \tag{3.3}$$

In these equations, h is the reservoir water level, $s = 2\pi n_d/365.25$ with n_d the number of days since 1st January, and t is the time since the dam creation. The model involves eleven parameters typically estimated using a LS regression. Variations of this model are discussed in [Salazar et al., 2017], with particular adaptations affecting the F_3 term, which is challenging to model.

The calibration of the numerical model involves assessing material elastic properties via the hydrostatic effect and deriving the coefficient of thermal expansion from the seasonal effect. An enhanced version is the Hydrostatic-Season-Thermal-Time model, which encapsulates the thermal behaviour of the dam, requiring temperature data. However, due to the high correlation between average thermal temperatures and seasons, the HST model remains more adaptable. Another improvement of the HST model is the introduction of delays in the model. In [Lombardi et al., 2008], the deformation at time t depends on the parameter values from current and previous times. As regression models, all these variants demand years of data for optimal effectiveness.

3.2.3.2 Geodetic network

At Enguri Dam, a geodetic network is used to monitor the dam, similar to what is presented in [Yigit et al., 2016]. The network is composed of 100 points on the dam, with a measurement done once a year between 2009 and 2019. Despite its precision, this monitoring approach's sparse dataset poses challenges in fully comprehending the dam's behaviour.

3.3 GB-SAR stations

For the monitoring of the Enguri Dam, an arrangement of four stations was established. While one station serves for continuous monitoring, the others enable multi-view epoch-wise monitoring, expanding the coverage across the dam's expanse. The epoch-wise stations are revisited once or twice a year, ideally at different water levels. The monitoring concept is designed to last several years, such that concrete foundations were built at each station to offer strong installation stability.

3.3.1 Continuous station

The long-term station is installed in a warehouse to ensure its safety and stability. The instrument started the acquisitions in April 2021 and is still active. The dataset used in this thesis consists of two years and five months of SLC images and goes from 20th April 2021 to 07th September 2023 with 573 075 SLC images. The daily water levels are also available, but only until 20th July 2023. Occasional gaps spanning up to 1 month occur due to epoch-wise measurements or some minor instrument problems which could not be solved remotely.

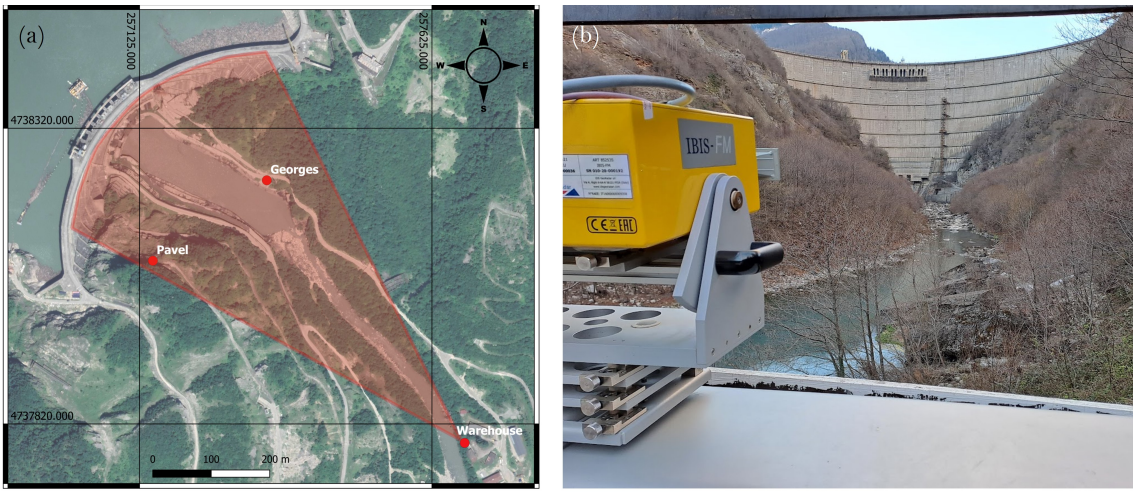

Figure 3.4: Continuous station. (a): Top view of the stations available with the field of view of the GB-SAR at *Warehouse*. (b): Visualisation of the visible part of the dam by the GB-SAR at *Warehouse*.

Figure 3.4 presents the situation of the station, located at nearly 800 m far from the dam. Due to the Enguri canyon configuration, only half of the dam's surface is visible. The InSAR analysis corresponding to this station is presented in detail in Chapter 7 as the final part of this thesis.

3.3.2 Epoch-wise stations

Two additional stations are strategically installed to fully cover the dam. The idea of these multi-view stations is to revisit their site at different water levels to better understand the dam's behaviour due to those variations. The presentation of the processing of the interferometric data for these stations is presented in Chapter 6.

The *Pavel* station exhibits the particularity of two possible viewing directions, with the same centre covering almost the whole dam when combined. *Pavel 1* station is focused only on the dam structure while *Pavel 2* extends its coverage to the dam-rock junction and the left embankment. In contrast, the *Georges* station covers the right part of the dam, including the embankment. These stations are approximately 300 m away from the dam, thereby experiencing fewer atmospheric disturbances than the *Warehouse* station.

The data collected at the epoch-wise stations are reported in Table 3.1. Five epochs are considered with temporal baselines ranging from three months to one year, representing very large baselines for GB-SAR interferometry. A campaign is missing at the *Georges* station due to the presence of a container in front of the foundations during our on-site measurements.

3.3.3 GB-SAR amplitude images

To provide a visual representation of the data acquired by the GB-SAR system, the amplitude images for all the stations are presented in Figure 3.6. To mitigate sidelobes, the presented images depict coherent averages over 30 acquisitions.

From a geometric perspective, the *Georges* station emerges as the optimal standpoint. Located near the base of the dam, the layover and foreshortening effects are reduced, facilitating straightforward

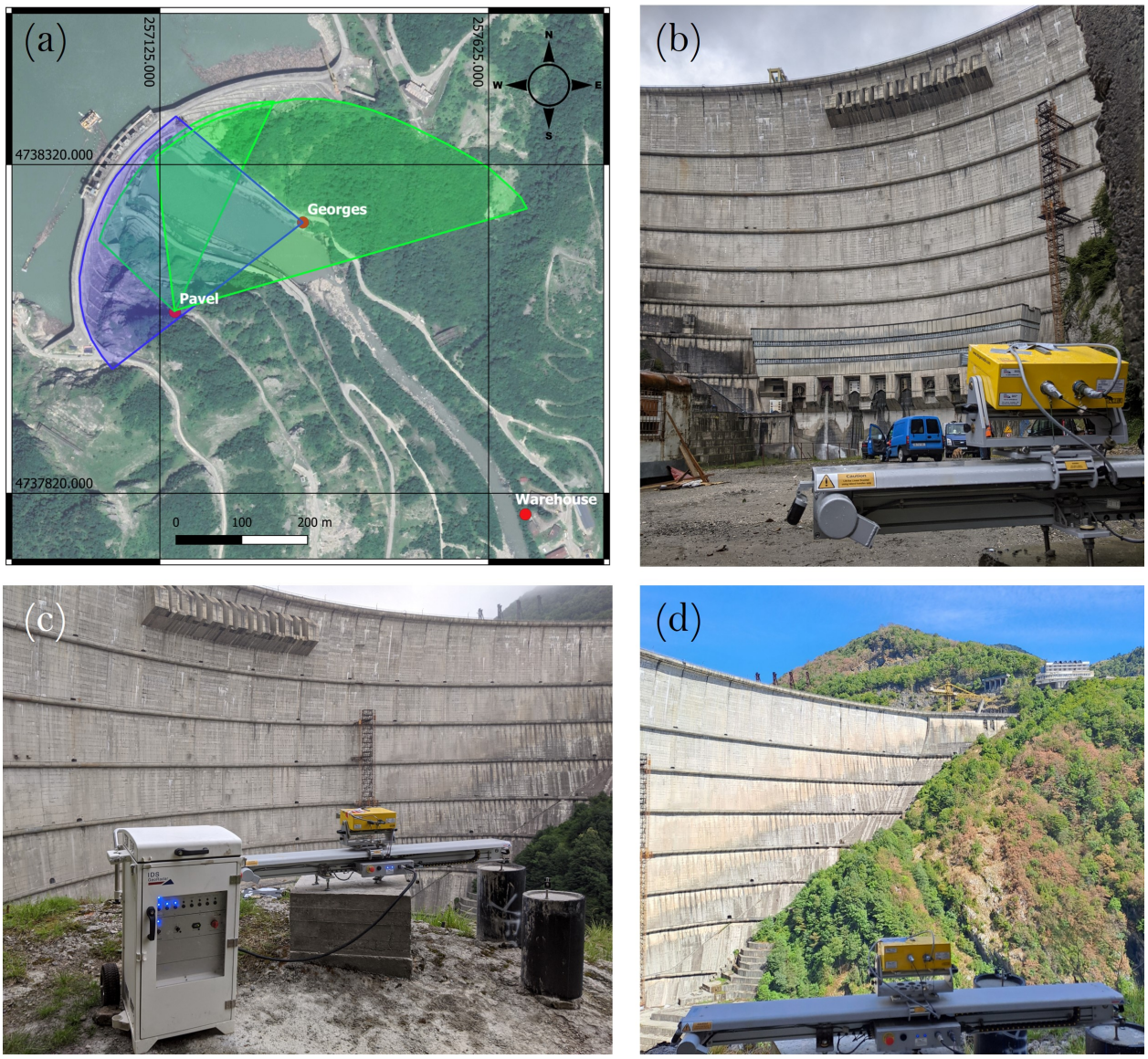

Figure 3.5: Multi-view stations. (a): Top view of the stations available with the FOV of the GB-SAR. Green: *Pavel* - Blue: *Georges*. (b): *Georges* station view. (c): *Pavel 1* station view. (d): *Pavel 2* station view.

Epoch	Station	Begin date	End date	Nb. of SLC	Mean W.L. [m]
1	*Pavel 1*	22.06.2021	25.06.2021	2267	489.5
	Pavel 2	25.06.2021	28.06.2021	1830	491.6
	Georges	30.06.2021	01.07.2021	811	492.8
2	*Pavel 1*	28.09.2021	30.09.2021	1132	482.8
	Pavel 2	30.09.2021	01.10.2021	797	482.1
	Georges	05.10.2021	06.10.2021	500	482.9
3	*Pavel 1*	07.04.2022	08.04.2022	630	415.9
	Pavel 2	08.04.2022	09.04.2022	576	416.5
	Georges	-	-	-	-
4	*Pavel 1*	09.09.2022	10:09:2022	649	457.4
	Pavel 2	10.09.2022	11.09.2022	692	456.2
	Georges	12.09.2022	13.09.2022	417	453.5
5	*Pavel 1*	22.03.2023	22.03.2023	182	438.9
	Pavel 2	23.03.2023	24.03.2023	648	440.6
	Georges	20.03.2023	21.03.2021	682	437.2

Table 3.1: GB-SAR campaigns lead at Enguri Dam.

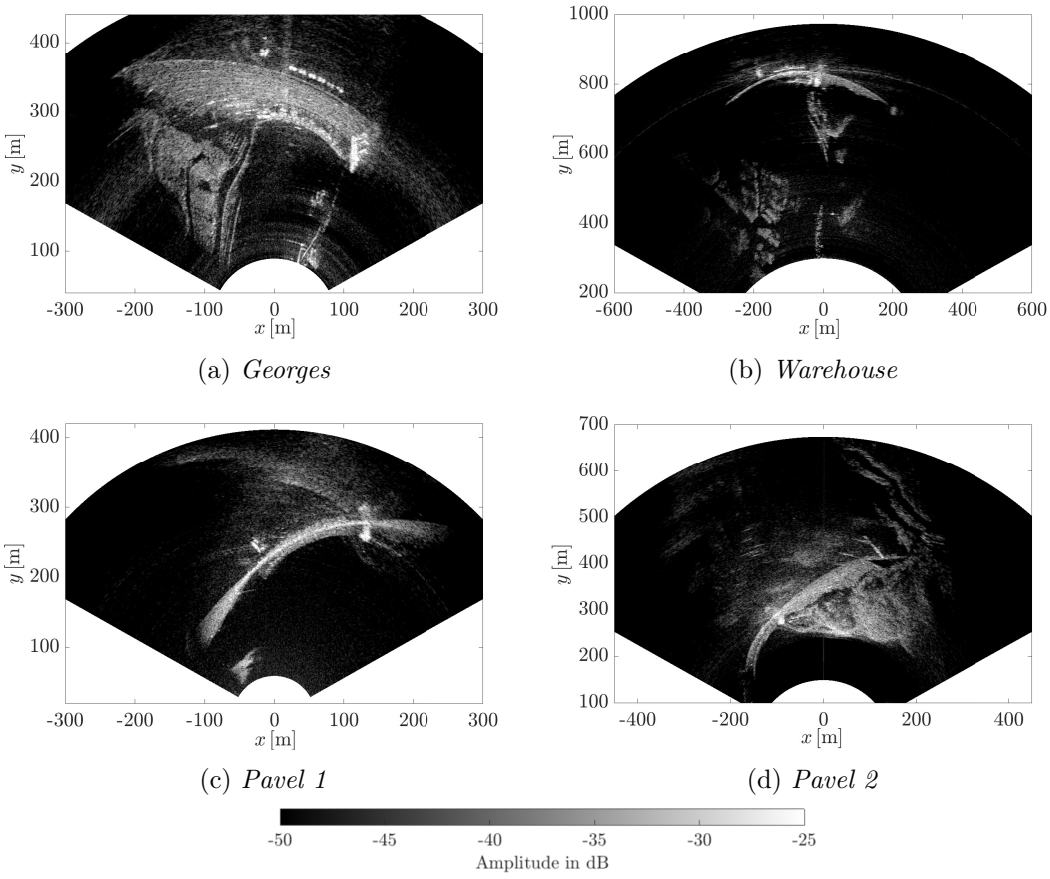

(a) *Georges* (b) *Warehouse*

(c) *Pavel 1* (d) *Pavel 2*

Figure 3.6: Amplitude images from the four stations.

data interpretation. Furthermore, the right embankment is captured effectively, manifesting coherent points useful for atmospheric and repositioning corrections. In contrast, *Warehouse* and *Pavel* stations are affected by a strong foreshortening due to the substantial reduction of the dam's 250 m height to less than 40 m in range. More details on these distortions are given in Chapter 5.

3.3.4 Sensitivity analysis

As the GB-SAR can only measure the projection of the displacement along the LOS, the installation of the station should consider the sensitivity of the measurements w.r.t. the underlying deformation process. In most GB-SAR monitoring scenarios, the expected displacement is considered along the slope of the terrain, as presented in [Noferini et al., 2009]. In the case of infrastructures, this consideration is meaningless, and other models must be considered for the a priori estimation of the displacement direction. Based on loading effects presented in Section 3.2.2, the company *Artelia* computed a numerical model resulting in a field of displacement vectors for the whole dam structure. The sensitivity is calculated point-wise as the absolute value of the normalised scalar product between the LOS vector and the theoretical displacement vector. A value of 0 means that the displacement vector is orthogonal to the LOS, implying that the GB-SAR is blind to any movement that affects these points. In contrast, a value of 1 enables the GB-SAR to observe the full magnitude of the displacement.

The results presented in Figure 3.7 reveal an optimal placement for the *Warehouse* station, with sensitivity nearly equal to one across most of the structure. Conversely, the remaining two stations exhibit sensitivity variations along the dam's expanse. The primary cause of lower sensitivity in certain dam sections can be attributed to the proximity of the two epoch-wise stations.

3.3.5 Station characteristics

Selecting the optimal location for GB-SAR monitoring involves an optimal balance among four key components: sensitivity, distortions, coverage and proximity to the target object. Ideally, the chosen station should be near the infrastructure, exhibiting sensitivity levels approaching one and remaining unaffected by SAR distortions. The higher the distance, the higher the effect of atmospheric changes on the measured signal.

Station	Distortions	Sensitivity	Coverage	Distance
Warehouse	high	very high	medium	medium
Pavel	high	medium	high	low
Georges	low	medium	medium	low

Table 3.2: Qualitative evaluation of the three GB-SAR stations.

The pronounced distortions affecting the stations *Pavel* and *Georges* will be exposed in Chapter 5 and especially Figure 5.13. Table 3.2 exhibits the advantages and drawbacks of each station. Nevertheless, a preference leans towards the *Georges* station, as it does not express significant limitations.

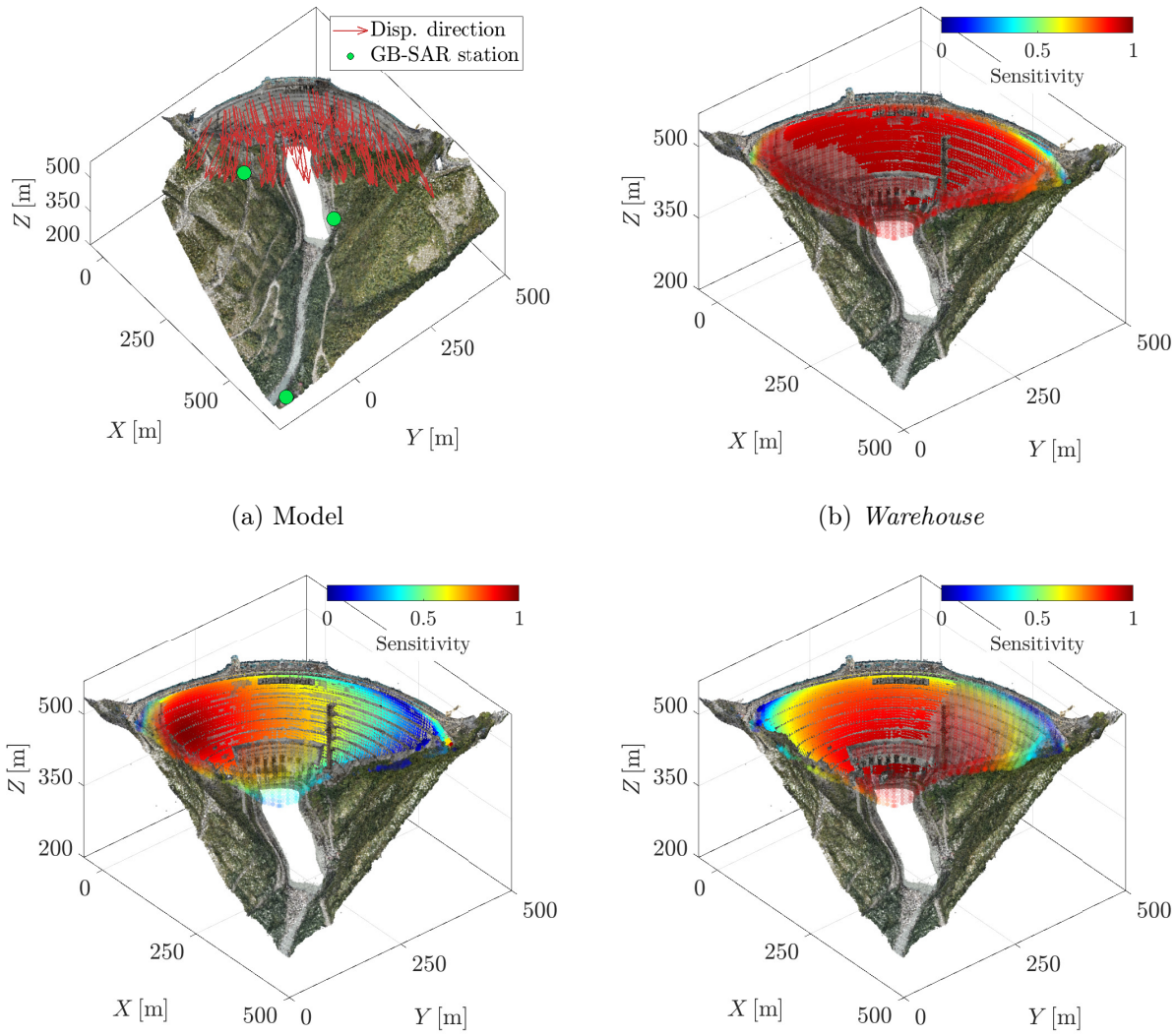

(a) Model

(b) *Warehouse*

(c) *Pavel*

(d) *Georges*

Figure 3.7: Sensitivity from the three stations. *Pavel 1* and *Pavel 2* offer the same sensitivity, as the orientation of the sensor does not influence it. The points not in the field of view are displayed with a transparent coefficient.

3.4 Geocoding support

3.4.1 3D model

As the geocoding is relevant in this thesis, we present the support used to map the GB-SAR data on the 3D world. The construction of the 3D model was achieved through unmanned aerial vehicle (UAV) photogrammetry equipped with a 45 MPix. camera. For the georeferencing, 12 ground control points and 3 checkpoints were employed, yielding mean accuracies of 0.10 m and 0.15 m, respectively. To facilitate local processing in *Matlab* on a notebook, the point cloud density has been reduced to maintain a 15 cm distance between points. This decision still ensures multiple points per GB-SAR resolution cell for subsequent analysis.

3.4.2 Corner reflectors

Nine corner reflectors were fixed to the dam to understand better the geometry of received radar signals. Their orientation is tailored to the *Warehouse* station, the primary station for data processing. However, due to the dam's shadow effects on GNSS signals, determining their 3D coordinates using this technique is infeasible. Consequently, their position is determined on the final 3D model output, with the help of the painted pattern visible in Figure 3.8. The accuracy of the pointing of the phase centre on this 3D model is expected to be around 10 cm.

Figure 3.8: Panoramic view from one corner reflector and station positions.

Figure 3.8 also provides the position of the three stations, and their distribution illustrates clearly the height difference between the station *Pavel* and the two others.

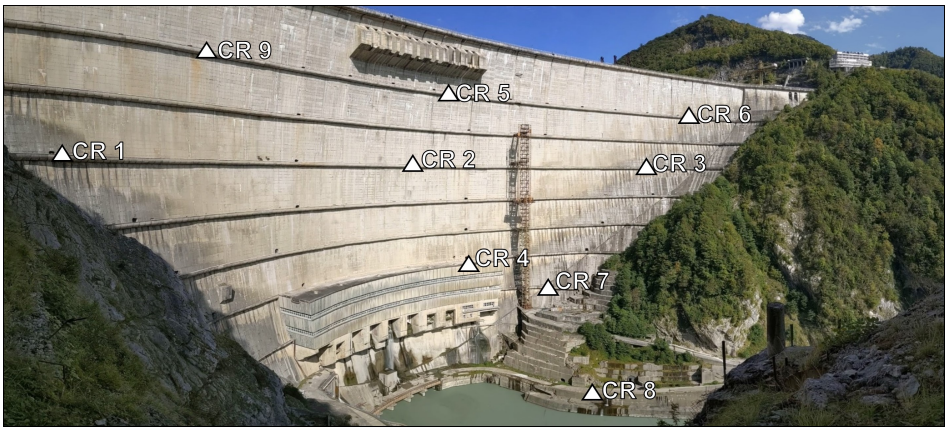

Figure 3.9: Corner reflectors location at Enguri Dam.

Figure 3.9 presents the placement of the corner reflectors on the dam. CR 1 to 3 are positioned on the same balcony, at *Pavel* station level, situated approximately 427 m above sea level. CR 5, 6, and 9 are located on two balconies higher, at an elevation of 475 m. CR 4 and 7 are positioned on the lower dam section, while CR 8 stands in front of the dam, nearly at the height of the *Warehouse* station.

CHAPTER 4

Autonomous position and orientation of a GB-SAR instrument

Contents

4.1 Introduction

GB-SAR systems usually work with an external model of the observed scenario to geocode the displacement information on the 3D world coordinate system. The geocoding is one of the crucial steps in GB-SAR processing, linking the 2D GB-SAR image and the 3D observed object. A problem arises from the required accuracy of the system's position and orientation to conduct adequate geocoding. Several works already noticed the necessity to correct this offset and are summarised in Section 2.6.4.

4.1.1 Measurement uncertainty

To determine the GB-SAR position within the global coordinate system, denoted as $\mathbf{X}_{\text{SAR}} = (X_{\text{SAR}}, Y_{\text{SAR}}, Z_{\text{SAR}})$, and its orientation angle relative to the north[1], Ψ_{SAR}, the conventional approach involves measuring the left and right extremities of the linear scanner. These extremities are marked by the manufacturer with small screws. Their average corresponds to the centre of the linear scanner and the offset with the array phase centre is negligible w.r.t. the GB-SAR resolution cells. The maximum difference is in elevation and reaches approximately 20 cm. Converted into a range offset with the Pythagoras' theorem, it corresponds to an offset from 0.4 mm to 0.02 mm for a range between 50 m and and 1 000 m. The measured extremities are designated by $\mathbf{X_L} = (X_L, Y_L, Z_L)$ and $\mathbf{X_R} = (X_R, Y_R, Z_R)$. All quantities refer to Figure 4.1, where three main coordinate systems are defined and used throughout the chapter.

- (X, Y, Z) is the global 3D reference frame, where the external 3D model is available.
- $(\tilde{X}, \tilde{Y}, \tilde{Z})$ is the 3D reference frame, centered on the GB-SAR, with $\tilde{Y}$ the looking direction of the instrument. The vertical vector is the same as the global reference frame, but the origin is located on the sensor. If no ambiguities exist, this reference frame is always given with the best available GB-SAR position and orientation parameters.
- (x, y) is the 2D SAR reference frame.

Six parameters must be determined in a complete positioning problem: the three translations and the three rotations around each axis. The rotations around the planar axes can be decomposed around $\tilde{X}$ and $\tilde{Y}$. Due to the system's inherent characteristics, a rotation of the phase centre around $\tilde{X}$ does not influence the acquisition. Additionally, the system is assumed to be well levelled, i.e. $Z_L = Z_R$. As a result, four parameters remain for the absolute positioning of the system: $\mathcal{X}_{\text{SAR}} = (X_{\text{SAR}}, Y_{\text{SAR}}, Z_{\text{SAR}}, \Psi_{\text{SAR}})$.

The measurements of the rail extremities can be achieved via a total station, a GNSS, or even a pointing on a georeferenced 3D model. The measured quantities can be represented using Gaussian distributions when employing these conventional techniques, assuming that $\mathbf{X_L} \sim \mathcal{N}(\overline{\mathbf{X}}_\mathbf{L}, \mathbf{\Sigma})$, and that $\mathbf{X_R} \sim \mathcal{N}(\overline{\mathbf{X}}_\mathbf{R}, \mathbf{\Sigma})$, with $\overline{\mathbf{X}}_\mathbf{i} = (\overline{X}_i, \overline{Y}_i, \overline{Z}_i)$, $i = \{L, R\}$ representing the vectors of true values of the parameters and $\mathbf{\Sigma} = \text{diag}(\sigma_H^2, \sigma_H^2, \sigma_V^2)$ is the covariance matrix of the observed variables. The horizontal precision σ_H is considered identical for the two axes, while the vertical precision σ_V is different. With GNSS measurements, $\sigma_V > \sigma_H$, while considering an insertion into a geodetic network with a total station and levelling, $\sigma_V < \sigma_H$.

[1] also referred as azimuth.

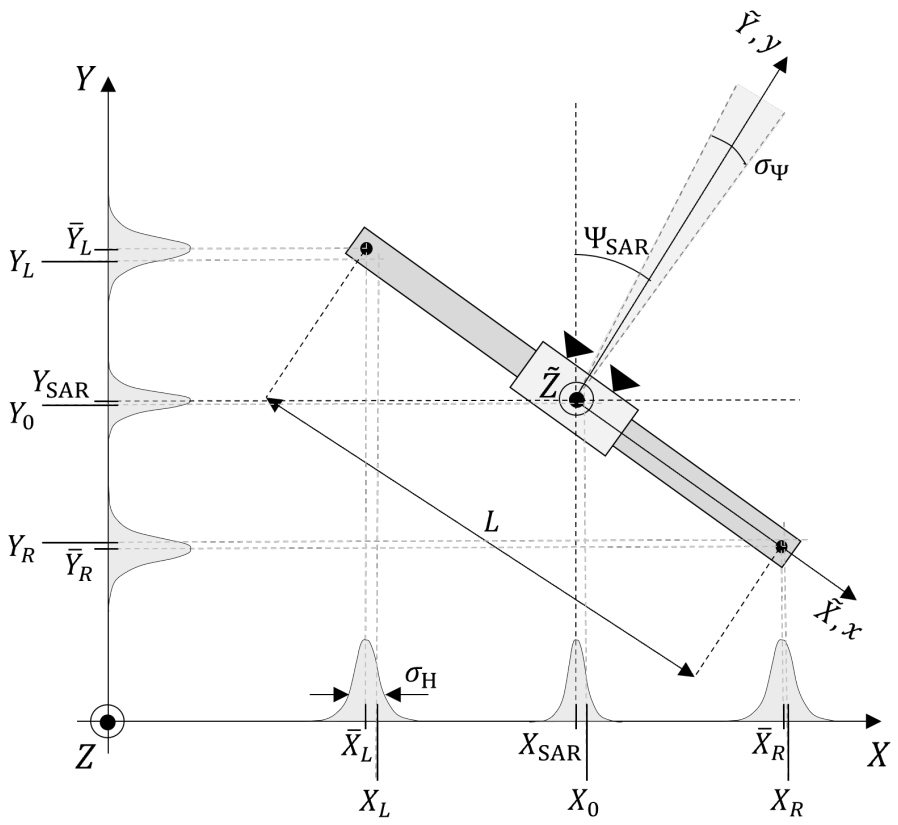

Figure 4.1: Uncertainty propagation during the georeferencing of a linear GB-SAR system.

4.1.2 Transmission to GB-SAR georeferencing parameters

The maximum likelihood estimate of the coordinates of the GB-SAR centre and its orientation using the measurement of the extremities are given by:

$$\mathbf{X_0} = \frac{1}{2}\left(\mathbf{X_L} + \mathbf{X_R}\right) \quad ; \quad \Psi_0 = \operatorname{atan2}\left((Y_L - Y_R), (X_L - X_R)\right) = \operatorname{atan2}\left(\Delta Y, \Delta X\right) \tag{4.1}$$

These values are stored in the vector of parameters $\mathcal{X}_0 = (X_0, Y_0, Z_0, \Psi_0)$ and differ from the true vector of parameters $\mathcal{X}_{\mathrm{SAR}}$. Their accuracy depends on the measurement accuracy of the linear scanner extremities, and a visualisation is provided in Figure 4.1. As $\mathbf{X_0}$ is a mean of Normal distributions, we can directly derive its PDF given by $\mathbf{X_0} \sim \mathcal{N}(\overline{\mathbf{X}}_\mathbf{0}, \mathbf{\Sigma_0})$ with $\overline{\mathbf{X}}_\mathbf{0} = \frac{1}{2}(\overline{\mathbf{X}}_\mathbf{L} + \overline{\mathbf{X}}_\mathbf{R}) = \mathbf{X}_{\mathrm{SAR}}$ and $\mathbf{\Sigma_0} = \frac{1}{2}\mathbf{\Sigma}$. However, the expression of the PDF corresponding to the orientation angle is not straightforward, and its derivation is proposed in Appendix A. Nevertheless, the standard deviation is directly accessible using the law of variance error propagation [Niemeier, 2008] and leads to the following formulation:

$$\sigma_{\Psi_0} = \frac{\sqrt{2}\,\sigma_H}{L} \tag{4.2}$$

As a numerical example, we take the rail length of the IBIS-FM, $L = 2\,\mathrm{m}$ and the most occurring case, when GNSS in real-time kinematic mode is used to measure the extremities. The typical precision

of such a measurement is about $\sigma_H^{\text{GNSS}} = \sigma_X^{\text{GNSS}} = \sigma_Y^{\text{GNSS}} = 2\,\text{cm}$ for the planar components and $\sigma_V = \sigma_V^{\text{GNSS}} = 5\,\text{cm}$ for the vertical component. Then, the propagation to the parameters $\mathcal{X}_0$ is given by:

$$\begin{aligned}
\sigma_{X_0}^{\text{GNSS}} &= \sigma_{Y_0}^{\text{GNSS}} = \frac{\sigma_H^{\text{GNSS}}}{\sqrt{2}} = 1.4\,\text{cm} \\
\sigma_{Z_0}^{\text{GNSS}} &= \frac{\sigma_V^{\text{GNSS}}}{\sqrt{2}} = 3.5\,\text{cm} \\
\sigma_{\Psi_0}^{\text{GNSS}} &= \frac{\sqrt{2}\,\sigma_H^{\text{GNSS}}}{L} = 14\,\text{mrad} = 0.8^\circ
\end{aligned} \tag{4.3}$$

Regarding the system's location $\mathbf{X_0}$, the accuracy is sufficient as the resolution in range satisfies $\rho_r = 0.75\,\text{m} > 20\sigma_H$. However, the major challenge emerges for the orientation Ψ_0. The uncertainty represents more than three resolution cells for the IBIS-FM, implying that the cross-range offset could reach up to 12 m at 1 km. The geocoded information may undergo considerable distortion in comparison to its real location. Therefore, reducing this error is essential to interpret the deformation map adequately. Figure 4.2 illustrates the impact when using only approximate external parameters. The black grid corresponds to the grid position obtained with the true GB-SAR external parameters $\mathcal{X}_{\text{SAR}}$. In contrast, the red one corresponds to the grid using the approximated values $\mathcal{X}_0$. The colourised pixels correspond to identical positions to their respective grids but to different areas in the 3D world.

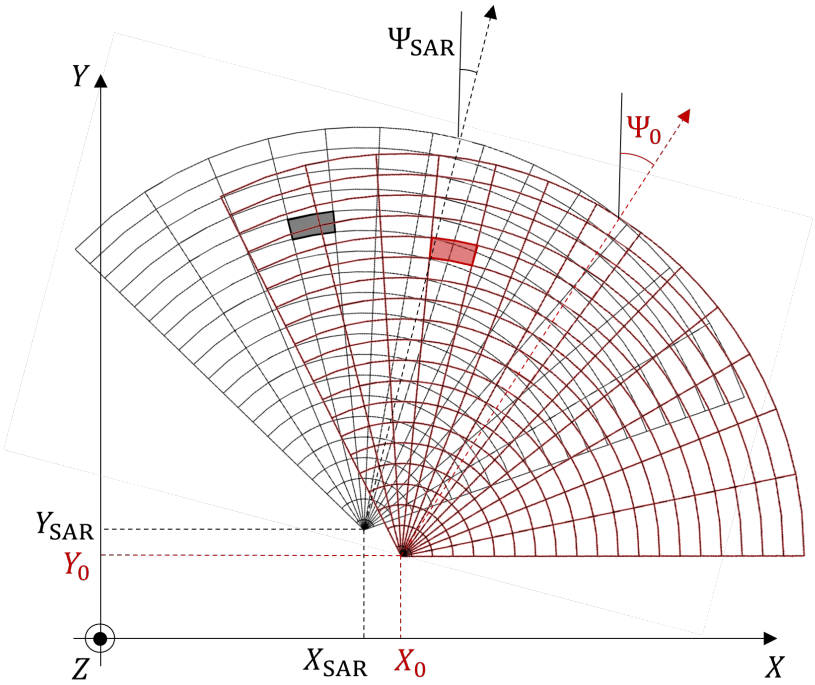

Figure 4.2: Effect of an offset in the position and orientation of a GB-SAR.

This chapter introduces a novel method for the estimation of the unknown parameters $\mathcal{X}_{\text{SAR}}$. The initial section of the chapter focuses on a theoretical analysis of the scenario, aiming to assess the

problem's separability between location and orientation correction. Subsequently, the first part of the algorithm, founded on image simulation and matching to estimate the system's azimuth, is presented. The new ray tracing algorithm and image simulation methodology are described in detail. The second part is based on tomographic reconstruction to estimate the system's location. The third part outlines the employed workflow. Finally, the methodology is applied to two case studies: the Enguri Dam and a large copper open-pit mine.

4.2 Separability of the correction in orientation and translation

A classical variance propagation analysis is conducted to assess the implication of inaccuracies in the four parameters of the GB-SAR. For a point of a 3D model with the coordinates (X, Y, Z), its radar coordinates (r, θ) can be expressed as follows:

$$\begin{cases} r &= \sqrt{(X-X_0)^2+(Y-Y_0)^2+(Z-Z_0)^2} = \sqrt{\tilde{X}^2+\tilde{Y}^2+\tilde{Z}^2} \\ \theta &= \arcsin\left(\frac{(X-X_0)\cos(\Psi_0)-(Y-Y_0)\sin(\Psi_0)}{r}\right) = \arcsin\left(\frac{\tilde{X}}{r}\right) \end{cases} \tag{4.4}$$

Without loss of generality, the functions are evaluated at $\mathcal{X}_0 = (0, 0, 0, 0)$, as the absolute position in the world coordinates has no role in the equations; only the position relative to the sensor matters. The following uncertainties are obtained:

$$\begin{aligned} \sigma_\theta^2 &= \sigma_\Psi^2 + \left(\frac{X^2}{r^4} + \frac{\cos^2(\psi)}{r^2}\right)\sigma_H^2 + \frac{X^2Z^2}{r^4Y^2}\sigma_V^2 \\ \sigma_r^2 &= \left(\frac{X^2+Y^2}{r^2}\right)\sigma_H^2 + \frac{Z^2}{r^2}\sigma_V^2 \\ \sigma_x^2 &= \sin^2(\theta)\sigma_r^2 + r^2\cos^2(\theta)\sigma_\theta^2 \\ \sigma_y^2 &= \cos^2(\theta)\sigma_r^2 + r^2\sin^2(\theta)\sigma_\theta^2 \end{aligned} \tag{4.5}$$

Various variance ratios are computed on the 3D model of the Enguri Dam to illustrate that, in most cases, the error in orientation is the most contributing parameter to the geocoding error. Two cases are considered, one with typical GNSS measurements and one with no external measurements.

In the first scenario, the following standard deviations are adopted. $\sigma_H = 0.03\,\text{m}$ and $\sigma_V = 0.10\,\text{m}$. The standard deviation on the radar coordinates is calculated using $\sigma_\Psi = 1°$ and $\sigma_\Psi = 0°$. The ratio of the two computed standard deviations enables gauging the impact of σ_Ψ on the radar coordinate offsets.

In the second scenario, an operator without access to external measurement data is considered. In this case, only a visual pointing of the radar position on the 3D model can provide approximate values. In worst cases, it can lead to $\sigma_H = 5\,\text{m}$, $\sigma_V = 10\,\text{m}$ and $\sigma_\theta = 3°$. Again, the simulation is conducted with and without error on Ψ_0, and the results on the 3D model are compared.

In the case of GNSS measurements available, the standard deviation ratio on the θ and x coordinate ranges from 0.1% to 1% on the whole 3D model. Thus, the offsets on these radar coordinates arise mainly from the inaccuracy of the system's orientation, and the components can be corrected sequentially. For the y coordinate, significant ratios are only observable in the narrow centre of the radar system's viewing direction. Differences emerge if no GNSS measurements are available and

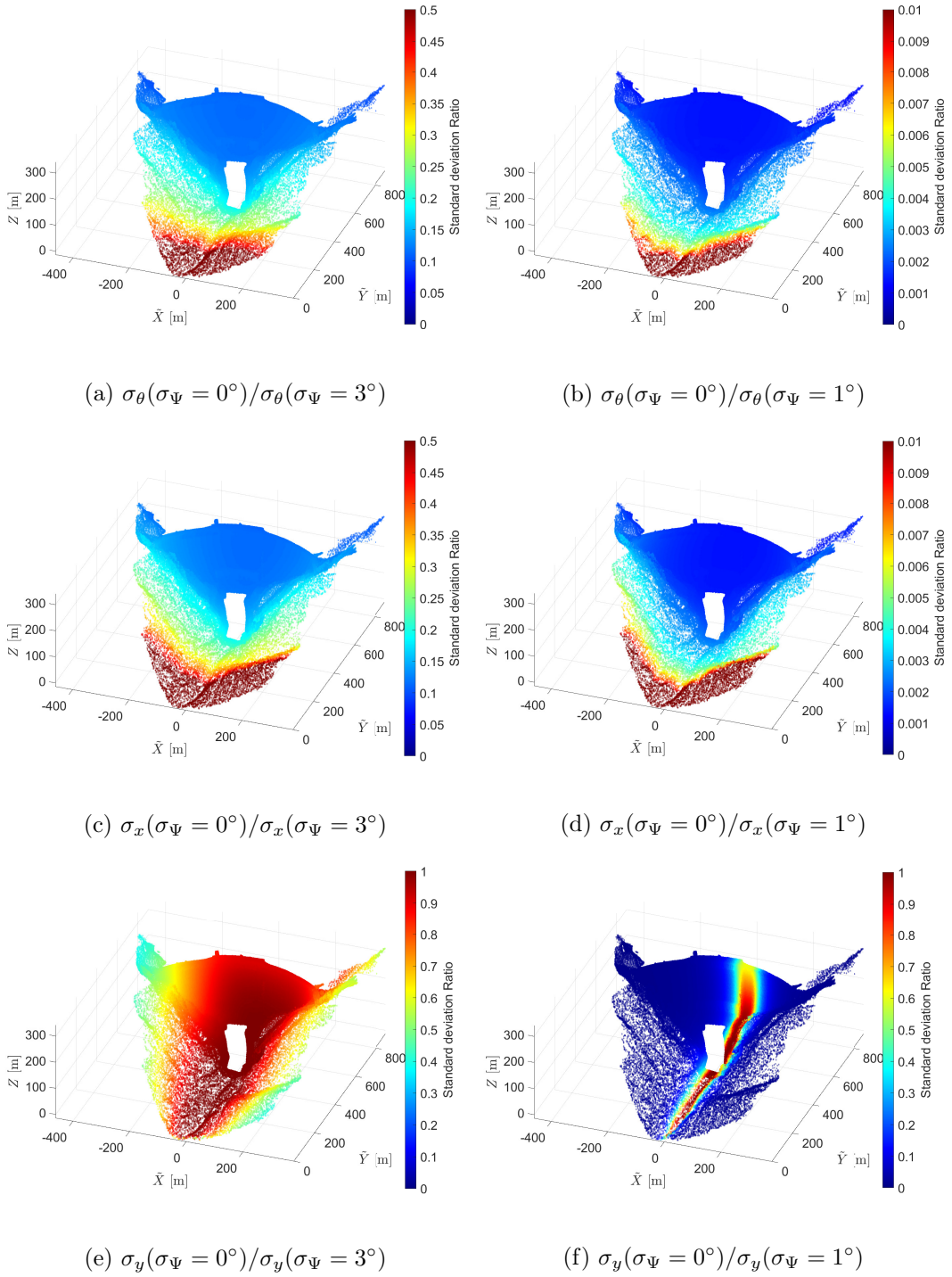

(a) $\sigma_\theta(\sigma_\Psi = 0°)/\sigma_\theta(\sigma_\Psi = 3°)$

(b) $\sigma_\theta(\sigma_\Psi = 0°)/\sigma_\theta(\sigma_\Psi = 1°)$

(c) $\sigma_x(\sigma_\Psi = 0°)/\sigma_x(\sigma_\Psi = 3°)$

(d) $\sigma_x(\sigma_\Psi = 0°)/\sigma_x(\sigma_\Psi = 1°)$

(e) $\sigma_y(\sigma_\Psi = 0°)/\sigma_y(\sigma_\Psi = 3°)$

(f) $\sigma_y(\sigma_\Psi = 0°)/\sigma_y(\sigma_\Psi = 1°)$

Figure 4.3: Standard deviation ratio on the radar coordinates. The example is computed with the instrument located at the *Warehouse* station. (a)-(c)-(e) is in the case of only coarse positioning of the instrument, while (b)-(d)-(f) is in the case of GNSS measurements available. The first column is for the θ coordinate, the second is for the x coordinate, and the third is for the y coordinate. The r coordinate is not presented as an error in the orientation does not impact it.

the horizontal offsets are significantly larger. Depending on the range of the observed points, the horizontal error has an impact ranging from 15 % to 50 %. We also see that the θ coordinate and the x coordinate are affected by a similar pattern. Nevertheless, even in situations with substantial horizontal errors, the impact of orientation errors remains more pronounced than the system's location for far enough monitored objects.

4.3 Ray tracing for image simulation

This section extensively presents the process of simulating GB-SAR images using the P-RaySAR algorithm. This technique combines ray tracing with intensity modelling to replicate the interaction between a GB-SAR system and a 3D scenario. The first presentation of P-RaySAR is available in [Rebmeister et al., 2022a]. Materials from the latter publication are marked with a blue frame.

4.3.1 P-RaySAR: A new algorithm for GB-SAR image simulation

4.3.1.1 Geometrical model

The use of ray tracing was already studied in the context of interpreting spaceborne SAR data. Notably, [Balz et al., 2015] conducted a comparison between three SAR image simulation algorithms. SARViz is an algorithm based on rasterisation, while RaySAR and CohRas are based on ray tracing principles. RaySAR is an open source SAR simulator and is used as the foundation of this work due to its emphasis on the geometric correctness of the simulated signals [Auer et al., 2016]. A detailed explanation of the RaySAR algorithm, implemented using *POV-Ray*, is provided in [Auer, 2011], with illustrative simulation examples. Given a 3D model or an object shape, RaySAR enables the simulation of SAR images adapted to the characteristics of a SAR sensor on a satellite. It employs an orthographic projection as the SAR sensor is located significantly far from the ground, i.e. the wavefront of the electromagnetic signal is assumed to be locally flat. This assumption does not hold in the case of a GB-SAR system, as the sensor is only some hundred meters away from the observed scene. Hence, a modification of the geometric equations in RaySAR is required for this work. Adopting a perspective camera model enables the simulation of the perspective imaging inherent to the GB-SAR, as depicted in Figure 4.4. In this way, we name this algorithm P-RaySAR for Perspective-RaySAR.

The model in P-RaySAR introduces a distinction between specular and diffuse reflections, specifically excluding diffuse-diffuse interactions. The algorithm processes one ray as illustrated in Figure 4.4.

- Step 1: A ray is projected along the path denoted as s_1.
- Step 2: The specular direction of reflection is computed, and the ray continues along s_2. Meanwhile, a diffuse contribution from this intersection is sent back to the sensor along d_1.
- Step 3: Another specular direction is computed, resulting in the ray s_3. The diffuse contribution d_2 returns to the sensor and crosses the grid.
- Step 4: The specular ray is computed and sent along s_4. The diffuse contribution is also computed with d_3. However, the ray is not fully visible as starting behind object 3 and will not be saved.

Notably, the algorithm refrains from computing diffuse rays originating from Object 1 and propagating in other directions. The coordinate axes depicted are the ones from *POV-Ray*, which are based on a left-handed reference frame, with the Z-axis being the viewing axis of the camera.

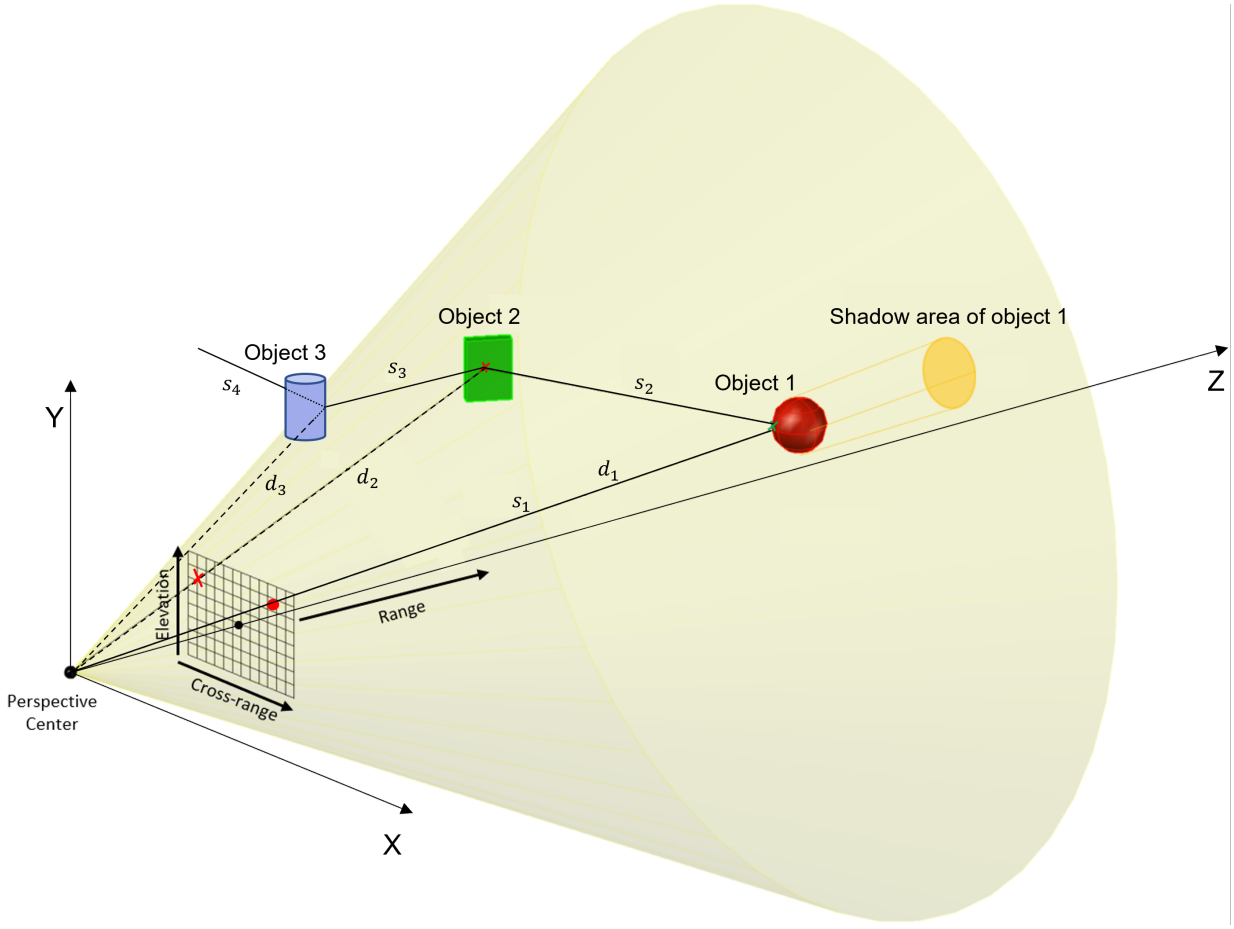

Figure 4.4: Example of a signal path with P-RaySAR. The rays s_i are specular and d_i are diffuse contributions. Rays are followed in the reverse direction ($s_1 \rightarrow s_2 \rightarrow s_3 \rightarrow s_4$).

The geometry of signal contributions in P-RaySAR involves two primary sources of information. The first one is the coordinates of intersection points on the 3D model, enabling the reconstruction of the whole path of the rays. The second information is the 2D coordinates of this signal in the GB-SAR imaging geometry that needs to be computed from the 3D intersection coordinates. For direct signal reflection, the link between the 3D intersection point and the corresponding 2D coordinates is straightforward and relies on Equation 2.12. For multiple signal reflections, a correction is computed using the full ray path. The application of this correction is called focusing, as the final azimuth and elevation coordinates are obtained by focusing the first and last rays together. There is no direct link with the classical use of the term focusing in the SAR context.

Figure 4.5 represents several points for the geometric modelling of a double bounce. The signal's path is shown as continuous black lines, divided into segments r_1 to r_3, each with a specific length. The intersections of the signal with the 3D model are represented with P_1 and P_2. The distance to the SAR sensor and two angles (horizontal, denoted with α, and vertical, denoted with β) are stored for each intersection point. With this information, the position of

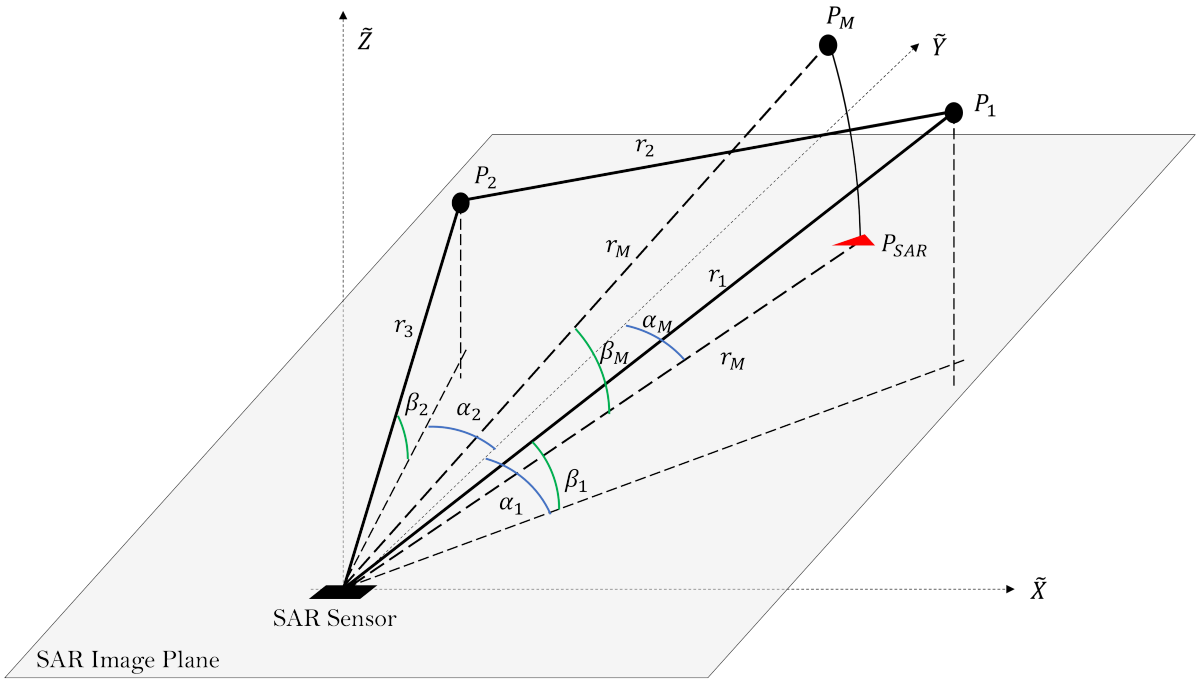

Figure 4.5: Double bounce simulated with P-RaySAR. P_M marks the signal phase centre in the 3D geometry, and the observation of the GB-SAR without resolution in height is represented with the red triangle P_{SAR}. The intersection points of the signal and the 3D model are the points P_1 and P_2, which correspond to the signal path linked to the observed red triangle. Adapted from [Rebmeister et al., 2022a].

the signal's phase centre for the observed point within the radar geometry is determined and depicted by the point P_M. Its polar coordinates are defined with Equation 4.6. The observed point is located on the SAR-image plane (red triangle, P_{SAR}) using the projection defined in Equations 4.4.

$$r_M = \frac{\sum_{i=1}^{n+1} r_i}{2} \qquad \alpha_M = \frac{\alpha_1 + \alpha_n}{2} \qquad \beta_M = \frac{\beta_1 + \beta_n}{2} \tag{4.6}$$

The range coordinate is calculated as half of the path distance of the whole ray. However, the horizontal and vertical angles are computed as the mean of the sent and received rays. Indeed, the SAR system can only interpret the direction of the sent and the incoming signal and is "blind" to what is happening in between. These equations are a direct adaption of the corresponding equations used in RaySAR with an orthographic projection presented in [Auer, 2011] (Equations 17, 18 and 19). In the latter work, the equations are validated with experimental results from a simulation applied to corner reflectors. The same experiment for the perspective projection is also presented in Figure 4.6. The path of the ray is documented by storing the coordinates of detected intersection points on surfaces and linking it to the received signal with GB-SAR coordinates (r, θ). As an example, the output for the double bounce presented in Figure 4.5 is exposed in Table 4.1.

This series of steps in P-RaySAR's geometric modelling allows for the simulation and analysis of signal reflections, intersection points, phase centre positions, and image plane coordinates. It is

Points	r	α	β	r_{int}	α_{int}	β_{int}	I	b	s
P_1	r_1	α_1	β_1	r_1	α_1	β_1	I_1	1	0
P_M	r_M	α_M	β_M	r_3	α_2	β_2	I_2	2	1

Table 4.1: P-RaySAR output for the ray path represented in Figure 4.5.The first three columns correspond to the 3D polar coordinates of the observed point. The three middle columns give the polar coordinates of the corresponding last intersection point. The last three columns are the related received intensity, the bounce level and a Boolean value specifying if the signal is specular or not.

essential for understanding the behaviour of signal reflections and their impact on GB-SAR images.

4.3.1.2 Simulation on a corner reflector

The algorithm is tested on a corner reflector (CR) model to validate the equations used for the focusing. It was created directly in *POV-Ray* and used for simulation with P-RaySAR. The CR is positioned at 20 m and oriented towards the sensor.

In Figure 4.6, the results of the P-RaySAR simulation for this CR are represented. The first noticeable result is that single and double bounces of signals do occur, which are related to diffuse signal reflections. However, the intensity is much smaller than occurring specular signal reflections. The focused positions of triple signal reflections are concentrated at the tip of the CR, and signal double reflections are focused on the edges of the CR, as pointed out in Figure 4.6a. This result corresponds exactly to what is expected. In Figure 4.6b, the position of the intersection points (ray-surface) is represented and colour-coded with the corresponding signal reflection level. In the case of signal triple bounces, the marked area corresponds to the findings reported in [Sarabandi and Chiu, 1996]. The main response of a corner reflector stems from signal triple reflections of specular type, whereas single and double signal bounces are of diffuse type.

4.3.2 Intensity model

The intensity and geometric information for each signal contribution are stored in P-RaySAR. A detailed explanation of the reflection models employed is presented in Section 4.3 and Appendix B.2 of the work by [Auer, 2011]. The computed intensity in P-RaySAR is done in a similar way as in the original RaySAR. For the diffuse and specular reflection, the models are given as follows:

$$\begin{aligned} I_d &= C_d I_0 \langle \boldsymbol{N}, \boldsymbol{L} \rangle^{F_d} \\ I_s &= C_s I_0 \langle \boldsymbol{N}, \boldsymbol{H} \rangle^{1/F_s} \end{aligned} \tag{4.7}$$

where I_0 is the intensity of the incoming signal, I_d and I_s are respectively the diffuse and specular intensity. $C_d \in [0\,;1]$ and $C_s \in [0;1]$ are the diffuse and specular reflection coefficients the user determines. $\boldsymbol{N}$ is the surface normal vector and $\boldsymbol{L}$ is the LOS vector. $\boldsymbol{H}$ denotes the bisection vector between $\boldsymbol{L}$ and $\boldsymbol{N}$. Finally, $F_d \in [0\,;1]$ is a brilliance factor (often set to 1), and F_s is a roughness factor. A signal coming back to the sensor is considered as specular if the angle between $\boldsymbol{S}$ and $\boldsymbol{L}$ is smaller than 1°, $\boldsymbol{S}$ being a specularly reflected ray.

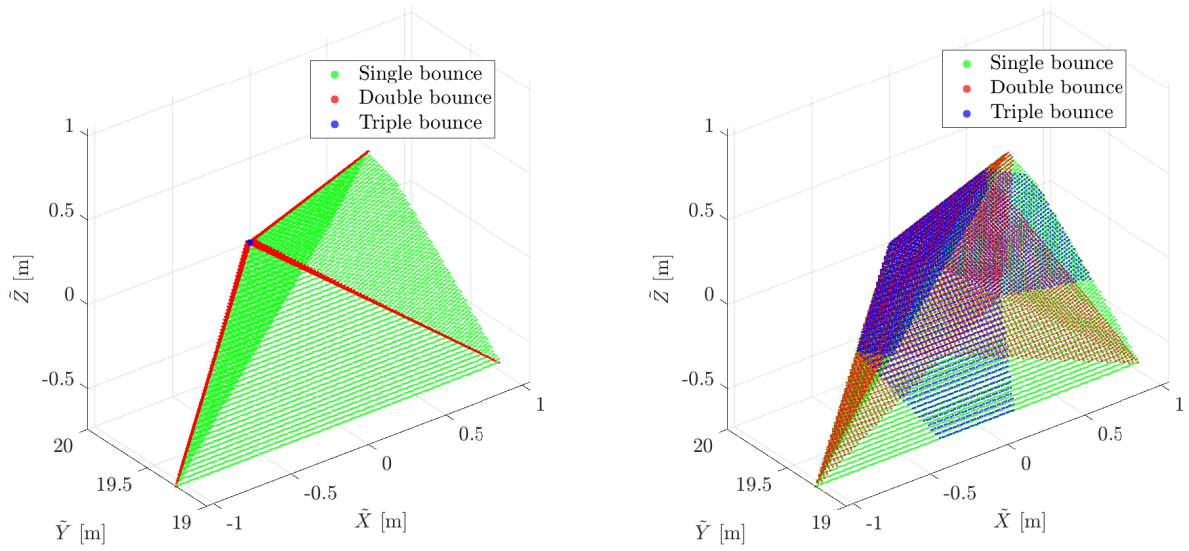

(a) Focused contributions

(b) Intersection points

Figure 4.6: Results of the simulation of a corner reflector with P-RaySAR. (a) is the position of the points as detected by the GB-SAR. (b) is the position of the intersection points between the 3D model and rays. Different colours represent the signal reflection levels 1-3. Adapted from [Rebmeister et al., 2022a].

4.3.3 From geometry to image simulation

The image simulation relies on the output table of P-RaySAR as presented in Table 4.1 and starts with the projection of all the detected signals by P-RaySAR in the GB-SAR geometry using Equation 2.12. Subsequently, the radar grid is computed, and the intensities within the same resolution cell are summed. Unlike the original RaySAR, only the non-coherent summation is proposed, as the phase information is irrelevant due to the inaccuracy of the 3D model.

An alternative approach is to consider only the geometrical output of P-RaySAR and to compute the received signal power with the *radar equation*, i.e. Equation 2.5. All elements of this equation are known except the RCS. An assumption could involve considering each point on the P-RaySAR model as a small disk as its RCS depends only on its area and the incidence angle. However, as pointed out by Figure 2.6, it is not a smooth function and can be strongly affected by the noise on the model. As a result, a simpler model grounded on the normalised radar cross section (NRCS) σ_0 is preferred. It corresponds to the RCS of an object divided by its area. For its computation, the model used in [Goering et al., 1995] and [Chen, 2001] is chosen and is given by:

$$\sigma_0(\theta_i) = \begin{cases} \kappa \cos^2(\theta_i) + \cos^n(2\theta_i)\cos(\theta_i) & \text{if } \cos(2\theta_i) > 0 \\ \kappa \cos^2(\theta_i) & \text{otherwise} \end{cases} \tag{4.8}$$

where θ_i is the incidence angle, computed with the normal vector $\boldsymbol{N}$ and the LOS vector $\boldsymbol{L}$ via the scalar product:

$$\theta_i = \arccos\left(\frac{\langle \boldsymbol{N}|\boldsymbol{L}\rangle}{\|\boldsymbol{L}\|\|\boldsymbol{N}\|}\right) \tag{4.9}$$

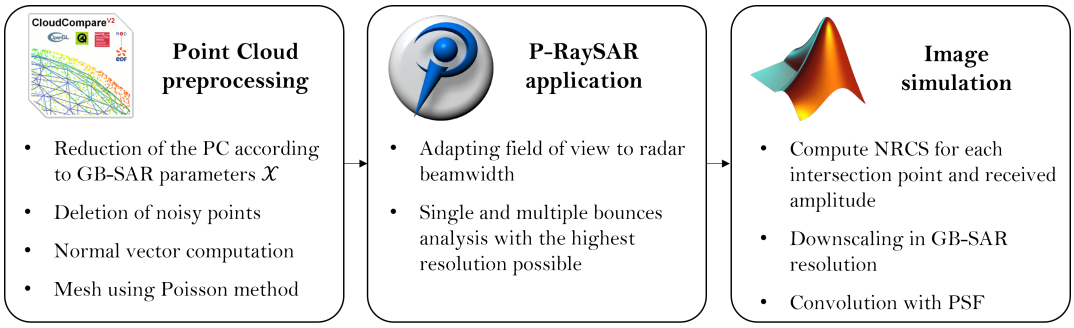

Figure 4.7: Flowchart of the image simulation steps with the different software packages used: *Cloud Compare, P-RaySAR, Matlab.*

In the model of Equation 4.8, the two elements of the top right term can be interpreted as a specular part and a diffuse part of the signal. κ represents the ratio of the contributing part of the specular and diffuse components. n determines the sharpness of the specular reflection peak. In [Goering et al., 1995], plausible values of the parameters κ and n are described by $n \in [8.5\,;13]$ and $k \in [0.1\,;0.3]$ such that values of $n = 10$ and $k = 0.2$ are set. Afterwards, considering a constant illuminated area for each point, the intensity can be computed using Equation 2.5. This simulation has more physical sense from the radar point of view. However, it can not yet take into account multiple signal reflections.

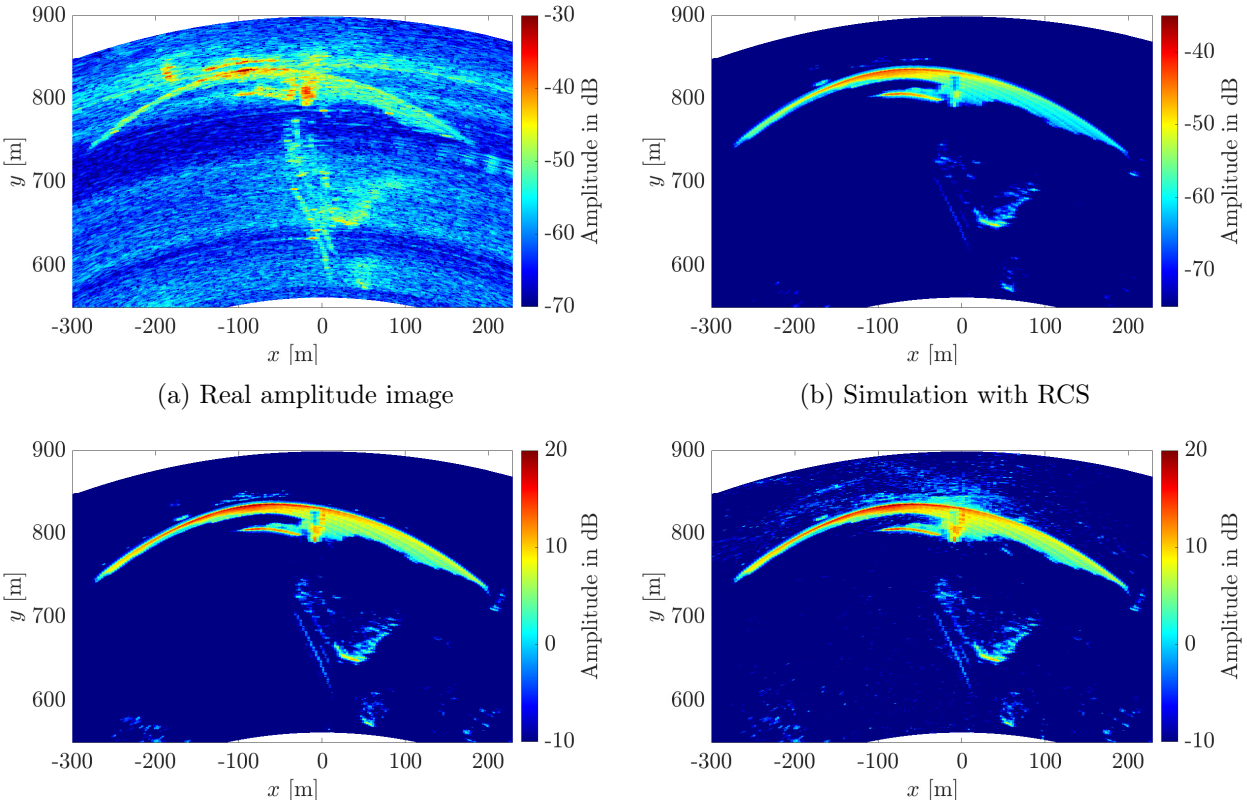

(a) Real amplitude image

(b) Simulation with RCS

(c) P-RaySAR with single signal reflection

(d) P-RaySAR with multiple signal reflection

Figure 4.8: Comparison of radar images at Enguri Dam. (a) is the real acquisition while (b-d) are simulations.

The resulting image is convolved with the system's point spread function, given by a *sinc* squared function. The final flowchart to simulate a GB-SAR image with the corresponding software packages used is presented in Figure 4.7. To convert a mesh in a usual format to the *POV-Ray* format, the *AccuTrans* software [AccuTrans, 2021] can be used.

Three simulation possibilities are conducted at Enguri Dam from the *Warehouse* station, and the outcomes are presented in Figure 4.8. The first impression is that all the images expose a similar behaviour. The amplitude proposed by the NRCS simulation is much more similar to the real image, whereas the others are considerably higher. It is essential to highlight that the real image displays certain bright spots not replicated by the proposed simulation methods. This divergence can be attributed to the nature of the scattering points. The created 3D model possesses a uniform diffuse scattering coefficient and is not classified before the simulation. Consequently, metallic objects, which reflect considerably more the radar signal, are not well recovered during the simulation. For instance, the line structures in front of the dam at $y \in [600\,;720]\,\mathrm{m}$ exhibit lower intensities than the real image. Moreover, these reflections are induced by very thin metallic safety railings that can be missed through the discretisation process of sending and receiving rays.

4.4 Tomography for GB-SAR

As presented further, the image simulation can only recover the orientation offsets and the planar translation. A 3D component from the system itself must also be introduced to correct a vertical error. The solution is to recover the 3D position of scattering points using vertical baselines.

4.4.1 Definition of the problem

In Chapter 2, the model of the interferometric phase as a function of the height using a vertical baseline $b_\perp$ between two acquisitions has been derived. It is possible to recover a 3D point cloud of the observed scenario using unwrapping algorithms, as demonstrated in [Noferini et al., 2007]. Tomographic solutions are better for estimating the height of the main scatterer(s) in each GB-SAR resolution cell, as they are independent of any criterion. Tomography using SAR data was first introduced in [Reigber and Moreira, 2000], where multiple acquisitions with varying view angles are used to synthesise an antenna in the elevation direction, enabling retrieval of the 3D position of one or multiple scatterers within the resolution cell. Tomography also allows the estimation of various other parameters, such as the linear and periodic motion proposed by [Zhu and Bamler, 2011a]. In our case, the tomography serves only to recover a 3D point cloud of the scenes, as the acquisitions are conducted within less than 2 hours, and no significant motion of the structure is expected.

For notation convenience, the elevation of a point w.r.t. the GB-SAR is given by $h = Z - Z_{\mathrm{SAR}}$ Assuming that N measurements indexed with $n \in [|1\,;N|]$ are available using different elevation baselines $b_{\perp,n}$, the continuous model of the tomographic acquisition is given by:

$$g_n = \int_V \gamma(h) \exp\left(-j\frac{4\pi b_{\perp,n}}{\lambda r}h\right) dh + \varepsilon_n \tag{4.10}$$

where g_n is the signal observed in a single pixel, and V represents the 3D volume projected in the resolution cell (visible in Figure 2.3). γ stands for the complex reflectivity profile in height and ε_n denotes Gaussian noise. A schematic representation of γ in case of layover at Enguri Dam is

available in 4.9. Considering a constant distribution in the plane and discretising the integral along the elevation direction leads to the following simplified equation:

$$g_n = \sum_{k=1}^{Q} \gamma(h_k) \exp\left(-j\frac{4\pi b_{\perp,n}}{\lambda r} h(k)\right) + \varepsilon_n \tag{4.11}$$

The unknowns of this equation are the reflectivity profile γ and the number of significant scatterers in the resolution cell Q. As several measurements are required, the system is written in terms of vector-matrix equation as follows:

$$\mathbf{g} = \mathbf{L}\boldsymbol{\gamma} \tag{4.12}$$

$$(\mathbf{L})_{p,q} = \exp\left(-i\frac{4\pi}{\lambda}\frac{b_{\perp,n}}{r} h_q\right) \tag{4.13}$$

In these equations, $\mathbf{g}$ is the measurement vector, $\mathbf{L}$ is the complex steering matrix, and $\boldsymbol{\gamma}$ corresponds to the reflectivity vector. Solving Equation 4.12 might first be straightforward as a linear equation system. However, around 4 to 20 measurements are typically available for hundreds of unknowns. Indeed, the columns of the measurement matrix represent a discretisation of the elevation axis and need to have a given resolution and a given bandwidth. It implies that the system of Equation 4.12 is underdetermined and can not be solved by a classical LS adjustment.

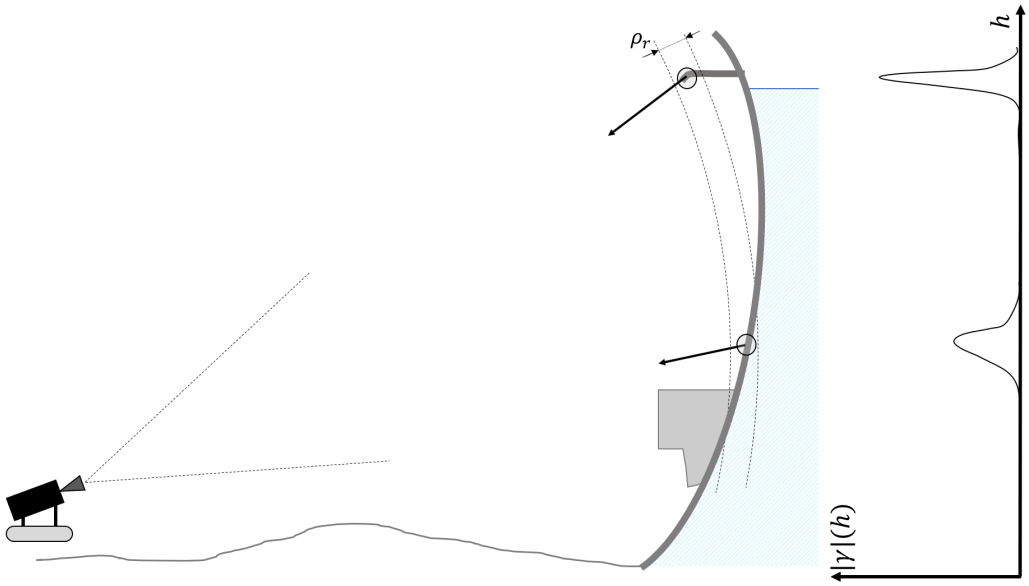

Figure 4.9: Tomographic GB-SAR principle. The two points fall in the same SAR resolution cell. The reflectivity profile γ is projected into the resolution cell and cannot be recovered without tomographic acquisitions.

Several methods exist such as the truncated singular value decomposition (TSVD) [Fornaro et al., 2005], multiple signal classification (MUSIC) [Gini et al., 2002], or compressive sensing (CS) methods [Zhu and Bamler, 2011a]. The last one is possible only when the unknown γ is sparse, i.e. its support is small compared to its dimension.

4.4.2 Compressive sensing for TomoSAR

The first usage of CS for TomoSAR is available in [Budillon et al., 2009]. Using the sparsity assumption, the CS problem related to Equation 4.12 is the following:

$$\text{minimise } \|\boldsymbol{\gamma}\|_0 \quad \text{subject to } \mathbf{g} = \mathbf{L}\gamma \tag{4.14}$$

where $\|.\|_0$ is defined as the support of the vector, i.e. the number of its non-zero entries. However, this problem is NP-hard, as explained in [Tillmann and Pfetsch, 2013] and does not lead to straightforward solutions. An easy method to solve the problem is to translate Equation 4.14 in the Basis Pursuit Denoising problem:

$$\hat{\boldsymbol{\gamma}} = \underset{\gamma \in \mathbb{C}^N}{\operatorname{argmin}} \left(\|\mathbf{g} - \mathbf{L}\boldsymbol{\gamma}\|_2 + \lambda_{\text{opt}} \|\boldsymbol{\gamma}\|_1 \right) \tag{4.15}$$

In Equation 4.15, the L_1-norm replaces the $\|.\|_0$-operator as it is a convex operator and implies sparsity as well. More information about the CS theory is available in [Foucart and Rauhut, 2013]. The parameter λ_{opt} is the Lagrange multiplier, and its choice is detailed in [Chen et al., 2001].

TomoSAR still presents some limitations. First, the theoretical Rayleigh resolution ρ_s gives the elevation resolution for non-parametrical linear spectral estimators. According to [Zhu et al., 2009] it is given by:

$$\rho_s = \frac{\lambda r}{2\Delta b} = \rho_s^{\circ} r \tag{4.16}$$

with Δb the length of the synthetic antenna in elevation and ρ_s° the angular elevation resolution. It means that two scatterers in the same resolution cell need to be at least separated by this elevation resolution to be distinguished with non-parametric spectral analysis. From this expression, the larger the baseline, the better the resolution. With the material at disposal, a baseline length of 22 cm is reachable, meaning that the angular resolution in elevation ρ_s° is about 40 mrad which is ten times smaller than the cross-range resolution of the IBIS-FM. At the observation distances for the Enguri Dam case study, the Rayleigh resolution ranges between 8 and 30 m. Considering the height of the Enguri Dam of 271.5 m, even this small synthetic antenna in elevation brings valuable information of the signal origin. Compressive sensing algorithms can perform better than the given Rayleigh resolution. In [Zhu and Bamler, 2011b], a deep study of the resolution of CS estimators was assessed. It was also shown that the Cramér-Rao lower bound on the accuracy of the elevation estimation for a single scatterer is given by:

$$\sigma_{\text{CR}} = \frac{\lambda r}{4\pi\sqrt{2\text{SNR}}\sqrt{N}\sigma_{b_\perp}} \tag{4.17}$$

where the SNR can be estimated via the amplitude dispersion and $\sigma_{b_\perp}$ is the standard deviation of the elevation aperture sample positions. For multiple scatterers, the model extends to more complex formulations.

Compressive sensing is a powerful tool for signal reconstruction, but it has some requirements on the steering matrix, which are not detailed in this thesis but can be found in [Foucart and Rauhut, 2013]. The minimising problem can be solved via different propositions. An effective algorithm is the so-called Scale-down by L1-minimisation, Model selection and Estimation Reconstruction (SL1MMER)

method from which the flowchart is detailed in [Zhu and Bamler, 2010]. The SL1MMER algorithm is very accurate but slow, and a compromising alternative is to use the orthogonal matching pursuit (OMP), very well presented in [Tropp and Gilbert, 2007] and used for TomoSAR in [Rebmeister et al., 2021]. In this chapter, CS methods are applied to recover the highest number of points achievable to get the highest TomoSAR point cloud density possible.

4.4.3 Acquisition concept

Several studies have demonstrated successful tomographic results using GB-SAR instrumentation. However, in most cases, the system is equipped with robotic components enabling motion in both horizontal and vertical directions. This automated configuration, as observed in works such as [Ji et al., 2014] and [Ferro-Famil et al., 2014], facilitates rapid and precise acquisitions along both axes, thereby enhancing the overall data collection process. The IBIS-FM has no vertical baselines, necessitating the manual creation of a vertical antenna by elevating the linear scanner and/or the radar head between two acquisitions. The atmospheric influence on interferograms is minimised by introducing a novel acquisition scheme tailored to mitigate this component in the observed phase. An acquisition with a specific elevation is surrounded by two acquisitions at the original height of the system. The complex average of these two SLC is computed and used as reference to reduce the atmospheric signal.

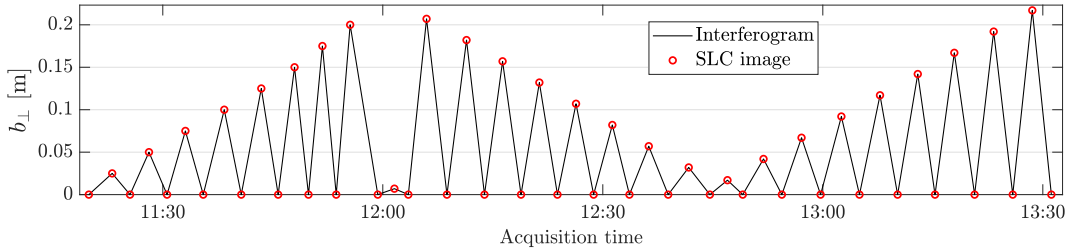

Figure 4.10: Proposed acquisition and interferogram formation for tomography with linear GB-SAR.

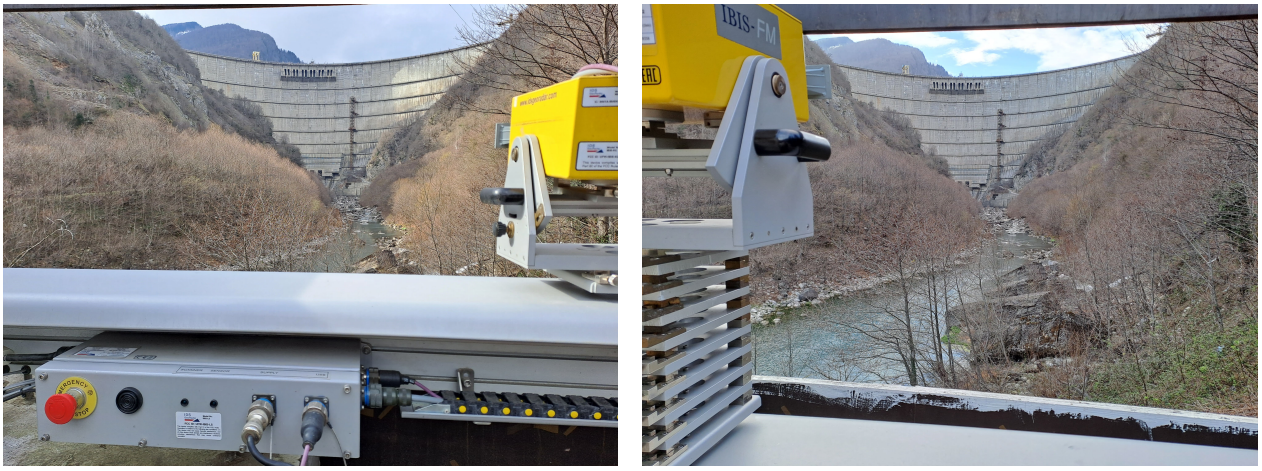

(a) Acquisition with $b_\perp = 0$ (b) Acquisition with $b_\perp = 17.5\,\text{cm}$

Figure 4.11: GB-SAR installed at *Warehouse* station without (a) and with elevated baseline (b).

Figure 4.10 represents an acquisition configuration tailored for achieving tomographic reconstruction from the *Warehouse* station. A total of 53 SLC images are acquired and result in 26 interferograms with varying baselines. As a result, a coherent and well-distributed synthetic antenna emerges, proportionally similar to what is achieved in satellite-based scenarios. Notably, the synthetic antenna reaches a spread of approximately $\Delta b = 22.5\,\text{cm}$. Using the insights afforded by Equation 4.16, the characteristics of the IBIS-FM system combined with this baseline configuration yields a Rayleigh resolution of $\rho_s = 31\,\text{m}$, for a point located at $r = 800\,\text{m}$.

4.4.4 Example at Enguri Dam

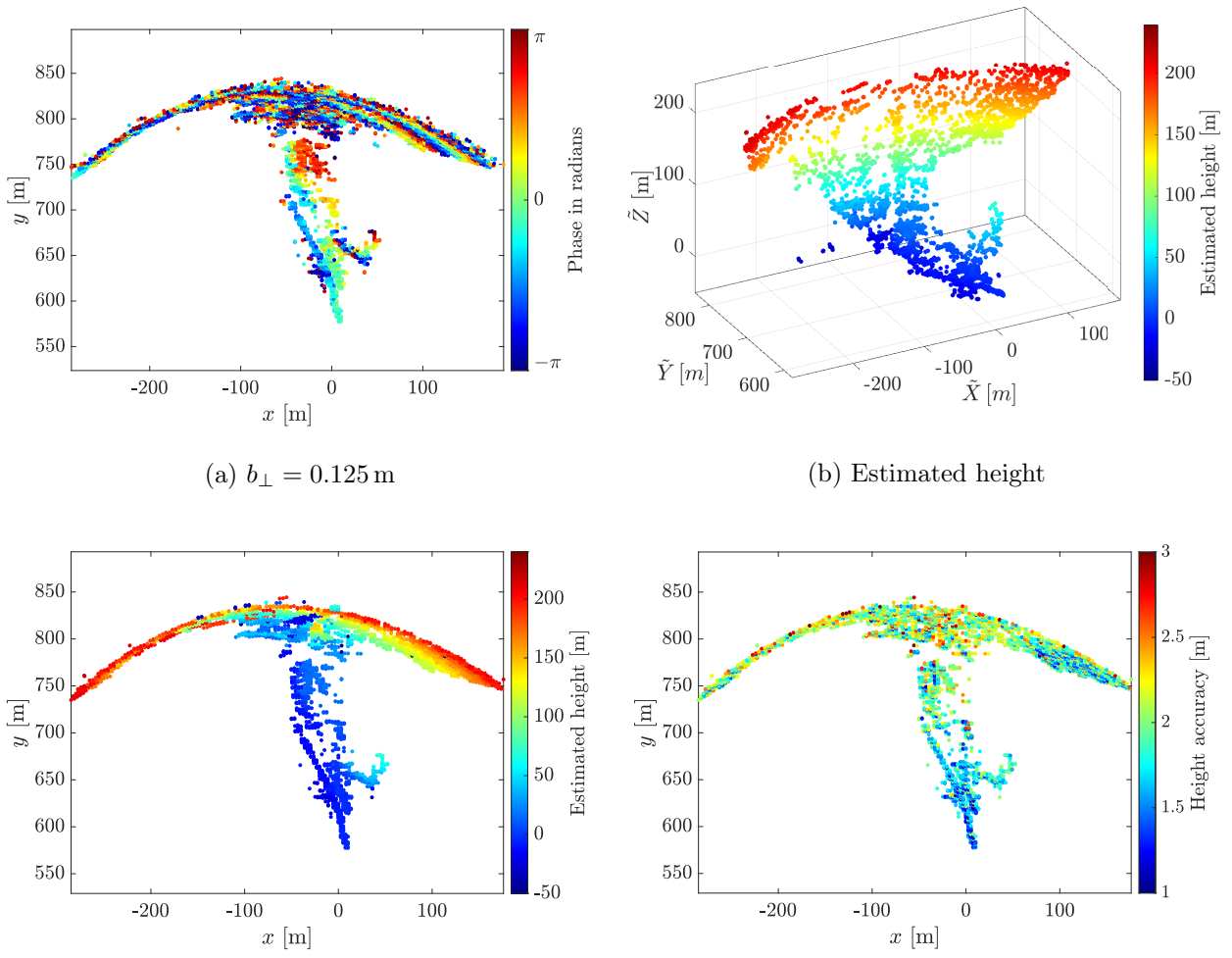

(a) $b_\perp = 0.125\,\text{m}$

(b) Estimated height

(c) Estimated height in (x, y) geometry

(d) Cramér-Rao lower bound of the estimated height

Figure 4.12: Result of the tomographic processing. (a) is an example of an input interferogram. (b) and(c) represent the results of the estimation, respectively in the 3D and the 2D geometry. (d) represents the Cramér-Rao lower bound of the estimated height.

Figure 4.12 offers a visual representation of the process. The interferogram in Figure 4.12a is an input data example. The rocks in front of the dam and the right section of the dam present visible fringes induced by a topographic gradient and could be solved by an unwrapping algorithm. Conversely,

the middle and left portions of the dam lack any discernible signal patterns. Figure 4.12b exhibits the final TomoSAR 3D point cloud. The dam structure is well represented, with only a few outliers. Representing this estimated height on the 2D geometry underscores the existence of a signal mixture originating from both upper and lower points in the middle of the dam. Furthermore, an intriguing observation emerges at $x \in [-40\,;-20]$ and $y \in [810\,;820]$, with points located under the dam. The situation is comparable with findings expounded in [Auer et al., 2011] with ghost persistent scatterers observed. In the continuous interferometric processing of Chapter 7, this area exhibits astonishing values. A deeper analysis with P-RaySAR is proposed in Appendix C.

4.5 Proposed workflow for autonomous GB-SAR georeferencing

As highlighted in Section 4.2, the predominant source of error in the georeferencing arises from the initial orientation of the system Ψ_0 and can be rectified separately from the position. The proposed workflow is available in Figure 4.13. The following subsections detail the algorithms on which the different steps are grounded. The illustration is based on the acquired data at Enguri Dam from the *Warehouse* station, presented in Chapter 3.

Firstly, the orientation is coarsely corrected based on the approximated coordinates $\mathcal{X}_0$ and the image simulation and matching techniques. Subsequently, if tomographic data are available, they are leveraged to assess the system's elevation. An offset in this coordinate can potentially introduce distortions in image simulation. However, due to a non-negligible bias that is exposed in simulated data, in Figure 4.17c, this correction is relevant only to detect coarse errors, with $\delta_{\text{thresh}} \approx 5\,\text{m}$. After that, a second rotation correction is conducted to refine the initial estimation. This correction employs the same methodology as the first step. Finally, if the position of the system is not accurately known, it is also corrected based on image-matching techniques or tomographic data if available.

4.5.1 Correction of the orientation

The initial step involves the simulation of an image in the (r, θ) domain, according to Section 4.3, using a 3D model of the scenario and the approximated set of parameter $\boldsymbol{\mathcal{X}}_0 = (X_0, Y_0, Z_0, \Psi_0)$. In this specific geometry, a horizontal shift in the image domain corresponds to a real-world rotation of the system around Z, as illustrated in Figure 4.14. The black grids correspond to the original geometry, and the red grids correspond to the ones obtained after a translation in θ of the original grid by 7°. In Figure 4.14b, the red grid coincides clearly with a rotation.

The link between (r, θ) and (x, y) coordinates of a point is given in Equation 2.13. After applying a translation of δ_Ψ along the θ axis in the polar geometry, the new coordinates of the points are represented as $(r', \theta') = (r, \theta + \delta_\Psi)$. Subsequently, the new Cartesian coordinates (x', y') can be expressed as:

$$\begin{aligned}
\begin{bmatrix} x' \\ y' \end{bmatrix} &= \begin{bmatrix} r\sin(\theta + \delta_\Psi) \\ r\cos(\theta + \delta_\Psi) \end{bmatrix} \\
\begin{bmatrix} x' \\ y' \end{bmatrix} &= \begin{bmatrix} r\sin(\theta)\cos(\delta_\Psi) + r\cos(\theta)\sin(\delta_\Psi) \\ r\cos(\theta)\cos(\delta_\Psi) - r\sin(\theta)\sin(\delta_\Psi) \end{bmatrix} \\
\begin{bmatrix} x' \\ y' \end{bmatrix} &= \begin{bmatrix} \cos(\delta_\Psi) & \sin(\delta_\Psi) \\ -\sin(\delta_\Psi) & \cos(\delta_\Psi) \end{bmatrix} \begin{bmatrix} x \\ y \end{bmatrix}
\end{aligned} \tag{4.18}$$

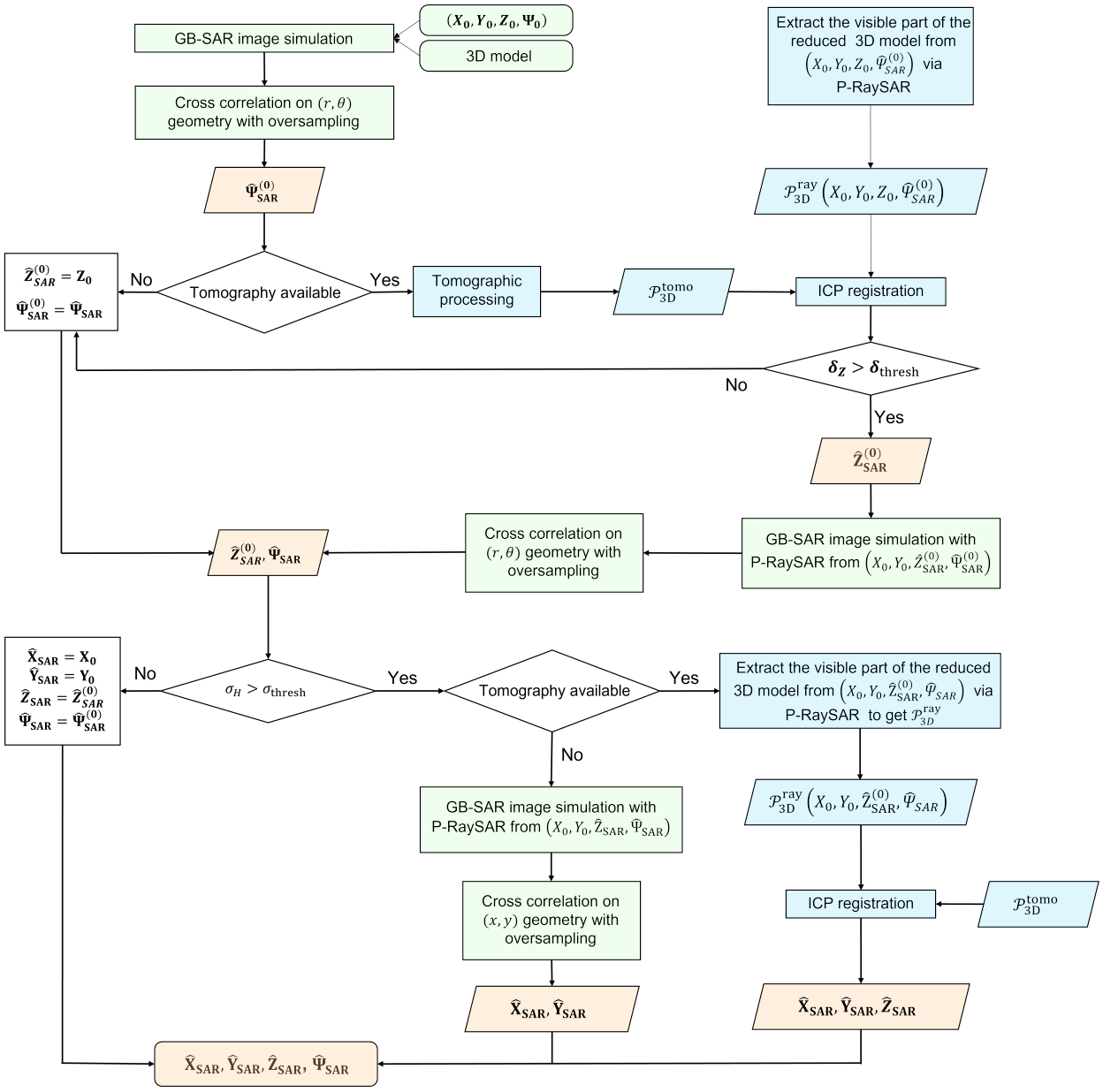

Figure 4.13: Flowchart of the proposed algorithm for orientation and location correction. Green is for image-matching techniques, while blue is for tomographic processing. Orange is for output quantities.

The matrix given by Equation 4.18 corresponds to a rotation of an angle δ_Ψ, confirming the illustration of Figure 4.14.

The real log-intensity image $\mathcal{I}_{\text{real}}$ and the simulated log-intensity image $\mathcal{I}_{\text{sim}}$ are preprocessed and transformed to the same scale, to ensure registration stability and robustness. As depicted in Figure 4.8a, real images exhibit a high level of noise primarily caused by thermal noise. To mitigate it, the coherence of the scenario is computed with at least ten images and used as a mask to delete all the areas where the coherence falls below the threshold of 0.6. Subsequently, both images are normalised in the scale $[0\,;1]$ and an equalisation is applied on the simulated image through a histogram matching

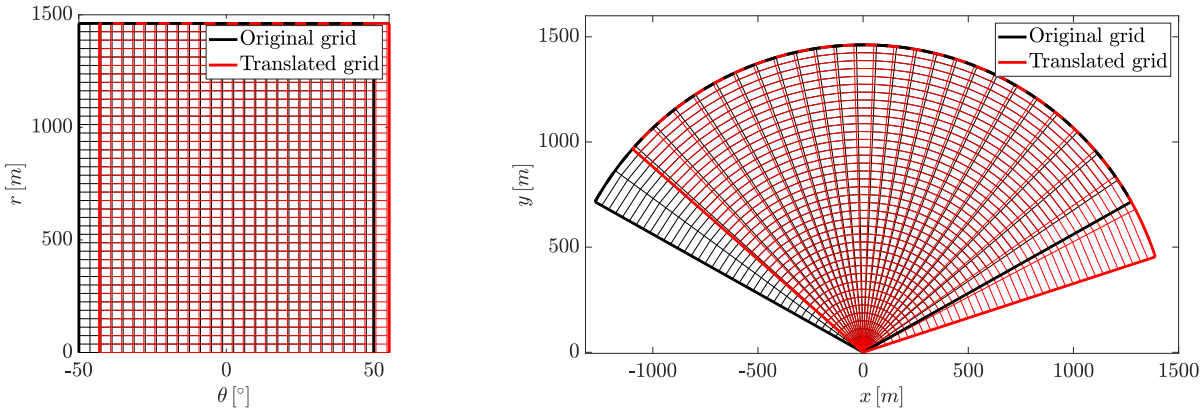

(a) Polar geometry (b) Cartesian geometry

Figure 4.14: Effect on a translation in the (r, θ) on the (x, y) geometry. For better visibility, only a percentage of the resolution cells are displayed.

algorithm as presented in [Gonzalez and Woods, 2018]. This normalisation process helps to ensure uniformity in the intensity distribution, aiding the subsequent image registration steps.

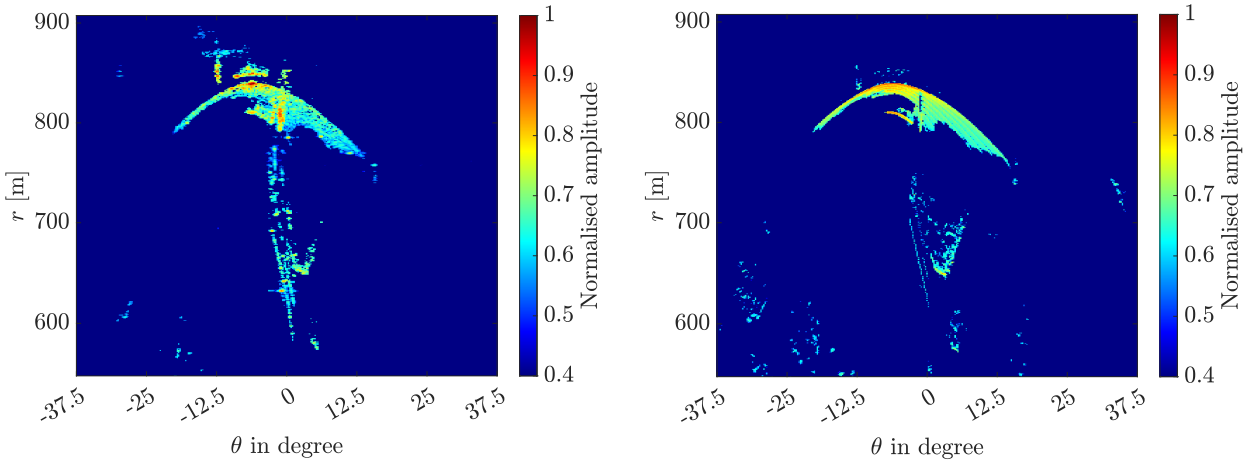

(a) Real image (b) Simulated image

Figure 4.15: Real and simulated normalised images in the (r, θ) geometry.

Following the preprocessing, the fast Fourier transform (FFT) is applied on the two images to compute the normalised cross-correlation (NCC) function $\gamma_{\mathcal{I}}$, employing an efficient approach proposed in [Lewis, 1995]. The obtained output is a matrix with twice the size of the input images, containing the NCC coefficient for each translation offset (δ_Ψ, δ_r). The estimated offset $\hat{\delta}_\Psi$ can be derived from the position of the maximum of $\gamma_{\mathcal{I}}(\delta_\Psi, \delta_r)$. However, this technique provides only pixel accuracy. By oversampling the NCC function, it is possible to reach a finer resolution of the angular shift δ_Ψ, obtained as the maximum of the oversampled NCC function $\gamma^{\text{os}}_{\mathcal{I}}(\delta_\Psi, \delta_r)$:

$$\hat{\delta}_\Psi = \underset{\delta_\Psi}{\text{argmax}}(\gamma^{\text{os}}_{\mathcal{I}}(\delta_\Psi, \delta_r)) \tag{4.19}$$

Finally, the azimuth of the system is given by:

$$\hat{\Psi}_{\text{SAR}} = \Psi + \hat{\delta}_{\Psi} \tag{4.20}$$

It leads to a new set of parameters for the radar represented by: $\mathcal{X}_{\text{rot}} = (X_0, Y_0, Z_0, \hat{\Psi}_{\text{SAR}})$.

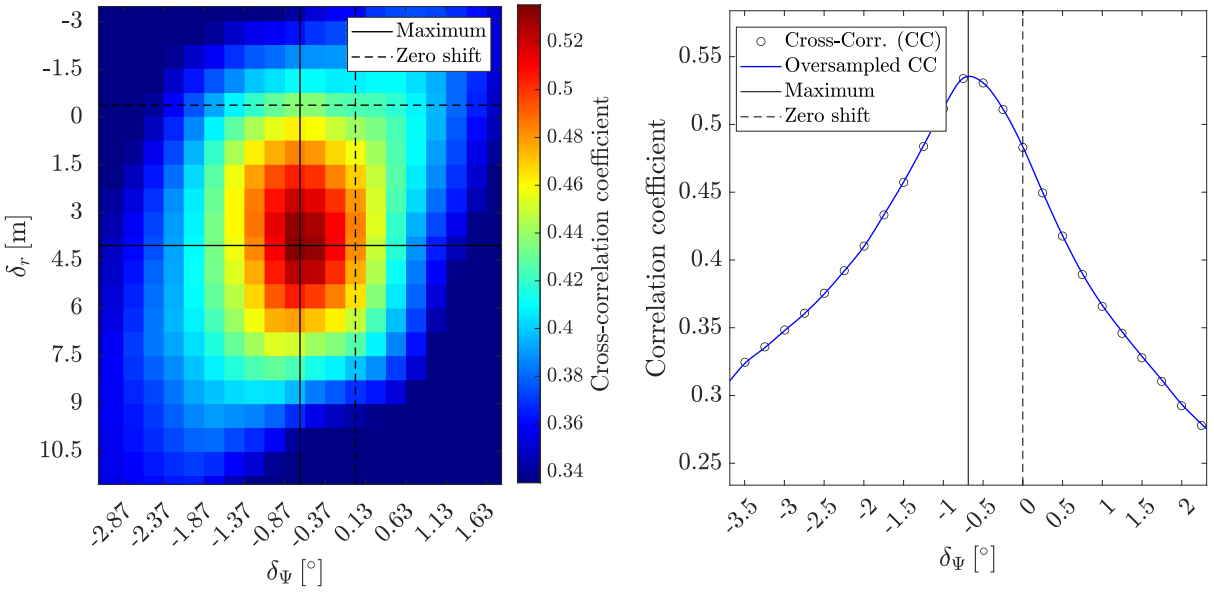

(a) 2D cross-correlation output

(b) Profile of the cross-correlation

Figure 4.16: Result of the normalised cross-correlation of the two images. (a) represents the 2D output, and (b) is the angular shift profile of (a) containing the maximum value.

The results of the orientation correction are provided in Appendix B for the *Georges* station as further proof of the method validation.

4.5.2 Correction of the position

Correcting the azimuth is usually necessary unless the initial value is established using highly accurate instruments such as a total station within a geodetic network. On the other hand, determining the position with adequate precision is also achievable using GNSS measurements. The only case requiring the location correction occurs when no external information about the system's external parameters is available. Still, two possible approaches to correct the system coordinates if their initial values express low accuracy are presented. Even if the results do not provide very high accuracy, the methods are an initial starting point for potential further works.

4.5.2.1 Tomographic measurement available

A 3D tomographic point cloud can be reconstructed when tomographic measurements are available. The set of pixels $\mathcal{P}_{\text{2D}}^{\text{tomo}} = (x_k, y_k)$, $k \in [|1\,;N_{\text{tomo}}|]$ is obtained by selecting the points having a high enough a posteriori coherence after the height estimation to be considered as stable. With the height estimate for each point $\tilde{Z}_k$, the corresponding coordinates $\tilde{X}_k$ and $\tilde{Y}_k$ can be determined using the following relations:

$$\begin{cases} \tilde{X}_k &= x_k \\ \tilde{Y}_k &= \sqrt{r_k^2 - \tilde{X}_k^2 - \tilde{Z}_k^2} \quad \text{with} \quad r_k^2 = x_k^2 + y_k^2 \end{cases} \tag{4.21}$$

Consequently, the set of pixels $\mathcal{P}_{3D}^{tomo}$ is also available in 3D, and each point has a considerably lower accuracy when compared to other methodologies as photogrammetry or laser scanner.

The idea to correct the offsets is to registrate the P-RaySAR single bounce point cloud $\mathcal{P}_{3D}^{ray}$ with the tomographic point cloud, and a difficulty to overcome is their different nature. Indeed, $\mathcal{P}_{3D}^{tomo} = (\tilde{X}_k, \tilde{Y}_k, \tilde{Z}_k), k \in [|1\,;N_{tomo}|]$ is dependant on the resolution of the GB-SAR which reaches several meters. However, only the translations need to be corrected, which is easier. The proposed method is based on the iterative closest point (ICP) algorithm originally described in [Besl and McKay, 1992], with the *point-to-plane* modification of [Chen and Medioni, 1992]. The goal of this step is to find the best translation $\mathcal{T} = [T_x\ T_y\ T_z]^\mathsf{T}$ to reach the following criterion:

$$\hat{\mathcal{T}} = \underset{T_x,T_y,T_z}{\operatorname{argmin}} \frac{1}{N_{tomo}} \sum_{k=1}^{N_{tomo}} d\left(\mathcal{T}(\tilde{X}_k, \tilde{Y}_k, \tilde{Z}_k), \mathcal{P}_{3D}^{ray}\right) \tag{4.22}$$

with d the operator that computes the Euclidean distance between each point of the tomographic point cloud and the corresponding local planes of $\mathcal{P}_{3D}^{ray}$. [Pang et al., 2023] studied the registration of optical and TomoSAR point clouds and validate the efficiency of the ICP algorithm for the translation correction.

To check the stability of the registration with the ICP algorithm, 200 random translations $\delta T = (\delta\tilde{X}, \delta\tilde{Y}, \delta\tilde{Z})$ in each axis following a Gaussian distribution $\delta\tilde{X}, \delta\tilde{Y}, \delta\tilde{Z} \sim \mathcal{N}(0, 25)$ are simulated. Some random rotations around the Z-axis are also added to simulate the residual offset in the orientation angle δ_Ψ such that $\delta_\Psi \sim \mathcal{U}(-0.5, 0.5)$ representing a maximum of two cross-range resolution cells in each direction. These offsets are added on the true GB-SAR external parameters estimated with the GNSS data for the horizontal position and manual tests minimising the offsets on the CR coordinates to find the azimuth and elevation. Indeed, the approximated parameters of the GB-SAR were measured via GNSS, which implies that the orientation angle may be affected by a non-negligible error. Moreover, an aberrant value for the vertical measurements due to a probable wrong reference system for the elevation was detected. The stability analysis results are displayed in Figure 4.17.

The mean and standard deviation of the differences between the simulated and estimated offsets are given in Table 4.2. Overall the estimation quality is much lower than what is traditionally achievable by the ICP algorithm due to the low accuracy of $\mathcal{P}_{3D}^{tomo}$, which points have uncertainties higher than 1 m. Moreover, the number of points is not high, which in the presented case is about 1 600. The bias in $\tilde{Y}$ is small and stable. The bias in $\tilde{X}$ has a magnitude approximately equal to a range pixel, explaining why it is not recommended to apply the correction if the location is measured with better accuracy. The latter offset is more complex to solve due to its stronger sensibility to a remaining offset in Ψ. Reaching 3.5 m, the bias in $\tilde{Z}$ is considerable. However, the influence on the radar image is much smaller than the offsets on the two other coordinates and is visible as a distortion along y for higher points. The effect of this strong bias in $\tilde{Z}$ on the final results is discussed in Section 4.6.1.1. Even if the proposed method is imperfect, it is also noticeable that offsets up to 15 m are considerably reduced. Moreover, it is the only tool to find coarse errors on $\tilde{Z}$.

Finally, this method expresses sensitivity to the input parameters of the ICP, especially the inlier ratio, which is known as a drawback of the ICP. Computing the transformation for a varying number

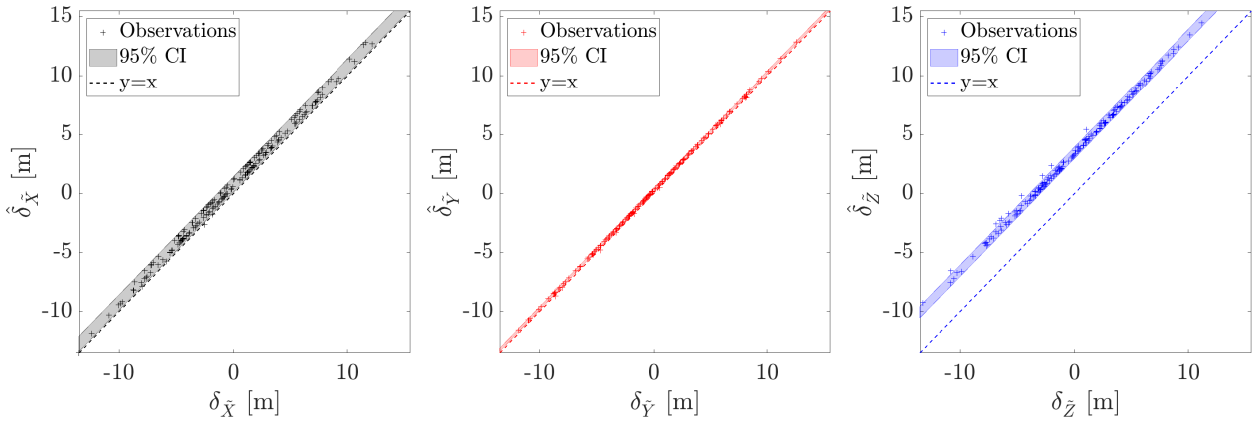

(a) Simulation in $\tilde{X}$ (b) Simulation in $\tilde{Y}$ (c) Simulation in $\tilde{Z}$

Figure 4.17: Simulation of the stability of the ICP algorithm for matching the TomoSAR and optical point clouds with different known offsets.

Quantity	$\mathbb{E}[\delta_{\tilde{X}} - \hat{\delta}_{\tilde{X}}]$	$\sigma_{\delta_{\tilde{X}} - \hat{\delta}_{\tilde{X}}}$	$\mathbb{E}[\delta_{\tilde{Y}} - \hat{\delta}_{\tilde{Y}}]$	$\sigma_{\delta_{\tilde{Y}} - \hat{\delta}_{\tilde{Y}}}$	$\mathbb{E}[\delta_{\tilde{Z}} - \hat{\delta}_{\tilde{Z}}]$	$\sigma_{\delta_{\tilde{Z}} - \hat{\delta}_{\tilde{Z}}}$
Value [m]	-0.78	0.32	-0.28	0.06	-3.45	0.24

Table 4.2: Statistics between simulated and recovered offsets over 200 simulations with the ICP.

of inliers from 75 % to 95 % with a step of 1 % enables the analysis of the dispersion of the bias for each coordinate. The standard deviations of the biases are 0.79 m, 0.20 m and 0.81 m for $\tilde{X}$, $\tilde{Y}$ and $\tilde{Z}$, respectively, which highlights this sensitivity. The results from Table 4.2 and Figure 4.17 summarise the case considering 93 % of inliers.

Once the offsets are determined in the local coordinate system, the final relation for the correction of the GB-SAR location is given by:

$$\begin{cases} \hat{\delta}_X = \hat{\delta}_{\tilde{X}} \cos(\Psi_{\text{SAR}}) - \hat{\delta}_{\tilde{Y}} \sin(\Psi_{\text{SAR}}) \\ \hat{\delta}_Y = \hat{\delta}_{\tilde{Y}} \cos(\Psi_{\text{SAR}}) + \hat{\delta}_{\tilde{X}} \sin(\Psi_{\text{SAR}}) \\ \hat{\delta}_Z = \hat{\delta}_{\tilde{Z}} \end{cases} \tag{4.23}$$

4.5.2.2 Image based correction

If no tomographic measurements are available, the first step is to assume that $\hat{Z}_{\text{SAR}} = Z_0$. Afterwards, another simulation with P-RaySAR is conducted with the set of parameters $\mathcal{X}_{\text{rot}}$ and the synthetic image is computed again. Subsequently, the image is resampled in the (x, y) geometry, such that the translation along x corresponds to a translation along $\tilde{X}$ and a translation along y corresponds to a translation along $\tilde{Y}$, at least for $Z = 0$. Similarly to the orientation correction, the NCC function $\gamma^{\text{os}}_{\mathcal{I}_{xy}}(\delta_x, \delta_y)$ on the (x, y) geometry is computed. The offsets along these two directions are determined by:

$$(\hat{\delta}_x, \hat{\delta}_y) = \underset{\delta_x, \delta_y}{\text{argmax}}(\gamma^{\text{os}}_{\mathcal{I}_{xy}}(\delta_x, \delta_y)) \tag{4.24}$$

As no elevation corrections are available, we need to assume that $\hat{\delta}_{\tilde{X}} = \hat{\delta}_x$ and $\hat{\delta}_{\tilde{Y}} = \hat{\delta}_y$. The offsets in the global coordinates are computed using the two first terms of Equation 4.23.

Finally, the estimated position is given by:

$$\begin{cases} \hat{X}_{\text{SAR}} = X_0 + \hat{\delta}_X \\ \hat{Y}_{\text{SAR}} = Y_0 + \hat{\delta}_Y \end{cases} \tag{4.25}$$

This leads to the final set of parameters $\hat{\mathcal{X}}_{\text{SAR}} = (\hat{X}_{\text{SAR}}, \hat{Y}_{\text{SAR}}, \hat{Z}_{\text{SAR}}, \hat{\Psi}_{\text{SAR}})$. The technique is applied at *Warehouse* station, and the NCC function displayed in Figure 4.18 is obtained.

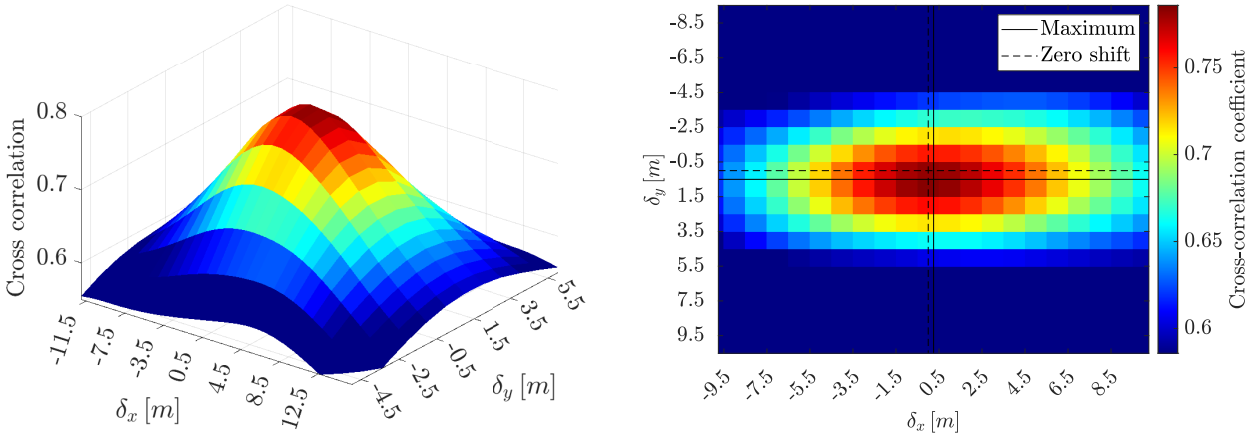

(a) NCC represented in 3D

(b) NCC with maximum

Figure 4.18: Result of the NCC of the two images in the (x, y). (a) represents the surface of the NCC to get an idea of the sharpness of the peak, and (b) is the top view of (a).

As for the tomographic version, the method is evaluated by simulating known offsets using the following characteristics. Only offsets on $\tilde{X}$ and $\tilde{Y}$ are introduced, as the offset in $\tilde{Z}$ cannot be estimated with this technique. The translation offsets follow the same distribution as for the tomographic case. Two cases for the rotation offsets are distinguished, with the first containing no offsets and the second following a uniform distribution. However, its magnitude is only set on one resolution cell, i.e. $\delta_\Psi \sim \mathcal{U}(-0.25, 0.25)$, which is two times less than for the tomographic case.

Quantity	$\mathbb{E}[\delta_{\tilde{X}} - \hat{\delta}_{\tilde{X}}]$	$\sigma_{\delta_{\tilde{X}} - \hat{\delta}_{\tilde{X}}}$	$\mathbb{E}[\delta_{\tilde{Y}} - \hat{\delta}_{\tilde{Y}}]$	$\sigma_{\delta_{\tilde{Y}} - \hat{\delta}_{\tilde{Y}}}$
Value with rotation [m]	-0.18	0.08	-0.56	0.07
Value without rotation [m]	-0.12	1.68	-0.57	0.14

Table 4.3: Statistics between simulated and recovered offsets with the registration based on the image correlation.

The results presented in Figure 4.19 show that the estimation of the $\hat{\delta}_{\tilde{X}}$, even a small offset in rotation decreases strongly the precision. As for the tomographic correction, $\hat{\delta}_{\tilde{Y}}$ is almost not influenced. The comparison of Table 4.2 and 4.3 exhibits a preference for the results from the tomography as it is less influenced by a rotation offset, even if the bias remains larger. Other studies on different datasets should be conducted to verify that the magnitude order of the bias does not reach several meters.

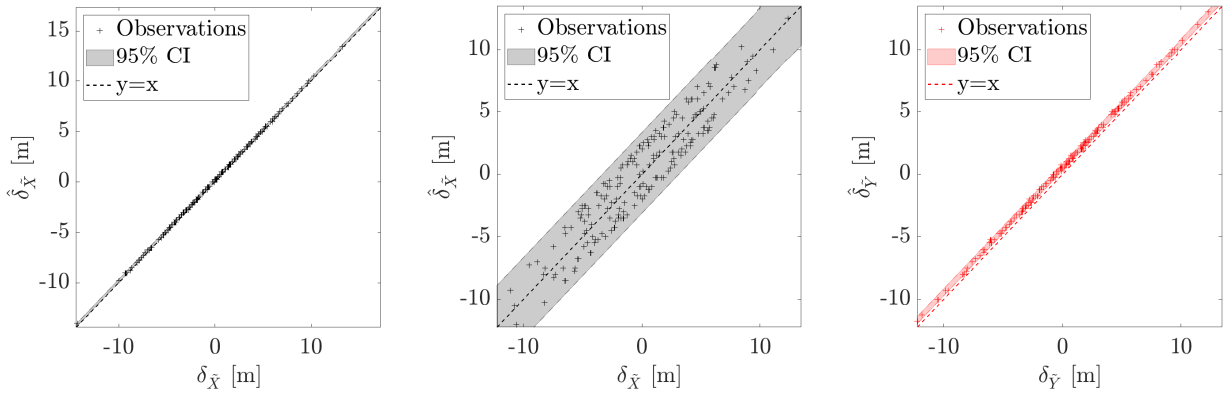

(a) δ in $\tilde{X}$ without rotation offset (b) δ in $\tilde{X}$ with rotation offset (c) δ in $\tilde{Y}$ with rotation offset

Figure 4.19: Simulation of the stability of the NCC algorithm to estimate the horizontal offset.

4.6 Evaluation

We propose two case studies based on real data to validate the method. The first concerns the Enguri Dam, which is affected by the specific vertical geometry. The second involves a large copper open-pit mine, a more conventional scenario for GB-SAR applications.

4.6.1 Case Enguri Dam

At Enguri Dam, the corner reflectors (CR) have been strategically placed, as described in Chapter 3. The precise position of these CR is known with an accuracy of approximately 10 cm which is seven times finer than the GB-SAR resolution cell in the range direction and thirty times finer in the cross-range direction at their average distance.

4.6.1.1 Algorithm steps

The 3D coordinates of the nine CR are transformed with the approximated parameters $\mathcal{X}_0$, and projected onto the GB-SAR geometry using Equations 4.4. A 2D peak detection algorithm is applied to the oversampled amplitude image to identify their positions in the real GB-SAR amplitude image. The highest peak near each projected coordinate for each point is selected as the potential signature of a CR. To further refine the CR identification process, the density-based spatial clustering of applications with noise (DBSCAN) algorithm [Ester et al., 1996] is applied to cluster the CR with similar offsets. Due to strong amplitudes in the central part of the dam, the CR within that region are not reliably identified. As a result, five CR are considered and presented in Figure 4.20a. The crosses correspond to the projection results, and the circles to their detected positions.

Figure 4.20 illustrates the difference between the detected positions of the CR and their projected coordinates in several cases. (a)-(b)-(c) display the progressive improvement achieved using our algorithm while (d) shows the result using IDS's method, which has been recently developed and introduced in [IDS-Georadar, 2022]. The improvement from (a) to (b) is due to the correction of the azimuth. From (b) to (c), it corresponds to the correction of the Z-coordinate and the second azimuth correction. The statistical analysis of the offsets between their detected and projected coordinates is given in Table 4.4. The errors resulting from $\mathcal{X}_0$ are reported in the first row. The

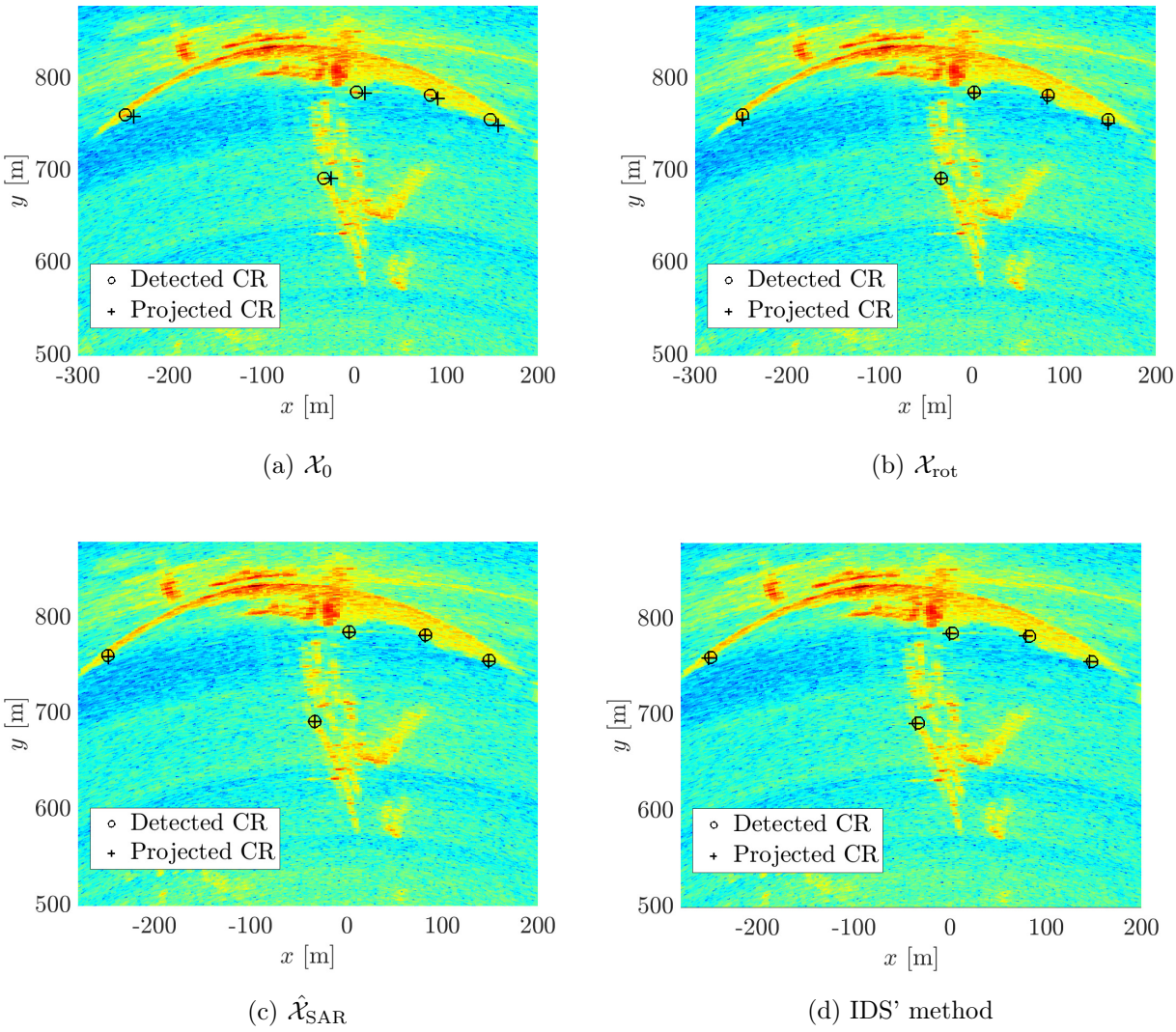

(a) $\mathcal{X}_0$

(b) $\mathcal{X}_{\text{rot}}$

(c) $\hat{\mathcal{X}}_{\text{SAR}}$

(d) IDS' method

Figure 4.20: Comparison of the localisation of the corner reflectors during the process. (a) corresponds to the initial position of the system. (b) is after the first correction of the azimuth. (c) corresponds to the final estimate, and (d) presents the results from IDS' software.

most prominent error is the x coordinate, approximately $-8.5\,\text{m}$ and completely induced by the error in azimuth. Although this may appear small on the scale of the entire 800 m dam, it represents a non-trivial offset of 1/100 of the dam's developed length. Moreover, nearby pixels can be located at different heights due to the foreshortening. The initial error in y is different depending on the elevation of the corner reflectors, indicating an offset in Z. The tomographic registration successfully reduces this offset. The X and Y coordinates of the system are known with the GNSS accuracy, i.e. 2 cm. Therefore, the remaining errors in x and y coordinates of the CR are due to a residual angle error and an elevation offset, respectively. The remaining 3.5 m bias observed in the simulation for the Z coordinate expresses the mean offset of 0.50 m in the y coordinate.

To assess the impact on the geocoding, the set of parameters $\mathcal{X}_0$ and $\hat{\mathcal{X}}_{\text{SAR}}$ are applied to project the persistent scatterers onto the dam's surface. While the details of various geocoding methods are

Quantity	$\mathbb{E}[x-\hat{x}]$ [m]	$\sigma_{x-\hat{x}}$ [m]	$\mathbb{E}[y-\hat{y}]$ [m]	$\sigma_{y-\hat{y}}$ [m]	$\mathbb{E}[r-\hat{r}]$ [m]	$\sigma_{r-\hat{r}}$ [m]	$\mathbb{E}[\theta-\hat{\theta}]$ [°]	$\sigma_{\theta-\hat{\theta}}$ [°]
$\mathcal{X}_0$	-8.54	0.66	2.40	2.51	2.44	1.82	-0.65	0.05
$(X_0, Y_0, Z_0, \hat{\Psi}^{(0)}_{\text{SAR}})$	0.41	0.47	2.46	1.85	2.44	1.82	0.03	0.05
$(X_0, Y_0, \hat{Z}_{\text{SAR}}, \hat{\Psi}^{(0)}_{\text{SAR}})$	0.41	0.47	0.51	0.27	0.53	0.29	0.03	0.03
$\hat{\mathcal{X}}_{\text{SAR}}$	-0.03	0.47	0.50	0.29	0.53	0.29	-0.00(2)	0.03
$\mathcal{X}_{\text{SAR}}$	-0.00(2)	0.47	0.00(6)	0.23	0.05	0.17	0.00(0)	0.04

Table 4.4: Offsets between detected CR and projected CR.

covered in the next chapter, the method consisting of projecting the GB-SAR information on all points of the model, and outlined in Figure 5.1d, is applied for visualisation purposes. The results are depicted in Figure 4.21. The improvement is notably visible on the right part of the dam (from an upstream point of view). In this area, almost all the points that are geocoded on the road with $\mathcal{X}_0$ are correctly geocoded on the wall when $\hat{\mathcal{X}}_{\text{SAR}}$ is used.

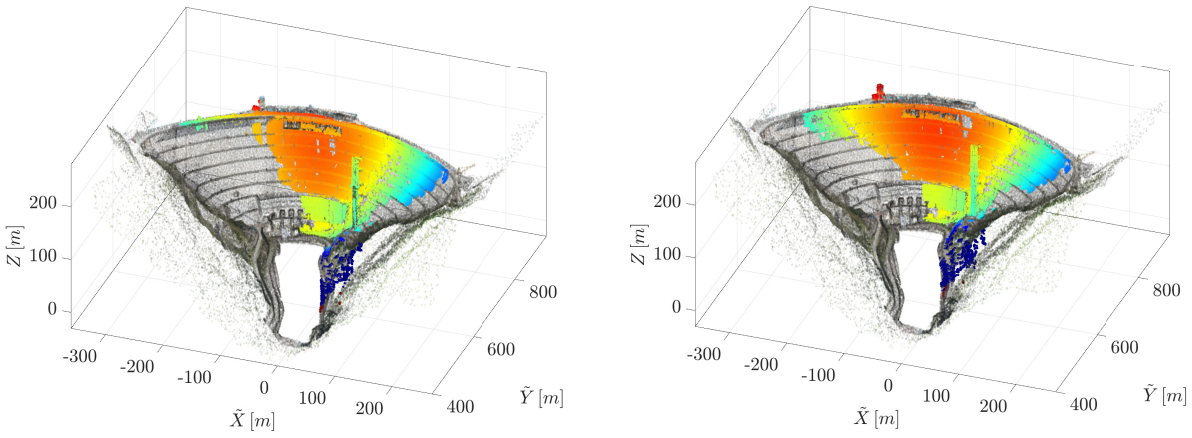

(a) Geocoding with $\mathcal{X}_0$

(b) Geocoding with $\hat{\mathcal{X}}_{\text{SAR}}$

Figure 4.21: Comparison of the localisation of the geocoding before (a) and after (b) the correction. The colour of the GB-SAR points has no meaning and is just applied to better distinguish the points on the dam.

4.6.1.2 Comparison with other methods

The proposed workflow is compared against two alternative methods. The first method is based on the tomographic processing. While our proposed flowchart employs the ICP algorithm primarily to correct the elevation location of the system, the original ICP algorithm has the capability to provide a complete transformation by aligning point clouds through rotations and translations. As shown in Section 4.13, the algorithm converges well even for substantial rotation offsets. Consequently, it is used to align the tomographic point cloud and the reduced 3D model with the approximated set of coordinates. The second comparison involves the IDS's software [IDS-Georadar, 2022], recently developed.

The statistical outputs presented in Table 4.5 highlight that even if the solely ICP method can

Quantity	$\mathbb{E}[x-\hat{x}]$ [m]	$\sigma_{x-\hat{x}}$ [m]	$\mathbb{E}[y-\hat{y}]$ [m]	$\sigma_{y-\hat{y}}$ [m]	$\mathbb{E}[r-\hat{r}]$ [m]	$\sigma_{r-\hat{r}}$ [m]	$\mathbb{E}[\theta-\hat{\theta}]$ [°]	$\sigma_{\theta-\hat{\theta}}$ [°]
$\mathcal{X}_0$	-8.54	0.66	2.41	2.52	2.45	1.83	-0.65	0.05
$\hat{\mathcal{X}}_{\text{SAR}}$ Tomo	2.23	0.47	1.41	0.51	1.39	0.78	0.16	0.04
$\hat{\mathcal{X}}_{\text{SAR}}$ IDS	3.54	0.50	0.18	0.81	0.16	0.20	0.27	0.03
$\hat{\mathcal{X}}_{\text{SAR}}$ Proposed	-0.03	0.47	0.50	0.29	0.53	0.29	-0.00(2)	0.03

Table 4.5: Offsets between detected CR and projected CR with three different methods.

reduce considerably the committed error, the offset in azimuth remains considerably larger than the one from the image-based approach. The proposed azimuth correction achieves the best results compared to the other methods.

4.6.2 Case open-pit mine

The second evaluation is carried out in a large copper open-pit mine. A single CR was installed to have a stable reference point for the monitoring and to check the reliability of the results. Unlike the previous case study, no tomographic acquisitions are available, which means that the verification and potential correction of the instrument's height can not be performed.

The approximated parameters of the station were accurately determined and can be considered as ground truth for the parameter evaluation, i.e. $\mathcal{X}_0 = \mathcal{X}_{\text{SAR}}$. The difference between the detected position of the CR and its projection via the original parameters is lower than the resolution cell size of the GB-SAR. A known offset is introduced to assess the algorithm's performance in recovering true positions. Known offsets of $\delta_\Psi = 2.00°$, $\delta_X = 3.00\,\text{m}$, and $\delta_Y = 0.00\,\text{m}$ are applied to the GB-SAR position and orientation. The proposed software and the one from IDS are applied to this dataset, yielding results outlined in Table 4.6. As a notable distinction with the previous case study lies in the input data, the real and simulated normalised amplitude images are depicted in Figure 4.22.

A short analysis of the simulated image depicts that the amplitude of the sides is too high. However, this dissimilarity does not impact the correlation, except by scaling down its peak height. Additionally, a stronger amplitude is observed in the central part of the image, which could potentially be attributed to the histogram matching algorithm employed.

Quantity	$X_{\text{SAR}} - \hat{X}_{\text{SAR}}$ [m]	$Y_{\text{SAR}} - \hat{Y}_{\text{SAR}}$ [m]	$\Psi_{\text{SAR}} - \hat{\Psi}_{\text{SAR}}$ [°]	$d(\text{CR}, \hat{\text{CR}})$ [m]
Offset	3	0	2	60.84
IDS	-0.82	-0.72	0.19	5.11
Proposed	1.22	-1.48	0.12	5.42

Table 4.6: Comparison between IDS's and proposed software on one simulated offset.

The outcomes of this comparison indicate that, like in the Enguri Dam scenario, the proposed algorithm compensates well the orientation error. However, in this case, the algorithm encounters more challenges in recovering the X and Y shifts compared to the version from IDS. Analyzing the overall improvement in the position of the CR, both algorithms demonstrate similar outcomes. For near targets IDS's solution is more effective while for far targets is the proposed solution preferable.

This simulation proves that the algorithm also works in a completely different environment to reduce

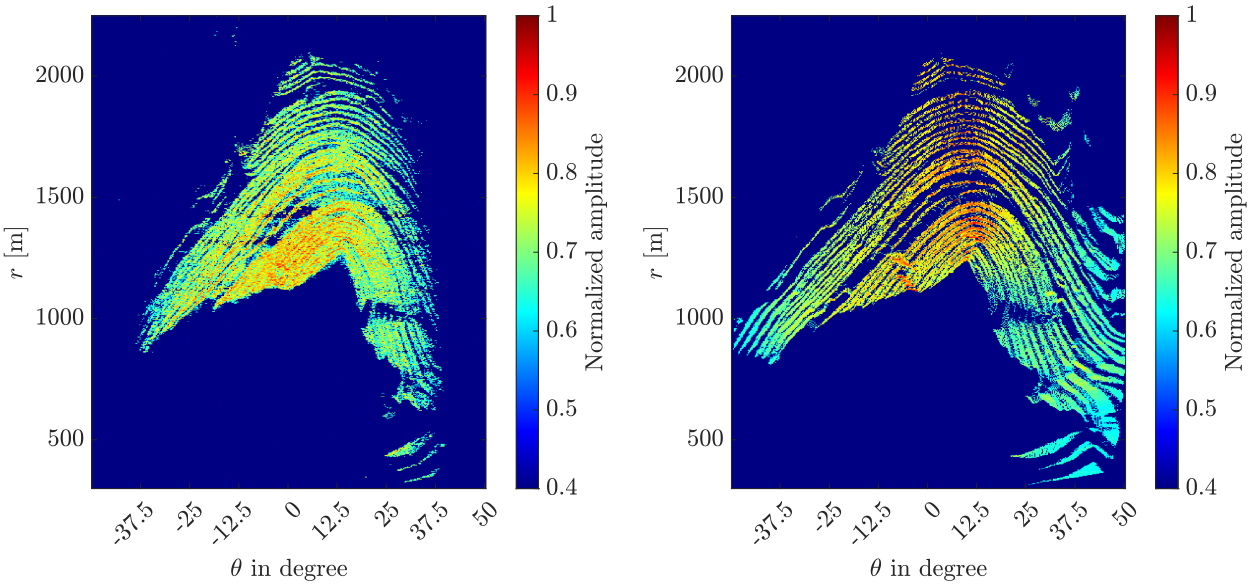

(a) Real image (b) Simulated image

Figure 4.22: Real and simulated normalised images in the (r, θ) geometry for the open-pit mine.

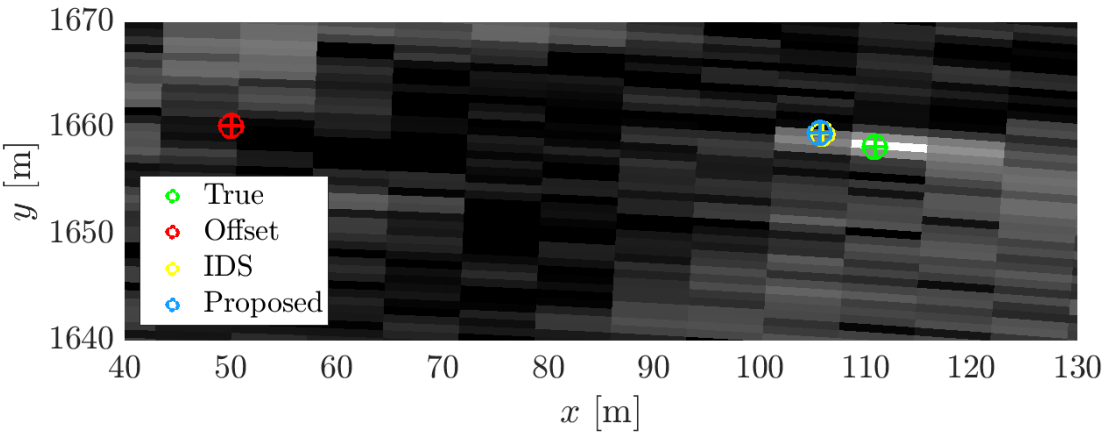

Figure 4.23: Simulation of offsets in the open-pit mine and recovering using both algorithms around the corner reflector which corresponds to the white pixel.

the orientation offset, even in the presence of a translation offset. This correction is crucial in the subsequent geocoding developed in the next chapter.

4.7 Conclusion

This chapter introduced a method to enhance the accuracy of external parameters, especially the azimuth of a linear GB-SAR system. The approach can be straightforwardly extended to other similar TRI. In the first part, the sources of uncertainty and their transmission to geocoding errors

were analysed, assessing the feasibility of correcting the orientation independently of the location in a first approximation. Subsequently, two independent algorithms and data processing methodologies were presented.

- P-RaySAR, a custom ray tracing software, was developed to understand the behaviour of the electromagnetic signal in complex scenarios and simulate radar images for perspective geometry in a GB-SAR system.
- The TomoSAR processing was applied on a terrestrial sensor to generate a point cloud of the observed scenario.

Based on these two tools, a flowchart was developed to automatically correct the azimuth and location of a GB-SAR. The orientation component is grounded on image-matching techniques and achieves subpixel accuracy, even in cases with significant location offsets, such as the open-pit mine dataset. Considering the application presented in Appendix B, this correction proved its efficiency on three datatsets and was consistently validated. The quality assessment on real scenarios was based on corner reflectors and showcased a significant reduction in error through the proposed method.

For the position correction, two methods were proposed. The first method leveraged tomographic measurements to register the TomoSAR point cloud with an external 3D model using the ICP algorithm. This approach enables to estimate the 3D translation. While exhibiting high precision, this method encountered biases in estimated offsets, potentially due to the low quality of the TomoSAR point cloud. Based on image matching, the second approach is less affected by biases, but the precision deteriorates with residual orientation offsets. Moreover, it can only recover a 2D planar translation. Both approaches could considerably reduce large offsets, but their overall accuracy could not reach one meter. The evaluation was done only on a single dataset, and more research on this topic should be addressed. This part of the correction does not reach accurate positioning but can help to correct large offsets when no external geodetic measurements of the GB-SAR are available. Considering real case scenarios, the position is rarely unavailable, and the azimuth correction is sufficient.

Besides, the proposed method presents some limitations that could be addressed in further works. Firstly, improvements in the image simulation can be achieved. A suggestion might involve classifying point cloud data, such as *metal*, *concrete/rocks*, and *vegetation*, to assign appropriate NRCS corresponding to material properties. Several improvements can be achieved for the tomographic processing using the last developed deep-learning techniques, such as in [Qian et al., 2022]. The ICP registration is also not optimal, and other algorithms more adapted to heterogeneous data should be considered, as proposed in [Pang et al., 2023]. Lastly, while separating orientation and location errors was effective on the first level, developing an algorithm that corrects both aspects in a single step could be a valuable improvement.

CHAPTER 5

Bayesian geocoding

Contents

5.1 Introduction

Chapter 4 introduced a method to determine the external parameters of the system accurately. The next step involves the clear identification of the 3D model points contributing to the observed signal for each resolution cell. As the GB-SAR is mainly used in open-pit mines or landslides, the geocoding is relatively straightforward due to the smooth terrain, allowing for a 2.5D DEM of the scenario. However, when dealing with complex infrastructures like dams, SAR distortion effects -such as layover, foreshortening, shadowing, and multiple bounces- become prominent in GB-SAR images.

This chapter proposes a novel geocoding algorithm that relies on Bayesian techniques and ray tracing. For clarity and simplicity, we assume the high-accuracy positioning of the GB-SAR system and that the 3D model is preprocessed to place the system at the origin $(0, 0, 0)$, looking along the Y-axis with sub-pixel accuracy. Notably, for notation convenience, (X, Y, Z) denotes reduced 3D coordinates instead of world coordinates, as the global reference is unnecessary.

This chapter contains materials from the publication [Rebmeister et al., 2022a], which are marked with a blue frame. Some minimal adaptations may occur.

5.2 Maximum a posteriori estimation for geocoding

The inverse projection method is the fundamental approach to project the SAR images on the 3D model, as described in [Monserrat Hernández, 2012]. Each point of the 3D model is projected via Equation 2.12 onto the GB-SAR geometry. The 3D model resolution is assumed to be higher than the size of the GB-SAR resolution cell, implying that several points of the 3D model are projected into a single pixel. Various methods are possible to find the 3D coordinates of the coherent SAR pixels.

Figure 5.1 illustrates several methods for projecting SAR images onto the 3D model. Two main categories are discernible.

- In (a)-(c), a single set of 3D coordinates is assigned to each pixel. (a) corresponds to the simplest approach, which consists of selecting the nearest point of the centre of the pixel and assigning its corresponding 3D coordinates to this pixel. In case (b), all the values of the 3D model points in the SAR resolution cell are considered, and the mean or an interpolation method can be applied to find the coordinates. In case (c), the point coordinates are taken from the 3D model point in the resolution cell with the highest posterior probability.

- In (d)-(e), it is the opposite way, as the phase values are projected onto the points of the external model. In case (d), the phase value represented by the green circle is assigned to all the 3D model points in the SAR pixel. However, points that are very implausible to send back signals should be neglected in case of layover. Following this idea, the last method is to assign the deformation value to all 3D model points with a probability at least higher than a given threshold, as done in case (e).

The calculation of the probability value of each 3D model point is detailed in the next part of the chapter. All the calculations are based on physical and geometrical principles, focusing on solving the problem efficiently rather than with an exact parametrical model.

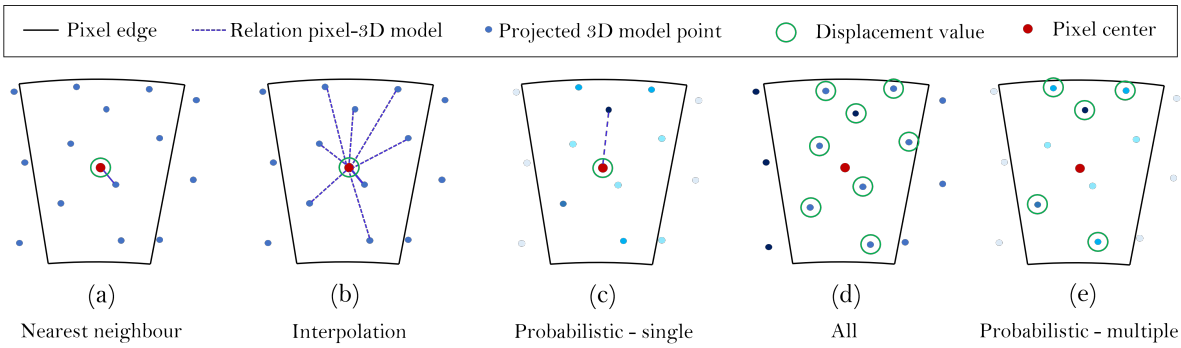

Figure 5.1: Five approaches to find the 3D coordinates of the SAR resolution cell. The black edges represent the pixel limits. The centre of the pixel is the red point. The 3D model points projected onto the SAR geometry are in blue. For cases (c) and (e), the darker the blue, the higher the probability. Adapted from [Rebmeister et al., 2022a].

5.2.1 Bayesian model

As depicted in Figure 5.1, there are usually several projected DEM or 3D model points in a GB-SAR pixel, each potentially contributing to the principal backscatter signal. For instance, in a 3D model generated by an UAV or a terrestrial laser scanner, the points are typically spaced by 5 cm, which is less than ten times the GB-SAR resolution cell size. Additionally, a single pixel may encompass signal contributions from points at varying heights in scenarios involving vertical structures. In such cases, calculating the mean or employing interpolation across all points in the resolution cell becomes meaningless. The challenge becomes the identification of the point that is most likely to have reflected the signal. An approach using prior knowledge and the Bayesian theorem can be formulated as follows:

$$f_{3D|2D}(X,Y,Z|r,\theta) = \frac{f_{2D|3D}(r,\theta|X,Y,Z)f_{3D}(X,Y,Z)}{f_{2D}(r,\theta)} \propto f_{2D|3D}f_{3D} \tag{5.1}$$

where $f_{2D|3D}(r,\theta|X,Y,Z)$ is the likelihood function, $f_{3D}(X,Y,Z)$ is the prior function and $f_{3D|2D}(X,Y,Z|r,\theta)$ is the posterior function. The purpose is to find the 3D coordinates with known 2D SAR coordinates; therefore, the maximum a posteriori (MAP) estimation is applied. The nearest neighbour (NN) case can also be seen as a probabilistic approach, where the prior distribution is a linear function parameterised by the distance w.r.t. the centre of the radar pixel.

5.2.2 Likelihood function

The likelihood function $f_{2D|3D}(r,\theta|X,Y,Z)$ is introduced as a binary function. Given a pixel to evaluate, a 3D model point P with coordinates (X,Y,Z) and projected SAR coordinates (r,θ), the following values for $f_{2D|3D}(r,\theta|X,Y,Z)$ are considered:

$$f_{2D|3D}(r,\theta|X,Y,Z) = \begin{cases} 1 & \text{if } (r,\theta) \text{ is inside pixel edges} \\ 0 & \text{if } (r,\theta) \text{ is outside pixel edges} \end{cases} \tag{5.2}$$

A more physically grounded approach would involve considering the system's point spread function. However, this more complex approach could potentially lead to points from neighbouring resolution cells to be located at the same 3D position, which must be avoided.

5.2.3 Prior distribution without TomoSAR

We aim to identify the point reflecting the highest intensity to discriminate the different points within a resolution cell and select the most plausible one. This concept serves as the basis to create the function $f_{3D}(X, Y, Z)$. Two main factors are considered to determine the most plausible point: the incidence angle at the evaluated point and the vertical antenna pattern of the radar system. In Figure 5.2, a profile view of a GB-SAR acquisition is represented. θ_i is the local incidence angle, η is the relative elevation angle, and $\eta_{\text{GB-SAR}}$ is the elevation angle of the centre of the antenna pattern. The operator sets the latter at the beginning of the measurements. These angles are crucial in determining how the radar signal interacts within the observed scenario.

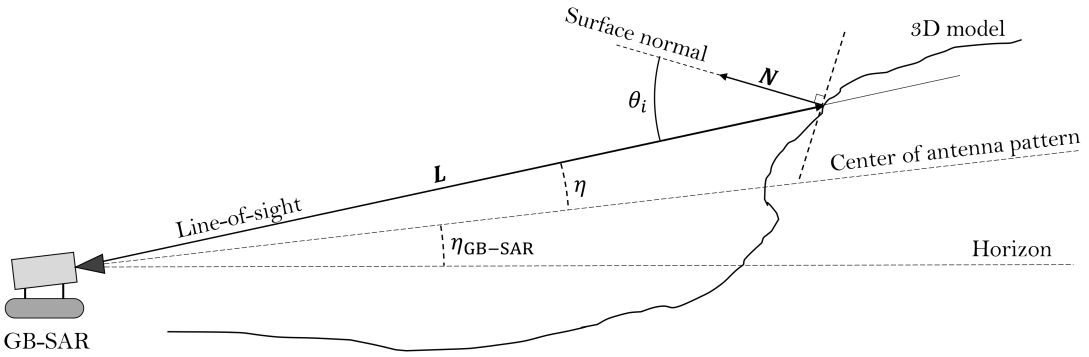

Figure 5.2: Geometry of an acquisition and angles used for the calculation of the PDF. Adapted from [Rebmeister et al., 2022a].

5.2.3.1 Incidence angle contribution

The first prior probability density function for the intensity of the received signal is defined by the local incidence angle θ_i. The considered model is similar to the one presented in [Chen, 2001] and already used in Chapter 4 for the image simulation. According to the former work, the expected value of the intensity can be expressed as:

$$\mathbb{E}(I) = C\sigma_0 A \tag{5.3}$$

where σ_0 is the local NRCS of the illuminated surface, A is the illuminated area and C is a constant. The value of C is irrelevant, as we are interested in creating a probability density function (PDF) that will be normalised later. Considering an equidistant sampling, the value of A can also be dropped from Equation 5.3. Finally, the relationship between σ_0 and the local incidence angle θ_i is established using the same model as presented in the previous chapter for the RCS simulation, i.e. Equation 4.8.

The construction of a PDF is achieved by normalising with the $\|.\|_1$ defining the L1-norm of the space $\mathcal{C}^0(\mathbb{R},\mathbb{R})$. In the given context, only the location of the maxima is of interest, regardless of the scaling factor. For a more intuitive representation, the applied normalisation is the $\|.\|_\infty$[1].

$$f_{\mathrm{LOS}}(\theta_i(X,Y,Z)) = \frac{\sigma_0(\theta_i)}{\|\sigma_0\|_\infty} \tag{5.4}$$

The incidence angle θ_i is computed using Equation 4.9 for each point of the 3D model projected within the resolution cell. A smaller angle indicates that the LOS of the radar and the normal vector of the surface are nearly parallel. Consequently, the reflecting structure is locally orthogonal to the radar, which means a high probability of receiving a strong amplitude signal. The resulting function $f_{\mathrm{LOS}}(\theta_i)$ is represented in Figure 5.3a.

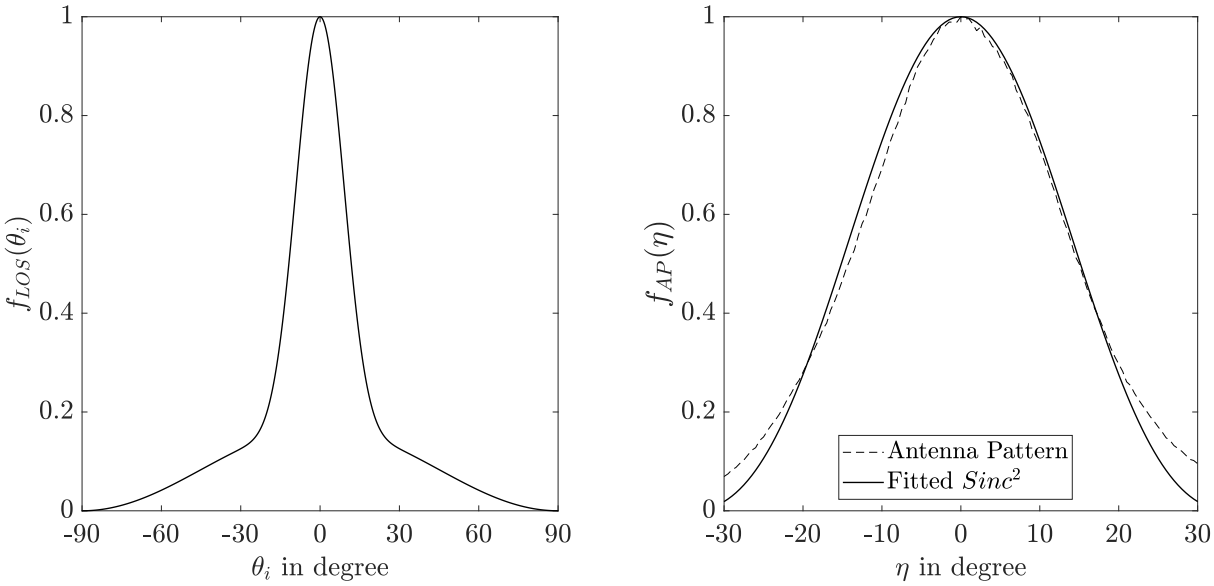

(a) f_{LOS} (b) f_{AP}

Figure 5.3: Density function of the two parameters. (a): Function for the incidence angle (b): Function for the antenna pattern. Adapted from [Rebmeister et al., 2022a].

5.2.3.2 Antenna pattern contribution

The horizontal antenna pattern is compensated following the acquisition, but the vertical one cannot be fully addressed due to the inherent limitations of the SAR geometry. Therefore, it is more reasonable to assume that the signal originates from a point in the centre of the vertical antenna pattern rather than from its edges. An antenna pattern model denoted as $f_{\mathrm{AP}}(\eta(X,Y,Z))$ is introduced to consider this effect. Constructing this model requires the knowledge of the antenna pattern of the radar system provided by the manufacturer. A squared *sinc* function is fitted to the empirical antenna pattern to achieve a smoother and symmetric

[1]The term PDF is inadequate for an exact mathematical description, as we do not use the appropriate normalisation. However, the expression PDF is conserved for easier understandability.

response. Consequently, the parameter c_0 from Equation 5.5 is estimated using the ordinary least squares.

$$\tilde{f}_{\mathrm{AP}}(\eta(X,Y,Z)) = \left(\frac{\sin(\eta\frac{\pi}{c_0})}{\eta\frac{\pi}{c_0}}\right)^2 \text{ and } f_{\mathrm{AP}}(\eta(X,Y,Z)) = \frac{\tilde{f}_{\mathrm{AP}}(\eta)}{\|\tilde{f}_{\mathrm{AP}}\|_\infty} \tag{5.5}$$

The vertical angle of a point of the 3D model is evaluated with $\eta = \arctan\left(\frac{Z}{\sqrt{X^2+Y^2}}\right) - \eta_{\text{GB-SAR}}$. The final function $f_{\mathrm{AP}}(\theta_i)$ is displayed in Figure 5.3a. The solid line corresponds to the fitted *sinc*, and the dashed line represents the measured antenna pattern.

5.2.3.3 Full model

The incidence angle and the antenna pattern are two completely independent parameters. Hence, the prior probability function can be obtained by multiplying their contribution functions as in Equation 5.6. The strength of the developed algorithm is that it does not require any geometrical baseline to find the best point.

$$f_{\mathrm{3D}}(X,Y,Z) = f_{\mathrm{AP}}(\eta(X,Y,Z)) f_{\mathrm{LOS}}(\theta_i(X,Y,Z)) \tag{5.6}$$

This joint PDF is represented in Figure 5.4. The function f_{3D} is inserted in Equation 5.1 to use the prior knowledge available. For a considered SAR pixel, each 3D model point has an assigned conditional probability.

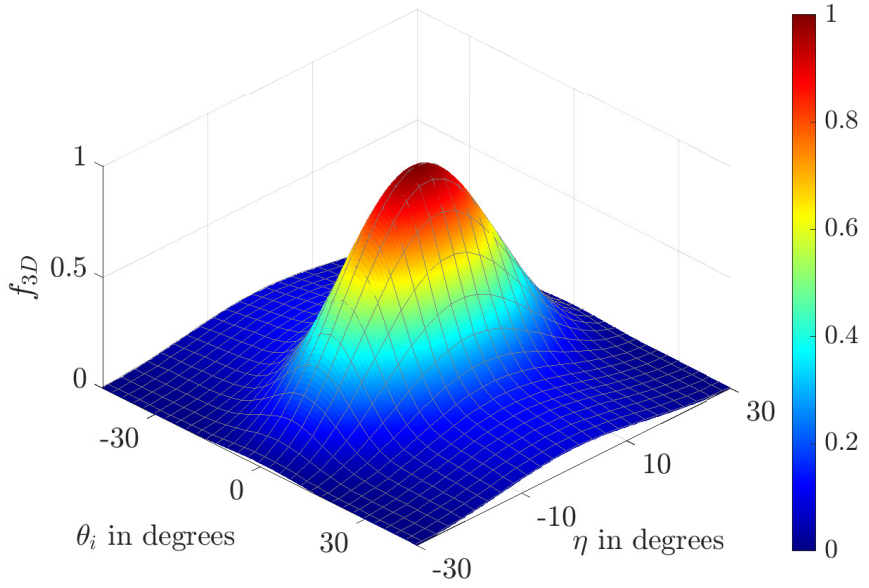

Figure 5.4: 2D joint density function of the two parameters.

5.2.4 Prior distribution with TomoSAR

In cases where TomoSAR results are available, or even if other methods using phase unwrapping algorithms are applicable, the height estimation can also contribute to the geocoding process. However, this information is only integrated for pixels with sufficiently high coherence after the parameter estimation. The TSVD inversion is performed in this context, similar to the approach in [Fornaro et al., 2005]. In this case, the elevation intensity spectrum is of more interest for geocoding, rather than a sparse solution, as it allows a smoother and wider function w.r.t. the elevation. The solution for the reflectivity profile $\hat{\boldsymbol{\gamma}}$ in Equation 4.12 is then given by:

$$\hat{\boldsymbol{\gamma}} = \mathbf{V}_q \boldsymbol{\Sigma}_q^{-1} \mathbf{U}_q^* \mathbf{g} \tag{5.7}$$

where $\mathbf{V}_q, \boldsymbol{\Sigma}_q$ and $\mathbf{U}_q$ correspond to the matrices of the singular value decomposition of $\mathbf{L}$ up to the q^{th} singular value and $\mathbf{g}$ is the observation vector. The choice of q is detailed in [Chan and Hansen, 1990] such that $q = \text{rk}(\mathbf{L}) - 1$ is set, with $\text{rk}(\mathbf{L})$ the rank of the matrix $\mathbf{L}$.

The vector $\hat{\boldsymbol{\gamma}}$ is a function of Z, giving a received intensity for a point at the corresponding elevation. To mitigate noise, all values of $\hat{\boldsymbol{\gamma}}$ satisfying $\hat{\boldsymbol{\gamma}}(Z) < \frac{1}{2}\max(\hat{\boldsymbol{\gamma}})$ are set to 0. After that, the reflectivity profile is normalised to obtain the following prior function:

$$f_{3\text{D}}(X, Y, Z) = \frac{\hat{\boldsymbol{\gamma}}(Z)}{\|\hat{\boldsymbol{\gamma}}\|_\infty} \tag{5.8}$$

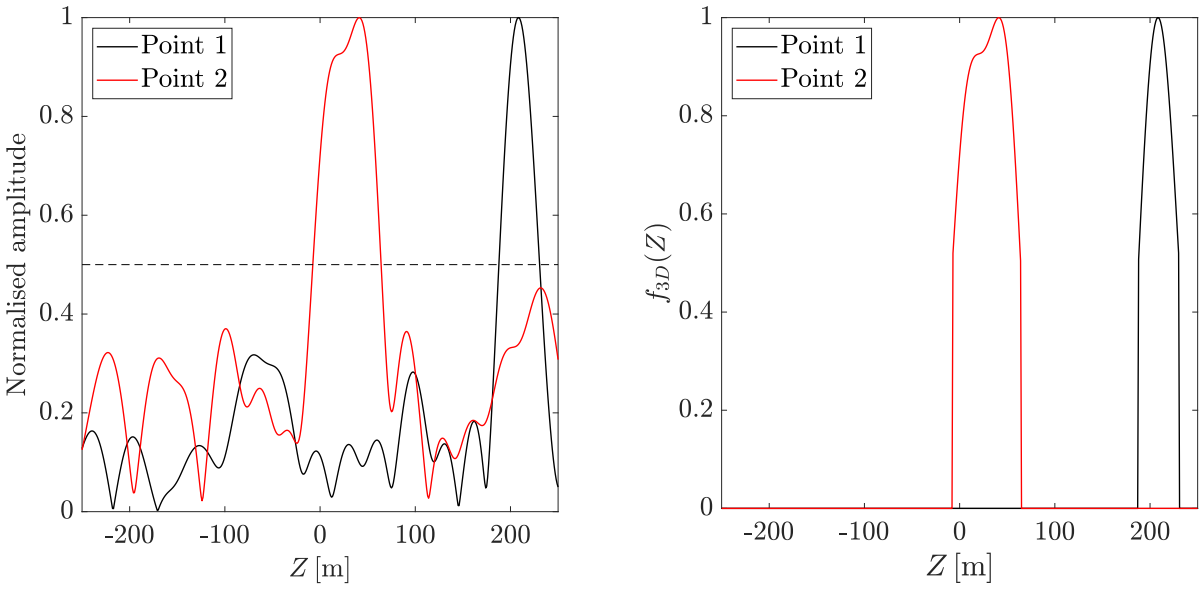

(a) TSVD inversion (b) Corresponding PDF

Figure 5.5: Creation of the likelihood function when tomographic data are available on two points at Enguri Dam. (a) is the normalised result of the inversion, and (b) is the corresponding PDF.

It is important to emphasise that the function becomes independent of X and Y when using this model. Its shape depends on the acquisition configuration and the SNR. For example, two points on the Enguri Dam are selected, where tomographic acquisitions were conducted. The results of the

TSVD inversion are given in Figure 5.5a and the corresponding PDF in Figure 5.5b. These figures provide insights into how the approach works in practice and how the prior function varies based on the acquired data and its processing.

If TomoSAR is available, it is preferred over the model of the previous subsection, as it provides a direct measurement and processing of the signal's origin, which inherently accounts for the geometry and phase information. Furthermore, TomoSAR data are not sensitive to the quality of the 3D model and the accuracy of surface normal vector calculations. Since TomoSAR directly captures the phase information from multiple radar passes, it effectively bypasses the need for model-based assumptions. As a result, it is a more accurate and reliable source of information compared to models that rely on calculated probabilities based on incidence angles and antenna patterns.

5.2.5 Point(s) estimation

The best 3D model point to geocode the information of the radar pixel is the one that maximises this relative a posteriori function and is the MAP estimate of the 3D coordinates, as expressed in Equation 5.9.

$$(X_{\mathrm{MAP}}, Y_{\mathrm{MAP}}, Z_{\mathrm{MAP}}) = \underset{X,Y,Z}{\operatorname{argmax}} \left(f_{\mathrm{3D|2D}}(X, Y, Z|r, \theta) \right) \tag{5.9}$$

To distribute the deformation value from the GB-SAR pixel to multiple points in the 3D model, thereby capturing an affected area by the measured deformation, the value of the maximum probability $P_{\max}$ in the pixel, calculated as in Equation 5.10, is required.

$$P_{\max} = \max_{X,Y,Z} \left(f_{\mathrm{3D|2D}}(X, Y, Z|r, \theta) \right) = f_{\mathrm{3D|2D}}(X_{\mathrm{MAP}}, Y_{\mathrm{MAP}}, Z_{\mathrm{MAP}}|r, \theta)) \tag{5.10}$$

All points with a probability $P > P_{\mathrm{thresh}}$ are considered as points contributing to the observed phase value, where $P_{\mathrm{thresh}} = TP_{\max}$. Here, T represents a threshold employed to allocate the deformation of the corresponding GB-SAR pixel to the most appropriate set of points. This choice encompasses the compromise illustrated in case (d) of Figure 5.1. Indeed, representing a GB-SAR pixel with a single point location is an abstract mathematical concept; the reality is that a surface reflects the signal. As the models used for the prior function are related to intensity-based models, finding all the points with a given probability is equivalent to finding points sending a certain amount of intensity w.r.t. the highest one. For instance, a threshold of $T = 0.8$ corresponds to an intensity ratio of $10 \log_{10}(0.8) = -1\,\mathrm{dB}$.

5.3 P-RaySAR for the geocoding

The presentation and initial use of P-RaySAR is made in Chapter 4, where it is employed for image simulation and subsequently for the correction of the system's azimuth. However, its application is further extended for the geocoding step, as the MAP estimation does solve neither the shadow effects nor the multiple signal reflection of the GB-SAR acquisition geometry.

Consequently, we propose to use the output of P-RaySAR to geocode the data. Indeed, the intersection points of the single signal reflection coincide exactly with the visible part of the 3D model. The a posteriori function is computed as in the previous section, but only on this new set of points.

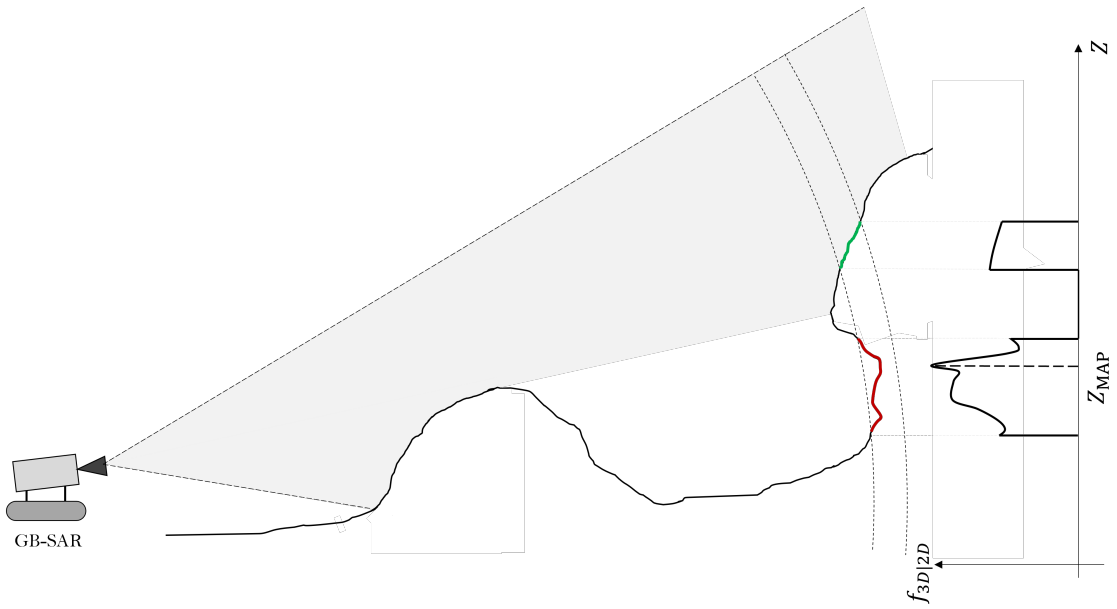

Figure 5.6: Cross-range profile of a case where the MAP estimation for the geocoding fails. The right axis represents the values of $f_{3D|2D}$ w.r.t. the elevation of the point.

However, unlike a full 3D model, this point cloud is not continuous, meaning that pixels detected as persistent scatterers may not correspond to any points on this model. It is assumed that they come from multiple signal reflections or sidelobes from very strong scattering objects and are discarded.

Figure 5.6 illustrates a scenario where the usage of the P-RaySAR 3D model is necessary. One resolution cell is emphasised with the pointed circles. For this pixel, the value for $f_{3D|2D}$ is displayed, and the maximum is clearly in the red area. However, this area corresponds to a shadow region where no signal can be received. By incorporating the single signal reflection information from P-RaySAR, only the intersections between the antenna's beamwidth and the 3D model are used for the back projection. Consequently, the shadow areas are excluded from the process. While such cases are relatively uncommon in typical GB-SAR scenarios, this approach promises to substantially improve geocoding in infrastructure monitoring applications.

5.4 Application at Linach Dam

The first application case focuses on a dam located in the Black Forest region in Germany. While the implemented method demonstrates its utility at the Enguri Dam, its effectiveness is even more pronounced at the Linach Dam. This heightened enhancement is more distinctive than at Enguri Dam due to its particular architectural characteristics.

5.4.1 Presentation of the test site

The Linach Dam is standing at a height of 25 m over a length of 143 m [Illner, 2008]. It is one of a few vaulted row dams worldwide, making it adequate for GB-SAR monitoring, as no plumblines can be installed in the vaults. Figure 5.7a represents the standpoint of the GB-SAR.

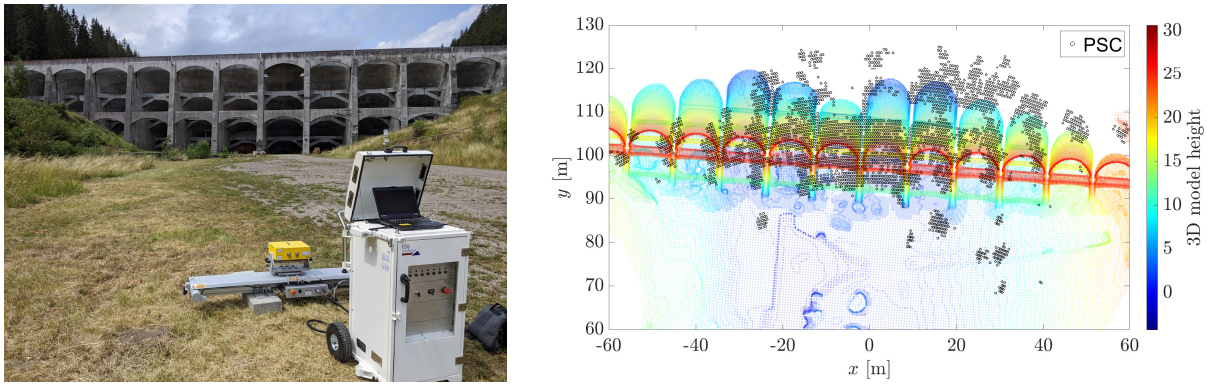

(a) GB-SAR position (b) PSC and 3D model

Figure 5.7: Acquisition at Linach Dam - (a): Standpoint of the GB-SAR in front of the Linach Dam - (b): GB-SAR PSC represented by unfilled black points and 3D model projected on the GB-SAR geometry. The projected 3D model is represented with the height w.r.t. the sensor as a colour code. Adapted from [Rebmeister et al., 2022a].

This dam is an ideal candidate for testing the effectiveness of the proposed geocoding algorithm due to its complex structural composition.

The 3D model was realised by combining a UAV flight and a terrestrial laser scanner (TLS) campaign. The complexity of the dam's structure implied a bad quality of the solely UAV 3D model, particularly within the vaults, where the UAV measurements were restricted. The GB-SAR was installed approximately 100 m away from the dam, with an elevation angle $\eta_{\text{GB-SAR}} = 5°$.

Assessing the geocoding complexity for this case is illustrated in Figure 5.7b. The visualisation displays the projection of the 3D point cloud onto the GB-SAR geometry using a transparent coefficient, allowing the identification of layover effects between the structures and the ground. Notably, specific PS points overlap with ground and dam points, introducing challenges in accurately geocoding these areas. Additionally, some PS are positioned behind the 3D point cloud of the dam, which is an indication of signals undergoing multiple reflections, which is expected due to the vaults.

5.4.2 Results analysis

The results are divided into two parts to better distinguish the contribution of the MAP geocoding and the usage of P-RaySAR. The analysis starts with the comparison of geocoding methods applied to the full 3D model and is followed by the same analysis applied to the P-RaySAR output.

5.4.2.1 MAP estimation on the full 3D model

Firstly, the NN approach is compared with the MAP estimation, corresponding to the concepts presented in Figure 5.1 (a) and (c) respectively. In case of a strong layover, interpolating the height of the 3D model points would be inappropriate, as it would assign geocoded points

between the ground and the dam.

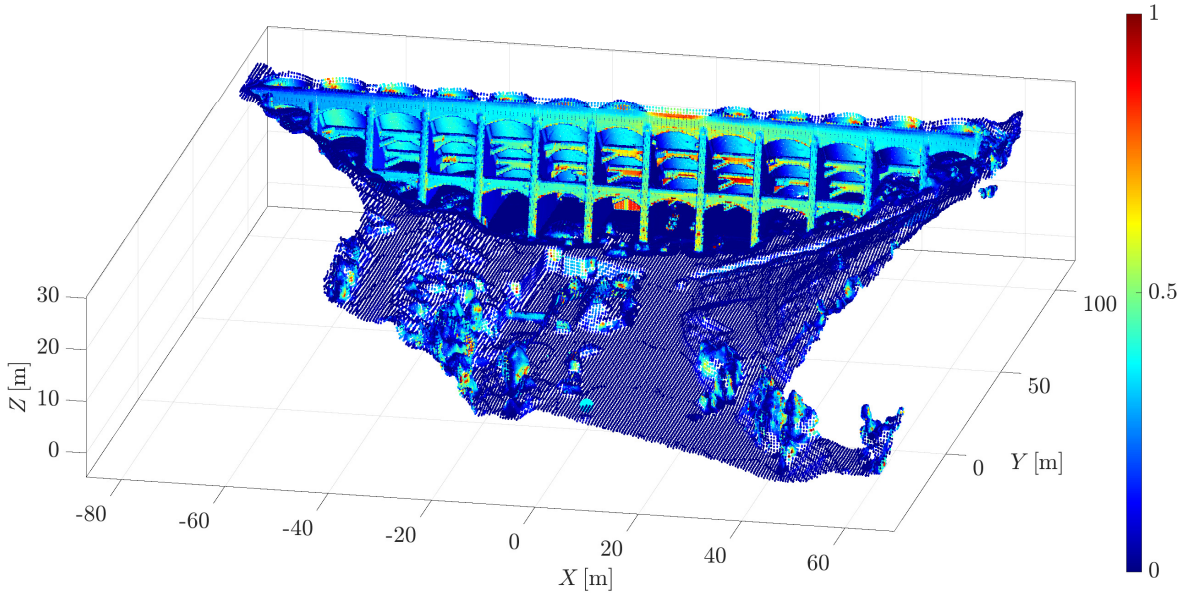

Figure 5.8: Evaluation of the prior PDF at the Linach Dam. Adapted from [Rebmeister et al., 2022a].

The values of the prior function $f_{3D}(X, Y, Z)$ applied to the dam's 3D model are presented in Figure 5.8. The influence of the incidence angle on the likelihood values is predominant in this case due to the low-ranging values of η for a small dam like this one. The horizontal structures facing the radar are highlighted by significantly higher values than the rest of the point cloud, which are also the structures expected to send back signals.

For a quantitative evaluation, ground truth data are unavailable due to the infeasibility of determining the true origin of the scattering points, except for corner reflectors or strong scattering objects. A series of steps are undertaken to assess the geocoding method's performance. Firstly, pixels containing any points of the 3D model are excluded from the geocoding analysis. Subsequently, points located under the dam and geocoded on the ground via the NN approach are considered as falsely geocoded. From the 4450 PSC, this subset includes an ensemble of 1300 points, representing a significant part of the set of PSC. This subset is represented by the red points in Figure 5.9a. In Figure 5.9b, the same points are also depicted in red after being geocoded with the MAP estimation. From this subset, approximately half of the points were correctly geocoded onto the dam rather than onto the ground, accounting for around 600 points. The difference between Figures 5.9a and 5.9b emphasises the improved results achieved through the MAP estimation.

To further demonstrate the effectiveness of the MAP estimation, a deeper analysis is conducted by selecting four distinct pixels from the GB-SAR image. Their specific locations are indicated in Figure 5.10 A. In all instances in this figure, the union of red and green points forms the complete set of projected points within the corresponding GB-SAR resolution cell. The green points in this context are those possessing a posterior probability $P > 0.8P_{\max}$, where $P_{\max}$ corresponds to the highest probability value for each of the selected pixels.

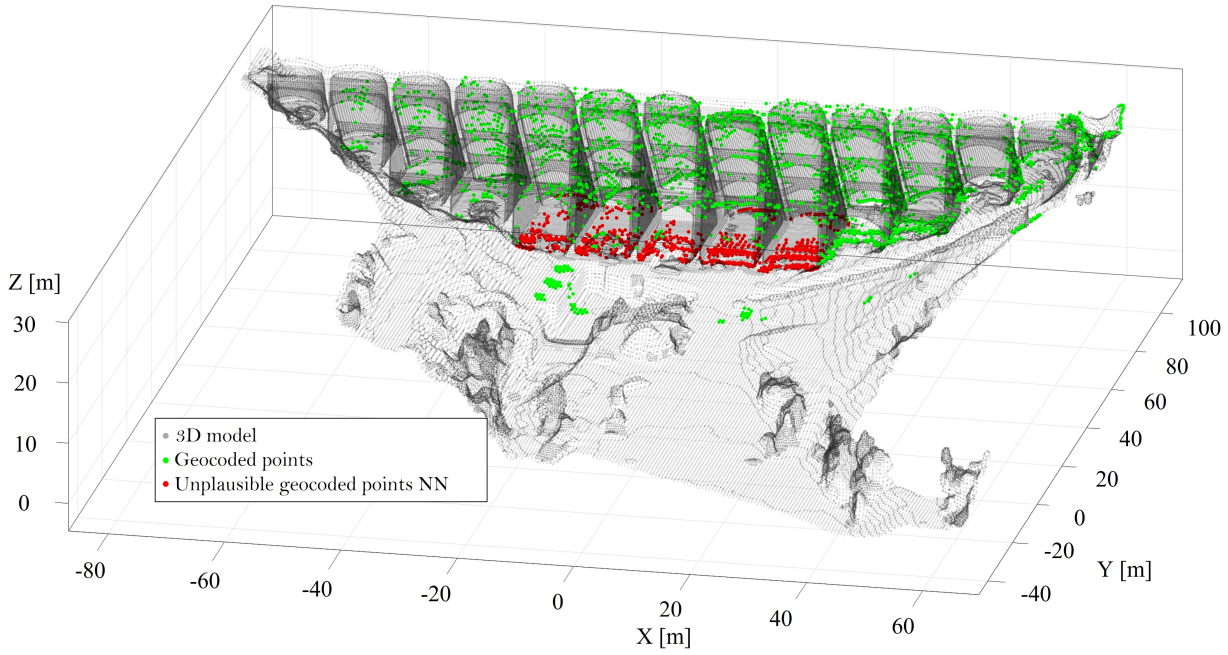

(a) Nearest neighbour projection of the PSC on the 3D point cloud of the Linach Dam.

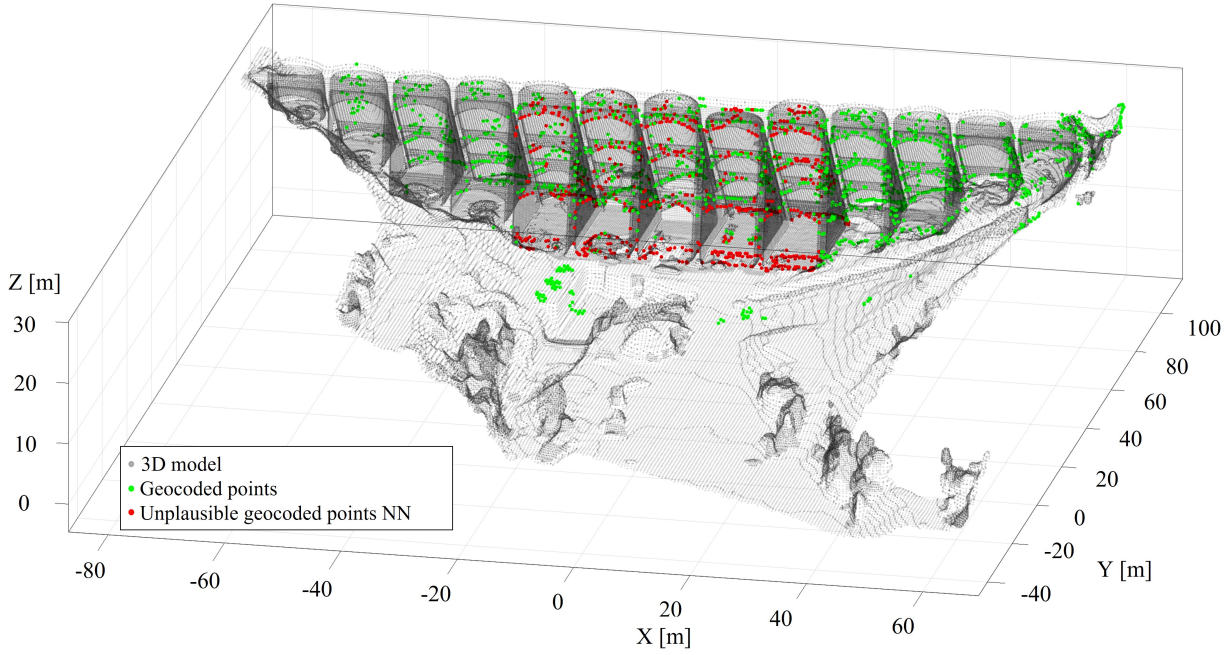

(b) Maximum A Posteriori projection of the PSC on the 3D point cloud of the Linach Dam.

Figure 5.9: (a): Result of the geocoding with the NN method - (b): Result of the geocoding using the MAP estimation. The red set of points represents implausible localisation with the NN method. Adapted from [Rebmeister et al., 2022a].

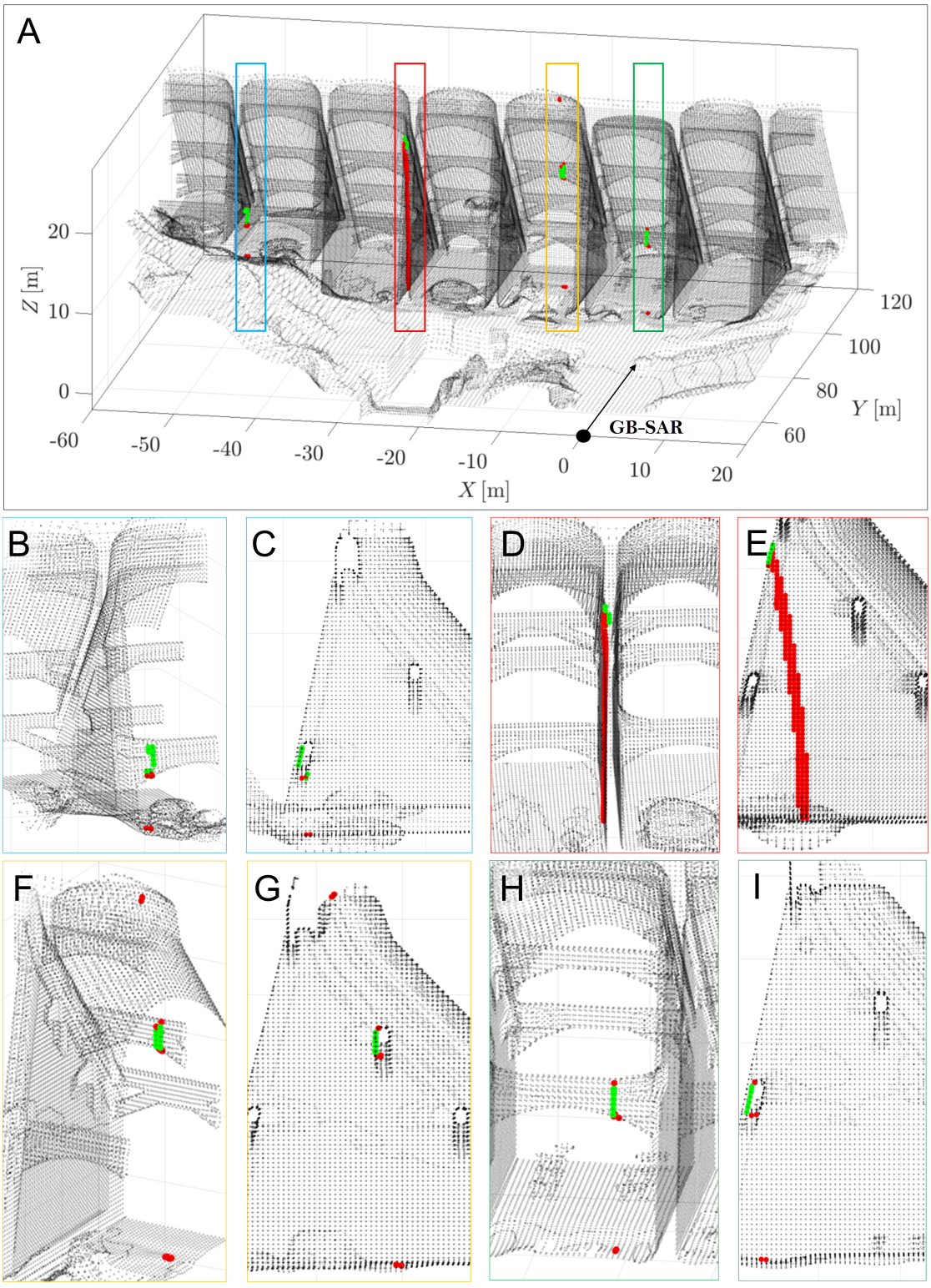

Figure 5.10: Insight of the MAP estimate represented on four pixels. Green points correspond to those contributing to the received signal, while red points are discarded for further processing. Adapted from [Rebmeister et al., 2022a].

The perspectives denoted by B, D, F, and H provide a frontal view of the 3D point cloud, while those labelled C, E, G, and I offer a side view. Similar geocoding outcomes are observed for pairs B-C, F-G, and H-I. Most of the corresponding 3D model points are situated on the horizontal concrete beams in these cases. However, there are also instances of points located on the ground as well as points on the bottom and/or top faces of the beams that are falling in the pixel. These red points are unrealistic, as they are positioned in shadow areas where signals cannot be received. Notably, only points on the frontal face of the beam are considered as observed points by the MAP geocoding. This outcome aligns precisely with expectations. In the scenario depicted by case D-E, the entire column is included within a single GB-SAR pixel. However, since only a tiny frontal part of the wall is illuminated by the radar, applying the observed displacement to the entire column is meaningless. The MAP geocoding algorithm identifies the green points as the best candidates for the geocoding and discards the rest, solely using the incidence angle and antenna pattern as criteria. Thus, even on the full 3D model, the proposed algorithm already considerably helps to eliminate implausible points from the geocoding.

5.4.2.2 MAP estimation on the P-RaySAR model

An examination of case B-C in Figure 5.10 highlights that specific green points are not solely situated on the frontal face of the beam but also on its back face. As the incidence angle and the relative elevation are nearly the same, the points are also considered by the MAP estimation. Therefore, the P-RaySAR algorithm generates a new 3D model without shadow areas. The application of the a priori function f_{3D} to this 3D model is visible in Figure 5.11. A substantial part of the original 3D model is missing, rendering geocoding unfeasible in these locations.

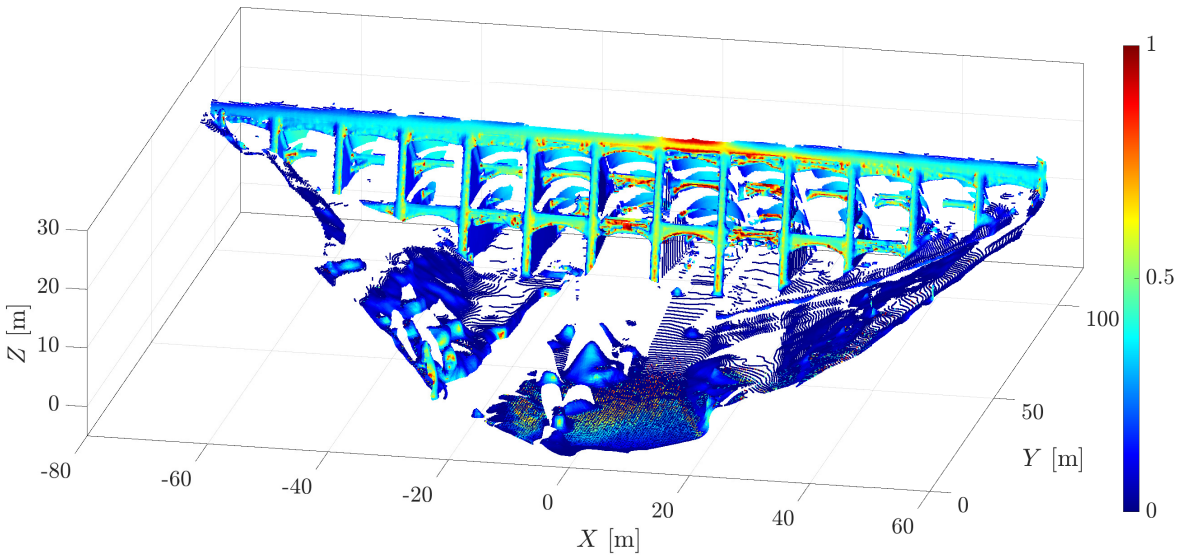

Figure 5.11: Evaluation of the prior PDF on the 3D model generated by P-RaySAR. Adapted from [Rebmeister et al., 2022a].

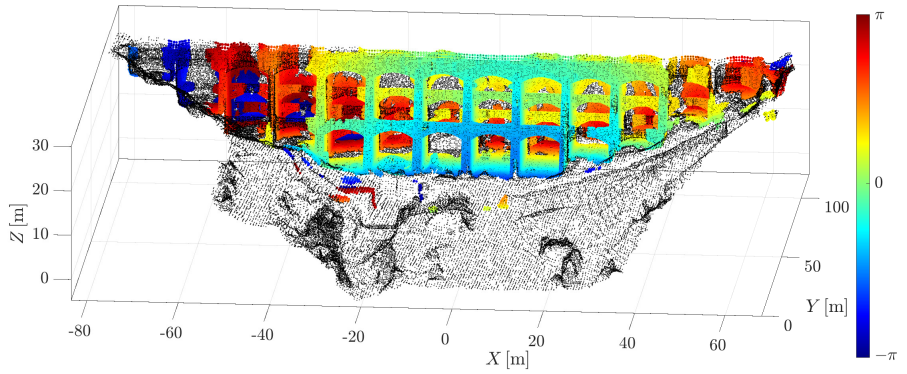

(a) Case 1: All points geocoded

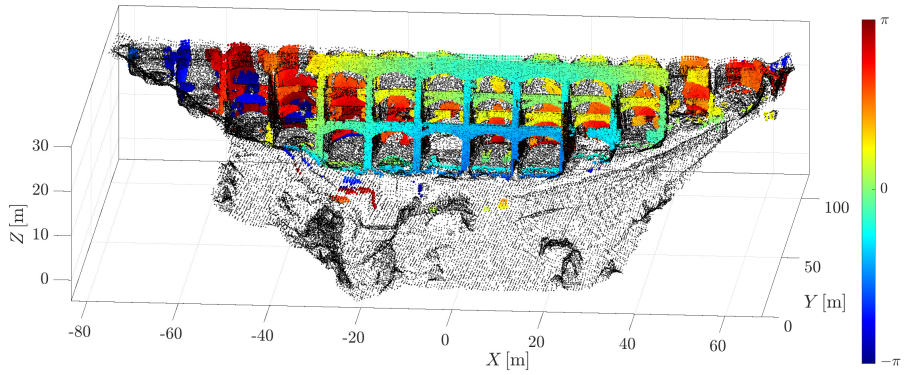

(b) Case 2: Most likely points geocoded on 3D model

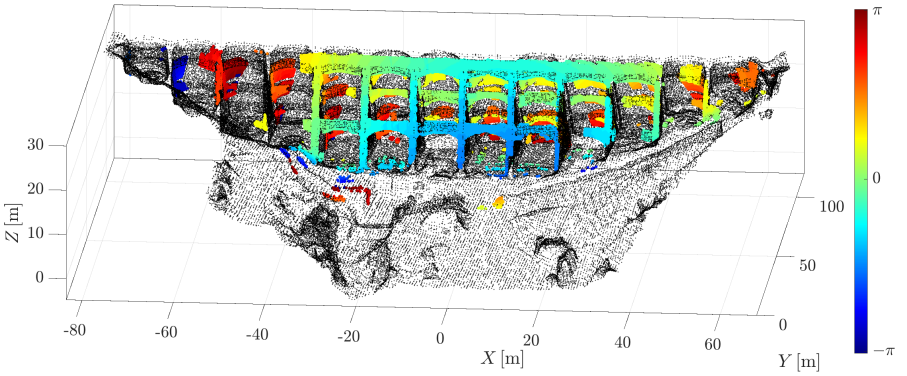

(c) Case 3: Most likely points geocoded on P-RaySAR single bounce

Figure 5.12: Comparison between the different geocoding methods at Linach Dam (a): Geocoding of all points - (b) Geocoding of most likely points using a threshold $T = 0.8$ - (c) Similar to (b) but using P-RaySAR output as support. Adapted from [Rebmeister et al., 2022a].

Three distinct cases are tested for the association of phase values from the GB-SAR pixel to the 3D model points:

- Case 1: All points of the 3D model projected in the corresponding resolution cell receive a phase value.
- Case 2: All points of the 3D model projected in the corresponding resolution cell and with an a posteriori probability higher than $0.8P_{\max}$ receive a phase value.
- Case 3: All points of the P-RaySAR 3D model projected in the corresponding resolution cell and with an a posteriori probability higher than $0.8P_{\max}$ receive a phase value.

Figure 5.7b illustrates the localisation of the PSC. An interferogram with a phase ramp along the range direction is simulated to enhance the visualisation of the geocoding. In Figure 5.12a, almost all parts of the dam contribute to the measured signal. However, as already explained, it is implausible that the surfaces at the side of the vaults or surfaces on the ground reflect signals as they are almost parallel to the radar LOS. To address these issues, the MAP estimation is introduced, and the outcome is demonstrated in Figure 5.12b, where a significant number of points on the ground are discarded, as anticipated.

In Figure 5.12c, the P-RaySAR algorithm is integrated into the process, preventing the geocoding of points located in shadow areas. The results for the central portion of the dam are comparable to that of the previous case. However, along the sides of the dam, fewer points are geocoded since a notable proportion of the PSC corresponds to signal multiple reflections occurring within the vaults.

Comparing Figures 5.12a and 5.12c might raise concerns about the potential loss of information. While Figure 5.12c exhibits fewer geocoded points from the 3D model, it is essential to note that Figure 5.12a contains a significant amount of false information. The improvement made by the developed method is that we can surely interpret the observed displacement as a single bounce and, therefore, as a LOS displacement. All other points geocoded without P-RaySAR could have come from multiple signal reflections and could have disrupted the further interferometric processing.

5.5 Evaluation at Enguri Dam

At Enguri Dam, the investigation of the geocoding is also of the highest interest, as exceptional layover affects the data, especially from the *Warehouse* and *Pavel 1* stations. Figure 5.13 shows the layover areas for both stations. All single signal reflections from P-RaySAR are clustered in their corresponding pixel, and for each one, the maximal elevation difference of its belonging points is displayed. The regions with the most pronounced layover correspond to the areas influenced by the dam's parabolic shape, extending along the elevation direction. It affects a significant portion of the dam's central section for both stations.

Tomographic data were acquired and processed at *Warehouse* station, enabling a comparison between the two proposed prior functions. The methods with and without tomographic data are denoted with MAP and TMAP, respectively.

In Chapter 4, corner reflectors (CR) are used to estimate the accuracy of the positioning of the system. They can also serve as a tool to estimate the geocoding quality. Indeed, the 3D coordinates

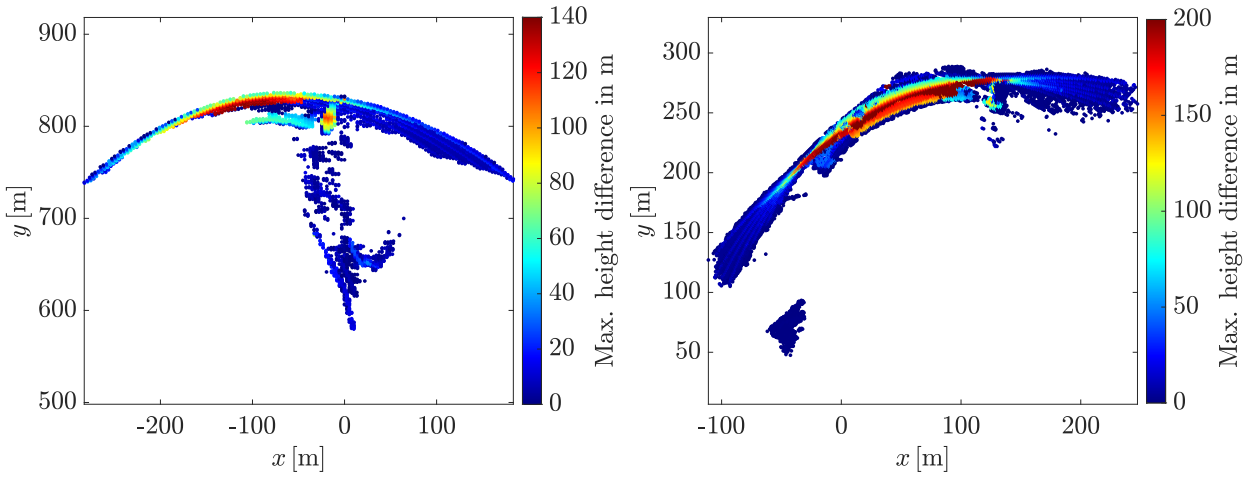

(a) *Warehouse* (b) *Pavel 1*

Figure 5.13: Layover on the PSC for the (a) *Warehouse* and for the (b) *Pavel 1* stations.

of the CR are known, and their corresponding pixels are identified as the nearest pixel's centre to their projected 2D coordinates. Then, the coordinates estimated during the geocoding of these pixels and their true coordinates can be compared. As the main concern is the layover in elevation, only the Z coordinates are provided.

The CR are installed on the dam, and their signal contribution within their respective resolution cell is expected to influence the tomographic results significantly. However, the likelihood function without tomographic acquisition only considers the direct incidence angle w.r.t. the observed surface and the antenna pattern. The material and the specific signal path implying a specular reflection are not yet involved. However, the CR are located on the dam balconies, where strong signal reflection is expected due to their curved shape.

The results are deeply analysed on four CR. Two CR clearly identifiable and two that lie in a more challenging context are selected. Figure 5.14a represents their position on the amplitude image. CR 3 and CR 6 are distinctly identifiable as 2D peaks, while CR 2 and CR 5 are located in areas with already high amplitudes and are not distinguishable. Their relative signal contributions within their respective pixels are not ensured to be the highest ones.

The analysis begins with the clear CR in Figures 5.14b and 5.14c. The true elevations of the CR are indicated with the dashed black lines. The naive NN projection leads to the blue vertical lines with an offset of 7 m and 10 m for CR 3 and 6, respectively. The blue points represent the elevation of all the points of the 3D model projected in the corresponding resolution cell. For both CR, the improvement made by the MAP geocoding is evident, as the offsets in elevation are reduced to respectively 3.5 m and 0.3 m. The green horizontal points denote the elevation where the displacement would be geocoded with the MAP method using a threshold $T = 0.8$. The orange horizontal points have the same signification for the TMAP method. For CR 6, the spread of elevation is reduced by a significant amount and solely points near the CR are considered. The point density is reduced because of the lower resolution of the P-RaySAR model used for both MAP and TMAP methods. The TMAP procedure provides an even better result, as the error is reduced to 1.5 m for CR 3. Additionally, for this reflector, the most likely elevations of the points are closer to the best one.

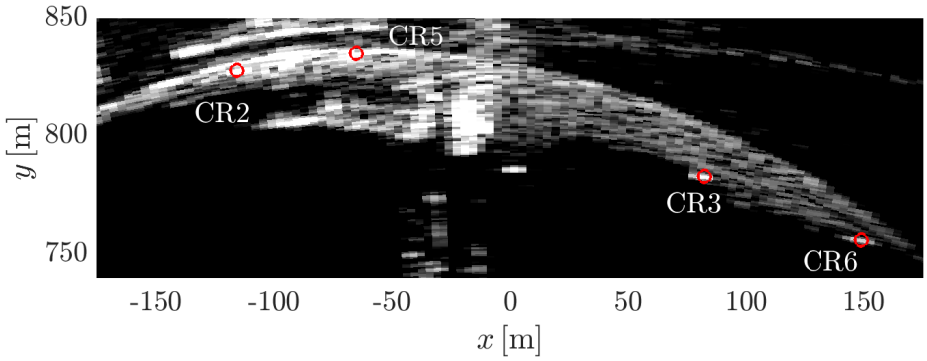

(a) Position of chosen CR

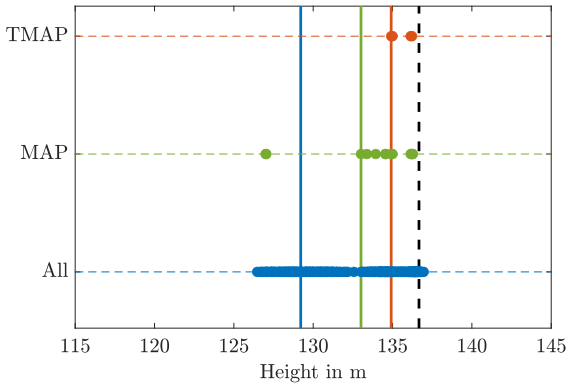

(b) CR 3

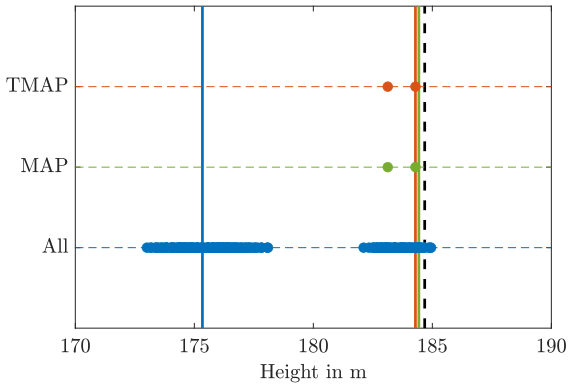

(c) CR 6

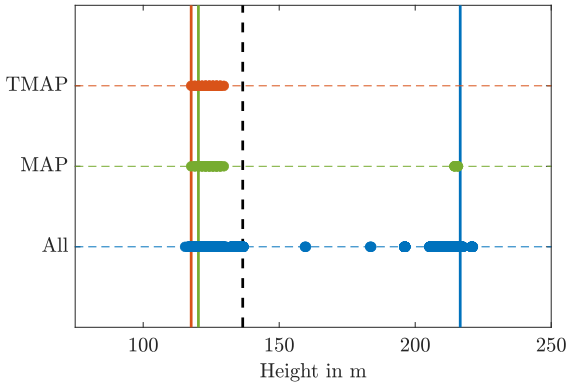

(d) CR 2

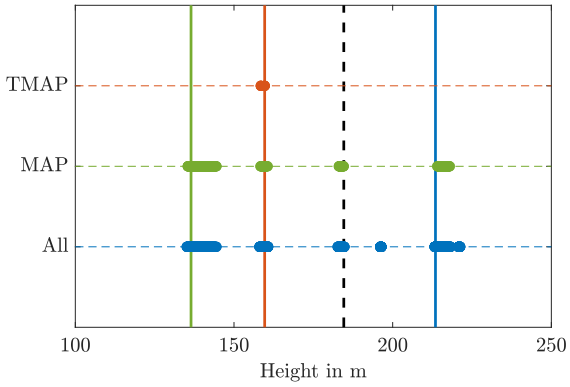

(e) CR 5

Figure 5.14: Evaluation of the different geocoding methods at Enguri Dam using the CR as ground truth. The vertical lines indicate the chosen Z coordinate with the corresponding method, i.e. the Z coordinate of the point with the largest probability value. For the line "All", the horizontal points represent all the points of the 3D model falling in this pixel. For MAP and TMAP methods, it corresponds to the single bounces using a threshold $T = 0.8$.

The analysis becomes intricate for the two remaining CR, located in areas with significant layover effects. This complexity is highlighted in Figures 5.14d and 5.14e, where the possible geocoding points exhibit a substantial elevation difference of nearly 100 m. The considerable limitations of the NN method are apparent for CR 2, as this approach selects almost randomly one of the points within the resolution cell. The MAP and TMAP methods geocode the information to a much lower part of the dam, approximately 20 m below the CR position. Due to the high-intensity values of neighbouring points, the presence of a strong scattering point at this elevation cannot be rejected. While the MAP method considers points on the higher part of the dam as relevant, the TMAP method does not recognise them as significant signal sources. The situation is even more complex for CR 5. Almost all the points in the corresponding resolution cell have a similar likelihood value, meaning they are nearly indistinguishable. The situation is more complicated than Linach Dam's, as points with similar incidence angles and locations fall in the same resolution cell. The MAP method considers four sets of elevation as plausible for the geocoding, and from these four sets, the TMAP method does not match with the one near the real CR location. Also, in this situation, the proposed comparison reaches its limit. Indeed, as the CR is installed in an area with a very strong layover and already sending a very high intensity back, it is impossible to assess if the CR position is the ground truth of the elevation of the received signal. This situation leads to questions such as: Is the interferometric signal observed in this resolution cell reliable for displacement analysis? Separating them with tomographic techniques would be impossible if they correspond to a mix of signals, as the linear GB-SAR has no elevation baselines in the continuous monitoring case.

5.6 Conclusion

This chapter pointed out that the geocoding step is significantly more complex in infrastructure monitoring than in natural scenarios. A new method for geocoding GB-SAR data has been introduced and extensively evaluated at two dams. The four major distortions in a GB-SAR image have been resolved through two main inputs: a Bayesian model and the ray tracing algorithm P-RaySAR presented in the previous chapter. The Bayesian approach utilises amplitude models to estimate the contributions from the external 3D model that have the most significant impact on the subsequent interferometric signal. When solely the external model is available, the creation of the prior function is based on the incidence angle and on the antenna pattern. When tomographic results are available, the prior function is based on the tomographic profiles for each pixel under consideration.

The contributions of each part of the developed geocoding approach can be summarised as follows:

- **Maximum a posteriori estimation**: This approach enables significant foreshortening and layover mitigation. The MAP method yields reliable estimates of observed point locations by addressing these distortions. It also identifies all areas in one resolution cell contributing to the observed signal. However, some uncertainties may persist in scenarios featuring strong layover and similar incidence angles.
- **P-RaySAR**: This method enables the identification of the shadow areas by using a 3D model exclusively from single signal reflections sampled from the original model. Resolution cells containing any projected 3D model points indicate signals undergoing multiple reflections. P-RaySAR also offers a preliminary framework for the analysis of scenarios involving multiple signal reflections.

The ability to localise the points contributing to the observed displacement is of major interest for subsequent usages. For example, thinking of calibrating a numerical or a finite element model with

the GB-SAR data, it would be inadequate to use classical methods, as pointed out by all the results in this chapter.

Two major next steps for further work are proposed. Firstly, the Bayesian model can be extended with other prior information. For instance, after the interferometric processing, the correlation between neighbouring time series could be used to ensure a continuous pattern on the geocoded displacement map. Secondly, there is potential to automate the identification of areas heavily impacted by multiple signal reflections. This could mitigate the potential misinterpretations during interferometric processing. Additionally, the joint analysis of multiple bounce phenomena alongside observed displacement could yield valuable insights into deformation processes.

CHAPTER 6

Epoch-wise infrastructure monitoring

Contents

6.1 Introduction

The preceding chapters have established a method for precisely localising observed points within a 3D model. The subsequent step involves the development of a workflow to extract displacements from GB-SAR measurements. This chapter introduces an approach to handle interferometric phase data collected over different epochs. Existing work by [Wang et al., 2020a] and [Wang et al., 2021] have detailed techniques for analysing discontinuous datasets, successfully applied to a dam and exhibited strong agreements with plumbline data. However, these approaches were only employed over a limited three-day span, facing fewer challenges than the analysis of data spanning several months. Furthermore, these studies predominantly addressed micro-deformations occurring over relatively short periods, while our focus is on retrieving larger displacements occurring over more extended measurement gaps. The feasibility of employing GB-SAR for substantial temporal baselines is provided in [Noferini et al., 2008], where six acquisition campaigns were conducted over approximately three years. In the specific context of dam monitoring, [Wieser et al., 2020] employed the TRI technique for epoch-wise measurements with a six-month temporal baseline, yielding plausible results, but only for a part of the monitored dam.

The chapter is divided into two main parts. Firstly, a new flowchart to process interferometric data in the presence of epoch-wise measurements is extensively presented, with illustrations from the stations *Pavel* at Enguri Dam. Secondly, the obtained results from both *Georges* and *Pavel* stations are compared to two numerical models computed by the company *Artelia*.

6.2 Epoch-wise displacement reconstruction

6.2.1 Preprocessing

The precise and stable installation of the GB-SAR is not a straightforward task, and once deployed, the sensor can acquire an image in a matter of minutes or even faster. Therefore, it is common for the system to be used for multiple acquisitions. Letting the system acquire several hundred images is reasonable, even for epoch-wise monitoring. A preprocessing step is undertaken to capitalise on the statistical benefits offered by these measurements. Furthermore, the methodology presented in this chapter is tailored to the specific context of infrastructure monitoring. It assumes the presence of a stable foundation beneath the instrument, thereby obviating the need for coregistration. However, if such foundations are missing, the coregistration tool developed in [Wang et al., 2019b] can be employed.

An initial pixel selection based on coherence analysis on the first 20 scenes is carried out, aiming to conduct the subsequent analysis only on points containing significant signals. The mean coherence $\overline{\gamma}$ is computed for each point, as presented from Equations 2.29 to 2.32. The similarity threshold S_{th} for the coherence estimation is set to 0.85. The pixels satisfying $\overline{\gamma} > 0.6$ are retained, and a set of N_{PSC} points is obtained for the subsequent processing.

After that, the goal is to enhance the SNR of the acquisitions by computing an average image for each epoch. Therefore, considering a single epoch, the quality of each scene n is evaluated with the mean amplitude dispersion $\overline{D_A}(n)$ over a surrounding temporal window of odd-size W, computed as follows:

$$\overline{D_A}(n) = \frac{1}{N_{\text{PSC}}} \sum_{k=1}^{N_{\text{PSC}}} \frac{\sigma_A(k,n)}{\mu_A(k,n)} \tag{6.1}$$

with $\mu_A(k,n)$ the mean amplitude for point k over the window centred on the acquisition n and of size W, and $\sigma_A(k,n)$ the corresponding standard deviation. In this work, the chosen size of W is one hour. For the first epoch at station *Pavel 1*, the moving average of mean amplitude dispersion is illustrated in Figure 6.1a. Afterwards, the index of the central scene to be averaged for the campaign p is given by:

$$I_p = \underset{n}{\operatorname{argmin}} \left(\overline{D_A}(n)\right) \tag{6.2}$$

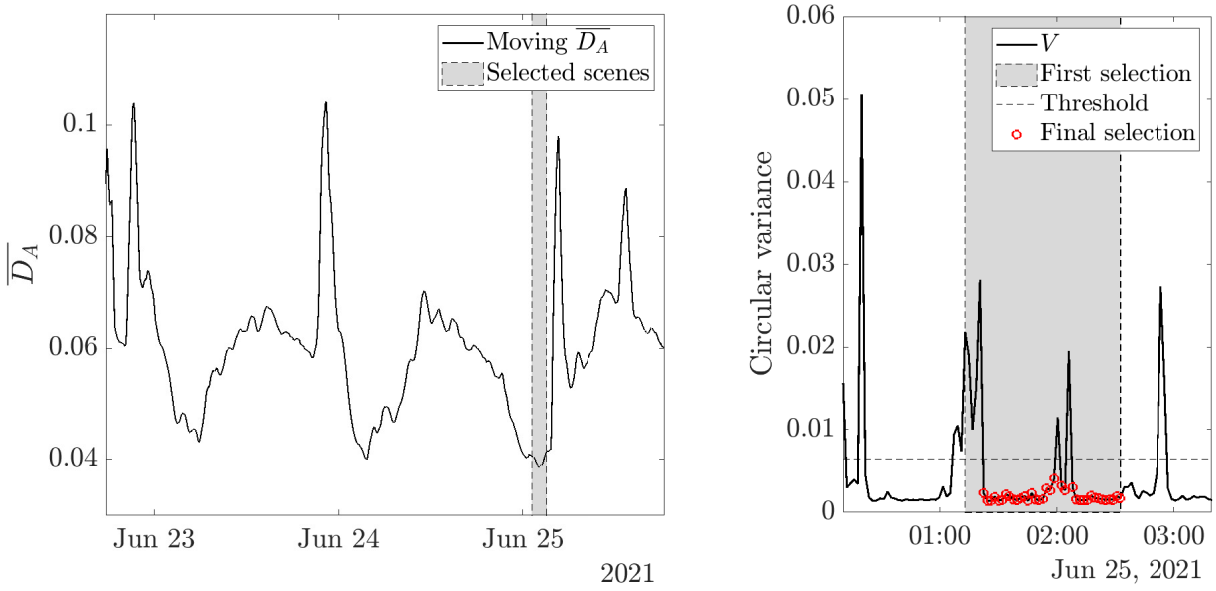

(a) Mean amplitude dispersion

(b) Circular variance

Figure 6.1: Scene selection for the computation of the average Epoch 1 for *Pavel 1* station. (a) coarse selection, and (b) fine-tuning.

Figure 6.2 illustrates two interferograms with a temporal baseline of 20 minutes. Within the selected time interval, the phase dispersion is notably weaker compared to a period with more disturbances, thus enhancing the quality of the averaging process.

The proposed criterion is based on a smoothed temporal benchmark. A more refined process is undertaken to analyse each scene using the circular variance $V(n)$ defined in [Mardia et al., 2000]. This metric is calculated on sequential interferograms to depict the dispersion of the phase values around the mean of each interferogram. The circular variance is computed as follows:

$$V(n) = 1 - \sqrt{\left(\frac{1}{N_{\text{PSC}}}\sum_{k=1}^{N_{\text{PSC}}}\cos(\phi(k,n))\right)^2 + \left(\frac{1}{N_{\text{PSC}}}\sum_{k=1}^{N_{\text{PSC}}}\sin(\phi(k,n))\right)^2} \quad \in [0;1] \tag{6.3}$$

with $\phi(k,n)$ the wrapped interferometric phase of point k between scene n and $n-1$. Then, the standard deviation σ_V of V is computed with all the scenes in the segment $[I_p - (W-1)/2\,;I_p + (W-1)/2]$ and is used as a threshold to delete all the scenes where $V > \sigma_V$. After that, the scenes to mean are given by the set $\mathcal{S}_e$:

$$\mathcal{S}_e = \left\{ n \in \left[I_p - \frac{W-1}{2}; I_p + \frac{W-1}{2} \right] \mid V(n) < \sigma_V \right\} \tag{6.4}$$

The set $\mathcal{S}_e$ is marked by the red dots in Figure 6.1b. Then, for each campaign, the mean acquisition $\mathbf{z_p} = \{z_p(k)\}_{k \in [|1\,;N_{\text{PSC}}|]}$ is computed via:

$$z_p(k) = A_p(k) e^{i\varphi_p(k)} = \frac{1}{|\mathcal{S}_e|} \sum_{n \in \mathcal{S}_e} z(k,n) \tag{6.5}$$

with $z(k,n)$ the SLC value of acquisition n at point k. This technique also provides an approximated quantity for the phase noise $\sigma_\varphi(k,p)$ of each PSC k and each campaign p via:

$$\sigma_\varphi(k,p) = \frac{\sigma_A(k, I_p)}{\mu_A(k, I_p)} \tag{6.6}$$

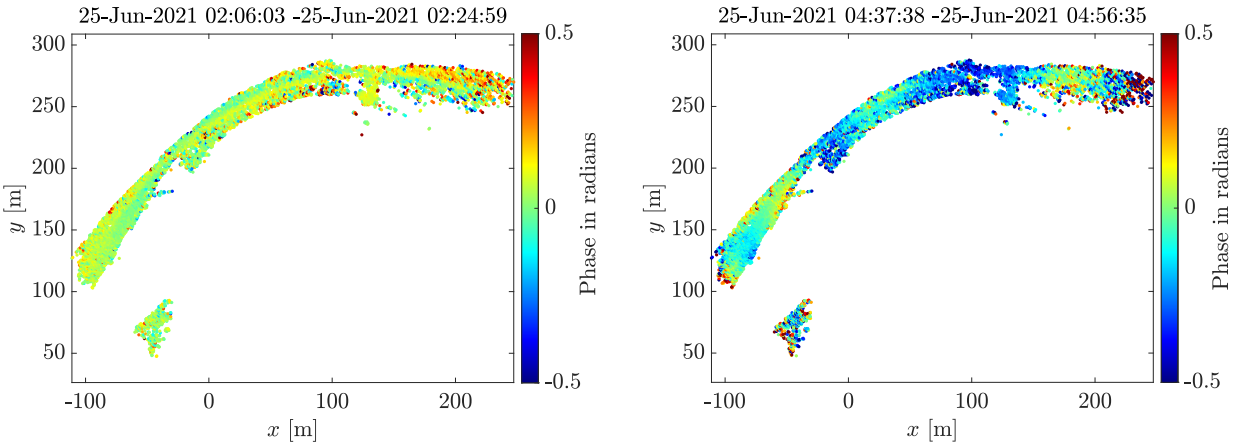

(a) Interferogram in low noise

(b) Interferogram in high noise

Figure 6.2: Comparison of 20-minute interferograms at two different periods of the day. (a) is during a period with a low noise identified, while (b) is during a period with a high noise identified.

6.2.2 Limits of a classical flowchart

The core of the flowchart for displacement estimation after the pixel selection for epoch-wise GB-SAR monitoring is detailed in Chapter 2. The main steps are summarised in Figure 6.3.

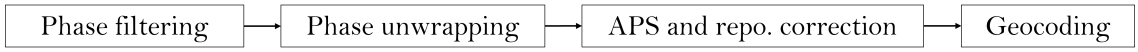

Figure 6.3: Classical main steps of an epoch-wise GB-InSAR processing chain.

The phase filtering used is the Goldstein filter [Goldstein and Werner, 1998], and the phase unwrapping is based on the SNAPHU routine [Chen and Zebker, 2001]. The atmospheric and repositioning correction is based on model fitting and is extensively discussed in Section 6.2.4.

This flowchart encountered substantial limitations at Enguri Dam. For instance, from the *Pavel* stations, the geometry is so distorted that the unwrapping algorithm can not reliably recover a displacement pattern, as shown further. For the rest of the development and analysis, the example of *Pavel 1* is used.

6.2.2.1 Analysis using P-RaySAR

In the previous chapter, Figure 5.13b demonstrated that several pixels at the *Pavel 1* station are heavily affected by layover. The single bounces resulting from the P-RaySAR computation are projected in the (x, y) GB-SAR Cartesian coordinate system to better understand the individual point projection in the GB-SAR geometry. The results of this projection are visualised in Figure 6.4 with a transparency coefficient to help the separation in the layover areas. Figure 6.4a presents a global view from the station, where the colour represents the elevation w.r.t. the radar.

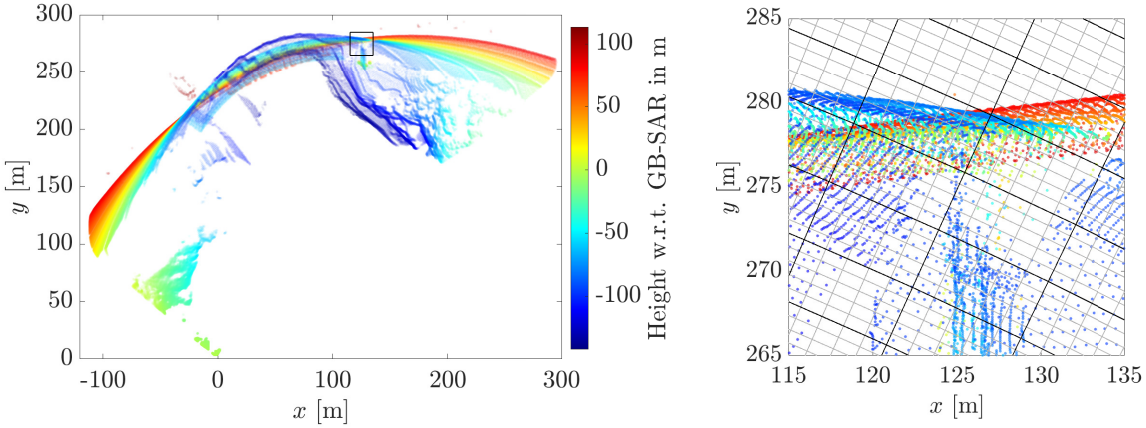

(a) Full P-RaySAR single bounce

(b) Zoom in highly impacted layover area

Figure 6.4: Single bounces from P-RaySAR analysis projected onto the GB-SAR geometry. The colour represents the height. (a) is a global view from the station, while (b) is a zoom with the grid size of the pixel represented in grey lines. Each black cell represents 5×5 pixels.

The left and right parts of the dam exhibit distinct elevation gradients that should lead to reliable unwrapping despite strong foreshortening. However, the figure also shows two nodes where the sensor's resolution falls to almost zero. To further analyse this effect, a zoomed-in view of the impacted layover area is presented in Figure 6.4b. At the highlighted locations, the elevation gradient changes abruptly, causing points with elevation differences of about 200 m to be projected into the same resolution cell.

6.2.2.2 Classical flowchart processing

The data processing from the *Pavel 1* station is conducted according to the workflow presented in [Crosetto et al., 2014]. A summary of this flowchart with only key steps is represented in Figure 6.3. The input interferogram contains the phase difference between 25$^{\text{th}}$ June 2021, and 30$^{\text{th}}$ September 2021. The raw wrapped interferogram and its corresponding unwrapped interferogram obtained after applying the phase filter and phase unwrapping are presented in Figure 6.5.

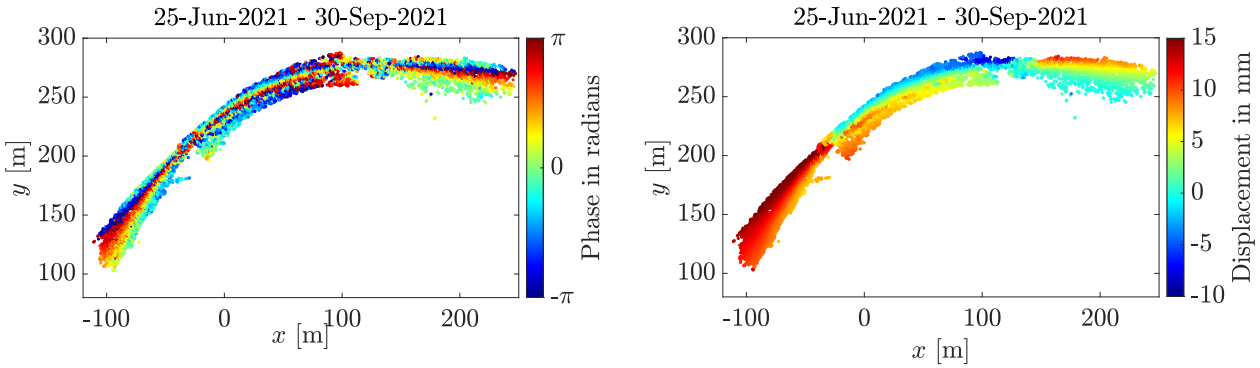

(a) Wrapped interferogram

(b) Unwrapped interferogram

Figure 6.5: Results of the unwrapping algorithm in the (x, y) geometry in (b) corresponding to the wrapped data of (a). The interferograms correspond to the phase difference between Epoch 1 and 2 from Table 3.1.

The raw interferogram shown in Figure 6.5a reveals an interesting phenomenon. Specifically, the left and right segments of the dam display a noticeable phase gradient, which can be linked to the elevation of the points, as clarified in Figure 6.4. As one moves away from the sensor, the phase predominantly increases. However, within the central portion of the dam, even with tightened fringes, the phase decreases with increasing distance from the GB-SAR. Consequently, two distinct nodes can be identified in the acquisitions, where a reversal occurs in the relative positioning of the PSC in terms of range concerning their elevation.

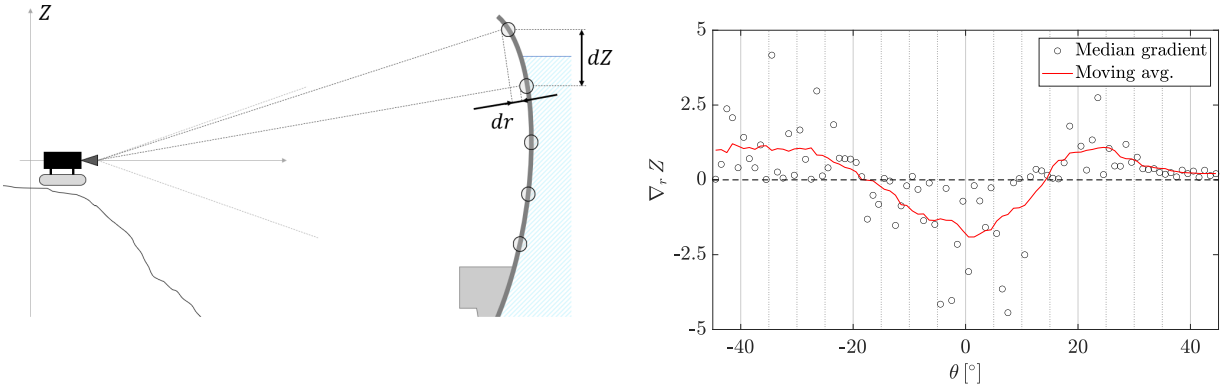

(a) Diagram

(b) *Pavel 1*

Figure 6.6: Gradient in elevation w.r.t. range in a cross-range profile. (a): Schematic representation of the conducted analysis. (b): Gradient change at *Pavel 1* station.

A small study of the elevation gradient w.r.t. the range coordinates $\nabla_r Z = dZ/dr$ is conducted to understand this effect better. A grid is arranged on the dam with a spacing of 10 m and matching the system's field of view. Subsequently, these points are regrouped by similar cross-range angle θ, forming a set of cross-range profiles. Figure 6.6a represents one of these profiles with the quantities dZ and dr for a pair of neighbouring points. The gradient $\nabla_r Z$ is computed between neighbouring points for each bin. The median of these gradients is calculated for each profile and represented in Figure 6.6b for the *Pavel 1* station. A moving average is also displayed to improve the visualisation. The

depicted phenomenon on the interferogram is confirmed by the two change points of the gradient's sign. As the atmospheric and deformation signals are highly correlated with the height[1], a fringe inversion is observed on the interferogram.

The unwrapping algorithm's outcomes, presented in Figure 6.5b, precisely illustrate this effect. Notably, the displacement map exhibits multiple discontinuities that are not immediately apparent. However, the geocoded result in Figure 6.9a lacks clear physical consistency.

6.2.3 Unwrapping in optimal geometry

To help the phase unwrapping algorithm solve the problem, we propose to work in an adapted coordinate system, as [Magnard et al., 2021] did for satellite SAR in the case of mountainous areas. In the latter work, the processing steps are not conducted in the *azimuth-range* coordinate system but in the corrected *longitude-latitude* one, which reduces the foreshortening effects in spaceborne SAR. Indeed, in mountainous areas, the slope of the terrain can have a similar orientation as the wavefront of the SAR signal, leading to extreme foreshortening in *azimuth-range*. As the goal is to work in a coordinate system that minimises the foreshortening without suffering layover, the *longitude-latitude* coordinate system is inadequate for the monitoring of a vertical structure. We are also looking for an optimum mapping for GB-SAR, but it is not straightforward, as it depends on the geometry of the imaged object and is related to the GB-SAR position.

The proposed transformation is based on the findings described in [Weinmann et al., 2015]. In the latter work, the structure tensor $\mathbf{S} \in \mathbb{R}^{3\times3}$ is computed for a point cloud segmentation purpose. This tensor can be seen as a 3D covariance matrix of the points distribution. To compute it, the input is the geocoded 3D point cloud of the PSC, denoted with the set of coordinates $\mathbf{X}_{\mathrm{PSC}} = [\mathbf{X}_{\mathrm{PSC},k}]_{k\in[|1;N_{\mathrm{PSC}}|]}$, with $\mathbf{X}_{\mathrm{PSC},k} = [X_{\mathrm{PSC},k}\,, Y_{\mathrm{PSC},k}\,, Z_{\mathrm{PSC},k}] \in \mathbb{R}^3$. The geometric centre of the scenario is computed as follows:

$$\bar{\mathbf{X}}_{\mathrm{PSC}} = \frac{1}{N_{\mathrm{PSC}}} \sum_{k=1}^{N_{\mathrm{PSC}}} \mathbf{X}_{\mathrm{PSC},k} \tag{6.7}$$

Then, the dispersion of the points from this centre along each axis is computed using the structure tensor $\mathbf{S}$:

$$\mathbf{S} = \frac{1}{N_{\mathrm{PSC}}} \sum_{k=1}^{N_{\mathrm{PSC}}} \left(\mathbf{X}_{\mathrm{PSC},k} - \bar{\mathbf{X}}_{\mathrm{PSC}}\right) \left(\mathbf{X}_{\mathrm{PSC},k} - \bar{\mathbf{X}}_{\mathrm{PSC}}\right)^{\mathsf{T}} \tag{6.8}$$

By definition, the structure tensor $\mathbf{S}$ is a symmetric positive definite matrix allowing for the computation of its eigenvalues and eigenvectors using the principal component analysis (PCA). The result of this transformation is the decomposition of $\mathbf{S}$ into the product of three matrices:

$$\mathbf{S} = \mathbf{V}\boldsymbol{\Lambda}\mathbf{V}^{\mathsf{T}} \tag{6.9}$$

with $\mathbf{V} \in \mathbb{R}^{3\times3}$ composed of the eigenvectors $\mathbf{v_1}$, $\mathbf{v_2}$, $\mathbf{v_3}$ of $\mathbf{S}$ and $\boldsymbol{\Lambda} = \mathrm{diag}(\Lambda_1, \Lambda_2, \Lambda_3) \in \mathbb{R}^{3\times3}$ the diagonal matrix with the corresponding eigenvalues. The two eigenvectors corresponding to the two largest eigenvalues represent the two main directions in which the point cloud exhibits the

[1] While the atmospheric signal expresses in most situations a high correlation with the elevation w.r.t. the GB-SAR, the deformation signal is also expected to exhibit such a correlation in case of the monitoring of a dam.

most significant dispersion. These eigenvectors essentially define a plane that captures the primary structural characteristics of the point cloud and helps mitigate the foreshortening effects. To project the point onto this plane, the projection matrix is given by $\mathbf{V_{2D}} = [\mathbf{v_1}, \mathbf{v_2}]$. The new 2D coordinates, denoted as $\mathbf{x_{pca}}$, are obtained using the following transformation:

$$\mathbf{x_{pca}} = \mathbf{X}_{\mathrm{PSC}}\mathbf{V_{2D}} \tag{6.10}$$

The transformation enables the expansion of fringe patterns in a wrapped interferogram, resulting in a more representative 2D image of the spatial signal. However, in the case of complex man-made structures, achieving precise georeferencing and geocoding is essential to ensure that the consistency of the observed signal in the GB-SAR geometry is accurately represented in the 3D geometry.

A valuable quantity when computing principal components is the cumulative explained variance CEV, defined in this specific case as:

$$\mathrm{CEV} = \frac{\Lambda_1 + \Lambda_2}{\mathrm{tr}(\mathbf{\Lambda})} \tag{6.11}$$

The CEV indicates how much information of the data's dispersion is retained up to the considered component. In Table 6.1, the value of the CEV considering the principal plane for each station is given. In all cases $\mathbf{x}_{\mathrm{pca}}$ contains more than 95 % of the data.

	Pavel 1	*Pavel 2*	*Georges*	*Warehouse*
CEV [%]	96.8	97.3	97.3	95.0

Table 6.1: CEV for all stations.

The CEV is adequate to ensure that no loss of information occurs during the projection, but no comparison is possible with the classical GB-SAR projection. To evaluate the amount of information earned, the area contained in the boundary of the set of PSC for each coordinate system $\mathbf{x}$ (classical) and $\mathbf{x}_{\mathrm{pca}}$ (transformed) is computed. Their values are given in Table 6.2, exhibiting a clear improvement of foreshortening reduction, especially for the *Pavel 1* and *Warehouse* stations.

	Pavel 1	*Pavel 2*	*Georges*	*Warehouse*
$\mathbf{x}$ area/10^4 $[m^2]$	0.95	4.80	3.24	1.21
$\mathbf{x}_{\mathrm{pca}}$ area/10^4 $[m^2]$	6.23	6.60	5.68	4.64
Ratio	6.56	1.38	1.75	3.84

Table 6.2: Area inside the boundaries encapsulating the PSC for each geometry at all stations.

The original flowchart from Figure 6.3 is modified to incorporate these enhancements into the processing flow, resulting in the updated version presented in Figure 6.7. The two new steps are the accurate geocoding followed by the developed geometric transformation. The proposed methods enable capitalising on the achievements reached in Chapters 4 and 5. It highlights the integrated role of these methods as a central step in the overall interferometric processing.

To visualise the improvement brought by the PCA coordinate system transformation, we can compare the filtered interferogram at the *Pavel 1* station in both the original coordinate system and the transformed PCA coordinate system. It helps to illustrate how the transformation enhances the fringe patterns and aids in the undistorted signal representation.

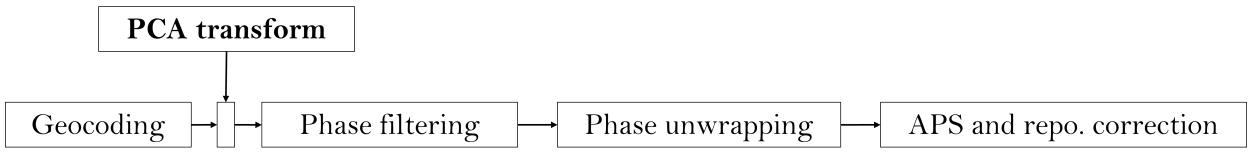

Figure 6.7: Modified main steps of the proposed epoch-wise GB-InSAR processing chain.

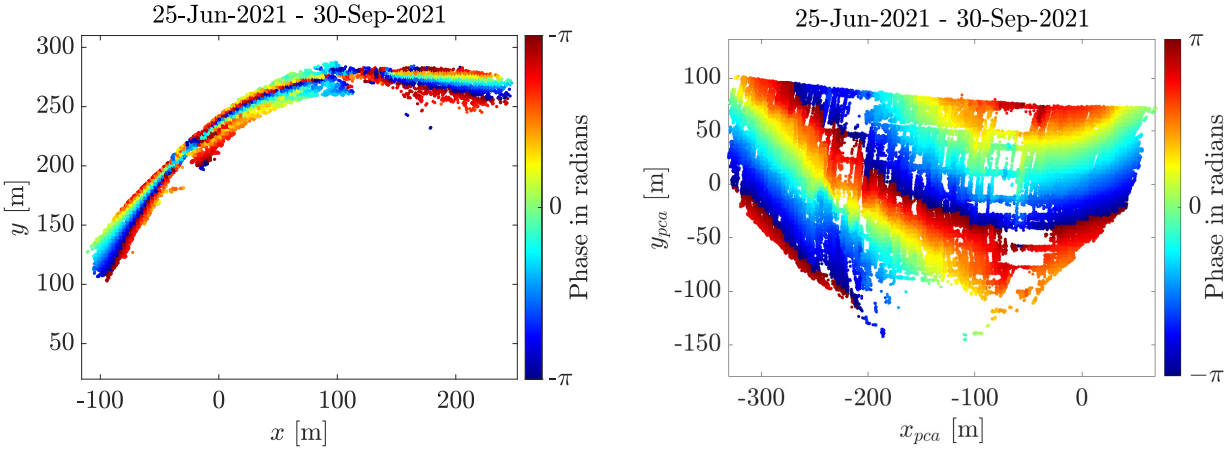

(a) SAR geometry (b) PCA geometry

Figure 6.8: Comparison of a filtered interferogram in the two coordinate systems. The one in the PCA geometry is much more understandable and easier for the phase unwrapping algorithm.

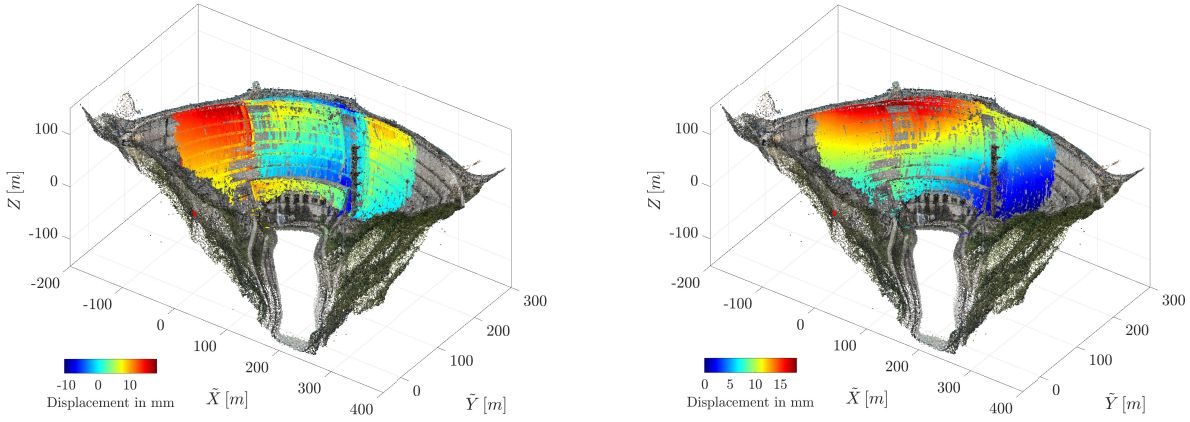

(a) Processing in SAR geometry (b) Processing in PCA geometry

Figure 6.9: Comparison of the geocoded unwrapped displacement map with the classical (a) and the new proposed flowchart (b).

As the *Pavel 1* station has only the dam in visibility, the PCA plane is almost parallel to its main directions. It enables the continuous consistency of the observed signal w.r.t. the physical deformation process of the dam. However, the PCA transformation does not increase the original SAR resolution, and its primary purpose is to improve the representation of the deformation signal.

The implemented Goldstein filter enables the enhancement of the resolution synthetically.

Represented in Figure 6.9, the geocoded displacement results after phase unwrapping and before any correction at *Pavel 1* station are pretty revealing. Two major discontinuities arise in the displacement map generated using the classical flowchart. The results of this flowchart could be used by dividing the dam into three parts and analysing each independently. The results of the proposed workflow lead to an unwrapped signal that is continuous and more physically consistent across the entire dam without significant discontinuities. Still, the user must check the projection result to ensure its injectivity and avoid the fact that two distinguished areas on the 3D model are projected on the same PCA plane.

6.2.4 Atmospheric and repositioning correction

With a large temporal baseline and a large part of the interferograms affected by a displacement phase term, the atmospheric estimation can only be computed on neighbouring stable areas. However, if the GB-SAR is near the structure, only points belonging to it would reflect coherent signals with extractable information. Therefore, locating neighbouring stable areas to interpolate the atmospheric signal is impossible. [Jacquemart and Meier, 2014] already raised this difficulty. Even if some stable scatterers are on the embankments for the specific dam case, no scattering points behind the dam can be observed. Therefore, the considered stable areas never surround the monitored object, leading to an extrapolation of the estimated signal and restraining the quality of the fit.

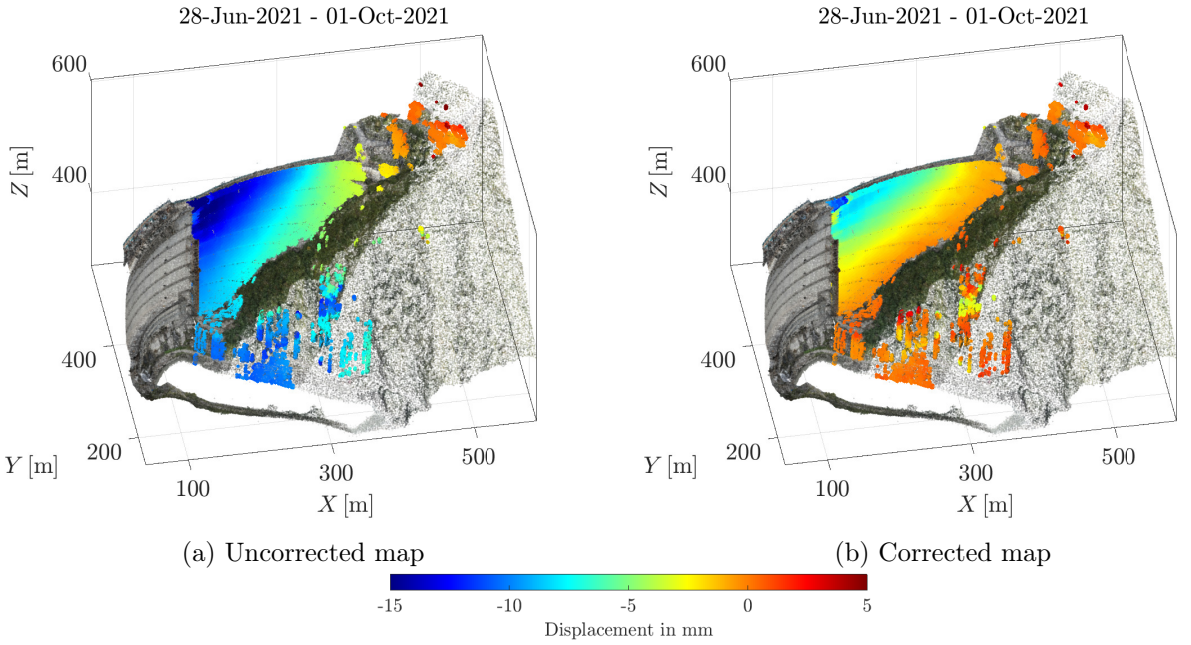

Figure 6.10: Correction of the atmospheric and repositioning spatial signal at *Pavel 2* station. (a) uncorrected displacement map - (b) corrected displacement map.

In the case of an epoch-wise measurement, the temporal sparsity of the measurements hinders the use of atmospheric correction methods that rely on the temporal behaviour of the atmospheric signal, and only its spatial behaviour can be used. Several spatial models are presented in Section 2.6.3 and can be used jointly with the model of the repositioning error, which is presented in Equation 2.23. However, these models assume they can be fitted in a non-negligible part of the interferogram,

where no deformation occurs. For instance, in [Caduff et al., 2013], the moving areas are masked from the interferograms by a visual inspection, and the atmospheric phase is estimated using a low-pass filter. In the case of observing large infrastructures, the nearby stable areas represent a much lower percentage of the scenario. For example, the number of PSC that are not on the dam for our three campaign stations represent 9% for *Pavel 2*, 7% for *Georges* and 0% for *Pavel 1*.

Moreover, no meteorological sensors have been installed, and the only way to correct the disturbing signal is to fit the polynomial model and analyse the consistency of the results. We apply the weighted least squares (WLS) estimator to fit the coefficients of the following model between campaign p and q. The observation vector is composed by the unwrapped interferometric phase between epochs p and q for each point k: $\psi(k) = \mathcal{U}(\varphi_p(k) - \varphi_q(k))$. Then, the spatial model equation for this point is given by:

$$\psi_{\text{spa}}(k) = \underbrace{C_0 + C_1 r(k) + C_2 r(k) Z(k)}_{\text{Atmospheric signal}} + \underbrace{C_3 \frac{X(k)}{r(k)} + C_4 \frac{Y(k)}{r(k)} + C_5 \frac{Z(k)}{r(k)}}_{\text{Repositioning error}} \tag{6.12}$$

Each observation point's weight $w(k)$ is determined by considering the individual phase noise contributions and applying error propagation principles. Referring to Equation 6.6, the weight for each point k is computed as follows:

$$w(k) = \left(\sigma^2_\varphi(k,p) + \sigma^2_\varphi(k,q)\right)^{-1} \tag{6.13}$$

Assuming that the observations are not correlated, the weight matrix is set as diagonal. Similarly to what is proposed by [Iglesias et al., 2013] in Equation 2.41 for the ordinary least squares (OLS) estimator, the error variance of the fit $\hat{s}^2$ is computed for the first WLS estimation. All points verifying $\sqrt{w(k)}|\hat{\psi}_{\text{spa}}(k) - \psi(k)| > 2\hat{s}$ are discarded for the second fit to remove strong outliers such as unwrapping errors.

In Figure 6.10, the impact of the atmospheric correction is visualised at the *Pavel 2* station between the first and the second epoch. Despite the challenges posed by the similarity between the spatial wavelength of the atmospheric pattern and the deformation of the dam, an intriguing observation emerges when focusing on the embankment of the dam in Figure 6.10a. A distinct signal ramp characterised by a change in phase w.r.t. the points' elevation is visible.

After applying the proposed correction technique, as depicted in Figure 6.10b, the previously observed phase ramp is significantly reduced on the surrounding rocks. The correction quality, as indicated by the two-step WLS standard deviation error, achieves a precision of approximately 0.6 mm. To underscore the quality of the correction, Figure 6.11 showcases the relationship between the unwrapped phase of the PSC and their corresponding elevations. As the correction process does not estimate a dependency coefficient solely based on elevation Z, it serves as a valuable validation check for the elimination of the observed ramp. The initial signal exhibits a linear dependency on elevation with a coefficient of 0.0411 mm/m, which is considerably reduced to a negligible value of 0.0002 mm/m in the corrected signal at *Pavel 2*. At *Georges* station, a small ramp remains and can impact more significantly the corrected signal during the extrapolation of the model.

To evaluate the quality of the correction, the slope in elevation is summarised for *Pavel 2* and *Georges* stations for all interferograms in Table 6.3. The averaged slope is considerably reduced by a factor 20, comforting the necessity of this correction.

	Slope in $[\mu m/m]$ - Interferograms between Epochs:										
Station	1-2	1-3	1-4	1-5	2-3	2-4	2-5	3-4	3-5	4-5	**Mean**
Pavel 2 b.c.	41.1	45.5	50.4	67.1	4.3	9.1	25.4	6.2	22.9	16.9	**28.9**
Pavel 2 a.c.	0.2	0.9	-0.6	-0.1	1.1	-0.5	0.2	-1.3	0.2	2.7	**0.8**
Georges b.c.	57.8	-	61.4	49.8	-	45.9	-6.7	-	-	-48.7	**45.5**
Georges a.c.	3.2	-	-0.1	-1.5	-	-2.8	-3.3	-	-	4.8	**2.6**

Table 6.3: Slope of phase w.r.t. the elevation of points before and after the correction. b.c. is for before correction and a.c. stands for after correction. The mean considers the absolute values of the signal amplitude.

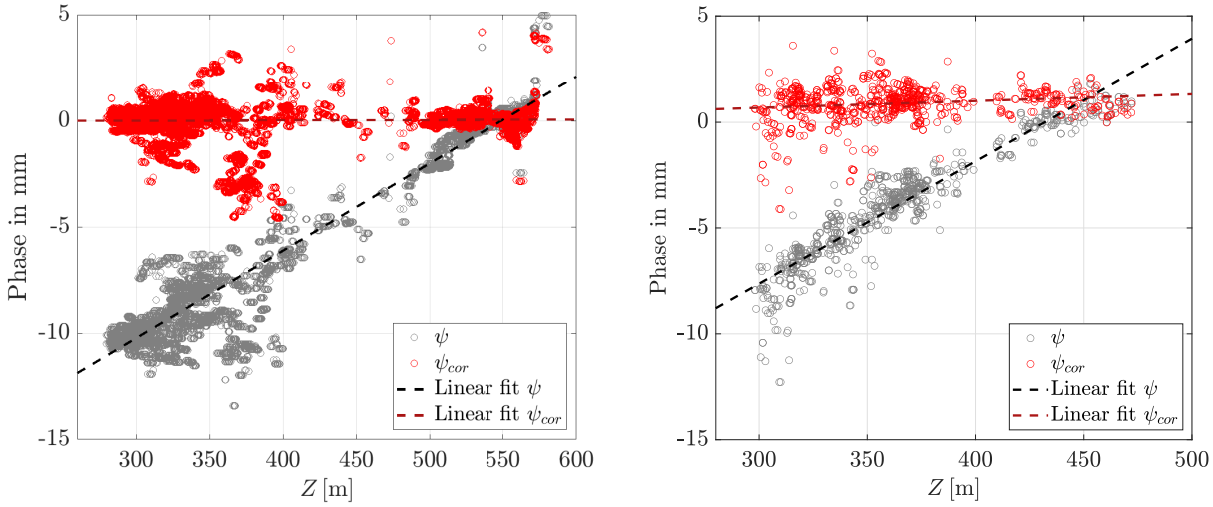

(a) *Pavel 2* (b) *Georges*

Figure 6.11: Dependency between the observed phase on the embankments and the PS point elevation between Epoch 1 and 2.

Moreover, to assess the consistency of the estimated signals, all the possible closed loops of interferograms between the epochs are computed. In an ideal scenario, all the offset values should be equal to zero, indicating consistent results between all interferograms. However, various factors such as filtering, unwrapping failures, and spatial signal corrections can introduce deviations from this ideal behaviour. Figure 6.12 illustrates the distribution of offsets for both *Pavel 2* and *Georges* stations. In the absence of corrections, the minor variations observed in both stations are attributed to the filtering step and are not relevant. Notably, there are no prominent peaks around ± 8.7 mm, corresponding to a phase of 2π, which indicates successful phase unwrapping. After the correction at the *Pavel 2* station, the spread of the histogram is slightly larger, still reaching a standard deviation smaller than 1 mm. The results are more spread for *Georges* station, and the standard deviation reaches 4.2 mm. This can be due to the position of the dam w.r.t. the reference area, which needs a stronger model extrapolation. Still, the detected offsets remain acceptable compared to the several centimetres of the dam's movement.

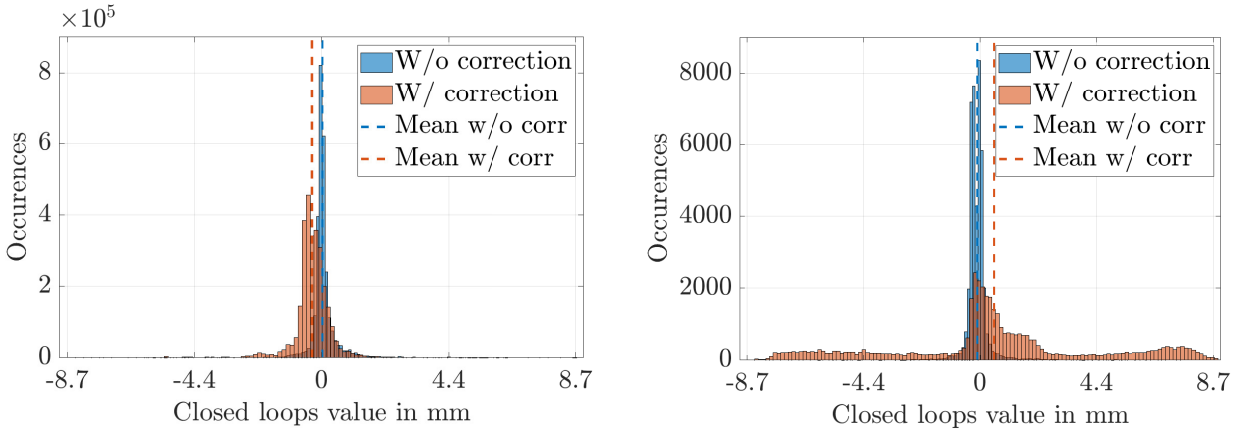

(a) *Pavel 2* (b) *Georges*

Figure 6.12: Histogram of closed-loop residues with and without spatial signal correction at (a) *Pavel 2* and (b) *Georges* station.

6.2.5 Station fusion

The correction of spatial signal distortions poses an additional challenge for the *Pavel 1* station, where no reliable points can be extracted from surrounding stable points. A solution leverages the presence of the two viewing angles available at *Pavel* stations, with an overlap in their respective fields of view, as presented in Chapter 3. Although these stations do not offer complementary observations in terms of LOS, they can be used for mutual correction. Indeed, the overlapping points describe the same LOS displacement vector for both stations, such that the phase term corresponding to the deformation $\boldsymbol{\psi}_{\text{defo}}$ is the same. Therefore, the corrected data obtained from *Pavel 2* station can be applied to correct the data from *Pavel 1* station. In the acquisition configuration proposed in this work, the data are not acquired simultaneously, and a minimum temporal baseline necessarily separates the acquisitions between *Pavel 1* and *Pavel 2*. However, the dam is assumed to move very slowly, such that the displacement possibly occurring is neglected. The technique presented in this section is only required in the case of a linear GB-SAR, which has a limited field of view. This limitation does not affect other TRI systems based on rotating antennas.

With general notations, the two sets of geocoded PSC are denoted with $\mathcal{P}_1$ and $\mathcal{P}_2$ for the two stations and with $\boldsymbol{\psi}_1$ and $\boldsymbol{\psi}_2$ for the corresponding unwrapped phase values of a specific interferogram. Assuming that $\boldsymbol{\psi}_2$ has been corrected for atmospheric and repositioning effects, resulting in $\boldsymbol{\psi}_{\text{cor},2}$ containing only the deformation component ($\boldsymbol{\psi}_{\text{cor},2} = \boldsymbol{\psi}_{\text{defo}}$), the common observed points $\mathcal{P} = \mathcal{P}_1 \cap \mathcal{P}_2$ can be used for calibration purposes, such that:

$$\boldsymbol{\psi}_1(\mathcal{P}) = \boldsymbol{\psi}_{\text{defo}}(\mathcal{P}) + \boldsymbol{\psi}_{\text{spa},1}(\mathcal{P}) \qquad \Leftrightarrow \qquad \boldsymbol{\psi}_{\text{spa},1}(\mathcal{P}) = \boldsymbol{\psi}_1(\mathcal{P}) - \boldsymbol{\psi}_{\text{cor},2}(\mathcal{P}) \tag{6.14}$$

The correction can be straightforwardly applied for the points in the set $\mathcal{P}$. However, each interferogram needs to be corrected for the whole set of points $\mathcal{P}_1$. In this sense, the correction model according to Equation 6.12 is used to fit the vector data $\boldsymbol{\psi}_1(\mathcal{P}) - \boldsymbol{\psi}_{\text{cor},2}(\mathcal{P})$ enabling the correction of the interferogram for the first station.

When a substantial overlap exists between the fields of view of the two stations, it is feasible to apply the correction model outlined in Equation 6.12, which encompasses all the possible distortions. However, since the model's parameters are determined based solely on the common area shared by

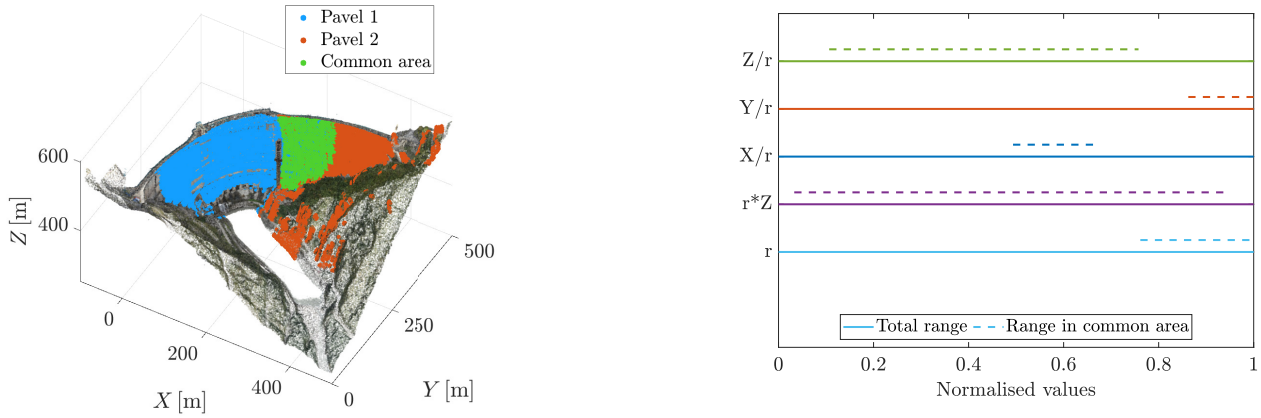

(a) PS points on the two stations

(b) Parameters range

Figure 6.13: (a) Visible PS points from the two *Pavel* stations and (b) distribution of the parameters for the correction model estimation.

both stations, it is crucial to assess the sensitivity of each component of the model when extrapolated to the entire area covered by the first station.

Figure 6.13a provides a visualisation of the distribution of the PS points for both *Pavel* stations. The correction model from the *Pavel 2* station is applied using the surrounding rocks. However, the green area, representing the visible points from both stations, is considerably limited for the *Pavel 1* station. While this area spans almost the entire elevation range, its limited coverage suggests potential insufficiency in correcting specific model parameters.

In order to assess the suitability of extrapolating the parameters of the correction model, Figure 6.13b offers a visual representation of the normalised ranges of the coefficients within the correction model. The dashed lines in the figure correspond to the parts lying in the common area for the corresponding parameters. A significant range of values is covered for height-dependant coefficients, such as rZ or Z/r, indicating that extrapolation to the rest of the model is feasible. Specifically, coefficients C_0, C_2, and C_5 from Equation 6.12 can be well estimated. These coefficients correspond to a constant offset, e.g. due to a difference in the reference phase, height-dependent atmospheric effects and changes in the sensor's height, respectively. Furthermore, even if its distribution is not optimal, coefficient C_1, accounting for range-dependent atmospheric signals, can not be rejected, as it is a key contributor to atmospheric disturbances. Coefficients C_3 and C_4 are dropped.

The results before and after the proposed station combination are presented in Figure 6.14a. The resulting deformation pattern exhibits a smooth gradient. In contrast, the uncorrected version displayed in Figure 6.14b demonstrates two prominent issues. Firstly, there is a noticeable aliasing effect between the two stations, which can be attributed to differences in reference points. Furthermore, the signal features a global phase ramp in the range direction that is challenging to explain from a mechanical perspective. Atmospheric disturbances predominantly induce this ramp.

The developed methodology enables the recovery of displacement values from GB-SAR epoch-wise data, even in very complex scenarios. The output of the processing chain provides plausible results but must be compared and validated through another source of information.

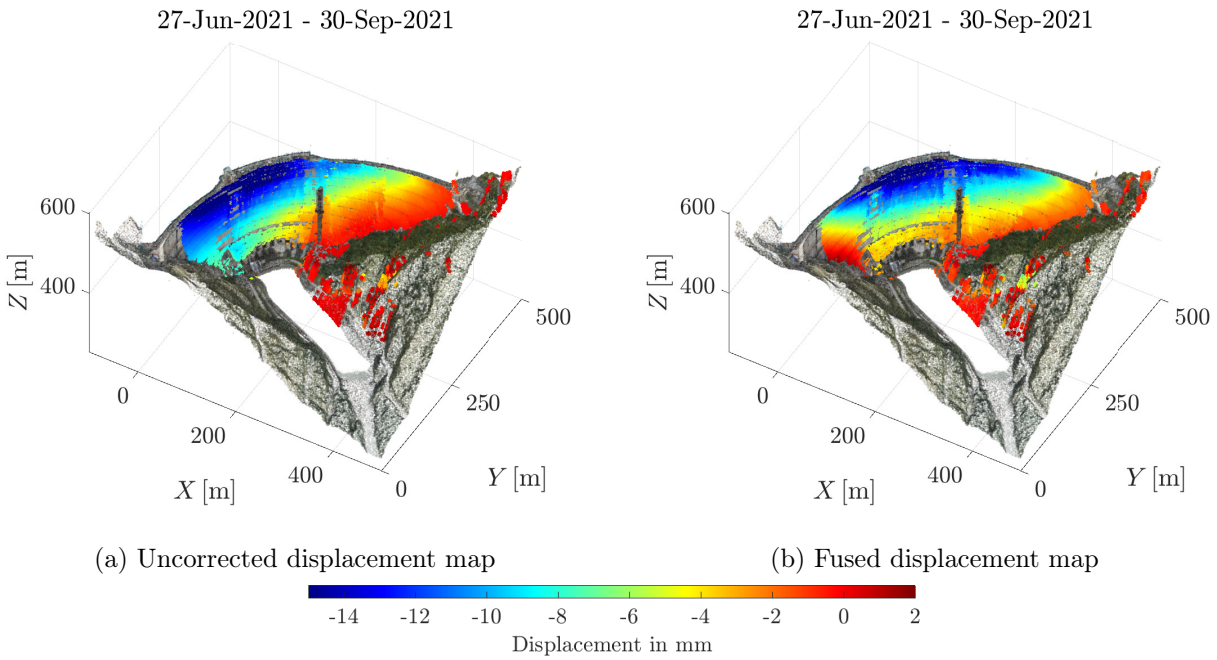

(a) Uncorrected displacement map (b) Fused displacement map

Figure 6.14: Fusion between the two *Pavel* stations between epoch 1 and 2. (a) is before and (b) is after the proposed correction.

6.3 Comparison with numerical models

To quantitatively assess the results obtained with the GB-SAR, a comparison is conducted between the final displacement maps and two numerical simulations. The company *Artelia* computed the models by calibrating a physical deformation model using plumbline data collected between 2001 and 2019 [Rebmeister et al., 2023]. Although the acquisition period of the data used to calibrate the numerical model does not directly match that of the GB-SAR data, the model provides insights into the physical properties of the material under study, which can be treated as constant. The first model is computed for a specific water level change, spanning from 492.7 m to 453.0 m, which aligns with the water level change between the first and fourth epochs of the GB-SAR monitoring. The second model is computed for a smaller water level change, i.e. spanning from 492.7 m to 482.0 m, which aligns with the water level change observed between the first and second epochs, as summarised in Table 3.1.

For both models, four main physical interactions are considered according to the presentation in Chapter 3 and especially Figure 3.2: the dam's weight, the hydrostatic pressure, the uplift pressure and the thermal effect. The latter is considered by computing a daily average of the temperature observed between 2001 and 2019 for each day.

The comparison between the numerical models and the GB-SAR results requires some preprocessing. Firstly, the resolution of the GB-SAR is downscaled to the one of the numerical models, which is a grid of approximately 10 m applied on the dam. The 3D displacement vector is available for each point of the numerical model. To compare the data with the GB-SAR observations, the displacement vectors are projected onto the LOS direction and only the magnitudes are compared. This comparison is carried out for both campaign stations *Georges* and the fused results of *Pavel*. The comparison between the models and the *Georges* station also contains an analysis of four different correction models for the GB-SAR data. As the data coming from the *Pavel* station are much more

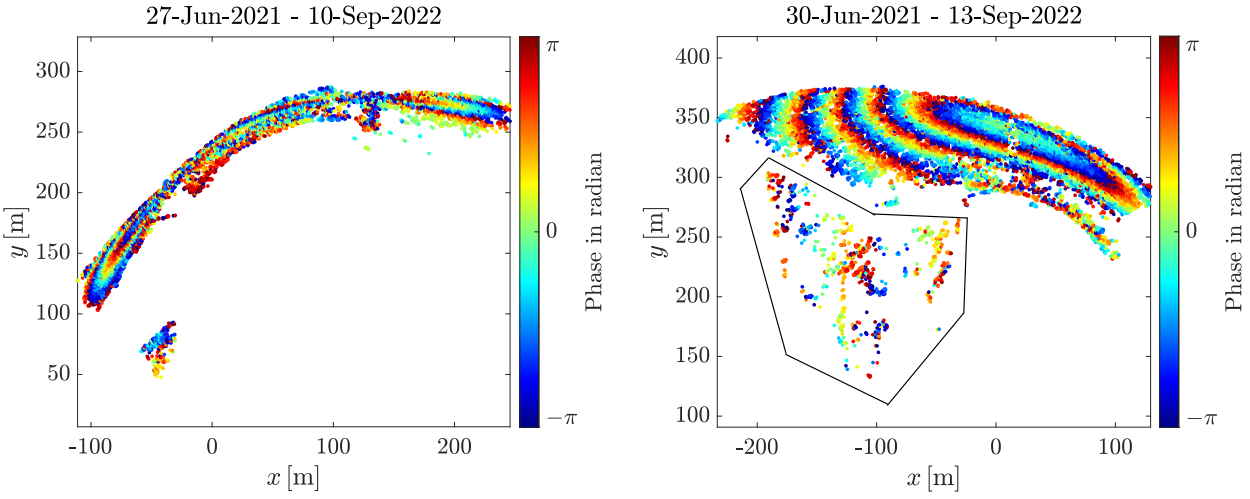

(a) *Pavel 1* (b) *Georges*

Figure 6.15: Raw interferograms at stations (a) *Pavel 1* and (b) *Georges* between Epoch 1 and 4. For the *Georges* station, the area in the black patch is used for the signal correction.

restrictive due to the station fusion, this analysis is less meaningful, and therefore, the study is solely done for the *Georges* case.

The raw interferograms on the SAR geometry for the first case study are presented in Figure 6.15. The interpretation of the signal is relatively straightforward for the *Georges* station. However, for the *Pavel 1* station, the interferogram is only comprehensible on the sides of the observed part of the dam.

6.3.1 *Georges* station - Numerical model 1

For the *Georges* station, 10 998 PS are identified, from which 776 are not located on the dam and could be used for correcting the atmospheric and repositioning errors. Four spatial models are applied to the unwrapped interferogram to gain deeper insights into the significance of choosing an appropriate correction mode. Their results are compared against the numerical model:

- M_1: The displacement map is not corrected.
- M_2: The model used in Equation 2.40 is applied to correct the atmospheric phase.
- M_3: The model used in Equation 2.23 is applied to correct the repositioning phase.
- M_4: The model used in Equation 6.12 is applied to correct both signals.

The histograms depicting the differences $\mathbf{\Delta d} = \mathbf{d}_{\text{GB-SAR}} - \mathbf{d}_{\text{NM}}$ and relative differences $\mathbf{\Delta d}_r = (\mathbf{d}_{\text{GB-SAR}} - \mathbf{d}_{\text{NM}})/|\mathbf{d}_{\text{NM}}|$ between the numerical model and each GB-SAR displacement map are shown in Figure 6.16. As the considered displacements are mainly negatives, the negative elements of $\mathbf{\Delta d}$ correspond to an overestimation by the GB-SAR. The key quantities of these histograms are summarised in Table 6.4. Focusing on the absolute differences with Figure 6.16a, the correction model with the smallest variance is M_1. It can be explained by the fact that all correction models

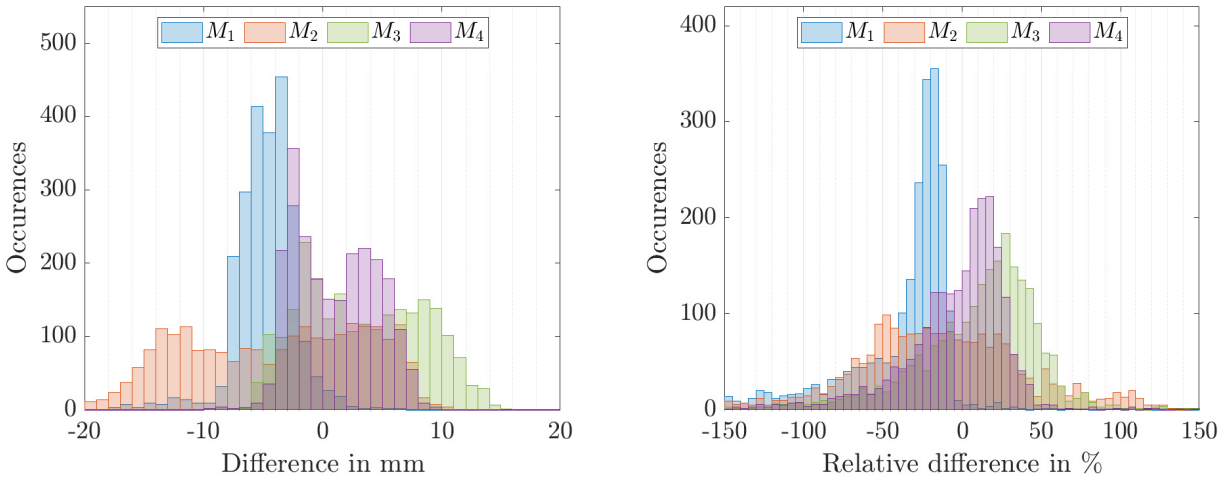

(a) Absolute difference (b) Relative difference

Figure 6.16: Histograms of differences between GB-SAR results and the numerical model for the four correction models used.

are applied on the surrounding rocks and extrapolated for the dam, which can lead to imprecision by increasing the distance to them. The analysis reveals that the models M_2 and M_3 do not yield any improvement and worsen the results. Although the standard deviation of the error using M_4 is slightly larger than that of M_1, the mean error significantly decreases from -4.78 mm to -1.01 mm, thus considerably enhancing the accuracy. A closer look at the relative error in Figure 6.16b underlines the improvement made by using model M_4. The distribution is centred with a smaller 95% confidence interval (CI), while the model M_1 considerably overestimates the deformation at the dam. The comparison between M_2 and M_4 exhibits that the correction of exclusively the atmospheric signal is insufficient, even if the GB-SAR is installed on concrete foundations with fixed screws.

	M_1	M_2	M_3	M_4
$\mathbb{E}(\mathbf{\Delta d})$ [mm]	-4.75	-3.92	3.26	1.01
$\sigma_{\mathbf{\Delta d}}$ [mm]	2.54	7.42	5.06	3.40
med$(\mathbf{\Delta d}_r)$ [%]	-62	-104	-12	-2
$\text{CI}_{95}(\mathbf{\Delta d}_r)$ [%]	[-160 ;-9]	[-257 ;81]	[-98 ;60]	[-83 ;40]

Table 6.4: Statistics of the difference between the first numerical model and the GB-SAR results. CI_{95} stands for the confidence interval containing 95% of the relative differences.

Figure 6.17 provides the spatial comparison between the GB-SAR displacement maps and the numerical model. Figure 6.17a is the visible part of the numerical model from the station and the corresponding displacement projected onto the LOS for each point. Figure 6.17b showcases the processed displacement without any correction (M_1). Due to the prominent similarities between the two patterns, it can be assessed that the deformation of the dam induces the primary signal in the measured map. However, the amplitude at the centre is larger, and the bottom part of the dam exhibits considerably greater displacement than in the model. Therefore, a phase ramp in elevation is mixed with the deformation signal, leading to the overestimation. The resulting map after correction is depicted in Figure 6.17c, and its higher correspondence with the model presented

in the histograms is confirmed. The absolute relative error is represented in Figure 6.17d. Across the majority of the dam, it remains under 25%. The absolute relative error increases as the distance to the rock decreases. This observation arises from the minimal movements observed and modelled in this region, implying that even a small absolute error can substantially impact the relative one. The overall comparison is satisfactory and underscores the reliability of the GB-SAR measurements and the developed workflow for the data processing.

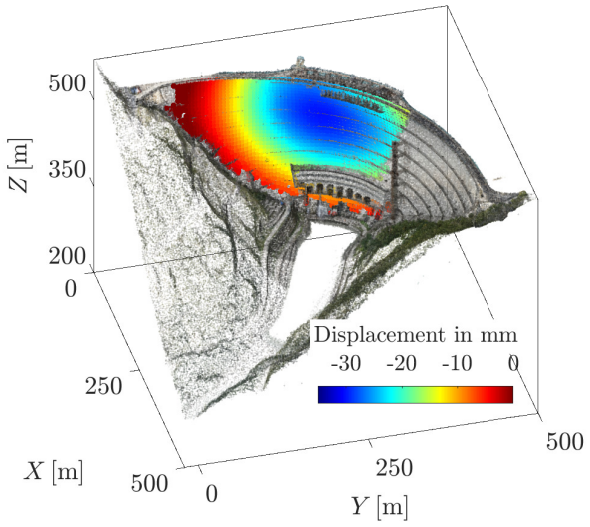

(a) Numerical Model 1

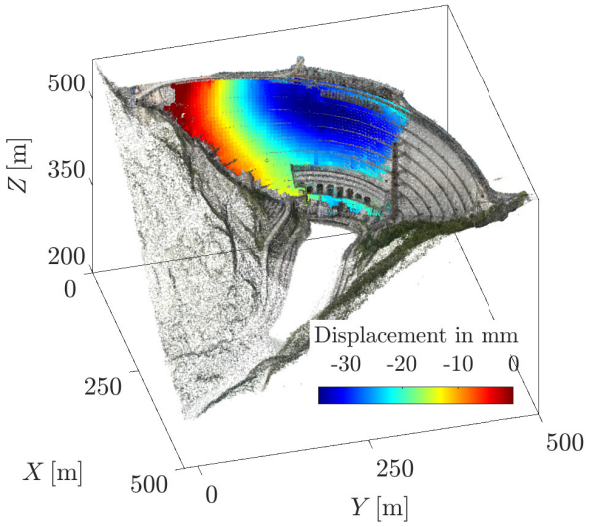

(b) Displacement map from M_1

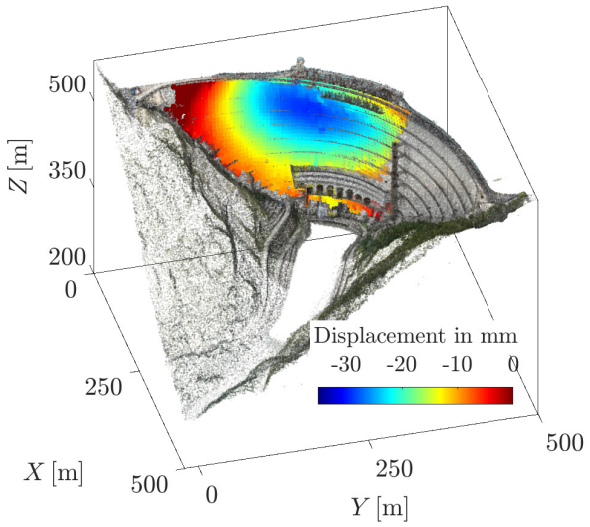

(c) Displacement map from M_4

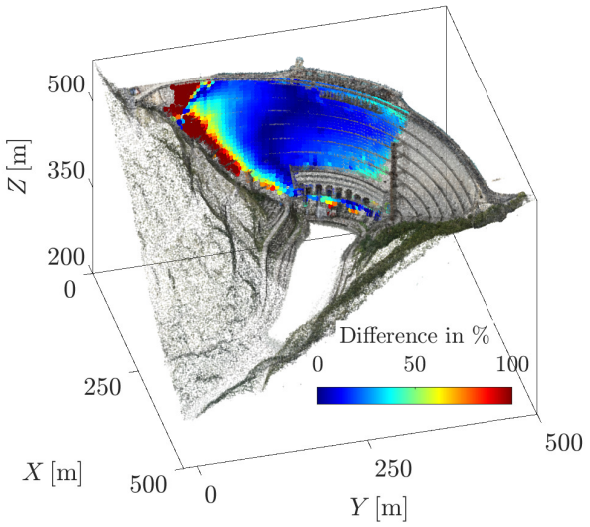

(d) Absolute relative difference $\mathrm{NM}_1 - M_4$

Figure 6.17: Spatial representation of the comparison between the first numerical model and the results of the GB-SAR processing from *Georges* station.

6.3.2 *Pavel* station - Numerical model 1

As developed in this chapter, the *Pavel* station is much more challenging for the processing. With the station fusion and the reduced resolution once the information is geocoded, its observation capacity is limited. Therefore, it can not be expected to recover as reliable results from this station as for the *Georges* station. The comparison with the numerical model provides an estimate of the achievable accuracy. It allows insights into the quality of the results for the GB-SAR, even in very complex and unsuited scenarios.

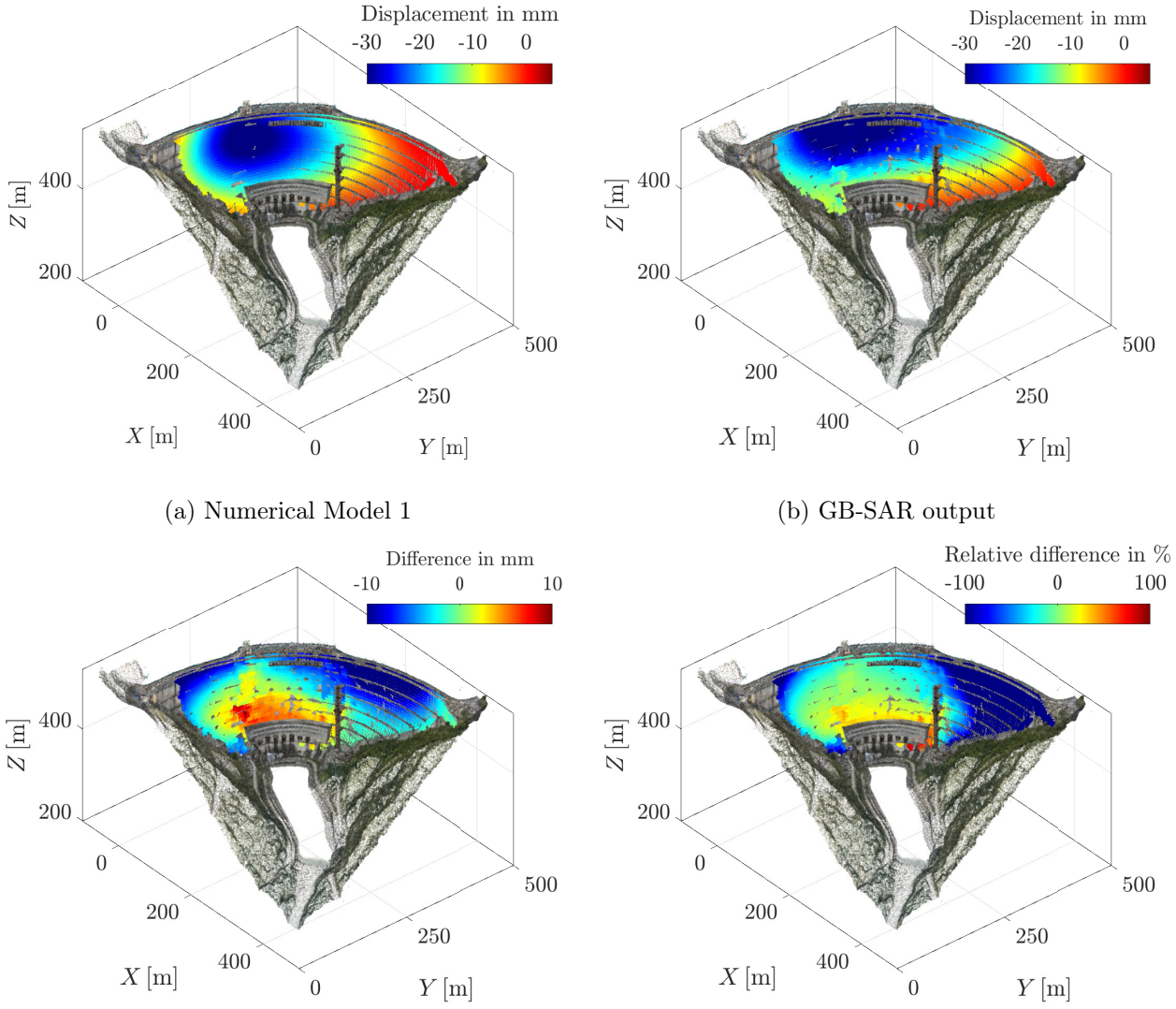

(a) Numerical Model 1

(b) GB-SAR output

(c) Difference

(d) Relative difference

Figure 6.18: Spatial representation of the comparison between the first numerical model and the results at *Pavel* station.

The first comparison between the model in Figure 6.18a and the processed displacement map from the GB-SAR in Figure 6.18b exhibits a different pattern. The model expresses almost concentric circles, while the GB-SAR results are more similar to concentric ellipses. This difference might suggest a part of the signal in the GB-SAR displacement map coming from elevation correlated

signal interpretable as remaining atmospheric changes. The middle of the dam undergoes the very small resolution of the system in this configuration. Even with the proposed advanced unwrapping algorithm, a remaining small discontinuity is visible in the middle of the dam, visible as a red spot.

A non-negligible negative difference on the left part of the dam is visible in Figure 6.18c. Due to its proximity with the stable areas from *Pavel 2* and the "limited" foreshortening, this signal can be considered as a significant difference. The significance of this difference is also underlined in the relative difference map. On the junction dam-rock, the relative error is very large but only due to absolute displacements lower than 2 mm. Conversely, the centre of the dam structure maintains a relative absolute difference under 30 %.

Combined with the layover and foreshortening, the water level induces a too-strong signal, leading to difficulties for the phase unwrapping. This process leads to an impossible complete and reliable interpretation of the displacement map. The station *Pavel* is not optimal in terms of foreshortening and geometry, which prohibits a usage for too strong water level changes.

6.3.3 *Georges* station - Numerical model 2

The second comparison study at *Georges* station also considers the four correction models M_1 to M_4. It proposes the same statistical analysis on the differences $\mathbf{\Delta d}$ and relative differences $\mathbf{\Delta d}_r$ between the numerical model and the GB-SAR results.

	M_1	M_2	M_3	M_4
$\mathbb{E}(\mathbf{\Delta d})$ [mm]	-4.33	-2.84	-5.02	-0.27
$\sigma_{\mathbf{\Delta d}}$ [mm]	2.57	4.38	4.22	2.11
$\text{med}(\mathbf{\Delta d}_r)$ [%]	-98	-49	-95	3
$\text{CI}_{68}(\mathbf{\Delta d}_r)$ [%]	[-189 ; -51]	[-164 ; 83]	[-189 ; -44]	[-47 ; 51]

Table 6.5: Statistics of the difference between the second numerical model and the GB-SAR results at *Georges* station.

The results in Table 6.5 show that partial models M_2 and M_3 deteriorate the original GB-SAR measurements. However, the complete correction model considerably enhances the correspondence quality, reducing the mean offset and the standard deviation. In this case, both accuracy and precision are enhanced by the correction.

The spatial representation of the comparison is accessible thanks to Figure 6.19. The numerical model in Figure 6.19a presents a similar pattern as the one computed in the first case, with a downscaled amplitude. However, in this case, it is more perceptible that the top 20 m of the dam are less susceptible to displacement due to a higher material stiffness estimated according to the plumblines data. The uncorrected GB-SAR results in Figure 6.19b significantly differ from the model and are affected by a disturbance, mainly a horizontal ramp. Atmospheric and repositioning signals may exhibit a similar amplitude than in the first comparison, but their relative impact on the displacement is considerably higher. The corrected version with M_4 exposed in Figure 6.19c closely resembles the numerical model. The difference between both displacement maps is provided in Figure 6.19d. The pattern is approximately a phase ramp in elevation exhibiting differences between -2 mm and 4 mm. This ramp is almost linear, except for the crest which is affected by an abrupt considerable difference.

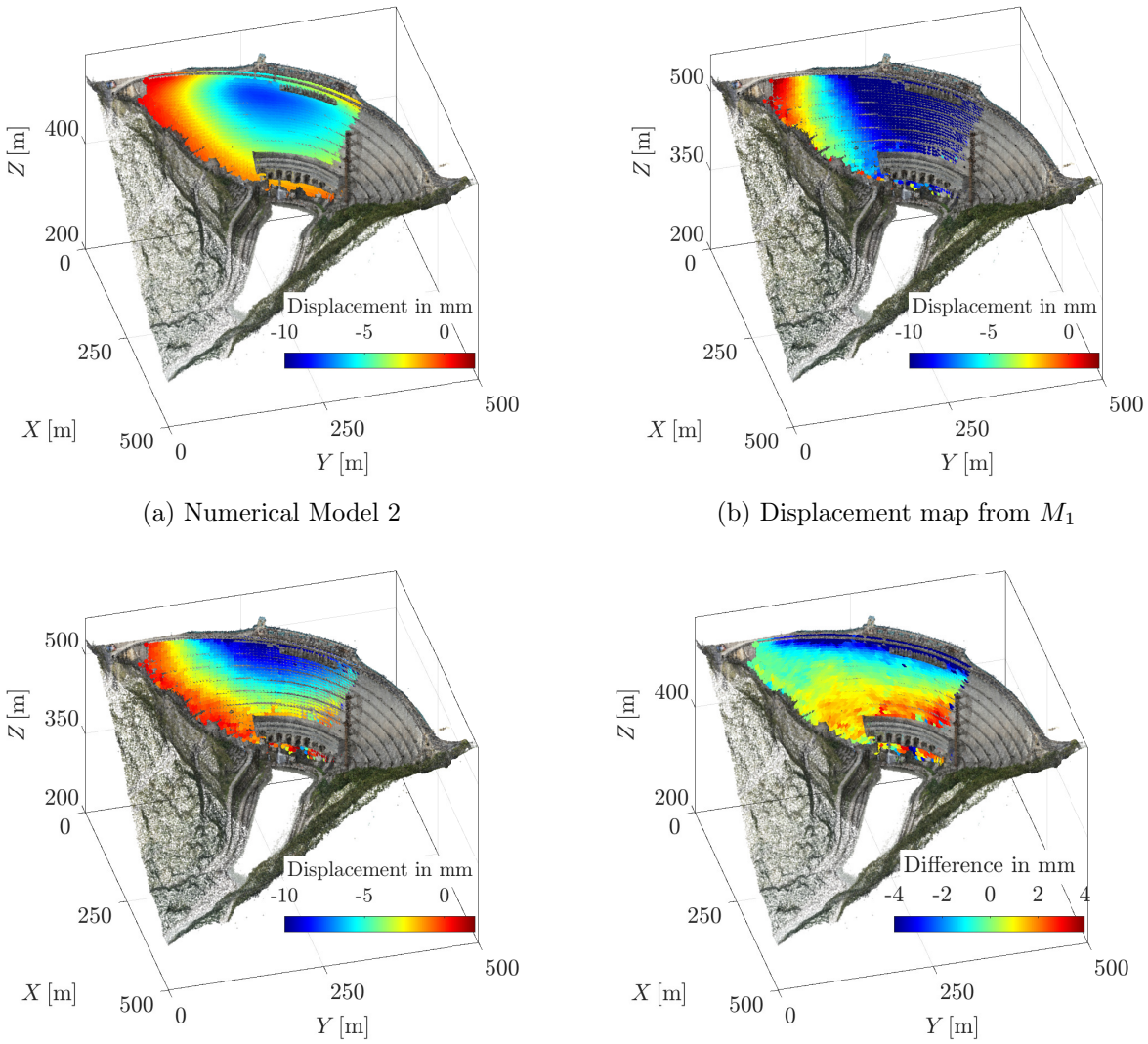

(a) Numerical Model 2

(b) Displacement map from M_1

(c) Displacement map from M_4

(d) Difference $\mathrm{NM}_2 - M_4$

Figure 6.19: Spatial representation of the comparison between the second numerical model and the results at *Georges* station.

6.3.4 *Pavel* station - Numerical model 2

The comparison of the numerical model and the results from the *Pavel* station is provided in Figure 6.20. For this case study, the spatial patterns of the model in Figure 6.20a and the GB-SAR results in Figure 6.20b are significantly different. The major difference is located on the top part of the dam, as pointed out by the difference and absolute relative difference maps in Figure 6.20c and 6.20d, respectively. The measured displacement is up to twice as large as the modelled displacement.

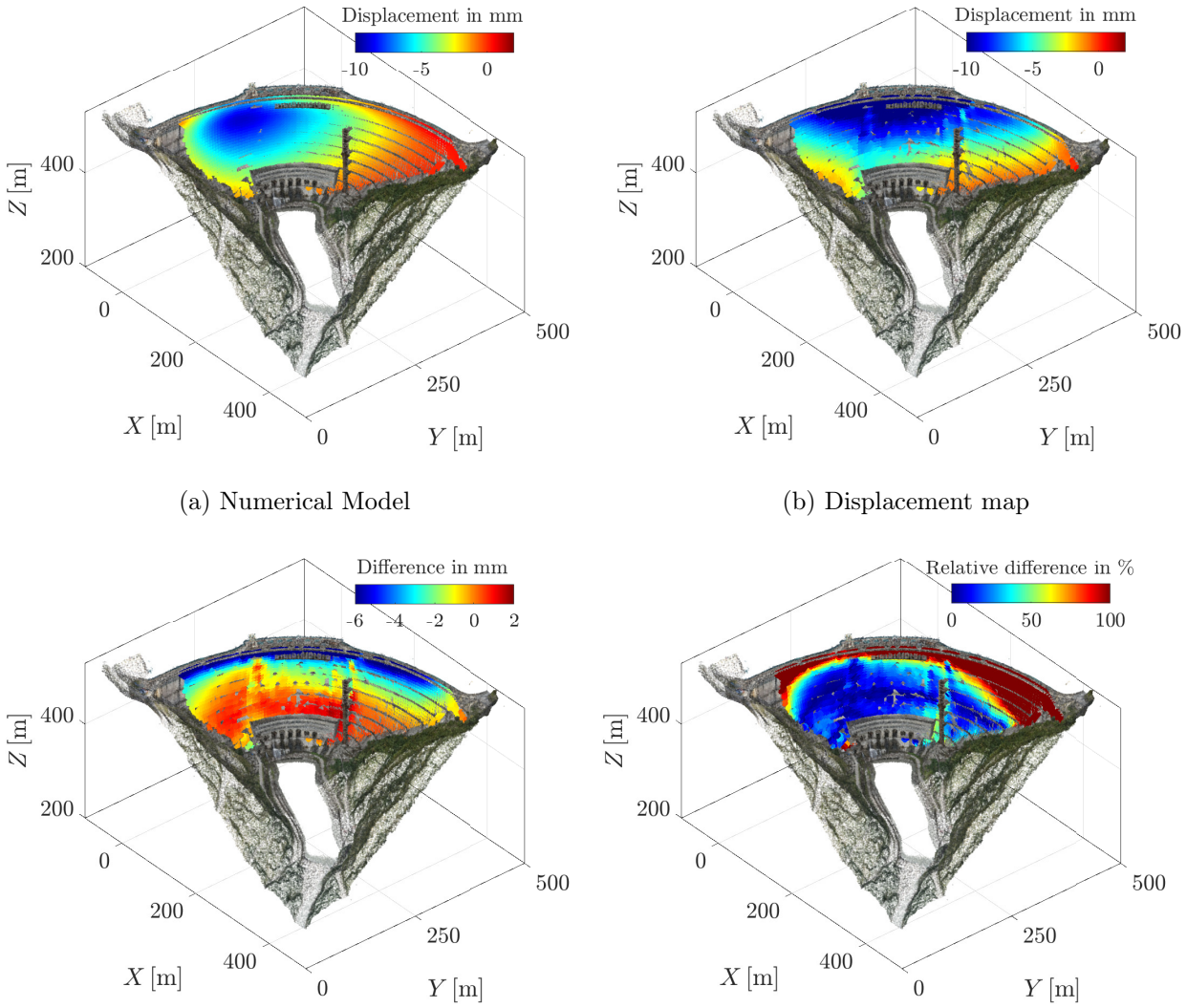

(a) Numerical Model

(b) Displacement map

(c) Difference map

(d) Absolute relative difference

Figure 6.20: Spatial representation of the comparison between the second numerical model and the results at *Pavel* station.

6.4 Discussion

The presented methodology based on the PCA extracts a plane from a 3D point cloud. The subsequent projection onto this plane for the unwrapping works well in the presented case because the Enguri Dam exhibits a geometry that is not far from a plane. If the geometry is strongly different, the method should be carefully applied. A possible way to apply it in any case, even on large scales is to process patch-wise. As an example, it would enable the application of this method for satellite SAR in mountainous areas.

The proposed comparison of the two stations effectively demonstrates a satisfactory accordance of the GB-SAR measurements with the first numerical model regarding displacement patterns and magnitude. The residual difference can have several reasons, but it should be kept in mind that the

numerical model can present some deviations from the measurements. The calibration of the model on the plumblines data present also differences which can be up to 35% of relative errors for this water level change [Rebmeister et al., 2023]. Considering this, the relative error observed between the model and the GB-SAR can not invalidate the results of the proposed processing.

The second comparison exhibits more substantial relative differences on the top of the dam. Indeed, the results of both stations provide a larger displacement of the dam crest. The consistency between both stations can indicate that it is an actual displacement. However, without further measurements, it is impossible to assess if this larger amplitude is due to a residual non-linear atmospheric signal or a real displacement.

For future work involving the monitoring of large dams or infrastructure, the choice of sensor location becomes crucial. The *Georges* station's lower and closer position relative to the dam minimises layover effects and simplifies the processing. On the other hand, the *Pavel* station's elevated position presented challenges, which were effectively addressed by the proposed methodologies. However, the high spatial resolution of the sensor is compromised once the information is projected onto the dam's surface. A solution is to use the developed P-RaySAR software to analyse the geometry of the SAR image before the installation of the sensor to avoid unpleasant surprises after the data acquisition.

6.5 Conclusion

This chapter deeply studied the Enguri Dam's monitoring based on GB-SAR epoch-wise measurements. A new workflow was developed to capitalise on the developments made in Chapters 3 and 4, considerably improving the phase unwrapping. The 3D point cloud of the PS is used to compute the optimal projection plane for the subsequent phase filtering and phase unwrapping. While this may not be adapted to all cases, the amount of information earned is significant for large vertical structures. The results presented in this chapter showed a significant improvement compared to the usual flowchart, and even the most complicated scenarios can be recovered. Without the proposed development, the treatment of the *Pavel* station does not provide meaningful results due to the incapacity to solve the problem in the SAR geometry.

The comparison with the numerical model presented a satisfying concordance with the GB-SAR results, making the system an interesting complement for epoch-wise monitoring. Its dense measurement surface gives a better understanding of the mechanisms behind the deformation. The comparison with the second numerical model presents a considerable difference between the GB-SAR measurements and the model. This finding is similar for both stations, so it is difficult to consider it an error. Further investigations on this topic are required to assess the reliability of the GB-SAR measurements. This may be the primary utilisation of a GB-SAR for epoch-wise infrastructure monitoring. The accuracy may not reach the given 0.1 mm because of different factors exposed in this chapter. However, it still can detect suspect anomalies, suggesting the installation of specific sensors for deeper investigations.

The results presented in this chapter, especially concerning the atmospheric disturbances and repositioning errors, support the installation of meteorological sensors and a stable and robust way to replace the GB-SAR between two campaigns with an accuracy higher than 1 mm. It would avoid any phase ramps that are difficult to estimate in case of large infrastructure monitoring. The quality and the accuracy of the GB-SAR can be fully exploited when support sensors are nearby to correct the observations.

In this chapter, the results of different stations for the monitoring of the Enguri Dam were presented.

As presented in Chapter 3, each station has a different sensitivity and field of view. If different GB-SAR monitor simultaneously the dam, the question of their optimal configuration would come naturally. Multiple instruments can be used for two main objectives: enhance the field of view and/or recover the 2D or 3D displacement vector for each common persistent scatterer. If the emphasis is made on the first objective, the stations should be placed on locations expressing high sensitivities with complementary orientations. Oppositely, if the displacement vector is the goal of the monitoring, the stations should have as much as possible orthogonal LOS vectors for the majority of the PS at the cost of a reduced sensitivity for each individual station. The different fields of view should overlap the same area as much as possible.

CHAPTER 7

Continuous geodetic deformation analysis

Contents

7.1 Introduction

The GB-SAR systems are mainly used for real-time monitoring and early warning in specific contexts, such as open-pit mines. The goal is to detect fast movements in an observed scenario and prevent geohazards. In the case of using the GB-SAR in a slow deformation context, additional challenges arise, such as handling the amount of data, the long-term stability, and the consistency of the observed time series. [Wieser et al., 2020] concluded that the GB-SAR models for predicting the uncertainty of the observed deformation are not sufficiently developed. Within this context, three primary sources of perturbations are identified: internal phase noise, atmospheric disturbances, and unwrapping errors. This chapter focuses on the post-processing of GB-SAR data and mitigating these aforementioned perturbations in continuous monitoring.

The chapter is organised in the following way. Firstly, the scene selection and the interferogram configuration are presented for further interferometric processing. Afterwards, several strategies are developed to reduce the influence of phase unwrapping error and lead to an accurate time series of the determined displacement. Thereafter, diverse tools for the time series analysis are presented, especially a continuous smooth time series estimation using functional data analysis (FDA). These parts correspond to the development of the methodology and are followed by two evaluations. Firstly, the integrated time series are compared to the numerical model. Secondly, the results of the GNSS processing of four antennas installed on the dam crest are compared to the GB-SAR time series. The last section, developing the near real-time monitoring concept, closes the chapter.

7.2 Preprocessing

7.2.1 Coarse pixel selection

The first step of the preprocessing is to considerably reduce the number of pixels stored, which is mandatory to reduce the amount of data. Indeed, taking the IBIS-FM parameters as an example, a monitoring of one year consists of a dataset of 250 000 acquisitions. Considering a mean size of 4 Mb per scene, the data stack weights approximately 1 Tb. Only a small part of the pixels contains persistent scatterers with exploitable information. To considerably reduce the processing time and ease the memory management, a data reduction is carried out based on the first 30 scenes. With these first acquisitions, the pixels of good quality are selected using two criteria. The first one is the same as the previous chapter; the points need to verify $\gamma > 0.6$. The second criterion is the amplitude dispersion D_A presented in Equation 2.37, and all the points with $D_A < 0.42$ are selected. The N_{PSC} pixels considered after this step are called PSC.

After this first coarse pixel selection, the position of the instrument is corrected according to the development made in Chapter 4, and the geocoding of the PSC is conducted according to the methods presented in Chapter 5.

7.2.2 Deletion of corrupted scenes

The second step with such many scenes is to delete any potentially corrupted or excessively noisy SLC images. Such images could significantly impact the processing procedure, particularly during phase unwrapping. To address this, a moving temporal window with a given size W, typically five days, is applied to compute the mean of the amplitude in this window. Taking this in consideration, the amplitude ratio $A_R(n)$ for the scene n is given by:

$$A_R(n) = \frac{W \sum_{k=1}^{N_{\mathrm{PSC}}} A(k,n)}{\sum_{p \in W} \sum_{k=1}^{N_{\mathrm{PSC}}} A(k,p)} \tag{7.1}$$

with $A(k,p)$ the amplitude of point k for the scene p. We also consider the noise in the phase, estimated with the circular variance $V(n)$ on sequential interferograms, computed via Equation 6.3. A scene n is discarded of the process if $A_R(n) < 0.7$ or $V(n) > 0.16$.

7.2.3 Optimal interferogram formation

The last part of the preprocessing is to determine an adequate balance for the temporal sampling rate. When monitoring slow deformations, processing data acquired every two minutes may be unnecessary. There is an increased risk of encountering unwrapping failures or periods of high noise due to atmospheric disturbances as the number of observations increases. Based on the findings of [Rödelsperger, 2011], only the data acquired during the night are considered. This choice is motivated by the fact that the amplitude dispersion tends to be lower during nighttime, meaning that the phase noise is lower as well. This behaviour is linked to more stable atmospheric conditions, as suggested by [Luzi et al., 2004].

For each day, we select only the scenes between 1 a.m. and 6 a.m. as a starting point for our further analysis. Then, to reduce the noise, the same strategy as the previous chapter is used, considering each day as an epoch. A running window of two hours to compute the mean amplitude dispersion is applied, and its minimum value corresponds to the scenes with the highest SNR. This step is represented in the grey dashed window in Figure 7.1 and also enables to coarsely estimate the phase noise σ_φ for each averaged scene and each point, as detailed in Equation 6.6.

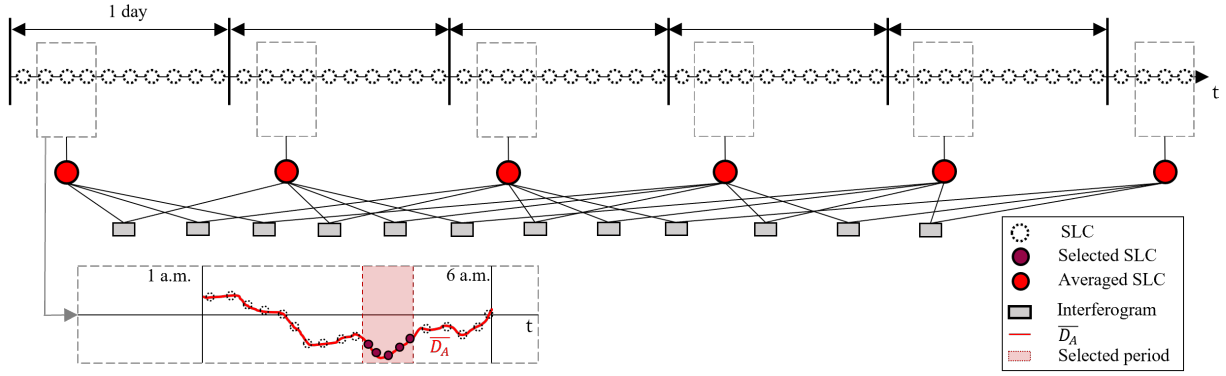

Figure 7.1: Optimal interferogram formation concept for continuous monitoring. The grey dashed box emphasises the selection process for each day. Then, in the whole acquisition line, the interferograms are computed using the red circles to obtain a network of interferograms represented by the grey boxes. A configuration connecting the three preceding and three succeeding scenes is represented. The temporal samplings are not consistent between the visualisations for perception considerations.

The interferograms are generated using the classical SBAS configuration to conclude the preprocessing. The main reason compared to a single master solution used for the PSI is that the interferograms are much easier to unwrap spatially, especially in the case of infrastructure monitoring, where the geometry can be complex. In our proposed configuration, each scene is linked to the four subsequent

and preceding scenes. This configuration balances between maintaining network redundancy and preserving the signal within the interferograms to be too intricate.

7.3 Phase unwrapping strategy

The phase unwrapping is a notably complex aspect of InSAR processing. Despite having a high temporal sampling rate of two minutes[1], instances of unwrapping failures can occur, as highlighted in [Wang, 2019]. The objective of ensuring a stable and consistent time series over extended periods further compounds the challenge. This constraint limits the available options for filtering or preprocessing strategies to mitigate disruptive signals. The following section aims to enhance the robustness of the phase unwrapping process.

7.3.1 Signal decomposition

The signal processing begins with the application of the Goldstein filter [Goldstein and Werner, 1998] to each interferogram. This procedure decomposes each point in an interferogram into two components: the smooth phase, denoted as ϕ_f, and the noisier complementary component, designated as ϕ_c. Their decomposition using either their respective whole complex number z or their phase representation ϕ is given by:

$$z_c = z z_f^* \qquad \Leftrightarrow \qquad \phi = \mathcal{W}\left(\phi_f + \phi_c\right) \tag{7.2}$$

Another step is added to the filtered phase to reduce the percentage of unwrapping errors. As studied in Chapter 2, the atmospheric signal can be modelled as a linear function of the range in a first order. Moreover, in SBAS interferograms for slow deformation analysis, this atmospheric signal is expected to have the largest amplitude. Removing this signal diminishes the complexity of the wrapped interferogram, thereby simplifying the subsequent unwrapping process. This step has not been implemented on the epoch-wise measurements because the atmospheric signal is not dominating in a scenario with very long baselines, short distances and moving infrastructures, meaning that the estimation is irrelevant.

As this step is applied before the phase unwrapping, the signal must be estimated in the complex domain. A strategy presented in [Yang et al., 2020] is based on phase differences of range bins. We propose an alternative approach based on the orthogonal matching pursuit (OMP) as it is a fast and reliable algorithm to estimate linear signal on wrapped data. For a single interferogram containing N_{PSC} points, the phase observations are arranged in the vector $\boldsymbol{\phi_f}$. The corresponding range values of the observed points are put in the vector $\mathbf{r}$. We search the coefficient α_r to estimate the range dependant part of the signal $\boldsymbol{\phi_r}$ described by:

$$\boldsymbol{\phi_r} = \mathcal{W}(\alpha_r \mathbf{r}) \tag{7.3}$$

The OMP searches to maximise the coherence of the estimated signal, i.e.:

$$\alpha_r = \underset{\alpha}{\operatorname{argmax}} \left(\frac{1}{N_{\mathrm{PSC}}} \sum_{k=1}^{N_{\mathrm{PSC}}} \left(\phi_f(k) - \phi_r(k)\right) \right) \tag{7.4}$$

[1]Similar linear GB-SAR sensors can have higher sampling rates, up to 10 seconds, e.g. the sensor described in [Rödelsperger et al., 2012].

To solve the task, the matrix $\mathbf{L} = [\boldsymbol{l_1} \dots \boldsymbol{l_p}]$ is created, with:

$$\boldsymbol{l_k} = \exp(i\alpha_k \mathbf{r}) \qquad \forall k \in [1\,;p] \tag{7.5}$$

In this matrix, α_k ranges between a minimum and a maximum value, similar to the TomoSAR elevation matrix. In TomoSAR, the corresponding parameter describes the height of the point w.r.t. the DEM or 3D model. The spread and discretisation step of the steering matrix for atmospheric estimation is determined assuming a maximal phase jump rate of $\frac{2\pi}{200}\,\mathrm{m}^{-1}$ and a sampling step of $\frac{2\pi}{8000}\,\mathrm{m}^{-1}$.

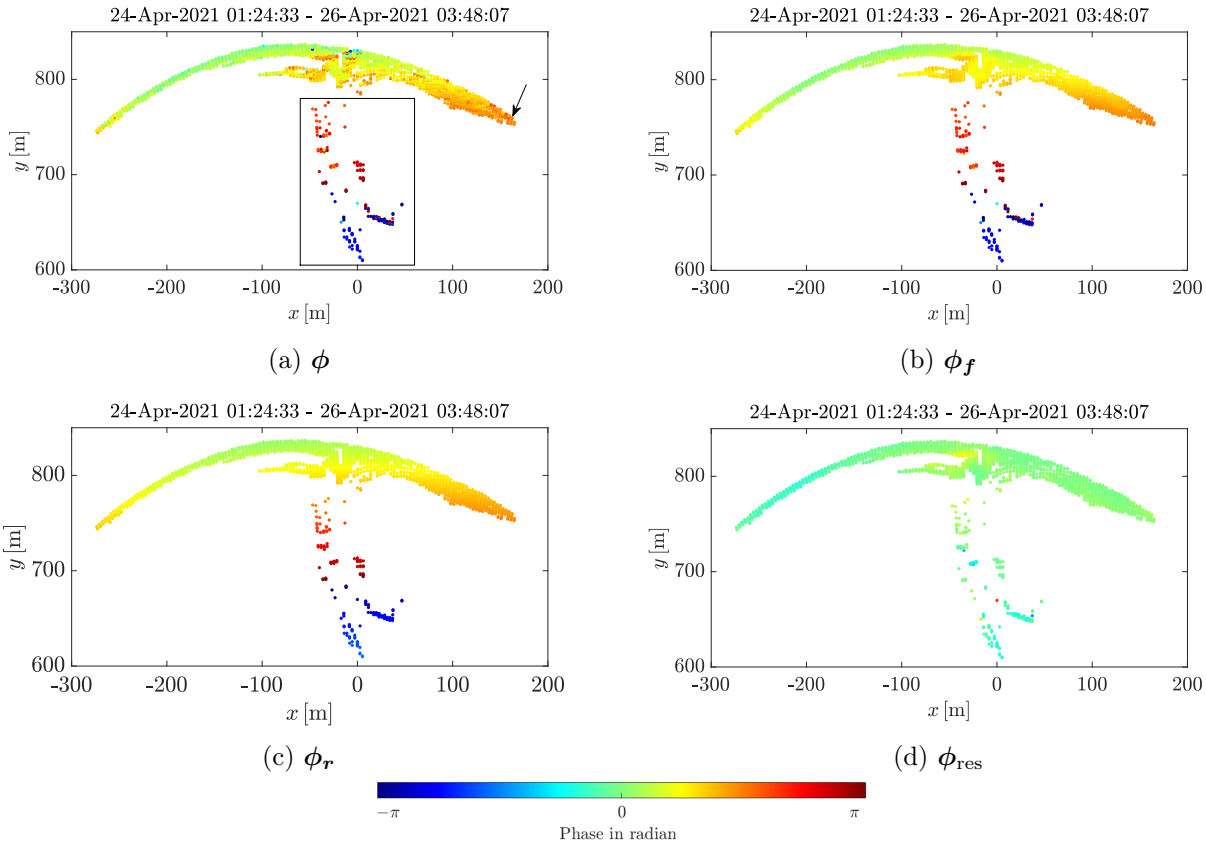

Figure 7.2: Signal decomposition: (a) Raw interferogram - (b) Filtered interferogram - (c) Range signal - (d) Residual signal. Only the signal in (d) goes through the 2D phase unwrapping. In (a), the black box represents the points not on the dam and used further in the processing. The black arrow exposes the point used as the spatial phase reference for the phase unwrapping.

The recovered signal from this estimation for each interferogram is $z_r = \exp(i\psi_r)$, with ψ_r the estimated phase as a range linear ramp. Using the OMP, a sum of linear signals can also be recovered if necessary. The advantage of this algorithm is the estimation of a parameterised component of the observed phase in the wrapped domain, which leads to an immediate estimate of the corresponding unwrapped phase ψ_r.

The estimated range-dependant signal is subtracted via the complex conjugate multiplication from the filtered phase to find the residual signal via:

$$z_{\text{res}} = z_f \overline{z}_r \tag{7.6}$$

Finally, the signal in the wrapped domain is divided into three parts as follows:

$$\phi = \mathcal{W}\left(\psi_r + \psi_c + \psi_{\text{res}}\right) \tag{7.7}$$

The unwrapped signal can be extracted as follows:

$$\psi = \psi_r + \psi_c + \mathcal{U}(\phi_{\text{res}}) \tag{7.8}$$

with ψ_r easily estimated via the parameters of the estimation, $\psi_c = \phi_c$ and $\mathcal{U}$ the unwrapping operator using SNAPHU. As for the epoch-wise processing, the interferogram's geometry is transformed to perform the unwrapping in the PCA geometry. The method is extensively presented in Section 6.2.3. After the 2D phase unwrapping, the referencing is achieved on the point marked with the black arrow in Figure 7.2a.

7.3.2 Phase integration

The phase unwrapping of each residual interferogram of the SBAS configuration is achieved preceding the phase integration. Unwrapping can be applied using various 2D or 3D unwrapping algorithms. For instance, the work by [Wang, 2019] suggests to use the 3D unwrapping approach from StaMPS. However, the algorithm is designed for spaceborne SAR using the assumption of linear displacements of the observed points to calculate the costs for the SNAPHU step. While this assumption is common in multi-temporal satellite InSAR, it is not applicable in the context of very long-term monitoring with GB-SAR data. In this case, the classical 2D SNAPHU routine is preferred to estimate the unwrapped interferometric SBAS vector $\boldsymbol{\psi}_{\text{sbas}}$ for each PSC. The goal of the phase integration is to recover the integrated time series vector $\boldsymbol{\psi} \in \mathbb{R}^N$ from $\boldsymbol{\psi}_{\text{sbas}} \in \mathbb{R}^M$, with N the number of acquisitions and M the number of interferograms.

7.3.2.1 System design

To illustrate the system of the phase integration, an example considering $N = 4$ and a maximum baseline of three scenes, consequently leading to a number of interferograms $M = 6$, is proposed in the following example:

$$\begin{bmatrix} 1 & 0 & 0 & 0 \\ 1 & -1 & 0 & 0 \\ 0 & 1 & -1 & 0 \\ 0 & 0 & 1 & -1 \\ 1 & 0 & -1 & 0 \\ 0 & 1 & 0 & -1 \\ 1 & 0 & 0 & -1 \end{bmatrix} \begin{bmatrix} \psi_1 \\ \psi_2 \\ \psi_3 \\ \psi_4 \end{bmatrix} = \begin{bmatrix} 0 \\ \psi_{1-2} \\ \psi_{2-3} \\ \psi_{3-4} \\ \psi_{1-3} \\ \psi_{2-4} \\ \psi_{1-4} \end{bmatrix} \quad \text{i.e.} \quad \mathbf{G}\boldsymbol{\psi} = \boldsymbol{\psi}_{\text{sbas}} \tag{7.9}$$

where ψ_{p-q} denotes the interferogram between acquisition p and q, ψ_p represents the integrated phase w.r.t. to the first acquisition i.e. $\psi_1 = 0$. Their respective vector notations are $\boldsymbol{\psi}_{\text{sbas}}$ and $\boldsymbol{\psi}$. The easiest and fastest inversion method is the ordinary least squares (OLS) method. The OLS estimator $\hat{\boldsymbol{\psi}}_{\text{OLS}}$ of Equation 7.9 is given by:

$$\hat{\boldsymbol{\psi}}_{\mathrm{OLS}} = \left(\mathbf{G}^{\mathsf{T}}\mathbf{G}\right)^{-1}\mathbf{G}^{\mathsf{T}}\boldsymbol{\psi}_{\mathrm{sbas}} \tag{7.10}$$

An improved approach corresponding to the maximum likelihood estimate of the integrated time series is the weighted least squares (WLS) estimator. This procedure assigns weights to observational data based on their quality. For the GB-SAR case, [Su et al., 2022] uses the inverse of the deviation of each point to the averaged phase in a local patch as weights. In the case of general InSAR data, [Yunjun et al., 2019] studied for different types of weights and concluded that considering a weight matrix $\mathbf{W} = \mathrm{diag}(1/\sigma_{\psi}^2)$ is the optimal variant. Therefore, the WLS estimator is given by:

$$\hat{\boldsymbol{\psi}}_{\mathrm{WLS}} = \left(\mathbf{G}^{\mathsf{T}}\mathbf{W}\mathbf{G}\right)^{-1}\mathbf{G}^{\mathsf{T}}\mathbf{W}\boldsymbol{\psi}_{\mathrm{sbas}} \tag{7.11}$$

Both LS solutions and especially the OLS are designed for Normally distributed measurements. They are susceptible to being severely affected by outliers, and unwrapping errors exert a substantial deterioration of the estimation. The residual sum of squares (RSS) equals 0 in scenarios where unwrapping errors are absent. Another possibility to mitigate the influence of unwrapping errors is to use the least absolute deviations (LAD) estimator, as in [Lauknes et al., 2010] and [Goel and Adam, 2012]. Contrary to the LS methods, there are no direct formulas to compute the estimated value for this minimising criterion. Prevailing techniques often centre around linear programming, with an illustrative algorithm outlined in [Amemiya, 1982]. Solving this criterion demands significantly more computational time than a LS estimator. One drawback with LAD estimation lies in its lack of inherent convergence to a unique solution, as pointed out in [Narula and Wellington, 1982]. In this thesis, the *convex* toolbox [Grant and Boyd, 2014] for *Matlab* was used to compute the LAD inversion.

A succinct summary of the advantages and disadvantages of the LS and LAD estimation for an over-determined system can be summarised in the following table:

Least squares	**Least absolute deviations**
Not robust	Robust
Unique solution	Non-unique solution
Fast	Slow

Table 7.1: LS and LAD characteristics.

Assessing the inversion quality can be achieved through the signal's temporal coherence γ_t, which quantifies the deviation between the re-wrapped integrated signal and the original wrapped time series $\boldsymbol{\phi} = [\phi(1)...\phi(N)]$. It is calculated as follows:

$$\gamma_t = \frac{1}{N}\left|\sum_{k=1}^{N}\exp(i\psi(k))\exp(-i\phi(k))\right| \tag{7.12}$$

Although this quantity is not flawless due to its circular nature, it effectively identifies deviations from the original data and serves as a reliable metric in cases where ground truth is unavailable, as stated by [Lauknes et al., 2010].

7.3.2.2 Comparison of LS and LAD estimator on synthetic data

The simulation of time series and its recovery using a SBAS configuration with different percentages of unwrapping errors is undertaken to gain a deeper insight into the superior capabilities of the LAD estimation compared to the LS estimation. A linear time series is simulated from a sampling vector, i.e. $y(t) = \alpha t$. In the conducted simulations, $t = [1...T]$ with $T = 200$. Contrary to the simulations performed in [Lauknes et al., 2010], no noise is introduced, as we retain all the signals in each interferogram. Subsequently, the SBAS network is constructed using the four preceding and succeeding averaged SLC of each scene, yielding an observation vector exempt from errors. Different percentages of unwrapping errors are randomly introduced into the observations, resulting in a realistic observation vector $\mathbf{y}_{\text{sbas}}$ with a length of $N = 794$. The linear system according to Equation 7.9 is $\mathbf{y} = \mathbf{G}\mathbf{y}_{\text{sbas}}$ and solved using both the LS and LAD algorithms to get $\hat{\mathbf{y}}_{\text{LS}}$ and $\hat{\mathbf{y}}_{\text{LAD}}$ as respective estimators. The simulated range of unwrapping error percentages spans from 0 to 20%, with a 1 % sampling interval. For each unwrapping error percentage, we conduct 2 000 individual phase integration instances.

The quality of the inversion is evaluated with three criteria represented in Figure 7.3. For each inversion, the temporal coherence γ_t is computed. However, due to its periodicity, an estimated time series and a true time series that are exactly separated by a constant of 2π result in a temporal coherence $\gamma_t = 1$. Therefore, the mean deviation $\overline{D}$ is introduced as a second quantity. This metric calculates the average absolute difference between the true and estimated time series, offering a more reliable assessment based on the ground truth data. Finally, the residues e of the estimation for 5 % of unwrapping errors are analysed.

The temporal coherence results for both estimators are depicted in Figure 7.3a. When using the LS estimator, its value decreases significantly fastly. Conversely, according to this metric, the LAD estimator recovers the signal up to 9% of unwrapping errors correctly. These findings are further supported by the analysis of the mean deviation, given in Figure 7.3b. Up to 9% of unwrapping errors, all the points are satisfactorily recovered. Beyond this threshold, although the LAD estimator remains markedly superior, it does not remain immune to the impact of unwrapping errors. The correlation observed between the two quantities also strengthens the usage of the temporal coherence to assess the quality of the inversion.

In Figure 7.3c, the upper and lower bounds of the 2 000 inversions with the LS estimator are provided with increasing levels of unwrapping errors: 1%, 5%, 10%, and 20%, to highlight the visualisation of the error propagation more effectively. For the two first percentages of unwrapping errors, the LAD estimator recovers well all the samples and achieves an exact reconstruction (therefore not plotted), while the LS solution can exhibit substantial drifts. Anticipating the Enguri Dam data enables us to quantify the possible induced drift. For the typical committed error of 5% and 200 days, i.e. only seven months of observations, the mean absolute deviation at the end of the time series is about 5 rad $\widehat{=}$ 7 mm. For two years of data consisting of approximately 730 days, the mean deviation over 2000 inversions represents 10 rad $\widehat{=}$ 13 mm.

The last graphic in Figure 7.3d is an example of the residues resulting from the two inversion processes. The chosen scenario is an amount of 5% of unwrapping errors. In contrast to the LS estimation, which primarily reveals non-prominent peaks around multiples of 2π, the LAD estimation presents peaks at multiples of π with notably narrower profiles. The appearance of π and $-\pi$ residuals is due to the non-uniqueness of the solution using this estimator. While a deeper examination of the residues extends beyond the scope of this thesis, delving into this aspect could potentially enhance the robustness of phase integration in cases involving significant unwrapping errors.

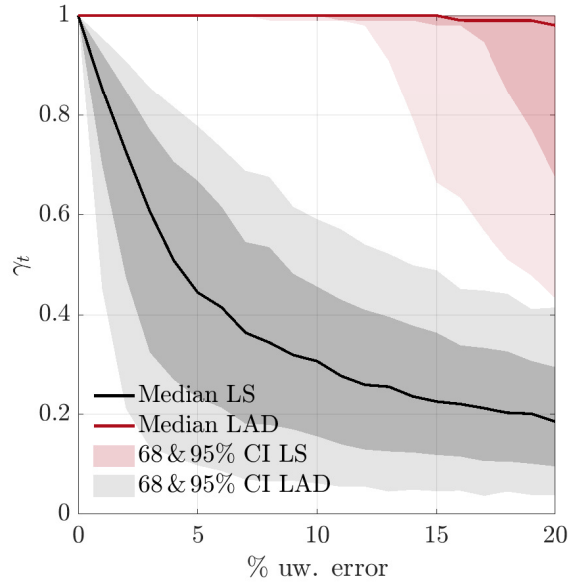

(a) Temporal coherence

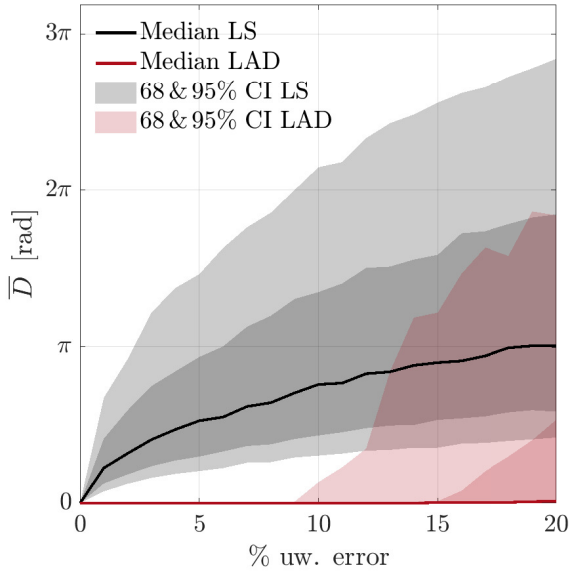

(b) Mean deviation

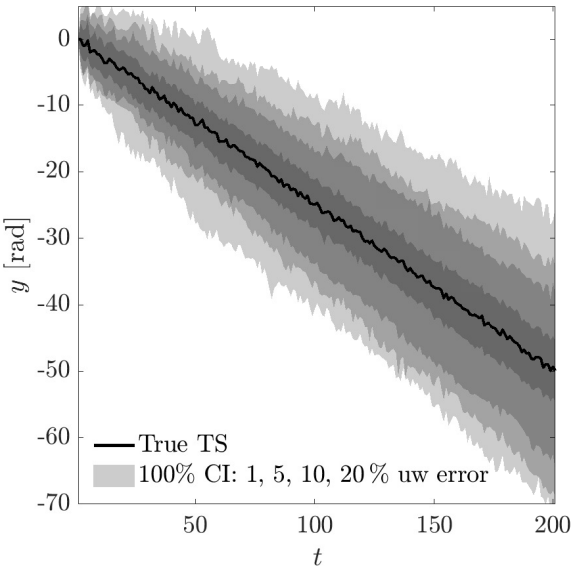

(c) LS inversion drifts up to 20% uw. error

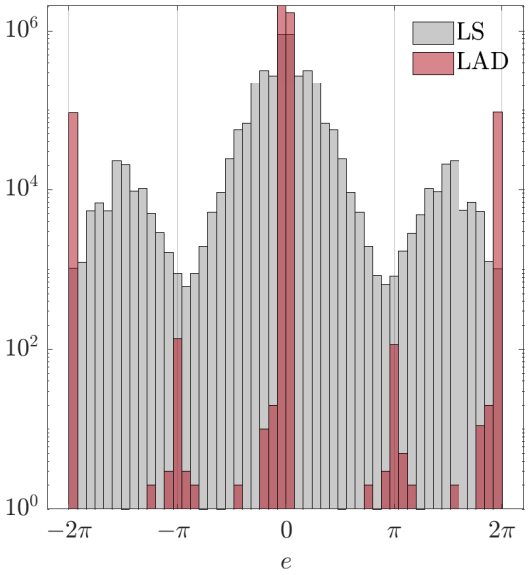

(d) Residues for 5% uw. error

Figure 7.3: Results of the Monte-Carlo simulation for the estimation of a time series using LS and LAD estimators from 0 to 20% of unwrapping errors.

7.4 Time series analysis

Following the completion of phase integration relative to the initial observation, the subsequent section aims at the atmospheric correction and the noise reduction. An initial step is the selection of the PS points. All PSC verifying $\gamma_t > 0.97$ are considered as stable PS after the phase integration. The criterion is based on the analysis of the simulation results, still enabling individual minimal deviations from the original time measurements.

In GB-SAR dam monitoring, the difference between the deformation signal and the atmospheric signal properties are mainly temporal. Indeed, the long wave part of the atmospheric signal is removed during the phase referencing after the phase unwrapping. For example, it includes the global temperature variations between summer and winter. In Section 7.3.1, the signal is decomposed by estimating the signal in range. One plausible approach involves subtracting this signal from each interferogram before proceeding with phase inversion. However, the range signal is estimated on the whole interferogram, possibly subtracting inadequate displacement signal that might be missing in the integration process. Furthermore, adhering to the conventional InSAR atmospheric model outlined in [Liu et al., 2011], the atmospheric signal is characterised as having a zero mean and being uncorrelated over time.

Consequently, atmospheric signal correction occurs in a two-step process. Firstly, the range component is re-estimated exclusively from stable points, delineated by the black box in Figure 7.2a. Only the range component is estimated, as all the points lie approximately on the same height as the GB-SAR and do not provide reliable elevation information. The residual part of the atmospheric signal is consequently treated as residual noise. The same principle as for all the atmospheric estimations in this work is applied to carry out the estimation. A first WLS estimation enables the detection of outliers that are rejected for the second estimation.

7.4.1 Displacement estimation using functional data analysis

Up to this point, the proposed processing chain aims to derive the optimal unwrapped time series estimate from the wrapped data. Although the smooth atmospheric signal is mitigated, the more turbulent components and noise are not fully addressed. Moreover, no quantity of the quality of the estimated signal is proposed. We use the temporal properties of the different signal contributions to estimate the precision of the estimated deformation. The remaining signal after the range atmospheric correction ψ_{cor} can be decomposed as:

$$\psi_{\text{cor}} = \psi_{\text{defo}} + \psi_{\text{atmo,res}} + \psi_{\text{noise}} \tag{7.13}$$

While no exact estimator for the disruptive terms $\psi_{\text{atmo,res}}$ and ψ_{noise} exist, their differentiation from the deformation signal can be achieved by use of their distinct temporal behaviours. Noise and the residual atmospheric signal can be regarded as high-frequency disturbances, whereas the deformation of the dam is a slower and smoother process. Additionally, it can be assumed that the mean of the disturbances term over time is zero.

functional data analysis (FDA) is a branch of mathematics that tries to statistically describe smooth functions from discrete observations, which is the case with the available measurements. This framework is provided in [Ramsay, 1991], although its conceptual foundations trace back to the Karhunen-Loève decomposition [Loève, 2017]. This statistical discipline is concerned with signals or images that vary across continuous spaces, with time being a predominant dimension. The applications of FDA are diverse and deeply explored in [Ramsay, 1991]. Within the context of long-term monitoring, the focus lies on smoothing the GB-SAR time series to mitigate noise. The core idea is to fit the time series with a basis function expansion and apply roughness penalties. The principal added value of FDA smoothing is the ability to estimate a confidence interval of the time series, considering the penalty term. We employed the toolbox described in [Ramsay et al., 2009] for the numerical implementation.

The observations $\mathbf{y}$ under consideration are the observed phase converted in millimetres, defined by:

$$\mathbf{y} = [y_j]_{j\in[1:N]} \quad \text{with} \quad y_j = \frac{\lambda}{4\pi}\psi_{\text{cor}}(t_j) \quad j \in [|1; N|] \tag{7.14}$$

with t_j, the acquisition time of the j^{th} acquisition and N the number of acquisitions. The central concept is to view the observations y_j as noisy samples originating from the smooth function x, which is an expansion composed of basis functions Υ. No weights are considered in the stochastic model of the observation such that: $\mathbf{Q}_{yy} = \mathbf{I}$. So the objective function to minimise is:

$$F(\mathbf{c}) = \sum_{j=1}^{N}(y_j - x(t_j))^2 + \lambda_{\text{pen}} \int Lx(t)dt \tag{7.15}$$

with $\mathbf{c} = (c_1...c_K)$ the coefficients of the basis expansion of x. Therefore, at time t_j, $x(t_j)$ can be defined by:

$$x(t_j) = \sum_{k=1}^{K} c_k \Upsilon_k(t_j) \tag{7.16}$$

In these two equations, Υ_k denotes the k^{th} basis function, λ_{pen} is the penalising parameter and L is an operator on x. A commonly selected form for the operator is:

$$Lx = \left(\frac{d^2x}{dt^2}\right)^2 = \left(D^2x\right)^2 \tag{7.17}$$

Opting for this operator results in a penalising criterion that quantifies the integrated squared second derivative, often called the total curvature. This penalty can be adapted based on the underlying physical principles governing the analysed process. Various basis functions are selectable, with the Fourier basis being suitable for periodic data and the B-spline basis for non-periodic data. This work will consider the B-spline basis, as the deformation is generally aperiodic. The B-spline basis is defined by the polynomial order and the sequence of knots, corresponding to the number of samples in the time series N in this context. A small presentation of the B-spline basis is proposed in Appendix D.1. For comprehensive guidance on parameter selection, including the spline order, we refer to [Ramsay et al., 2009]. For instance, a thumb rule is that the order of the spline basis needs to be at least two higher than the order for the derivative used for the penalising criterion.

We also introduce the $N \times K$ matrix $\mathbf{\Upsilon}$ containing the values of $\Upsilon_k(t_j)$, and define the symmetric roughness penalty matrix of size $K \times K$ and given by:

$$\mathbf{R} = \int D^2\Upsilon(t)D^2\Upsilon^{\mathsf{T}}(t)dt \tag{7.18}$$

This penalty function is proposed as a meaningful criterion for infrastructure and relatively smooth deformation monitoring. There is no penalisation on possibly strong velocities, but abrupt accelerations are penalised, as they are not expected. The final estimate of the coefficients of the basis function using this penalty function is given by:

$$\hat{\mathbf{c}} = \left(\mathbf{\Upsilon}^{\mathsf{T}}\mathbf{\Upsilon} + \lambda_{\text{pen}}\mathbf{R}\right)^{-1}\mathbf{\Upsilon}^{\mathsf{T}}\mathbf{y} = \mathbf{S}\mathbf{y} \tag{7.19}$$

From this, the estimated smooth time series $\hat{\mathbf{y}}$ is given by:

$$\hat{\mathbf{y}} = \boldsymbol{\Upsilon}\mathbf{S}\mathbf{y} = \mathbf{H}\mathbf{y} \tag{7.20}$$

with $\mathbf{H}$ denoted as the *hat*-matrix which is a square symmetric matrix. λ_{pen} is a penalty parameter, and the estimation of its optimal value is detailed in [Ramsay et al., 2009] and shortly presented in Appendix D.2.

7.4.2 Confidence interval on functional data

The study on the estimation quality is also of major interest and can be concisely summarised through the following equations. The initial operation is the computation of the residual vector $\mathbf{e} = \mathbf{y} - \hat{\mathbf{y}}$. The estimated error variance $\hat{s}^2$ of the estimation is given by:

$$\hat{s}^2 = \frac{1}{N - \nu(\lambda_{\text{pen}})}\|\mathbf{e}\|_2^2 \tag{7.21}$$

$\nu(\lambda_{\text{PEN}})$ represents the degree of freedom of the equation system. The penalisation reduces the degree of freedom of the estimation such that $\nu(\lambda_{\text{PEN}}) \neq K$. In this sense, the *hat*-matrix $\mathbf{H}$ plays a central role as it contains the degree of freedom via:

$$\nu(\lambda_{\text{pen}}) = \text{tr}(\mathbf{H}) \tag{7.22}$$

with tr(.) being the trace operator. Alternative definitions exist, such as $\nu(\lambda_{\text{pen}}) = \text{tr}(\mathbf{H}\mathbf{H}^{\mathsf{T}})$, but we remain consistent with the choice made by [Ramsay et al., 2009].

To conclude the development, [Ramsay, 1991] uses an estimation on the covariance matrix of the residues to estimate the variance of $x(t)$. If only a single instance of the time series is smoothed, auto-regressive models are proposed. In this work, we followed the covariance matrix propagation to obtain the variance of the estimated vector $\hat{\mathbf{y}}$. Indeed, the evaluation of the function x at time t is given by:

$$\forall\, t,\;\; x(t) = \boldsymbol{\Upsilon}(t)\hat{\mathbf{c}} = \boldsymbol{\Upsilon}(t)\mathbf{S}\mathbf{y} \tag{7.23}$$

The covariance matrix $\boldsymbol{\Sigma}_{\hat{c}\hat{c}}$ of the estimated coefficients can be computed using the matrix $\mathbf{S}$ from Equation 7.19 with:

$$\boldsymbol{\Sigma}_{\hat{c}\hat{c}} = \hat{s}^2\mathbf{S}\mathbf{S}^{\mathsf{T}} \tag{7.24}$$

Finally, the estimated covariance matrix of the estimated noiseless time series $\hat{\mathbf{y}}$ is given by:

$$\boldsymbol{\Sigma}_{\hat{\mathbf{y}}\hat{\mathbf{y}}} = \boldsymbol{\Upsilon}\boldsymbol{\Sigma}_{\hat{c}\hat{c}}\boldsymbol{\Upsilon}^{\mathsf{T}} \tag{7.25}$$

The average variance of the estimated curve $\overline{\sigma}^2_{\hat{\mathbf{y}}}$ is then computed by averaging the diagonal of the covariance matrix $\boldsymbol{\Sigma}_{\hat{\mathbf{y}}\hat{\mathbf{y}}}$, i.e.:

$$\overline{\sigma}_{\hat{\mathbf{y}}} = \frac{1}{N}\text{tr}\left(\boldsymbol{\Sigma}_{\hat{\mathbf{y}}\hat{\mathbf{y}}}\right) \tag{7.26}$$

7.5 Application at Enguri Dam

For a comprehensive overview, the processing chain is depicted in Figure 7.4. In the figure, green boxes denote the input and output stages. The processing flowchart is designed to transform the geocoded set of PSC into a reliable displacement map. The different phase components outputs are presented in the orange boxes to clarify the notation. Due to its daily average foundations, this method is called daily baseline subset (DBAS).

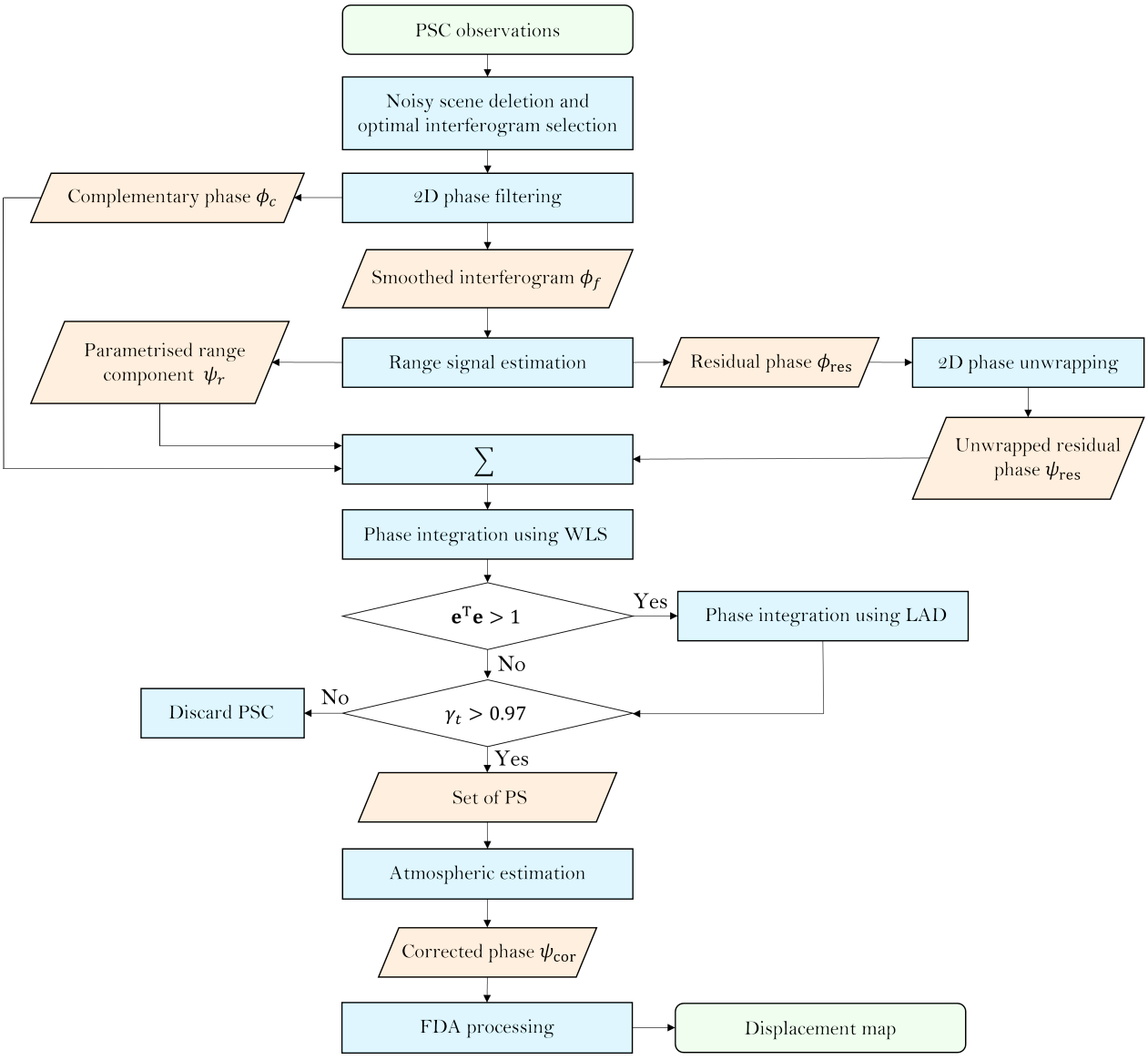

Figure 7.4: Flowchart of the proposed DBAS processing chain.

The flowchart is tested on the data acquired at Enguri Dam from the *Warehouse* station presented in Chapter 3. Out of the initial 573 075 SLC images, the preprocessing results in 756 averaged acquisitions for 2 365 PSC. The application is conducted in two main parts. Initially, various types of flowcharts are analysed to validate the proposed development's efficiency. Subsequently, the deformation analysis is performed based on the DBAS workflow.

7.5.1 Consistency analysis of the DBAS workflow

The parameters of the various configurations tested are presented in Table 7.2. The first version is the full proposed DBAS flowchart. The second configuration compares the improvement gained by unwrapping in the PCA geometry based on continuous data. The third test examines the necessity of adding the residual signal after filtering ϕ_c, even if it contains most of the noise. The fourth configuration aims to assess the enhancement using the LAD estimator on real data. Lastly, the final tested configuration explores the outcomes when none of the proposed enhancements are applied. The evaluation metric is the temporal coherence γ_t for all the PSC before the atmospheric correction.

Version	Geometry	ϕ_r estimation	Filt.	Add res. signal	Inv. estimator
1	PCA	✓	✓	✓	LAD
2	SAR	✓	✓	✓	LAD
3	PCA	✓	✓	-	LAD
4	PCA	✓	✓	✓	WLS
5	SAR	-	✓	-	OLS

Table 7.2: Comparison between the DBAS workflow and other possible workflows.

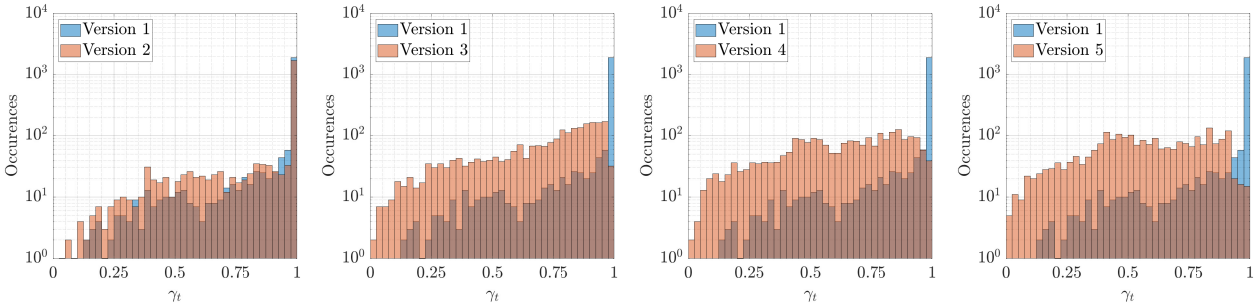

(a) 1 vs. 2 (b) 1 vs. 3 (c) 1 vs. 4 (d) 1 vs. 5

Figure 7.5: Histograms of the different workflow versions presented in Table 7.2. The y-axis is given in log-scale.

A global overview of Figure 7.5 demonstrates that each step enhances the temporal coherence, improving consistency with the raw integrated wrapped time series and increasing the number of PS. Notably, incorporating the complementary signal ϕ_c after phase filtering and before the phase integration is of the highest importance to ensure consistency between the original and estimated signals. Moreover, it is apparent that using the classical flowcharts like the StaMPS one, without any of the proposed enhancements, leads to lower coherence values.

A particular emphasis is placed on comparing version 1 and version 3. Adding the residual signal after filtering might be surprising, given that it mainly contains noise. However, as the employed filter is spatial, it can introduce smoothing to the displacement signal, which could induce drifts over longer timescales. Two points on the dam were selected and analysed to provide a more precise visualisation of this effect, shown in Figure 7.6.

In the first month, the undesired effect is not visible. However, a drift becomes apparent for both the green and blue points after this period. , While their noise is reduced due to the filter, it is perceptible that the two time series diverge from the original wrapped one. This divergence intensifies over time and becomes particularly pronounced towards the end of the time series. For the green point with a

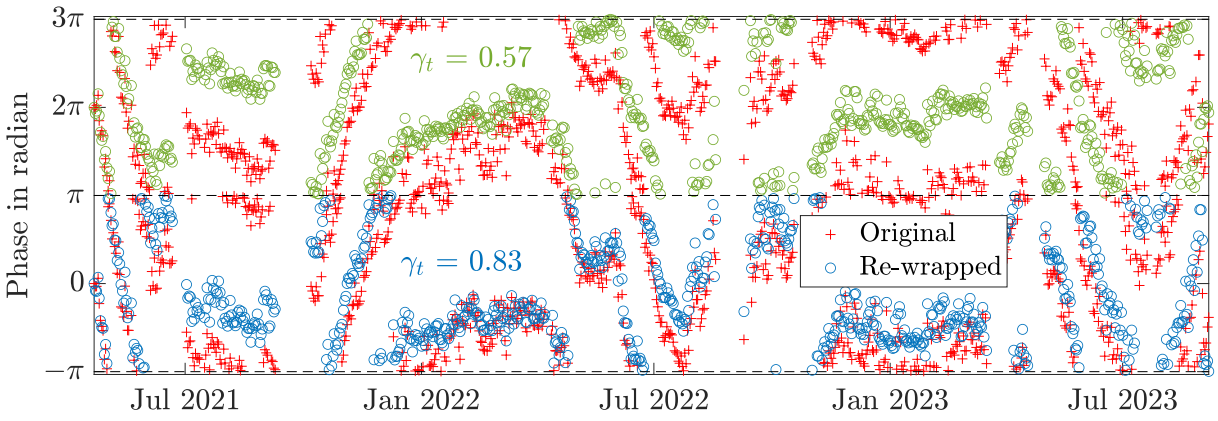

Figure 7.6: Drift analysis on two points at Enguri Dam. The red crosses are the original time series while the circles represent the re-wrapped processed time series. For better visualisation, 2π is added to the data corresponding to the second point.

Version	1	2	3	4	5
PSC w/ $\gamma_t > 0.97$	1947	1753	48	118	15
Ratio PS/PSC	82%	74%	2%	5%	1%

Table 7.3: Number of selected PS for each version.

lower coherence of $\gamma_t = 0.57$, the time series diverges at the end with an offset of nearly π (January 2023), corresponding to approximately 4.25 mm once converted. This bias is critical for geodetic monitoring and needs to be mitigated. The proposed flowchart demonstrates the best alignment with the original data, as evidenced by the largest number of points with $\gamma_t > 0.97$. Table 7.3 summarises the number of selected PS from the initial set of PSC.

7.5.2 Displacement time series

Two visualisations are provided to visualise the behaviour of the Enguri Dam. Firstly, four points are chosen on the dam, situated at approximately the same height and spanning the dam's structure. The precise positions of these points can be seen in Figure 7.7a, while their corresponding time series are presented in Figure 7.8. This configuration is particularly informative to understand the deformation mechanisms as the distance from the embankment increases. The second configuration focuses on the behaviour of four other points, having a similar horizontal position and distributed along a vertical profile. The exact positions of these points are displayed in Figure 7.7b, while their corresponding time series are depicted in Figure 7.9. This arrangement enables the examination of vertical deformation characteristics. In the time series, a negative displacement corresponds to a reduction in the distance between the dam and the GB-SAR, indicative of displacement towards the radar sensor. The displacement maps presented in Figure 7.7 correspond to the time t_{ifg}, marked by the dashed red line on the respective time series.

The analysis of Figure 7.8 shows several properties of the processed observations acquired by a GB-SAR. The results reveal a striking consistency with the reservoir's water level, indicating a strong correlation between deformation patterns and water level variations. This correlation is particularly evident during significant water level changes. The observation period starts in late

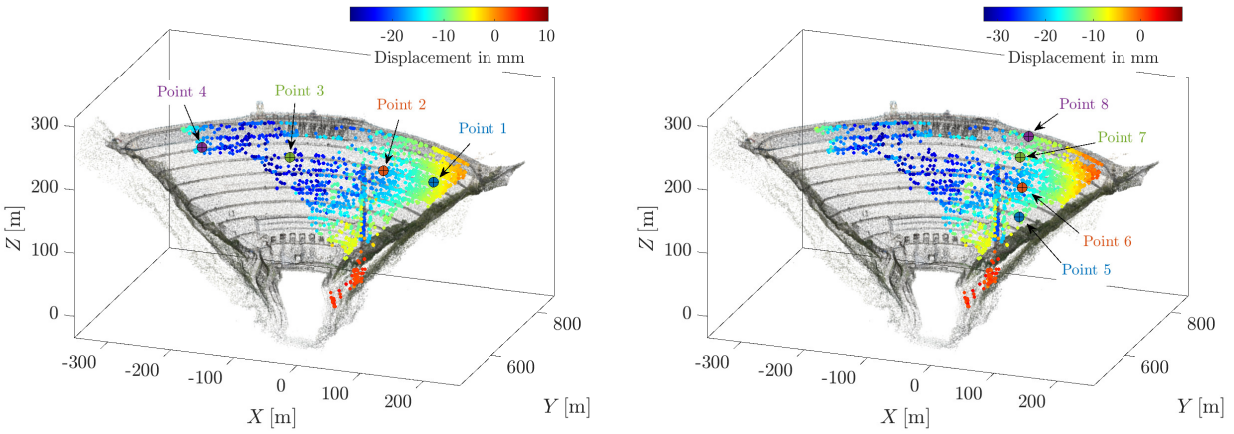

(a) Horizontal profile

(b) Vertical profile

Figure 7.7: Position of the selected points on the dam.

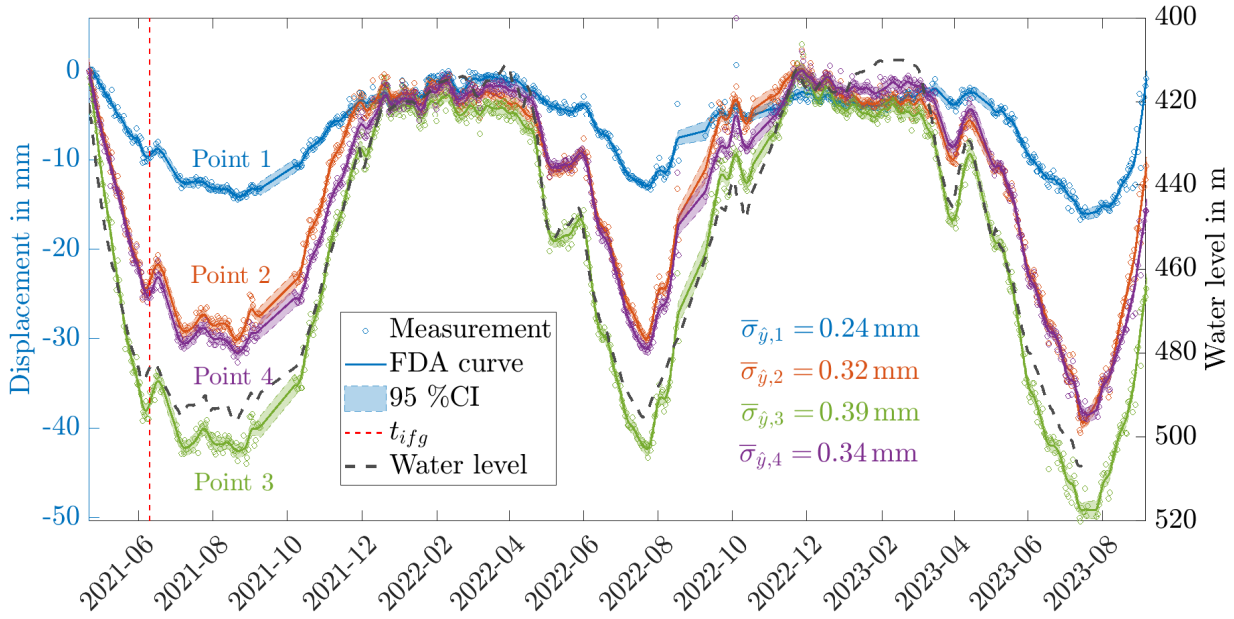

Figure 7.8: Time series of the four selected points for the horizontal case, i.e. Figure 7.7a.

April 2021 at a water level of 420 m. Each time this water level is reached, i.e. in January 2022, April 2022, November 2022, and March 2023, the displacement curves converge. Each point on the curves is characterised by a calculated standard deviation $\sigma_{\hat{y}}$, computed using Equation 7.31, and represented as a 95% CI. Additionally, the mean uncertainty over time, denoted as $\overline{\sigma}_{\hat{y},k}$ for each respective point k, is determined and illustrated on the graph. Remarkably, this average uncertainty consistently falls within the magnitude order of 0.4 mm across the four selected points. This outcome exposes the high precision of the GB-SAR system, which can reliably capture subtle changes in deformation over time.

Points 2 and 4 are symmetrically located at the same distance from the dam's central part and reveal very close displacement curves. Especially, the precision of Point 4 is not lower, even if it is

located considerably further from the reference point.

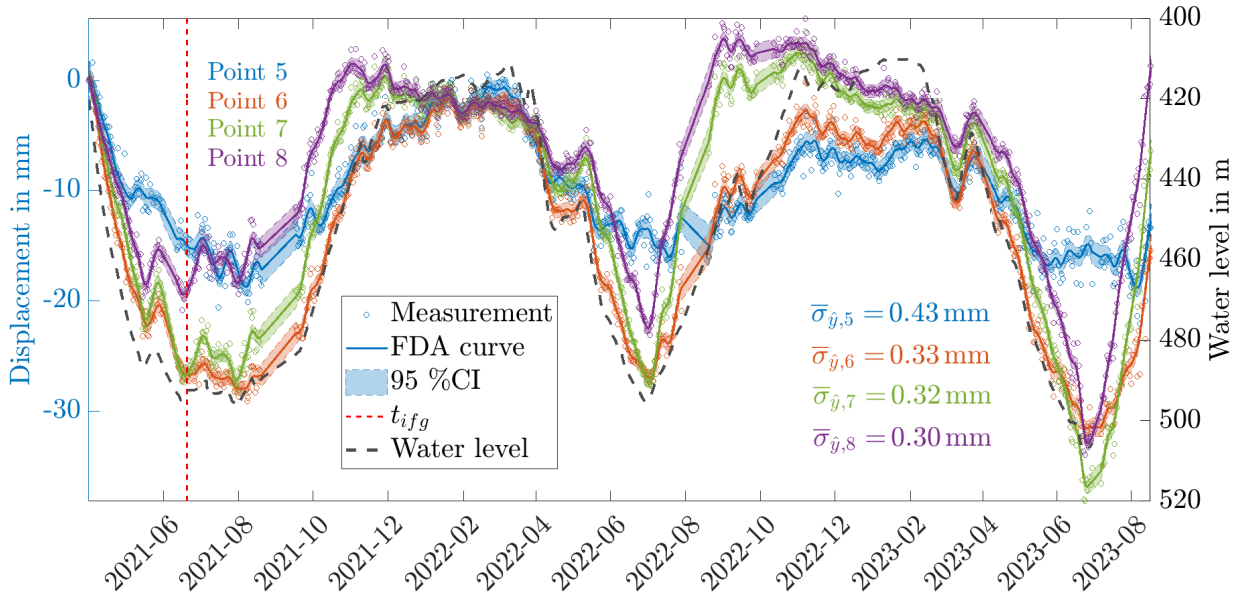

Figure 7.9: Time series of the four selected points for the vertical case, i.e. Figure 7.7b.

Among the four selected points along the vertical profile, the findings on the time series in Figure 7.7b reveal some deviations from the established correlation with the water level, especially in autumnal periods. This discrepancy becomes notably apparent in the behaviour of the two highest points, namely Point 7 and Point 8, when the water level remains low and relatively stable. During specific periods, such as from December 2021 to April 2022 and from October 2022 to February 2023, the time series for these points demonstrate a consistent displacement toward the radar sensor, similar to a water level increase. Despite this phenomenon, all curves converge when the water level and the period in the year are similar to the origin.

This observation can be attributed to a thermal displacement phenomenon within the dam structure. When the water level is low, a substantial portion of the dam's structure on the reservoir side is exposed to the surrounding air. In such cases, variations in air temperature become significantly more pronounced than water temperature variations, consequently exerting a stronger influence on the deformation of the dam. Notably, during the winter season, the metal components of the reinforced concrete are particularly susceptible to thermal contraction processes, leading to observable movements toward the radar sensor.

7.5.3 Regression of HST model

The conventional approach to estimate motion patterns using InSAR is to estimate a linear velocity. This linear model often provides accurate estimates for short observation periods, as any continuous function can be approximated by its tangent within a localised context. For instance, in a study such as [Qiu et al., 2020], a linear displacement rate might be estimated for dam deformation, but only over 3.5 days of observation. However, as the observation time increases, the plausibility of a linear motion diminishes, requiring the employment of higher-order models to better fit the data. Nonetheless, in Chapter 3, we introduced the HST model in Equation 3.1, which offers a

comprehensive representation of dam deformation by accounting for 11 parameters divided into three contributions: water level, periodicity and long-term ageing. The HST model's ability to capture more complex deformation patterns underscores its utility for characterising dam behaviour over extended observation periods. This model is used in [Rebmeister et al., 2023] to estimate the coefficients of the model at Enguri Dam based on the plumbline data. The quality of the estimation of the HST model to the times series is the first indicator to estimate the consistency of the processing.

Using the DBAS approach, at least 11 days of observation are required, as the number of parameters of the HST model is 11. However, the periodical motion is based on a yearly behaviour, which is why it is better to collect data over at least one year to conduct the parameter estimation. For this task, the OLS technique is applied, as the FDA smoothing is robust against outliers and proposes a smooth version of the data. The water level data are available only until 20$^{\text{th}}$ July 2023, restricting the parameter estimation up to this date.

The same four points marked in Figure 7.7a are selected. Their standard deviation error is also displayed on the graph and denoted with $\sigma_{HST,k}$ for the k^{th} point. For all these points, the model exhibits a strong adequacy to the data. The standard deviation error of this model verifies for all the points $\sigma_{HST,k} < 1\,\text{mm}$. Especially, the major part of the curves are contained in the 95% CI of the displacement time series. Residual atmospheric signals can explain the small remaining deviations.

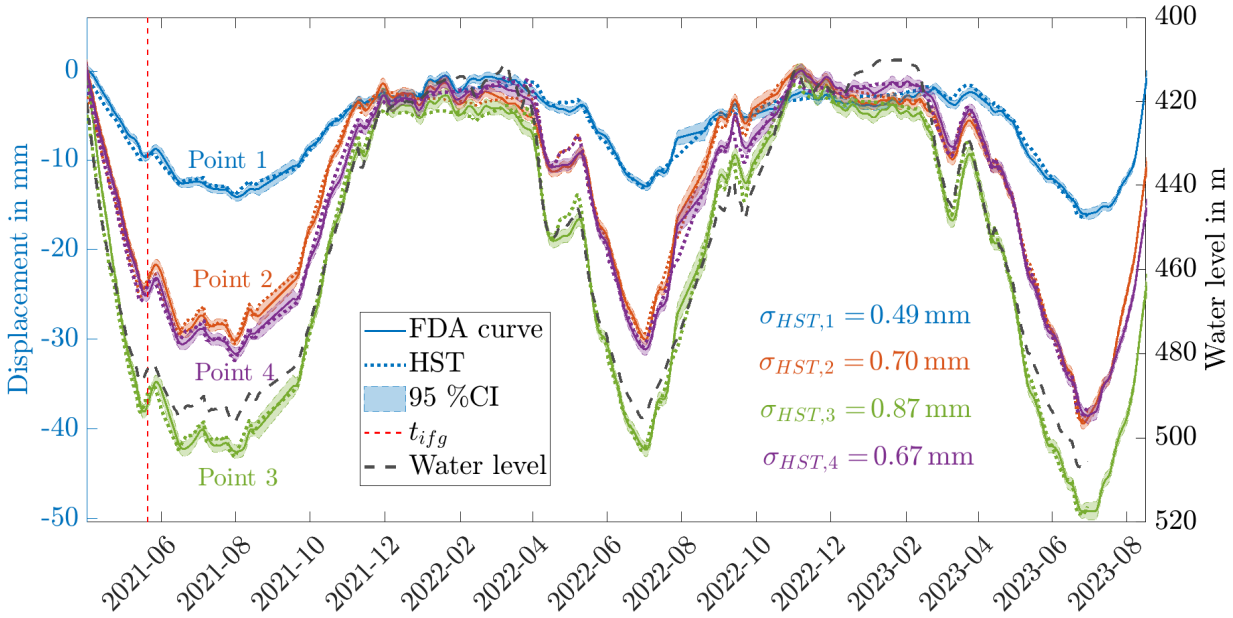

Figure 7.10: Estimation of an HST model based on the GB-SAR time series. Horizontal profile.

A temporal zoom spanning from December 2022 to July 2023 is applied to both Figures 7.8 and 7.10 to provide a clearer view of the achievable precision with an adequate processing on GB-SAR measurements. Figure 7.11a focuses explicitly on the CI obtained for the four points. The FDA mitigates the typical CI expansion associated with conventional methods. Indeed, all CI depicted in the figure do not reflect the confidence of individual measurements but rather on the estimated curve with the given hypothesis. As a result of this approach, the 95 % CI expresses the probability that the estimated curve lies in this interval with replicate measurements having the same precision and the same penalty term. On the other hand, Figure 7.11b underscores the close correspondence observed between the HST regression and the actual time series.

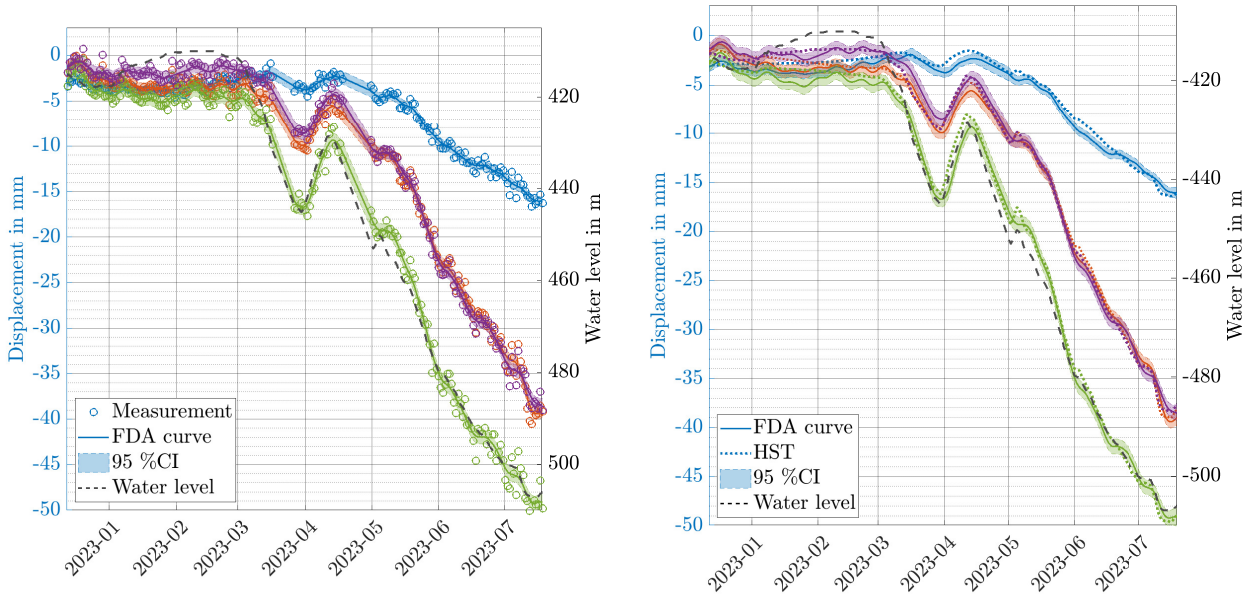

(a) Measurement + FDA

(b) FDA + HST

Figure 7.11: Zoom on the time series obtained between August 2022 and March 2023. (a) comports the measurements and the FDA smoothing. The y-axis is more zoomed to better analyse the confidence interval w.r.t. the observations. (b) emphasises the adequacy between the HST regression and the FDA fit.

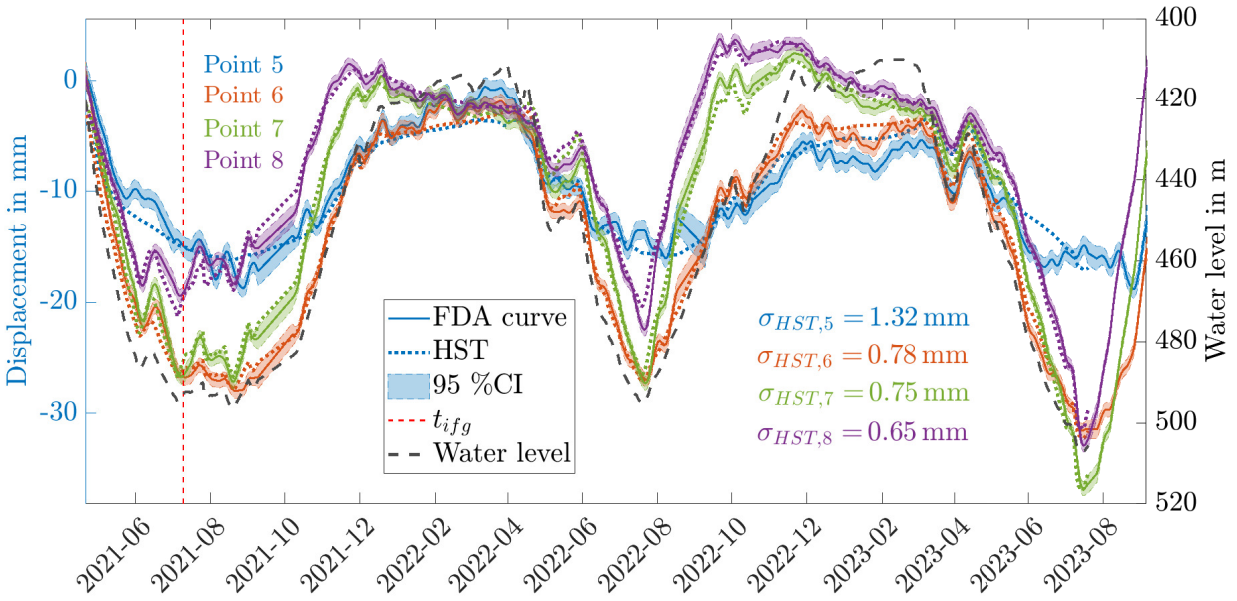

Figure 7.12: Estimation of an HST model based on the GB-SAR time series. Vertical profile.

The regression of the HST model can also confirm if the depicted phenomenon described for Points 6 and 7 on the elevation profile has a physical meaning. As visible in Figure 7.12, the standard

deviation of the regression is also under 1 mm for these two points, and the periodic terms compensate well for the deviation of the displacement from the single water level dependency. It is also visible that the lower the point, the higher the standard deviation. It may be height-dependent atmospheric disturbances that can not be removed. Indeed, the chosen reference point is located on the dam crest, mitigating correctly the latter part of the atmospheric signal only for the points at a similar elevation.

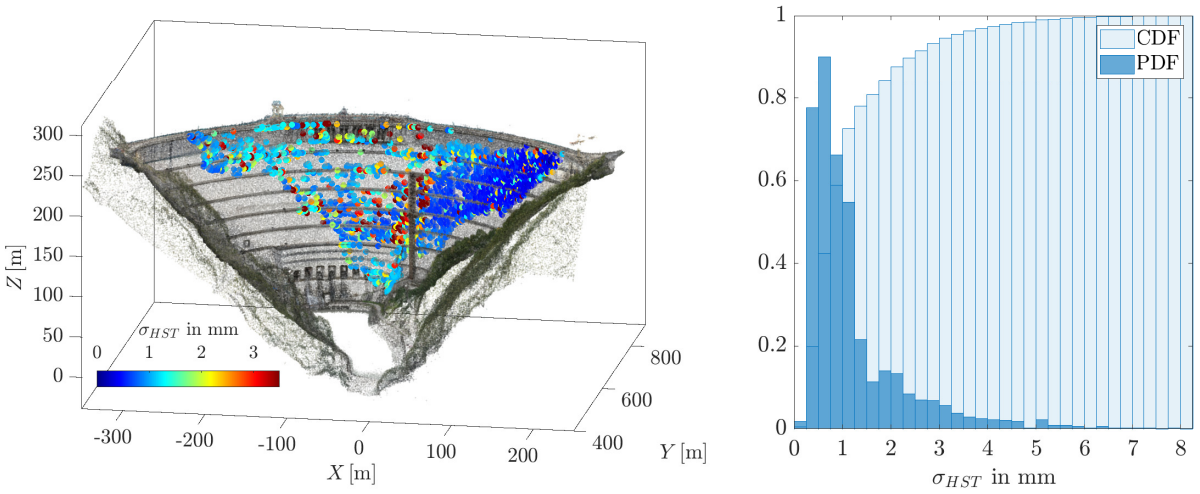

(a) Map of σ_{HST}

(b) Histogram of σ_{HST}

Figure 7.13: Statistics of σ_{HST} (a) Representation as a map on the dam structure and (b) Normalised histogram with PDF and CDF normalisation

The standard deviation error of the regression is also displayed in Figure 7.13a and mapped on the dam. While certain points exhibit high standard deviations, they account for less than 20% of the cumulative histogram depicted in Figure 7.13b. These outliers are distributed throughout the visible part of the dam, with a noticeable concentration around the metallic structure. This clustering might suggest a potential influence on neighbouring points. The consistency of the overall fit underscores the reliability of the proposed processing methodologies over more than two years of data. Given that the HST model encompasses multiple periodic terms with a one-year cycle, the fact that the fit remains accurate after this extended duration underscores the consistency of the processed displacement with a GB-SAR system in relation to water level variations.

A visualisation of two terms from the model is provided to quantify the estimated parameters. The first one is the most significant contribution of the dam's movement, i.e. the velocity w.r.t. the water level (a_1 in Equation 3.1). Displacement rate always refers to the rate w.r.t. the water level to lighten the description in the following paragraphs. The second factor is the periodicity, depending on the factor $s = 2\pi n_d/365.25$ with n_d the number of day since 1 January. The provided coefficient is a_6 in Equation 3.1, corresponding to the term before $\sin(s)$.

Figure 7.14a exhibits a pattern of higher displacement rates at the dam's centre, which is also what is expected. To offer a better visualisation, not only the single point geocoding is applied, but on all plausible points, according to Section 5.2.5. Subsequently, the resulting map is smoothed with a 3D Gaussian filter. The distribution of these rates, provided in Figure 7.14b points out maximal rates corresponding to 0.7 mm/m.

The periodic component of the displacement is significant, as it reaches a magnitude larger than one

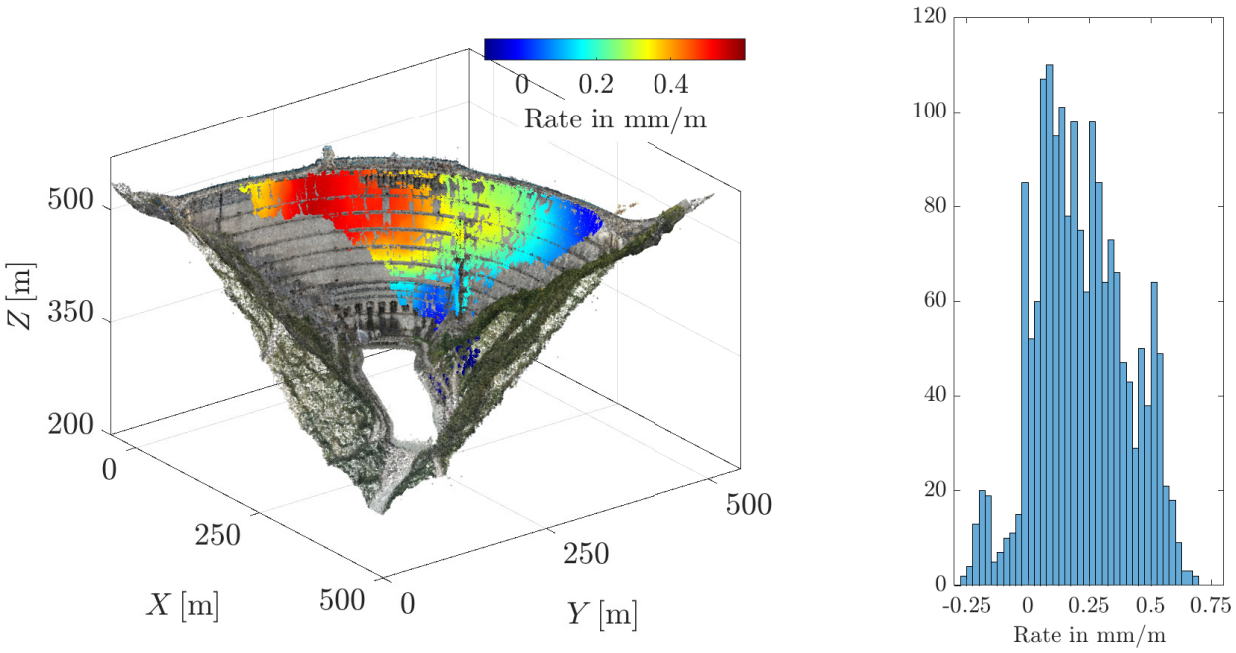

(a) Map (b) Histogram

Figure 7.14: Displacement rate w.r.t. the water level via HST regression

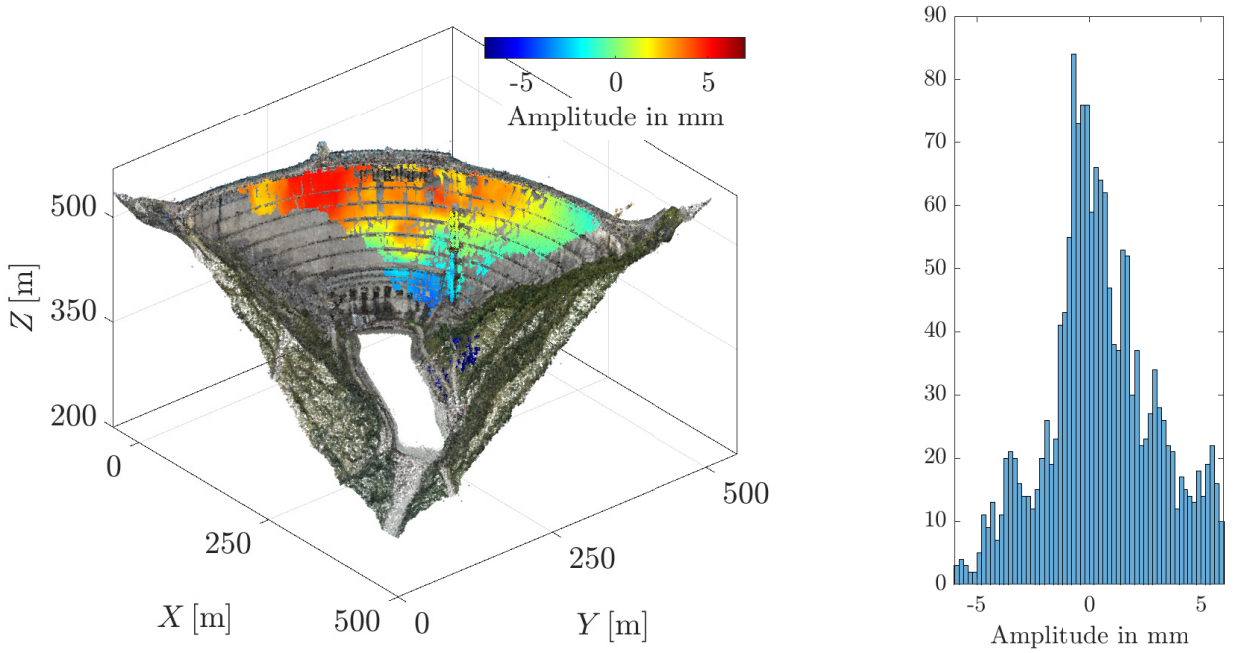

(a) Map (b) Histogram

Figure 7.15: Amplitude of the yearly periodic signal via HST regression.

centimetre over the dam in a year, as outlined by Figure 7.15b. The pattern provided in Figure 7.15a combines a gradient w.r.t. the dam's centre with an elevation gradient. This result is explained by the fact that points on higher levels are most of the time exposed to the air and consequently to temperature variations. In contrast, lower points are exposed mainly to the water, which exhibits a lower variability in temperature.

While more intricate deformation models could have been considered, this thesis does not delve into an exploration of the various factors influencing dam displacement and their underlying mechanisms.

7.6 Comparison with a numerical model

7.6.1 General considerations

The comparison is conducted on the first numerical model, computed for the comparison between the first and the fourth epochs. Therefore, the corresponding water levels are $wl_1 = 492.7\,\text{m}$ and $wl_2 = 453.0\,\text{m}$. As the averaged temperatures for the thermal effects are also in the model, we must consider periods around June and September. Figure 7.16 provides a visualisation of the comparable data from the continuous GB-SAR time series. The red patches describe the similar water levels $\pm 1\,\text{m}$ and similar dates $\pm\,15$ days as the parameters used in the numerical model for the first epoch. The blue patches consider the parameters for the second epoch. Then, interferograms can be constructed by finding the intersections of the patches and the curve corresponding to the water level at the SLC averaged acquisition time. The reference point used for the InSAR processing has been identified on the numerical model and its displacement has been subtracted on the whole model to conduct a relevant analysis.

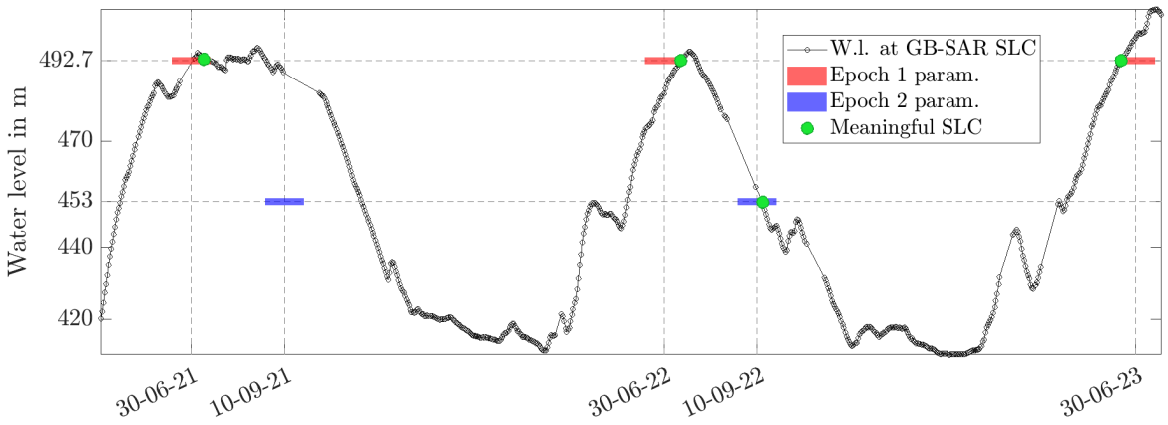

Figure 7.16: Comparable GB-SAR data with the numerical model.

Four acquisitions are identified as similar to the conditions of the numerical model parameters, but only one with the lowest water level and similar thermal considerations. Therefore, three distinguished comparisons are considered with the parameters given in Table 7.4.

	Water level 1 [m]	Epoch 1	Water level 2 [m]	Epoch 2
Numerical model	492.7	30 June	453.0	13 September
Comparison 1	493.0	10 July 2021	452.7	14 September 2022
Comparison 2	492.7	13 July 2022	452.7	14 September 2022
Comparison 3	492.7	19 June 2023	452.7	14 September 2022

Table 7.4: Parameters of the considered periods for the comparison.

7.6.2 Results

The GB-SAR displacement maps are obtained by computing the adequate differences on the integrated time series according to Table 7.4. As for the epoch-wise monitoring, the comparison requires resampling the GB-SAR data on the numerical grid with an averaging interpolation of the nearest neighbours.

Figure 7.17 provides the displacement maps for the numerical models and the three GB-SAR measurements. The displacements expected by the numerical model in Figure 7.17a differ slightly from the GB-SAR displacement maps. However, they expose very similar patterns between each other, which is another qualitative indicator of the consistency of the developed workflow for the processing of GB-SAR data.

The computation of the differences and relative differences between the numerical and the GB-SAR is conducted as in Section 6.3, i.e. $\mathbf{\Delta d} = \mathbf{d}_{\text{GB-SAR}} - \mathbf{d}_{\text{NM}}$ and $\mathbf{\Delta d}_r = (\mathbf{d}_{\text{GB-SAR}} - \mathbf{d}_{\text{NM}})/|\mathbf{d}_{\text{NM}}|$ respectively. The analysis of the histogram in Figure 7.19a enables accessing the distribution of the difference, and the key statistics are summarised in Table 7.5.

	Comp. 1	Comp. 2	Comp. 3
$\mathbb{E}(\mathbf{\Delta d})$ [mm]	2.94	3.80	2.20
$\sigma_{\mathbf{\Delta d}}$ [mm]	4.48	4.44	4.04
$\text{med}(\mathbf{\Delta d}_r)$ [%]	12	17	14
$\text{CI}_{95}(\mathbf{\Delta d}_r)$ [%]	$[-57\,;100]$	$[-55\,;73]$	$[-55\,;60]$

Table 7.5: Statistics of the difference between the numerical model and the GB-SAR at *Warehouse*.

The mean difference for all comparisons is lower than 4 mm but always positive, meaning that the results tend to a lower displacement extracted from the GB-SAR measurements than the one from the numerical model. The standard deviations are similar and lower than 5 mm. These quantities are in adequacy with what has been observed in Section 6.3. Up to minor variations, the three difference maps in Figure 7.18 show nearly identical patterns. Both maps attest to a more significant displacement measured by the GB-SAR on the dam's left upper side (from an upstream point of view). However, the central part of the dam exhibits lower displacements from the GB-SAR measurements. The analysis of the relative displacement map emphasises the significance of the negative cluster on the left embankment of the dam, corresponding to a higher measured displacement. The bottom part of the dam may be affected by lower displacements, according to these graphics.

The difference of the displacement maps between the same model and the *Pavel* station (Figure 6.18c) shows the same tendency as what is observable from the *Warehouse* station, i.e. the central part presents lower displacement values from the GB-SAR. At the same time, the left side is affected by larger displacements. For the latter part of the dam, the GB-SAR measurements are reliable and

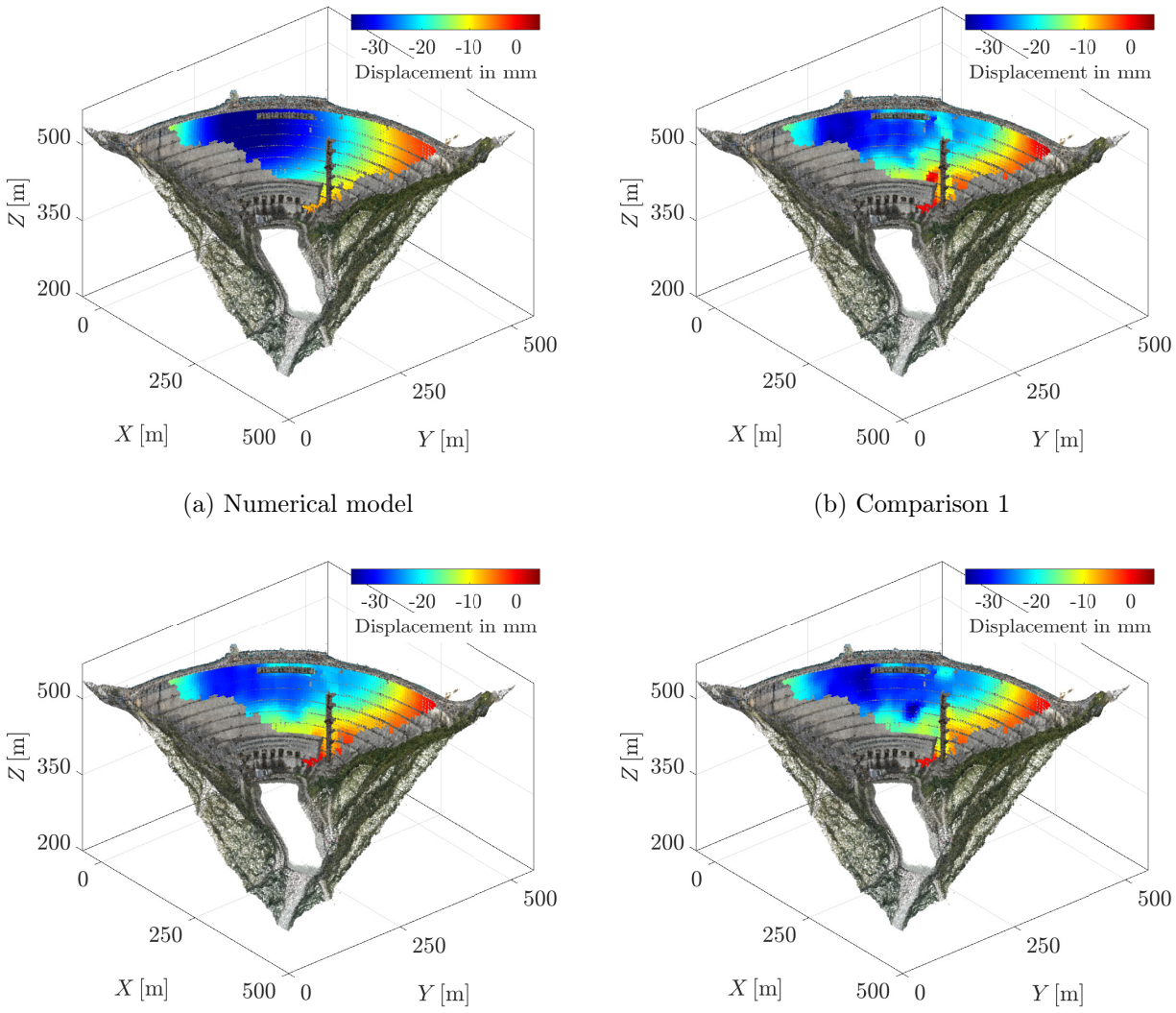

(a) Numerical model

(b) Comparison 1

(c) Comparison 2

(d) Comparison 3

Figure 7.17: Displacement from the model and the three corresponding GB-SAR measurements.

can provide a way of improving the numerical model parameters. Especially, taking a closer look at the plumbline layout in Figure 3.3, the line P26 does not go up to the dam crest, meaning that the model may undergo inaccuracy due to the lack of information available. However, the central part is affected by significant layover for both stations, and doubts can subsist in the signal's origin, which may expose an underestimation of the true displacement values.

A more intensive analysis of the relative error histograms in Figure 7.19b indicates that most relative differences for both comparisons are between 0% and 50%. Their spatial representations in Figure 7.18 emphasise that the difference in the central part of the dam is considerably less significant than the difference on the left side of the dam.

The comparison does not provide information about the precision of the results extracted from the GB-SAR measurements, as too many parameters can introduce deviations between the numerical models and real measurements. However, it proves the consistency of the developed workflow for

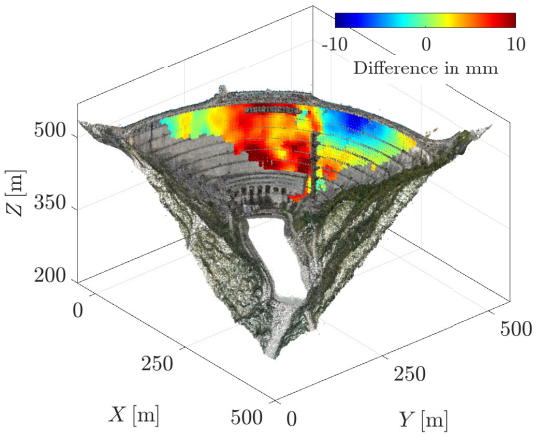

(a) Difference - Comparison 1

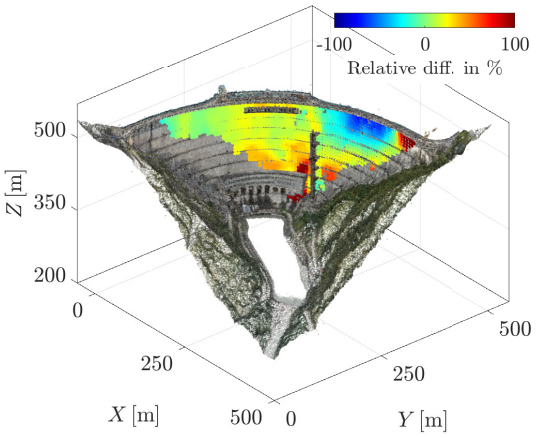

(b) Rel. difference - Comparison 1

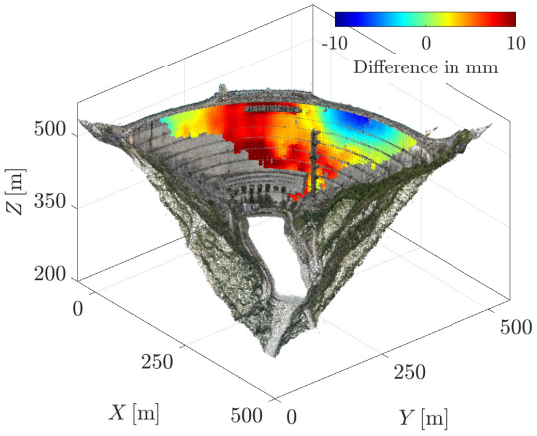

(c) Difference - Comparison 2

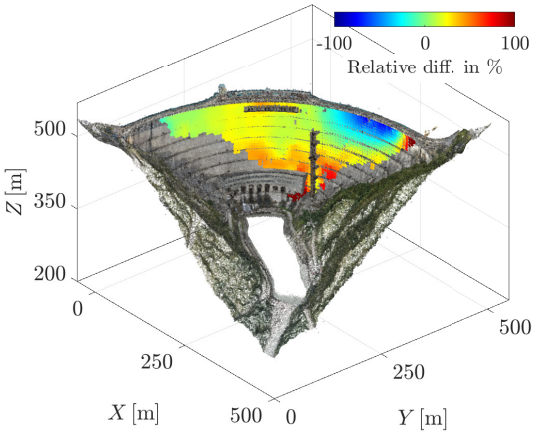

(d) Rel. difference - Comparison 2

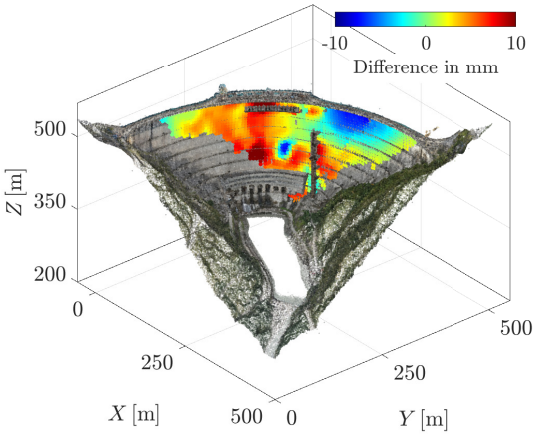

(e) Difference - Comparison 3

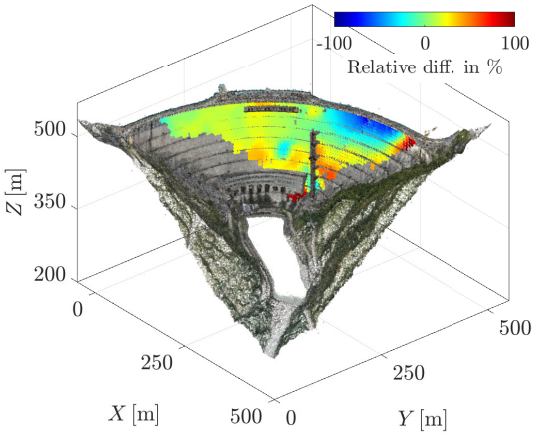

(f) Rel. difference - Comparison 3

Figure 7.18: Difference and relative difference maps between the GB-SAR and the numerical model.

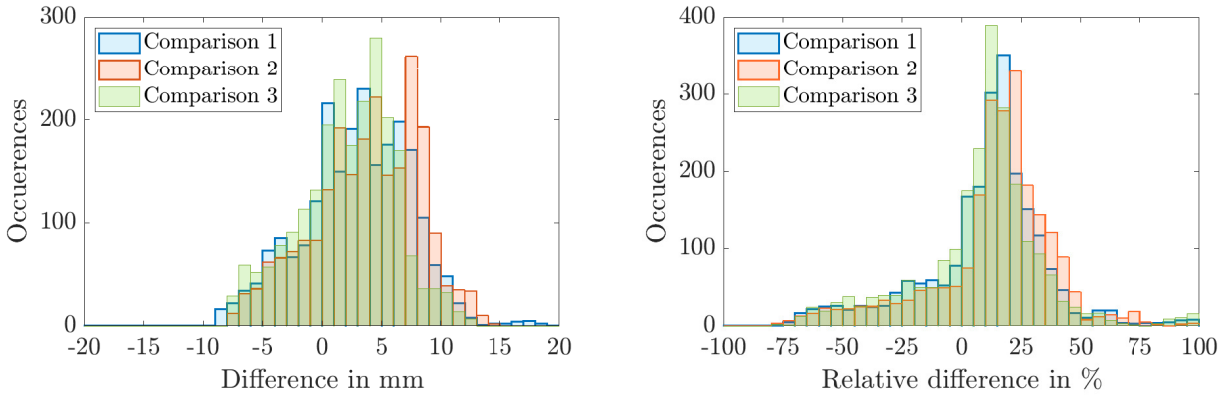

(a) Histogram of differences

(b) Histogram of relative differences

Figure 7.19: Histograms for the evaluation of the differences between the numerical model and the GB-SAR displacement maps.

GB-SAR monitoring over two water level cycles.

7.7 Evaluation with GNSS sensors

7.7.1 General considerations

In April 2023, four GNSS antennas were installed on the dam crest to assess its deformation with a continuous and absolute measurement tool. Their localisation is provided on an aerial view with Figure 7.20a. The stations G_1, G_2 and G_4 are located on the downstream side of the dam, while G_3 provides a similar location as G_2, but on the upstream side.

The measurements consist of the station positions measured every 30 seconds on the L_1 frequency. From 1st April 2023 to 4th September 2023 for the three points G_1 to G_3. An interruption occurred at point G_4 from 31st July 2023 and was not solved remotely. The data processing was achieved by the *Geodetic Institute of Karlsruhe* using the software *RTKLib*, with a reference station based 1.3 km far from the dam. The results are daily averages of the 3D displacement vectors for each station. In the study of [Hassan et al., 2018], the GB-SAR and GNSS time series are compared by estimating the 3D displacement vector based on the assumption of the motion's direction. The results of the latter work based on one day of data show only a low correlation of the time series due to the amount of noise in the data. In the proposed case study, the GNSS displacement vectors are projected on the LOS of the GB-SAR for adequate comparison. The GB-SAR processing using the DBAS approach is conducted in the same period.

The comparison with the GNSS stations enables us to examine the effect of the reference point on the GB-SAR results. Indeed, the choice of this reference point should be an adequate compromise between the detected displacement and error propagation. Therefore, four different spatial references are selected, and the resulting time series are compared to the GNSS results. The reference areas are visible in Figure 7.20b and are noticed with the letters R_k, $k \in [|1\,;4|]$. They express different meaningful choices for the GB-SAR processing. R_1 is the choice aiming at recovering the absolute displacement of the dam. It is located at 150 m of the dam and can be assumed as fixed. However, atmospheric turbulences between this point and the dam are possible sources of increasing noise in

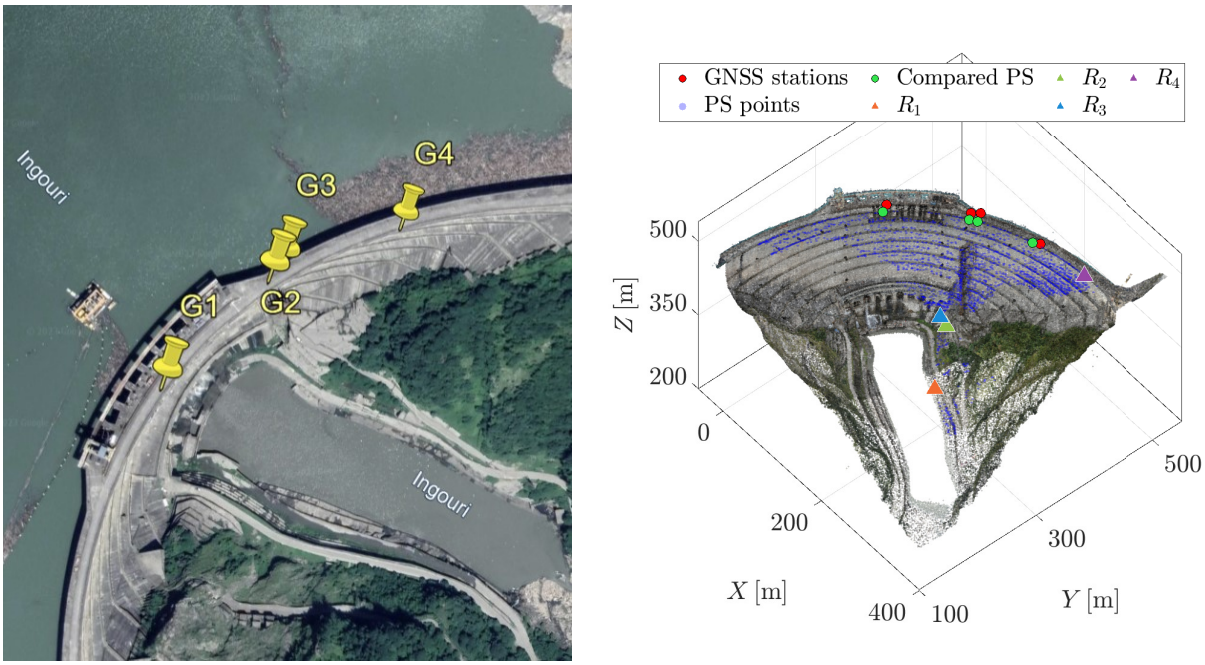

(a) GNSS stations ©Google Earth

(b) Data used for the evaluation

Figure 7.20: Presentation of the GNSS stations available at Enguri Dam. (a) is an aerial overview, and (b) exposes the data used for the comparison.

the processed time series. R_2 is the nearest point to the dam that is not located on it. R_3 and R_4 are two possibilities of reference on the bottom and the side of the dam, respectively. The recovered times series using the latter references are expected to expose a smaller displacement, as it is relative to the dam itself. However, the precision should be higher as fewer external perturbations should occur. The latter figure also contains the position of the GNSS stations in red and the nearest PS point to each station in green. The distance can be up to 12 m, which needs to be considered for the comparison.

7.7.2 Results

The results for each GNSS station and the corresponding nearest PS point are provided in Figure 7.21. A general consideration over all the points is that GB-SAR results provide lower displacement values, which are substantially accentuated using reference points on the dam. However, it is also evident that the dispersion of the time series around the displacement curves is reduced using those reference points. As an example, the mean and standard deviation values of $\overline{\sigma}_{\hat{\mathbf{y}}}$ from Equation 7.31 over all the selected PS are given in Table 7.6.

Reference	Far: R_1	Near: R_2	Bottom: R_3	Side: R_4
$\mathbb{E}(\overline{\sigma}_{\hat{\mathbf{y}}})$ [mm]	0.71	0.68	0.49	0.43
$\mathrm{Std}(\overline{\sigma}_{\hat{\mathbf{y}}})$ [mm]	0.17	0.14	0.13	0.14

Table 7.6: Evaluation of the precision of GB-SAR measurements, depending on the reference point.

The maximum amplitude of displacement, reached in the middle of July 2023, is well recovered using

the furthest reference point for points G_1 and G_2. The corresponding magnitude of displacement is slightly smaller using the nearest reference point. What is interesting is the considerable difference existing between the blue and green curves, expressing the use of point R_3 and R_2, respectively. Even if the reference points are separated by a distance of 33 m, the reference point R_3 on the dam undergoes a non-negligible displacement up to 12 mm. The displacement magnitude is considerably smaller for the comparison with points G_3 and G_4, even using the furthest reference point. Point G_3 is on the opposite side of the dam, which can explain this difference. The remaining atmospheric contributions are supposed to be the major factor of the difference arising for the antenna G_4.

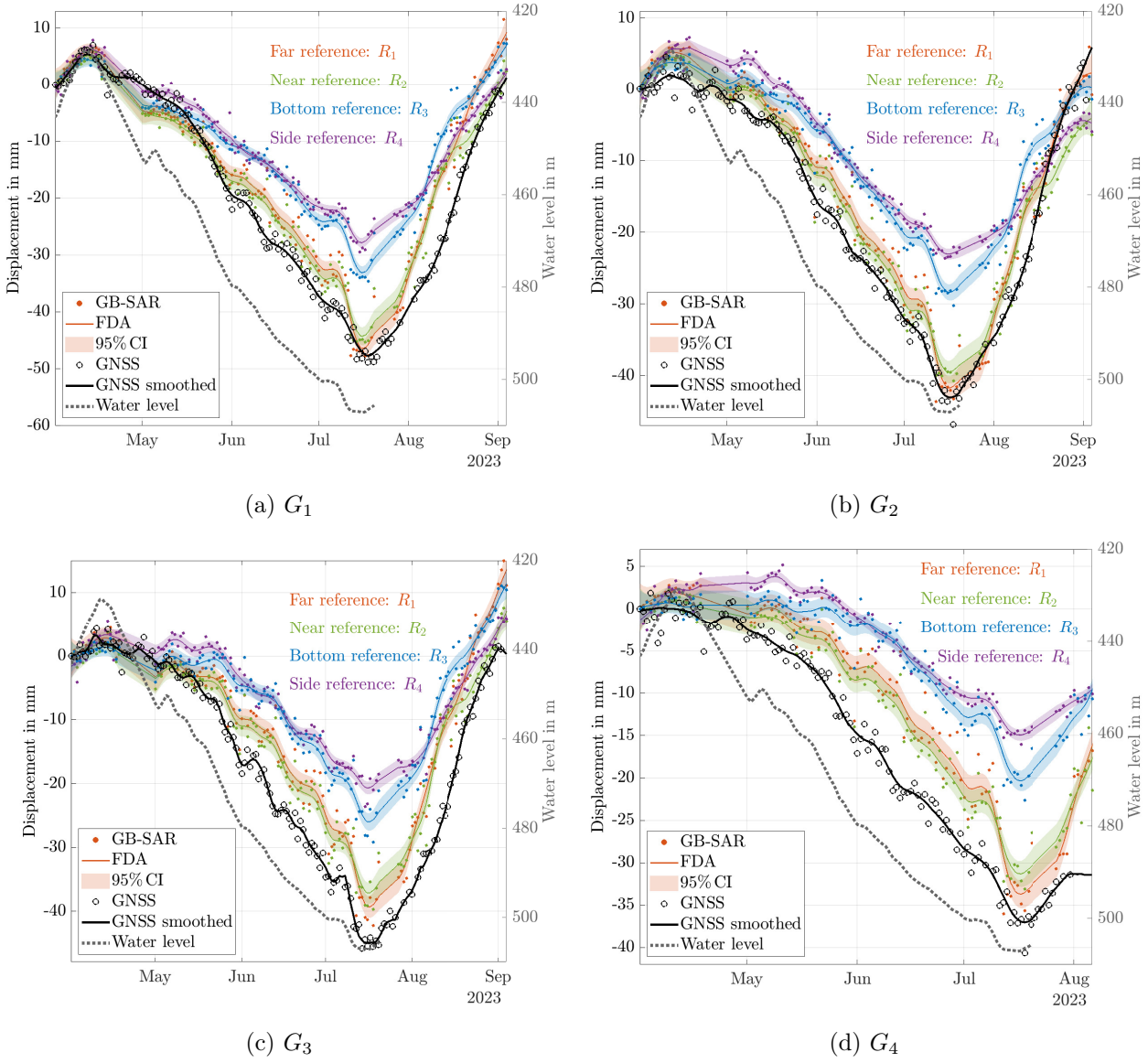

(a) G_1 (b) G_2

(c) G_3 (d) G_4

Figure 7.21: Displacement from the GNSS and the GB-SAR measurements using the four different reference points.

To have a quantified analysis of the difference occurring between the GB-SAR results and the GNSS, the differences with the time series referenced with the point R_1 are computed, and the histograms are exposed in Figure 7.22. For most of the time series and all the GNSS stations, the magnitude of

the differences is below 10 mm, corresponding to a relative difference under 50 %. Several factors can explain this difference. Firstly, the compared points are different, as the GNSS points are installed on pillars on the dam crest while the GB-SAR PS points are on the wall. The thermal expansion of the reinforced concrete does not affect the points identically. Secondly, residual atmospheric signals (both for GNSS and for the GB-SAR) can achieve a magnitude order of several millimetres. Finally, the reference points are not the same as already presented.

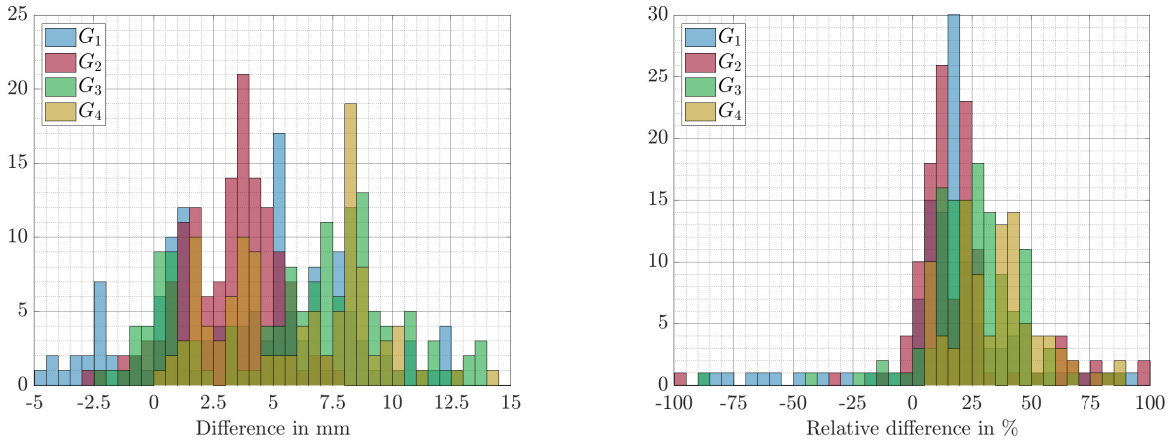

(a) Histogram of differences

(b) Histogram of relative differences

Figure 7.22: Histogram of (a) differences and (b) relative differences between GNSS and GB-SAR, using the reference point R_1.

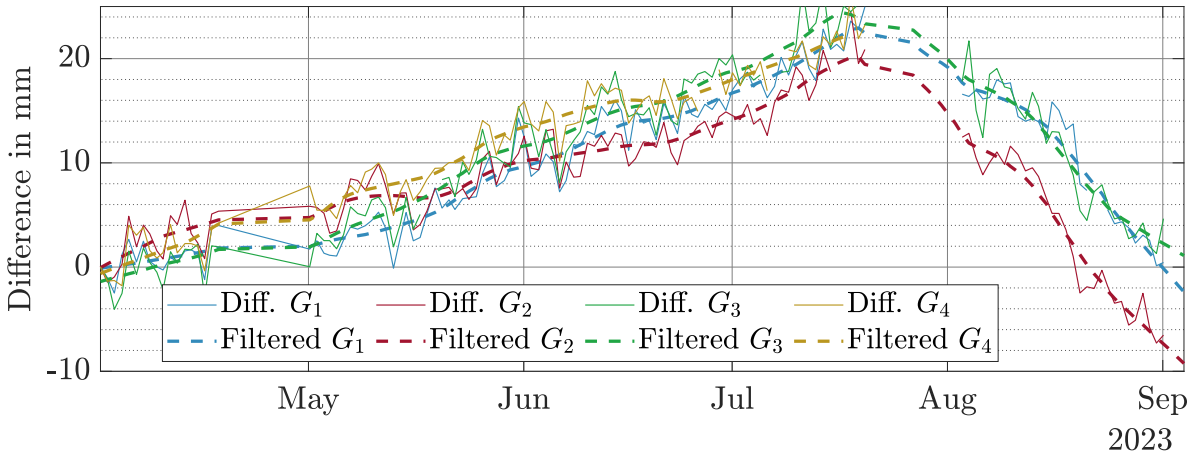

Figure 7.23: Time series of the differences between the GB-SAR and GNSS time series using the reference R_1.

The time series of the residues between the results from both instruments are given in Figure 7.23. The GB-SAR reference point considered is R_1. The raw residues are represented with solid lines, and a filtered version is proposed with dashed lines. The latter curves show a similar trend for the four points, expressing the difference in reference points used for the respective processing. Therefore, it is possible to analyse if a consistent trend is also expressed using the reference point R_4, located on the top of the dam crest. These curves expressing the differences between the GNSS and GB-SAR

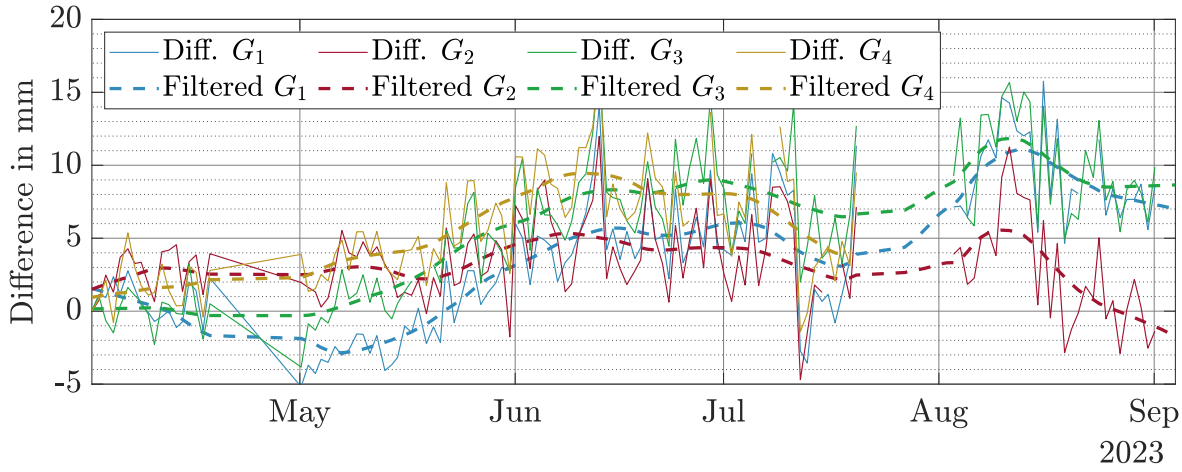

Figure 7.24: Time series of the differences between the GB-SAR and GNSS time series using the reference R_4.

time series are provided in Figure 7.24. The consistency between the four curves validates this hypothesis. The magnitude of the differences compared to those using the reference point R_1 is two times larger, reaching up to 25 mm. Nevertheless, the amplitude of the noise is considerably smaller. For each curve, the variations of the noisy differences around the filtered ones reach magnitudes of 5 mm, which is twice lower than the preceding case.

For both differences, the red curve corresponding to point G_4 starts to significantly deviate from the two others in August. Even if this drift resembles an unwrapping error integration, the use of the LAD estimator rejects this hypothesis. Indeed, the unwrapping errors are identifiable as jumps using this estimator and not as smooth deviation as with the LS inversion.

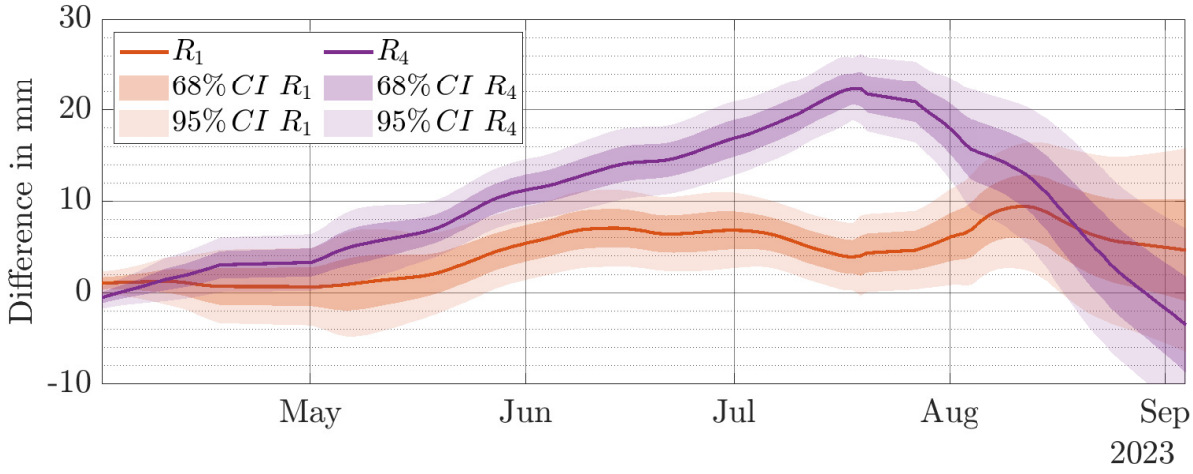

Figure 7.25: Absolute offset between the GB-SAR and the GNSS using the reference points R_1 and R_4.

This analysis enables the proposal of an enhanced absolute geodetic monitoring method, combining both solutions. The core concept is to reference the GB-SAR results on the structure itself to recover its relative displacements with very high precision. Following that, the use of GNSS antennas on

the structure enables an estimate of the absolute offset. The offset between the GNSS sensors and the GB-SAR can be used to determine the motion of the reference point. The computation of this mean offset with the Enguri Dam data is achieved for reference points R_1 and R_4. The mean curve of Figure 7.25 is computed using the filtered differences from Figures 7.23 and 7.24. After that, the standard deviation is calculated and represented as 68 % and 95 % intervals respectively. The average standard deviation over the time is lower than 2.5 mm for both cases.

The GNSS time series presented in Figure 7.21 consistently present a displacement near 0 mm at the end of the observation periods, expressing that the points are at the same location as in April. Interestingly, the purple curve in Figure 7.25 also falls to zero. Therefore, the GB-SAR time series using the reference R_4 expresses the same consistency as the GNSS results. However, the average difference using R_1 remains above this value and does not express the same behaviour. The main reason is the atmospheric signal. Due to the coordinates of the stable area, only the range component of the atmospheric signal is estimated. As the reference point R_4 is also on the dam crest, the height-dependent part of the atmospheric signal is not expressed on the PS-point used for the comparison. However, the reference point R_1 is 230 m under the dam crest and the difference of height-dependent atmospheric conditions is included in the time series.

Even if the comparison could not have been achieved on the whole GB-SAR data, the consistency of the proposed workflow over six months comforts the precision of the GB-SAR sensor for infrastructure monitoring. Further investigation on longer periods should be undertaken to estimate any signal drift in the GB-SAR processing chain due to atmospheric signals.

7.8 A final detour: adaptation for near real-time monitoring

Up to this point, the developed method enables long-term monitoring by daily averaging ideal scenes. The estimation of the time series is achieved as a single post-processing. However, this approach does not fully harness the potential of the very high temporal sampling rate of the GB-SAR. In this section, we introduce an alternative flowchart that considers all the data for continuous monitoring and is based on a temporal block decomposition of the data. Inside a signal block, the processing is the same as the one described in Figure 7.4, excluding the atmospheric correction and the FDA processing. Therefore, only the block creation and concatenation are detailed. A single difference is that the phase unwrapping is only performed when at least one value of the set of residual phase ϕ_{res} falls outside the range of $[-\frac{\pi}{2}\,;\frac{\pi}{2}]$. When all phase values remain within this interval, it can be reasonably assumed that the phase gradient between neighbouring points will always remain under π. With two minutes between acquisitions, it can avoid unwrapping up to 70% of the interferograms. This modified approach is referred to as block-wise SBAS (BW-SBAS).

7.8.1 Block decomposition

In a study conducted in [Rebmeister et al., 2022b], it is demonstrated that the most effective approach to have a reliable highly sampled and extended GB-SAR time series is to decompose them into blocks and conduct an SBAS inversion for each one. For near real-time (NRT) monitoring, the comparison in the latter work is conducted against a sequential and a block-wise single master (BW-SM) approach. The sequential configuration consists of creating interferograms with only a baseline of one acquisition. The time series is recovered by summing the phase differences. While it offers the advantage of not requiring to wait for multiple acquisitions, its susceptibility to unwrapping errors is substantial due to a lack of redundancy and sensitivity to noise and atmospheric

disturbances. The BW-SM approach requires waiting for several acquisitions to be applied. When the acquisitions of one block are completed, the scene in the middle of the block is chosen as the master for the interferogram formation. While lacking network redundancy, the unwrapping errors are not integrated, as each interferogram in a block is unwrapped independently of the preceding ones. Despite these alternatives, the BW-SBAS strategy, which incorporates network redundancy in each block, emerged as the superior choice for the GB-SAR processing chain. Despite the longer processing time attributed to the LAD estimation, it remains significantly shorter than the acquisition time. [Wang et al., 2019a] also shares this preference for this configuration. However, the workflow proposed in that work has a significant limitation: all blocks are treated independently. They are processed consecutively, and if users require information covering the period spanning two blocks, they need to process both blocks entirely to obtain the integrated time series across the desired period. This approach becomes impractical for extended periods, as the number of scenes can quickly escalate into several thousand, rendering the SBAS inversion computationally infeasible.

As it is valuable to reconstruct the integrated time series, a method is proposed to merge the individual blocks. Indeed, as part of the DAMAST project, the study at Enguri Dam presented in [Ottenburger et al., 2023] required the most extended integrated displacement time series with the highest sampling rate possible. This displacement time series is used to train a neural network to better understand the relationships between the displacement of the dam and external factors like water level or global temperature. A certain degree of overlap is introduced during the creation of the individual blocks to facilitate this fusion process. This overlap is strategically incorporated to ensure that the overlapping sections correspond to time intervals with the smallest noise.

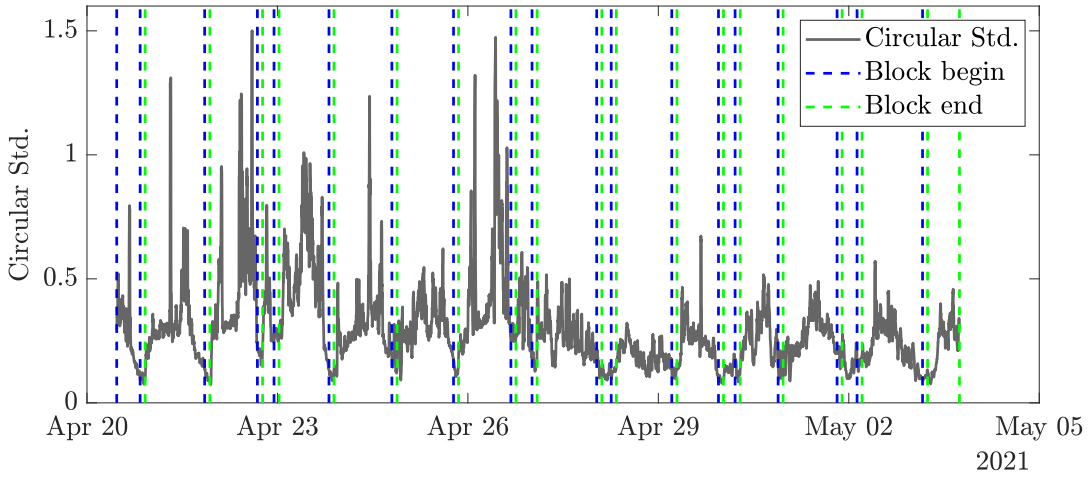

Figure 7.26: Blocks separation over 10 000 scenes with $N_{\min} = 200$, $N_{\max} = 800$, $N_{\text{ov}} = 60$ from *Warehouse* station.

The preprocessing is achieved on the first 20 scenes as for the DBAS approach. The output of this step is a substantial reduction of data, yielding a set of geocoded PSC $\mathcal{S}_{ini}$. A statistical analysis is conducted on sequential interferograms to determine the optimal block overlap. Certain parameters need to be predefined, such as the minimal and maximal block sizes, denoted as $N_{\min}$ and $N_{\max}$ respectively, and the number of overlapping scenes desired N_{ov}. It follows that the number of scenes processed within the k^{th} block must satisfy the condition $N_k \in [|N_{\min}\,;N_{\max}|]$. From a recursive point of view, assuming that for the k^{th} block, the last scene is acquired at the instant $t_{N_k}^{(k)} = t$, then the new block starts at $t_0^{(k+1)} = t - N_{\text{ov}}\Delta t$. After the beginning of each new block,

all the acquisitions until $N_{\max}$ must be awaited to compute the circular standard deviation[2] of each sequential interferogram and determine for each new scene its amount of noise. This procedure generates a 1D curve that is smoothed with a moving average window of size N_{ov}. The minimum of this curve is computed and defines the end of the current block. The results on a reduced stack of 12 days are presented in Figure 7.26. The peaks observed on the curve coincide with scenes characterised by elevated noise levels and should be avoided as periods to merge blocks.

7.8.2 Block concatenation

A different number of PSC is processed for each block. For all the PSC in $\mathcal{S}_{\text{ini}}$, the pixel selection is refined in each block, retaining only the points that provide a mean amplitude dispersion over the block lower than 0.5. Therefore, each block k contains a different number of PSC $\mathcal{S}_k \subseteq \mathcal{S}_{\text{ini}}$. Considering block k and $k+1$ and their respective temporal sampling sets $\mathcal{T}_k$ and $\mathcal{T}_{k+1}$, the temporal overlap segment is denoted by $\mathcal{T} = \mathcal{T}_k \cap \mathcal{T}_{k+1}$ and the same convention is used for the points i.e. $\mathcal{S} = \mathcal{S}_k \cap \mathcal{S}_{k+1}$. These notations are illustrated in Figure 7.27.

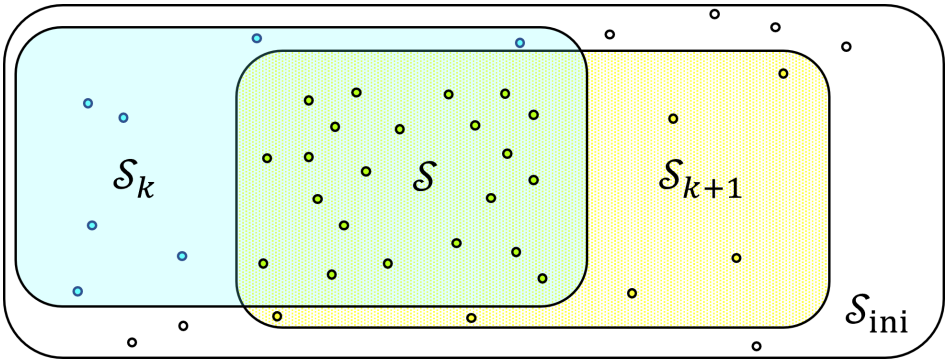

Figure 7.27: Common sets of points in block overlaps.

Two cases must be distinguished depending on the results of the two blocks processing. Either the considering point belongs to the two blocks, and the combination is relatively straightforward, or it appears in the current processed block and is missing in the previous one.

7.8.2.1 Consecutive processing

For a point P belonging to the two blocks, i.e. $P \in \mathcal{S}$, with the respective time series vector $\boldsymbol{\psi}_k$ and $\boldsymbol{\psi}_{k+1}$, the offset m is computed via the median to avoid the influence of potential localised unwrapping failures.

$$m = \text{med}\left(\boldsymbol{\psi}_k(\mathcal{T}) - \boldsymbol{\psi}_{k+1}(\mathcal{T})\right) \tag{7.27}$$

Then, the integrated and concatenated phase ψ is given by:

$$\boldsymbol{\psi}(j) = \begin{cases} \boldsymbol{\psi}_k(j) & \forall j \in \mathcal{T}_k \setminus \mathcal{T} \\ \frac{1}{2}\left(\boldsymbol{\psi}_k(j) + \boldsymbol{\psi}_{k+1}(j) + m\right) & \forall j \in \mathcal{T} \\ \boldsymbol{\psi}_{k+1}(j) + m & \forall j \in \mathcal{T}_{k+1} \setminus \mathcal{T} \end{cases} \tag{7.28}$$

[2]The circular standard deviation v is similar to the circular variance V (Equation 6.3) and is defined in [Mardia et al., 2000] as: $v = (-2\log(1-V))^{1/2}$.

7.8.2.2 Non-consecutive processing

The second case arises when a point P has not been processed in the previous block, i.e. $P \in \mathcal{S}_{k+1} \setminus \mathcal{S}_k$. In this context, only the unwrapped phase information $\boldsymbol{\psi}_{k+1}$ is available, and referencing on an existing time series is unfeasible. The proposed solution assumes a spatial local smooth deformation pattern. In this sense, the referencing can be done using neighbouring points belonging to $\mathcal{S}_k$ with an interpolation, as proposed in [Dörr et al., 2022a].

The $k_{nn} = 5$ nearest neighbours of the point P belonging to $\mathcal{S}_k$ are identified in the geocoded coordinates[3]. Based on the assumption, their inverse distance to P is used as weight for the interpolation. Then the offset m for the point k is computed via:

$$m = \text{med}\left(\overline{\boldsymbol{\psi}}_k(\mathcal{T}) - \boldsymbol{\psi}_{k+1}(\mathcal{T})\right) \tag{7.29}$$

with $\overline{\boldsymbol{\psi}}_k(\mathcal{T})$ the weighted mean of the integrated time series of the k_{nn} neighbouring points.

7.8.2.3 Uncertainty propagation

The standard deviation for the added time series is computed via:

$$\sigma_{\mathcal{T}_{k+1}} = \frac{1}{|\mathcal{T}| - 1} \sum_{j \in \mathcal{T}} \left(\boldsymbol{\psi}_k(j) - \boldsymbol{\psi}_{k+1}(j) - m\right)^2 \tag{7.30}$$

This uncertainty holds for the phase values in the newly aggregated segment. Then, considering M blocks and integrating them consecutively, the error propagation law can be applied and gives the final standard deviation for the last block $\sigma_{\mathcal{T}_M}$ with:

$$\sigma_{\mathcal{T}_M} = \sqrt{\sum_{k=2}^{M} \sigma_{\mathcal{T}_k}^2} \tag{7.31}$$

The relation shows that the uncertainty can only increase by increasing the number of blocks. As the residual signal after the filtering and unwrapping is added back, there is a theoretical constant offset between all the points of the two time series, and the uncertainty goes down to 0. If this signal is not added back or if unwrapping failures occur, it should be taken into consideration. The major uncertainty will be induced in case of blocks appearing and disappearing.

7.8.3 Results

For the analysis of the method capacities, the proposed flowchart is applied from the *Warehouse* station on a reduced data stack of 150 000 SLC images. The range of the possible block size is defined as $N_{\min} = 200$ and $N_{\max} = 800$ leading to more than $N_b = 300$ blocks and an overlap $N_{\text{ov}} = 5$. Data quality is assessed for each block, and two criteria are adopted. Each scene n that verifies $V(n) > 0.1$ is discarded to avoid strong atmospheric signals disturbing the processing. After that, only points expressing an amplitude dispersion in the block lower than 0.45 are processed.

[3]Again in this situation, it is important to work in the geocoded coordinates, as neighbouring points in the 2D GB-SAR geometry can express large distances in 3D.

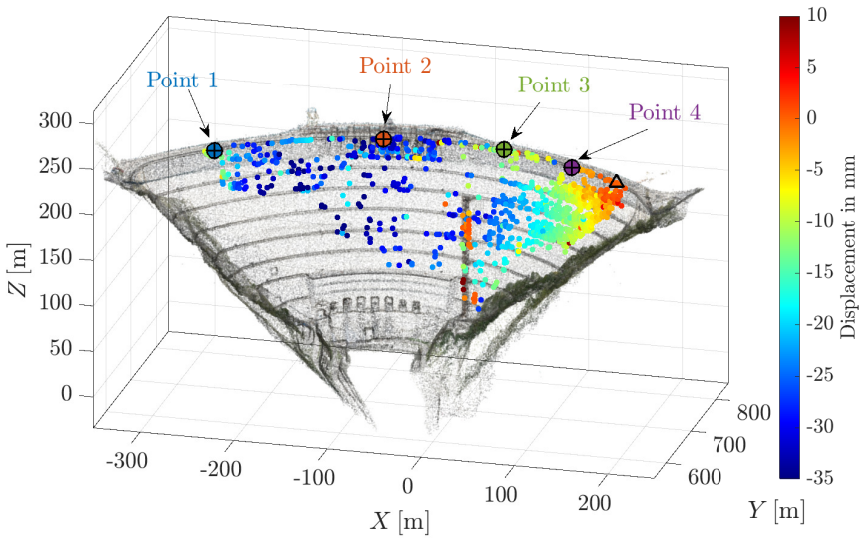

Figure 7.28: Selected points on the dam crest. The reference point is marked with a black triangle.

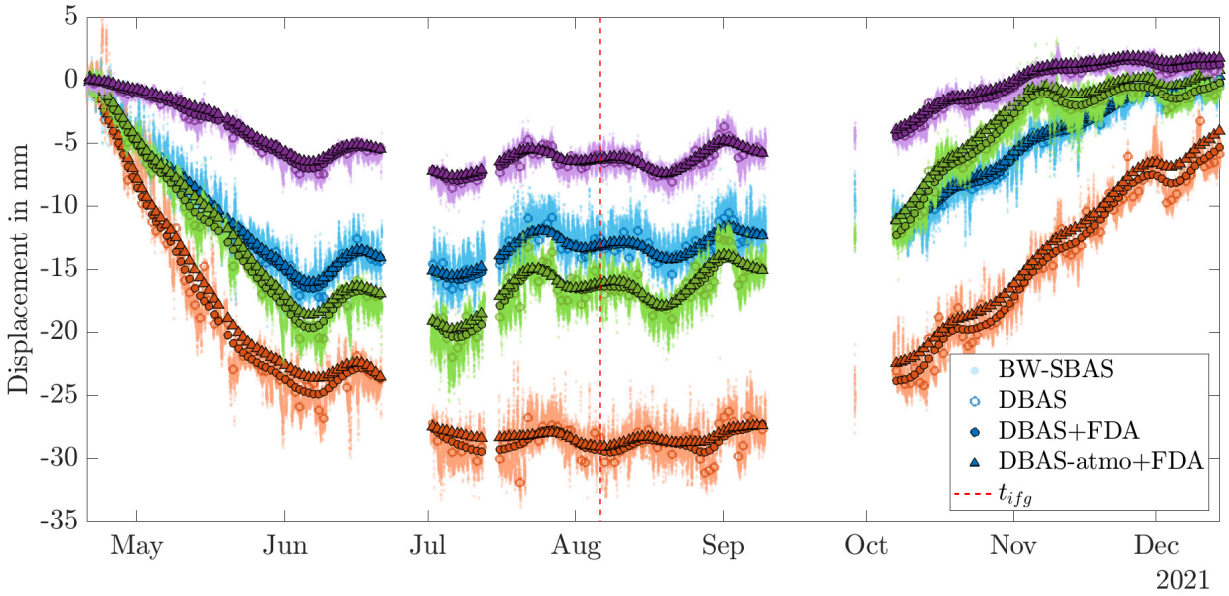

Figure 7.29: Time series of the four selected points for the comparison between BW-SBAS and DBAS..

After the phase integration of each block, the concatenation is applied, and the PSC that verify $\sigma_{\mathcal{T}_{N_b}} > 0.5$ are discarded. Compared to the DBAS approach where 1 947 points from 2 365 are conserved, only 900 remain with this approach, considerably reducing the number of reliable observations. No points lie on the surrounding rocks, meaning that the atmospheric correction can not be conducted on spatial assumptions as for the full DBAS approach.

Four points are selected on the dam crest, as pointed out in Figure 7.28. The displayed displacement map on the dam corresponds to the displacement observed at the time t_{ifg}, indicated by the red line on Figure 7.29, i.e. August 06, 2021. In the latter figure, three time series are compared for

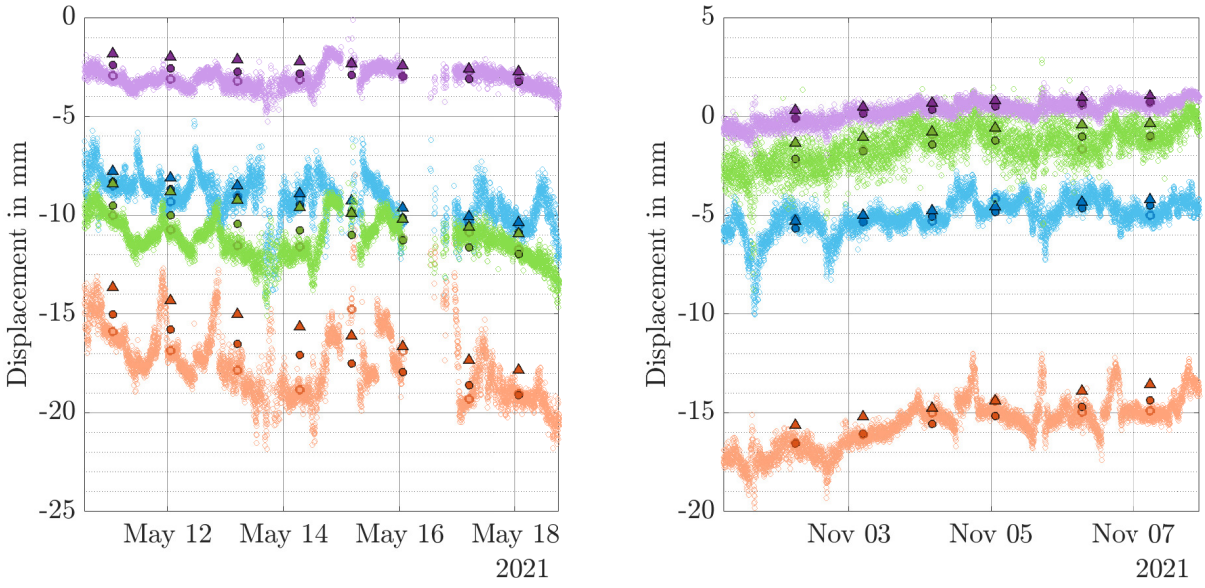

(a) Zoom in May

(b) Zoom in November

Figure 7.30: Focus on two specific periods for the comparison between BW-SBAS and DBAS.

each point, corresponding to the BW-SBAS solution and the DBAS solution, respectively, with and without the FDA processing. When the FDA is lead, another distinction is made by correcting and not correcting the range component of the atmosphere signal. To adequately compare the methods, the reference point is set at the same location, corresponding to the black triangle in Figure 7.28.

As the entire dam structure extends on similar ranges, the linear atmospheric range correction only has a maximum effect of 2 mm. The correspondence between all the time series is very strong, which validates both measurement concepts.

Figure 7.30 is focused on two specific weeks to have a deeper understanding of the BW-SBAS results. As no FDA processing is applied, the noise and the atmospheric signal are still contained in the time series. The internal variations of the measurements can be evaluated by the spread of the curves reaching up to 1 mm. However, the daily periodic variations of the points due to atmospheric turbulences reach a mean of 5 mm, which is non-negligible for geodetic monitoring. Using a temporal filter to remove these variations is equivalent to reducing the high temporal sampling of the GB-SAR and is not an enhancement w.r.t. the DBAS approach.

7.9 Conclusion

The proposed flowchart has been designed to enable long-term monitoring in a complex environment with a GB-SAR. The emphasis was made on the long-term stability to avoid drifts on the signal, and an approach based on daily average acquisitions called DBAS has been presented. Therefore, the signal was decomposed into three main parts to lighten the phase unwrapping step. Afterwards, the usage of the LAD estimation was applied for the phase integration. After deep modelling, the LAD estimator presented robustness even for 10% of the interferograms affected by unwrapping errors. The last significant advancement was the introduction of the FDA concepts to reduce the amount of noise through smoothness hypotheses. Working with continuous functions enabled us to

make assumptions on the derivatives of 2nd order to constrain the acceleration of the time series. Moreover, it can reduce the confidence interval through the restrictions the hypothesis requires.

The internal quality check via the temporal coherence showed a high quality reachable by the GB-SAR measurements through the proposed workflow. The time series investigation presented excellent adequacy to classical dam deformation models over two years and five months of data. The high temporal and spatial resolution enabled the fit of the time series with the HST model with a precision under 2 mm for the majority of the points. We provided a comparison with a numerical model that proved the high consistency and reliability of GB-SAR measurements with an adequate processing chain. Moreover, it provided the localisation of a possible model deficiency that requires further investigation.

The last validation was achieved using the four GNSS stations installed on the Enguri Dam crest in April 2023. The comparison over six months enabled us to assess the importance of choosing the reference point for GB-SAR processing. Regarding the precision, using a reference point on the dam is the best option, at the cost of only observing a relative and underestimated structure displacement.

A second flowchart was proposed to recover the integrated time series on a full temporal sampling with the GB-SAR. However, an internal quality check showed that less than half of the points could be preserved over a half-year period. On this time stamp, the atmospheric and noise influence could not be corrected due to the unavailability of points on surrounding rocks for a sufficient time. This influence represents daily variations up to 5 mm and the usage of GB-SAR for real-time and early-warning monitoring for infrastructure should consider a way to correct the atmospheric signal quickly with meteorological sensors.

Two major investigations on the proposed method with the FDA could be developed. Firstly, the hypothesis in the specific context of dam monitoring could be based on more relevant physical assumptions. The restriction on acceleration is the most common criterion. However, applying a penalty based on the HST model, or at least on the water level, could avoid a too severe smoothing in case of strong and fast water level change. The second advancement could be the utilisation of spatial information. Currently, the spatial information is only used for the phase unwrapping. Using FDA in a spatial context could also avoid some outliers and would allow the recovery of a smoother spatial displacement map.

Finally, the comparison with GNSS antennas also offers insights into the possible future integration of both systems. The GB-SAR provides spatially and temporally dense, relative, 1D displacement maps. Referencing the latter results on the GNSS point-wise, absolute, 3D time series using adequate integration can provide an incomparable geodetic monitoring system. This geodetic monitoring system would have the full potential to calibrate an accurate numerical model through the dense coverage of the GB-SAR combined with the absolute information of the GNSS.

CHAPTER 8

Conclusion and outlook

8.1 Conclusion

This work aimed to explore the potential use of GB-SAR for large-scale infrastructure monitoring, in particular dams. While GB-SAR offers notable advantages, such as high-resolution imaging and high precision, its limitations can hinder its effectiveness for this specific purpose. Through a considerable dataset acquired at Enguri Dam in Georgia, this research delved into developing novel methods and algorithms to optimise the usage of GB-SAR for geodetic monitoring. Three significant contributions were introduced to enhance the processing of GB-SAR data for this specific application. The first one was focused on the acquisition geometry. The second one was the development of interferometric processing techniques for dam monitoring. Finally, the third contribution was the assessment of the GB-SAR as a reliable additional sensor for continuous dam monitoring through diverse comparisons.

Geometry

The GB-SAR must be adequately referenced in an external 3D model to analyse the acquired data correctly. A complete workflow was developed in Chapter 4 to correct these parameters automatically. The first significant improvement of the processing chain is the ray tracing algorithm P-RaySAR, specifically adapted for the GB-SAR geometry. Indeed, the path of the signals falling in each pixel can be reconstructed by introducing a perspective point of view and applying the GB-SAR focusing equations. The introduction of the *radar equation* on the signal reflection enables the simulation of radar images, which are used to correct the system's azimuth. This estimation was conducted on three different datasets, and the evaluation with corner reflectors depicts an accuracy higher than the resolution of a pixel. The other development is the reconstruction of the elevation of the observed points from the system itself via TomoSAR techniques. This approach offers substantial advantages over traditional DEM interferometry, particularly for large-scale infrastructure monitoring, where non-smooth behaviours can characterise interferograms. The utilisation of this output allows for the recovery of the system's position relative to an external 3D model. While the accuracy of this method is low compared to external measurements, it can help to significantly decrease large offsets on the instrument's position when no external information is available.

Once the system is referenced on the external 3D model, the two aforementioned tools (namely P-RaySAR and TomoSAR) were used in Chapter 5 for a deeper understanding of the sources of the observed signal. At Linach Dam, the arches induce multiple signal reflections and strong shadows. The developed tools enable to avoid the geocoding of coherent signals in the shadow areas. At Enguri Dam, two of three stations suffer from extreme layover with points of the external model with elevation differences up to 150 m falling in the same pixel. A Bayesian estimator based on an intensity model has been developed to overcome layover and foreshortening problems. This model is grounded on the incidence angle of the signal and the antenna pattern of the sensor. The TomoSAR output replaces these models if tomographic measurements are available, as the tomographic intensity profile can be used to construct the prior function. TomoSAR is based on real signal processing and can recover the origin of the signal. Therefore, it is considered superior to the intensity model. The method was evaluated at Linach Dam, where the classical method geocoded several points on the ground. The introduction of the proposed algorithm enabled the correction of a significant part of this false geocoding. At Enguri Dam, the evaluation with corner reflectors indicated a notable improvement in areas suffering from medium layovers. When the layover reaches extreme values, i.e. up to 150 m, the results showed the limitation of the method. In the case of the *Warehouse* station, up to a slight curvature, almost all the dam is perpendicular to the LOS of the system, and it is challenging to geocode the information of a pixel affected by such a layover. These difficulties also emphasise the plausibility of the signal and raise the question of its origin. If the observed signal is a combination of several areas on the dam without significant differences in amplitude, it remains challenging to interpret for deformation analysis.

The two developed techniques enable a considerable improvement in the accuracy of the point location in case of complex infrastructure monitoring. This point is crucial when conceiving the combination of GB-SAR and other sensors, as the correction of the PS location can be up to several tens of meters.

After this focus on the geometry, this thesis proposed the development of interferometric processing chains to estimate the displacement of the dam.

Interferometry

The interferometric processing was studied in the case of epoch-wise monitoring in Chapter 6. An alternative unwrapping approach was developed for stations involving highly complex geometry to recover the full displacement signal. It uses a very accurate position of the points on the structure as a prerequisite, available through the preceding developments. As the geometric properties of specific infrastructures may not lend themselves well to conventional phase unwrapping, it is possible to process the observed GB-SAR interferograms in an alternative image plane. This technique becomes feasible when the monitored infrastructure's geometry can be approximated using two principal axes. The displacement signal can be effectively recovered by projecting the wrapped interferogram onto this plane and unwrapping it along these directions. The plane is determined by extracting the two main eigenvectors of the principal component analysis of the geocoded point cloud of the persistent scatterers (PS). Considerable improvements have been achieved using this geometry for the phase unwrapping. Furthermore, the correction of atmospheric and repositioning signals was investigated. In contrast to many natural scenarios, the latter signals cannot be estimated by assuming stable areas as predominant in the interferogram. It can only be determined from a small subset of PS assumed stable. The effects of extrapolating the estimation on this limited set were examined, underscoring a decreased precision. Installing meteorological sensors on the structure could help to conduct this estimation.

The final improvement developed in this thesis was conducted on long-term continuous monitoring with a GB-SAR, illustrated through a practical case study spanning a period of two years and five months. The methodology was strategically designed to use the GB-SAR as a robust tool for displacement mapping. The first step is an effective data reduction concept, focusing on computing daily averages from the set of SLC images based on their low mean amplitude dispersion. This approach aims to enhance the data's overall signal-to-noise ratio. During the interferometric processing, various optimisations were proposed to address potential temporal inconsistencies arising during SAR processing, such as those linked to phase filtering or the integration process within SBAS networks when employing classical least squares estimators. Implementing the least absolute deviations estimator for the inversion of SBAS networks can reliably recover the correct time series up to 10 % of unwrapping errors. The employment of functional data analysis concepts considerably reduces the noise in the output time series. Applying the developed workflow at Enguri Dam enables obtaining approximately 2 000 points on the dam as reliable PS. When external parameters like water level and temperature converge, time series of points across the dam also converge, expressing a high consistency through time. Displacement time series show strong stability over time and fit the classical Hydrostatic-Season-Time (HST) dam deformation model with high adequacy.

The final part studied the feasibility of processing all the scenes for long-term monitoring. The results provided a significant decrease in the number of observed PS, even for a period of six months. With the high amount of data provided by the sensor, it seems not yet possible to achieve a geodetic monitoring over several years with a sampling of two minutes. Despite this, it remains valuable for short-term emergency analysis of dams in seismic environments.

The results of both methodologies were extensively evaluated to assess the validity of the GB-SAR for long-term deformation monitoring.

Validation

The time series of the GB-SAR monitoring at Enguri Dam were compared to two independent sources of information. The first one is composed of two numerical models calibrated on the plumblines. The second one is the GNSS time series of four stations installed on the dam crest.

The comparison of the epoch-wise monitoring on two different GB-SAR stations and the two numerical models presented a global similarity that can assess the validity of the developed methodology. However, as the structure covers a significant part of the interferograms, the correction of the atmospheric signal with spatial models is limited. Therefore, the accuracy of the estimated displacement maps is downgraded. Still, the GB-SAR can be used in an epoch-wise configuration to detect anomalies in the model. Indeed, the case studies showed a significant difference between the model and the GB-SAR results from both stations on the dam crest, encouraging their validity.

For continuous monitoring applications, the GB-SAR system has been demonstrated to be a reliable tool for determining dam displacements based on daily samples. Indeed, this research marks the first instance of using a GB-SAR system for long-term dam monitoring and proposed an in-depth evaluation of the system's characteristics and capabilities. Firstly, the results of the GB-SAR were compared to one numerical model by computing adequate differences on the integrated time series. The consistency of the differences exhibits that the proposed flowchart is reliable and does not suffer from strong unwrapping errors. Secondly, the time series of each nearest PS point was compared to the corresponding GNSS sensor and exposed the importance of the choice of the referencing point for the InSAR analysis with ground-based systems. The high correlation between both time series proved the correctness of the GB-SAR results but also the lack of being an absolute geodetic

measurement sensor. Moreover, it must be noticed that the *Warehouse* station used in this study is not optimal in terms of its geometry, coverage of the dam, and average distance to the dam. If a more stable environment could have been established at the *Georges* station, it is reasonable to expect that the quality of results would have been substantially enhanced.

Throughout this work, several benefits, as well as remaining constraints, were underscored. Specifically, for the purpose of dam monitoring, employing a GB-SAR system for epoch-wise observations emerges as an effective sensor to obtain a dense and highly precise displacement map. The usage of adequate tools for accurate repositioning, as well as meteorological sensors, are still required to capitalise the full accuracy of the system. While these additional requirements come with associated costs, they remain significantly lower than the investment needed for acquiring a GB-SAR or any other TRI system, and should not be considered as limiting factors.

When compared to plumblines, the GB-SAR does exhibit a lower accuracy, typically within the range of a magnitude order, as the plumblines have an average measurement accuracy of 0.01 mm, with a repeatability of 0.1 mm. Moreover, specific algorithms should be applied to extract the benefits of the GB-SAR. The key advantage that the GB-SAR offers over all other geodetic sensors is its dense spatial and temporal coverage. For instance, at Enguri Dam, the presence of 38 plumblines yields only eight full lines, and not all of them go up to the dam crest. In contrast, the GB-SAR facilitates monitoring several thousands of points across the structure.

The plumblines can contribute to determining a spatial model for the material properties, as described in Chapter 3. In this context, the exceptionally high accuracy of plumblines is not a strict requirement, and the availability of denser measurements through GB-SAR could facilitate the estimation of parameters like Young's modulus even in regions with significant material property contrasts. This is particularly pertinent for arch dams, where parameters such as stiffness and material strength yield a substantial influence over the dam's behaviour and performance. At Enguri Dam, the comparison with the numerical model and the GB-SAR exposed a significant difference on the top left embankment of the dam where no plumblines are available. This outcome was observed consistently throughout the whole time series from the continuous monitoring and from the epoch-wise monitoring. Further investigations with other sensors should be considered to validate this information.

The plumblines also have two practical constraints compared to the GB-SAR. Firstly, their applicability is not feasible at all dams. The case of the Linach Dam is such an example, as plumblines can not be installed into the vaults. Furthermore, plumblines are restricted in terms of their range of motion (< 10 cm), which poses a significant challenge for dams with extensive displacement ranges or those exhibiting time-dependent drift in their displacements. In contrast, being a remote sensing technique, the GB-SAR is free from such physical limitations. Secondly, in terms of costs, a full installation of plumblines with a remote transmission at Enguri Dam would not be under 700 000 €, as pointed out in [Rebmeister et al., 2023], while the cost of a GB-SAR system is about 200 000 €. With the same budget, it would be feasible to deploy three GB-SAR systems and their collective information could be combined to enhance phase unwrapping consistency and to retrieve comprehensive 3D displacement vectors, thereby providing more valuable insights and data than a single set of plumblines.

8.2 Outlook

This thesis improved the quality of the results using a GB-SAR for long-term dam monitoring both in a continuous and epoch-wise configuration. The challenges that were overcome were the most important for a deep understanding of the potential of the GB-SAR for dam monitoring. Further investigation directions were also discovered for further autonomous usage of GB-SAR sensors for this specific purpose.

Multiple signal reflection analysis: The data acquired at Enguri Dam showed strong scattering signals behind the dam structure at different stations. Even if these points were discarded from the processing because they were not geocoded on the P-RaySAR signal reflection model, their high coherence could potentially lead to a selection as persistent scatterers. The use of P-RaySAR enables the identification of the multiple signal reflection path, but no processing was conducted to extract information. Their path analysis through the scene could be a way to enhance the comprehension of atmospheric effects through a tomography reconstruction.

Tomography: The introduction of tomographic measurements enabled to gain valuable knowledge for the subsequent deformation analysis. Several directions can be evoked for further improvement. First, the usage of more complex emerging algorithms based on deep learning could help to enhance the tomographic reconstruction. Secondly, the acquisition of several campaigns over time could help to further recover the elevation and a linear velocity w.r.t. to a given parameter.

Bayesian geocoding: Currently, the developed Bayesian model enables distinguishing the signal's origin in a pixel based on intensity models. As visible at Enguri Dam, in case of strong layover from similar structures, it is difficult to estimate the true origin of the point. The Bayesian model can be enhanced with other knowledge to refine the PS location. For example, a similarity criterion based on the time series of the PS, such as the coherence, could be introduced to ensure a smooth pattern in extreme layover scenarios.

Unwrapping improvement: Due to the development proposed for the unwrapping, the LAD estimator has a large majority of residues equal to $\pm 2\pi$. A smaller part can also have a value of $\pm\pi$. From this analysis, a study can be conducted to propose a robust correction method to avoid the rare deviation that can still happen during the phase integration of the SBAS network. Another possible improvement of the phase unwrapping could be the introduction of machine learning techniques. Indeed, with an available numerical model of the displacement and atmospheric models, it is possible to simulate many interferograms and give the wrapped and unwrapped versions for the training step. It could be helpful for very complex geometries as the *Pavel* station.

Functional data analysis: In the proposed work, FDA was used to estimate the continuous function behind the samples acquired by the GB-SAR. This method can also be applied to images [Wang et al., 2020c], and a significant enhancement of this method would be to find the adequate basis to work with FDA for GB-SAR image time series. It would be able to notably reduce the spatial point-wise noise still observable in some data.

Combination with meteorological sensors: In the case of large infrastructures, the current spatial models reach their limit. The installation of weather sensors to measure the three main parameters, i.e. temperature, pressure and humidity, is of highest importance. A reasonable spatial distribution of the sensor to create a refractivity index model for each acquisition would considerably enhance the accuracy of the system. Subsequently, it would be interesting to compare the results with and without the sensors and quantify the uncertainty resulting from their usage. At Enguri Dam, the sensor installation started in August 2023.

Full 3D displacement determination: The measurement setup at Enguri Dam was not optimal for a full 3D displacement reconstruction, which is why it was not achieved. As the dam is expected to undergo a smooth deformation pattern, promising methods developed in [Baumann et al., 2023] could be applied. It would be interesting to consider at least three stations offering extensive dam coverage with a shorter temporal baseline to assess the reliability of GB-SAR for vector reconstruction.

Fusion with other sensors: In this study, the system was considered as an autonomous monitoring system. The usage of other geodetic sensors is a promising way to enhance the possibilities offered by the sensor. First, a combination with an absolute measurement tool such as GNSS could convert the relative information from the GB-SAR through an absolute displacement map. Moreover, a fusion with plumbline data could be another valuable knowledge for atmospheric estimation and unwrapping failures mitigation.

GB-SAR and, more generally, terrestrial radar interferometer is a technology that is more and more used for different types of monitoring goals. While it is established for landslides and open-pit mines surveillance as an indispensable tool, its weaknesses hinder it from reliable structure monitoring. This thesis developed several processing tools that considerably reduce the weaknesses of the system, making it a valuable add-on for the latter purpose. In the specific context of dam monitoring, the application of GB-SAR helps to better understand the behaviour of the structure with a finer resolution, enhancing the safety of the dam's operations. Further hardware developments arose since the beginning of the thesis that could be valuable for dam monitoring. Rotating SAR [Michelini et al., 2019] or SAR with smaller wavelength [Pettinari et al., 2023] can offer wider coverage, higher sensitivity and easier deployment.

The final recommendations for the reliable application of the GB-SAR for dam monitoring are the following:

- Prioritise a deep study of the monitored site to find the best location for the GB-SAR which minimises the distortions and conserves the highest sensitivity possible. An external 3D model and the P-RaySAR simulator adequately solve this task.
- Consider the high influence of the atmospheric changes and find a way to minimise their influences. The use of external sensors and adequate reference points can mitigate these effects.
- Apply an adequate data processing strategy to mitigate unwrapping errors and drifts, with the advancements outlined in Chapter 7 offering significant improvements in this regard.
- Fuse the data of the GB-SAR with an absolute geodetic measurement to enhance and complete the obtained results.

APPENDIX A

Probability density function of the orientation angle

This appendix analyses the PDF of the orientation angle Ψ_0. Indeed, its standard deviation is easy to derive, but knowing the shape of the possible taken values is also interesting. A Gaussian distribution would present a much narrower peak than a uniform one. The presented solution has been derived by Alberto Michelini from *IDS Georadar*.

We consider the measurements X_L, X_R, Y_L, Y_R having the same standard deviation σ. We want to estimate X_0, Y_0 and Ψ_0. From Figure 4.1, we can extract the following quantities:

$$\begin{aligned} X_L - X_0 + \frac{L}{2}\cos(\Psi_0) &\sim \mathcal{N}(0, \sigma^2) \\ X_R - X_0 - \frac{L}{2}\cos(\Psi_0) &\sim \mathcal{N}(0, \sigma^2) \\ Y_L - Y_0 + \frac{L}{2}\sin(\Psi_0) &\sim \mathcal{N}(0, \sigma^2) \\ Y_R - Y_0 + \frac{L}{2}\sin(\Psi_0) &\sim \mathcal{N}(0, \sigma^2) \end{aligned} \tag{A.1}$$

The likelihood function $\mathcal{L}$ is given as a 4D symmetric Gaussian function with:

$$\mathcal{L}(X_0, Y_0, \Psi_0) = \frac{1}{(2\pi^2)\sigma^4} \exp\left(-\frac{1}{2\sigma^2} F(X_0, Y_0, \Psi_0)\right) \tag{A.2}$$

with $F(X_0, Y_0, \Psi_0)$ defined by:

$$\begin{aligned} F(X_0, Y_0, \Psi_0) = &\left(X_R - X_0 + \frac{L}{2}\cos(\Psi_0)\right)^2 + \left(X_R - X_0 - \frac{L}{2}\cos(\Psi_0)\right)^2 + \\ &\left(Y_L - Y_0 + \frac{L}{2}\sin(\Psi_0)\right)^2 + \left(Y_R - Y_0 + \frac{L}{2}\sin(\Psi_0)\right)^2 \end{aligned} \tag{A.3}$$

The maximisation of the likelihood function is determined by searching the 0 values of the partial derivatives, which are given by:

$$\begin{aligned} \frac{\partial F}{\partial X_0} &= -2(X_L + X_R - 2X_0) \\ \frac{\partial F}{\partial Y_0} &= -2(Y_L + Y_R - 2Y_0) \\ \frac{\partial F}{\partial \Psi_0} &= L\left[\cos(\Psi_0)(Y_L - Y_R) - \sin(\Psi_0)(X_L - X_R)\right] \end{aligned} \tag{A.4}$$

The maximum likelihood estimates of the parameters are given by:

$$\begin{aligned} \hat{X}_0 &= \frac{X_L + X_R}{2} \\ \hat{Y}_0 &= \frac{Y_L + Y_R}{2} \\ \tan(\Psi_0)) &= \left(\frac{Y_R - Y_L}{X_R - X_L}\right) \end{aligned} \tag{A.5}$$

With those parameters, the length of the rail is estimated via:

$$\hat{L} = \sqrt{(X_R - X_L)^2 + (Y_R - Y_L)^2} \simeq L \tag{A.6}$$

The expression of the maximum likelihood function can be given by:

$$\mathcal{L}(\hat{X}_0, \hat{Y}_0, \hat{\Psi}_0) = \frac{1}{(2\pi)^2\sigma^4} \exp\left(-\frac{(\hat{L} - L)^2}{4\sigma^2}\right) \tag{A.7}$$

Finally, the probability density function of Ψ_0, denoted with $f_{\Psi_0}(\psi_0)$ is expressed as follows:

$$f_{\Psi_0}(\psi_0) = \frac{\mathcal{L}(\hat{X}_0, \hat{Y}_0, \psi_0)}{\int_{-\pi}^{\pi} \mathcal{L}(\hat{X}_0, \hat{Y}_0, \psi_0))d\psi_0} \tag{A.8}$$

$$= \frac{1}{2\pi I_0\left(\frac{L^2}{2\sigma^2}\right)} e^{\frac{L^2}{2\sigma^2}\cos(\psi_0 - \hat{\Psi}_0)} \tag{A.9}$$

with the approximation that $L \simeq \hat{L}$. We can recognise a Von Mises distribution with the parameters $\mu = \hat{\Psi}_0$ and $\kappa = \frac{L^2}{2\sigma^2}$, which is also known as the circular normal distribution.

APPENDIX B

Orientation estimation at *Georges* station

This appendix presents the results of the georeferencing of the GB-SAR station at the *Georges* station with the method presented in Chapter 4. The estimation of the azimuth based on image simulation is presented.

At *Georges* station, the coordinates were also measured with a GNSS antenna, meaning only the orientation angle needs a correction. As the CR were oriented in the direction of the long-term *Warehouse* station, they are less visible from the *Georges* station. However, three of them are identifiable, enabling computation of some statistics of the offsets, as in Chapter 4.

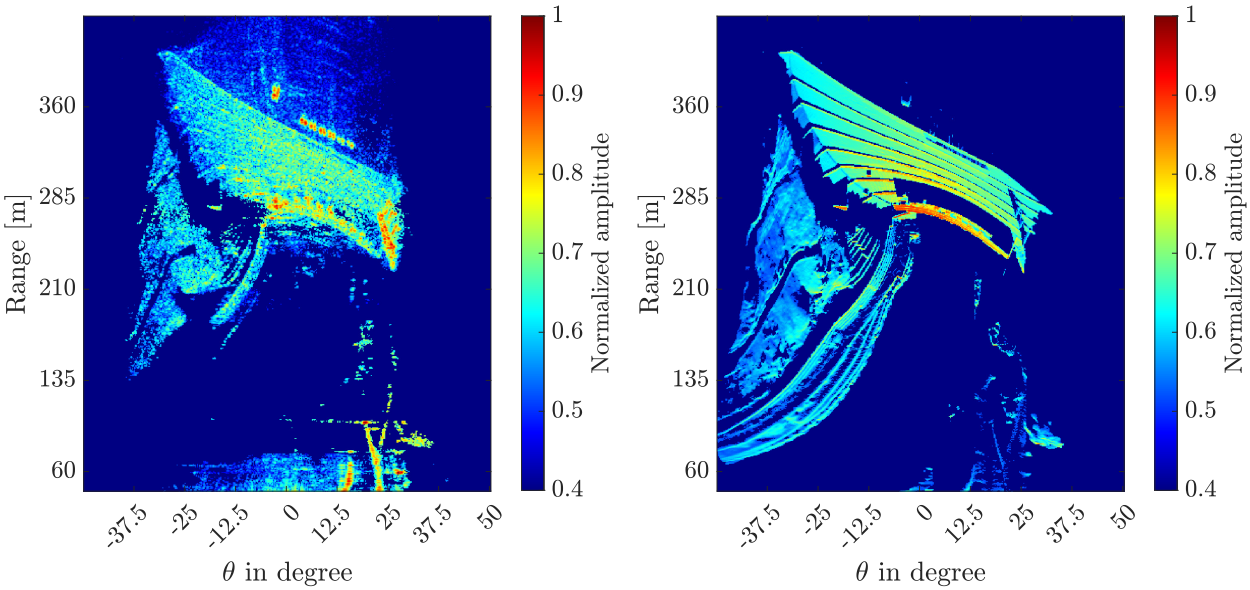

(a) Real normalised image

(b) Simulated normalised image

Figure B.1: Comparison between real and simulated radar image.

Figure B.1 shows the real and simulated images in the (r, θ) geometry. The main differences come from the metallic structures that reflect strongly the radar signal but are not well simulated. This point can be overcome by manually separating the point cloud during the image simulation and enhancing the RCS coefficient for the metallic structures. The NCC output is displayed in Figure B.2 and recovers an offset of more than 1.5°. The offsets presented in Table B.1 show a considerable reduction, up to 9 m for the x coordinate.

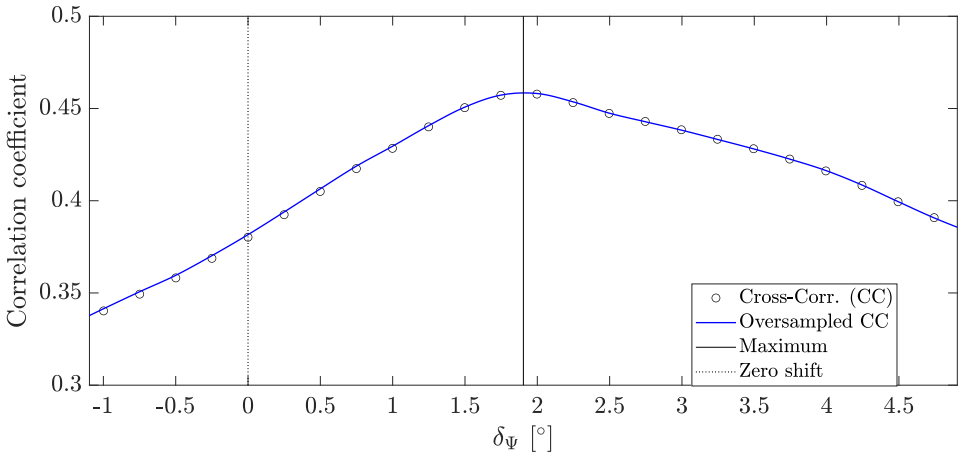

Figure B.2: Cross correlation output.

Quantity	$\mathbb{E}[x - \hat{x}]$	$\sigma_{x-\hat{x}}$	$\mathbb{E}[y - \hat{y}]$	$\sigma_{y-\hat{y}}$	$\mathbb{E}[r - \hat{r}]$	$\sigma_{r-\hat{r}}$	$\mathbb{E}[\theta - \hat{\theta}]$	$\sigma_{\theta-\hat{\theta}}$
$\mathcal{X}_0$	8.99	0.56	-2.42	0.61	-0.23	0.36	1.76	0.09
$\hat{\mathcal{X}}_{\text{SAR}}$	0.14	0.46	-0.29	0.41	-0.23	0.36	0.03	0.09

Table B.1: Offsets between detected CR and transformed and projected CR.

APPENDIX C

Multiple signal reflection using P-RaySAR

This appendix is dedicated to the analysis of a disturbing area in the PSC at Enguri dam from the *Warehouse* station. According to these results, the TomoSAR results recovered the position of points under the dam. This is the first indicator that some other signals disturb the phase in the acquisition. This phenomenon is confirmed during the interferometric process, where the same area presents a completely different phase than the neighbouring points. Figure C.1 shows the area on both tomographic and interferometric data.

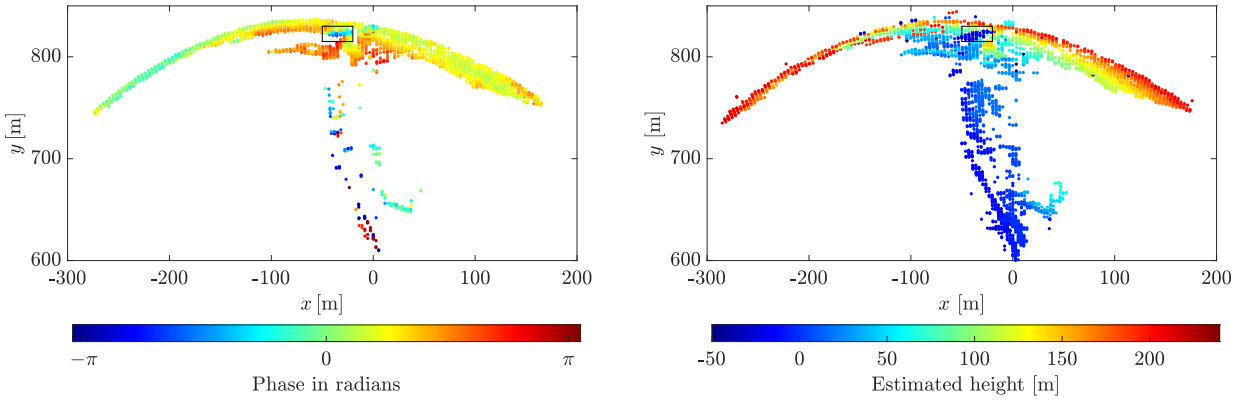

(a) Example of Interferogram

(b) TomoSAR results

Figure C.1: Disturbed area at Enguri dam (a) Example of interferogram and (b) results of the TomoSAR processing (First pixel). The black box is focused on the area.

Using P-RaySAR, it is possible to select these pixels and to recover all signal reflection paths that fall in the corresponding resolution cells according to Equation 4.6.

Figure C.2 represents in red the single bounces of the corresponding area. The interferometric phase of these points is interpretable as a LOS displacement. The blue lines are the rays corresponding to double bounces in this area. The signals are first reflected against the left side of the bottom

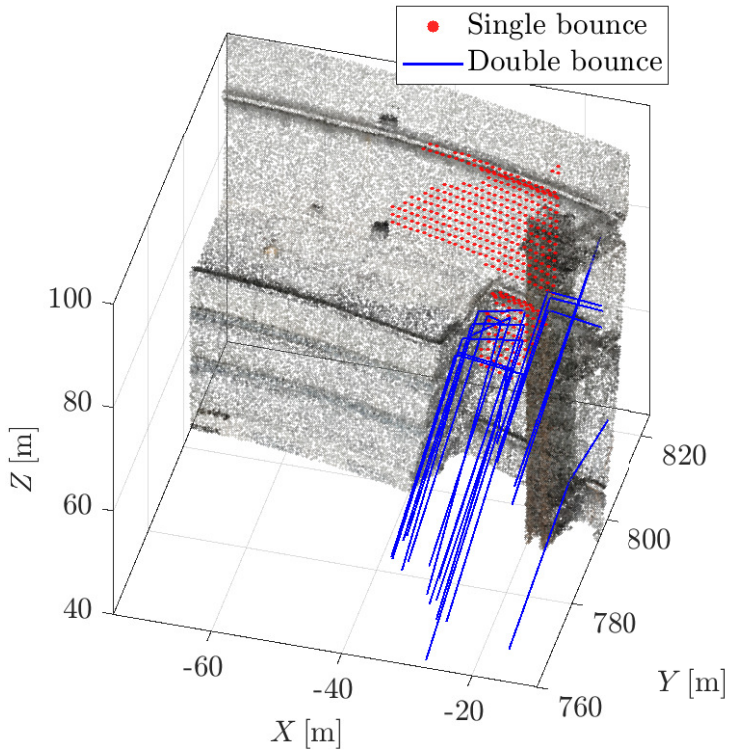

Figure C.2: Signal path of the selected pixels.

structure of the dam and then on the dam wall after returning to the sensor. The mesh of the neighbouring metallic stairs was of lower quality, meaning that it is not possible for P-RaySAR to recover the signal path through it accurately. However, we can also consider that the proposed signal path is extendable to a similar pattern with this structure. The signals following this path are not directly extractable in LOS displacement as the increased length of the path could not necessarily correspond to LOS movement anymore but could happen on each part of the ray.

A further step is to detect automatically disturbed areas using P-RaySAR. A solution would be to compute the received intensity based on physical models and analyse if the amplitude is significantly stronger for multiple signal reflections than for single ones.

APPENDIX D

FDA spline smoothing

D.1 Basis functions

The basis used for estimating the continuous function x is the B-spline basis. The small introduction presented in this appendix is inspired from [De Boor, 1978] and [Ramsay et al., 2009].

We consider the observations available by the vector $\mathbf{y} = [y_1, ..., y_N] \in \mathbb{R}^N$ and sampled at time $\{t_1, ..., t_N\}$ also called the knot sequence. The sequence is sorted in non-decreasing order, with possibly multiple knots equal to the same value. It is possible to construct piece-wise polynomial functions of degree $n-1$ from these knots. The higher the degree, the smoother the output function, in the sense of continuous derivatives up to a certain order. The B-spline basis elements constructed with these piece-wise polynomials are of order n. The definition of the basis components is achieved recursively using the following Cox-de Boor relations:

$$B_{k,0}(t) = \begin{cases} 1 & \forall\, t \in [t_k; t_{k+1}] \\ 0 & \text{otherwise} \end{cases} \tag{D.1}$$

$$\forall\, j \in [1; n-1], \quad B_{k,j}(t) = \frac{t - t_k}{t_{k+j} - t_k} B_{k,j-1}(t) + \frac{t_{k+j+1} - t}{t_{kj+1} - t_{k+1}} B_{k+1,j-1}(t) \tag{D.2}$$

A B-spline curve is a linear combination of the basis components, such that the curve $\boldsymbol{B}$ is expressed as:

$$\boldsymbol{B}(t) = \sum_{k=1}^{N} c_k B_{k,n}(t) \tag{D.3}$$

the coefficients c_k are determined in this thesis using Equation 7.19. The number of B-spline basis n_b used is defined in [Ramsay et al., 2009] as:

$$n_b = n + \underbrace{N - 2}_{\text{number of interior knots}} \tag{D.4}$$

The B-spline basis functions of order four and for ten knots are displayed in Figure D.1.

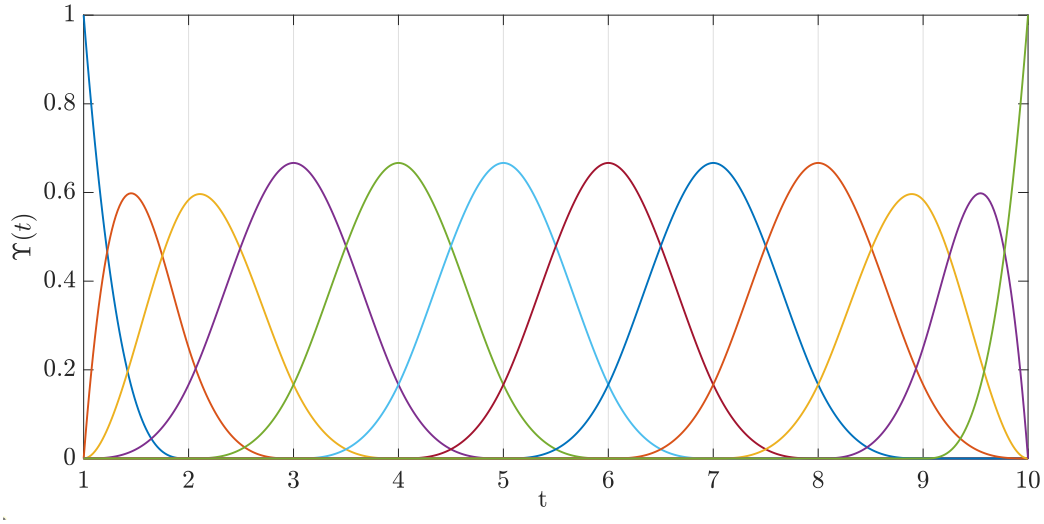

Figure D.1: B-spline basis of order 4 and 10 knots.

The advantage of B-spline basis functions is their link with the Bernstein polynomial, as derived in [Ershov, 2019], leading to a possible analytical expression. This property directly links the B-spline curves with the Stone-Weierstrass theorem, assessing that every continuous function on a closed interval can be uniformly approximated as closely as desired using a polynomial function. The derivation of this theorem is based on the construction of the Bernstein polynomials.

D.2 Choice of the penalty parameter

In Equation 7.19, a penalisation parameter λ_{pen} is introduced to estimate the coefficients of the B-spline basis according to Equation 7.19. The choice of this parameter is of the highest importance as it expresses the impact and the strength of the imposed penalty criterion. When $\lambda_{\text{pen}} \to 0$, the penalty has no effect, while $\lambda_{\text{pen}} \to \infty$ does not take in consideration the measurements.

A purely theoretical analysis is not available, and the method consists of testing several parameters and analysing the generalised cross-validation $\mathcal{G}$, defined as:

$$\mathcal{G}(\lambda_{\text{pen}}) = \left(\frac{N}{N - \nu(\lambda_{\text{pen}})}\right)\left(\frac{\|\mathbf{e}\|_2^2}{N - \nu(\lambda_{\text{pen}})}\right) \tag{D.5}$$

with the same notations as in Section 7.4, i.e. $\mathbf{e}$ is the vector of the residues and $\mu(\lambda_{\text{pen}})$ is the degree of freedom of the equation system. The right part corresponds to the error variance of the estimation $\hat{s}$, and the left part can be seen as a discount factor.

An example with the same dataset used in Section 7.5 is displayed in Figure D.2. The generalised cross-validation is tested on a wide range from 10^-4 to 10^4. The minimum is displayed with the red dotted line, indicating a minimum for $\lambda_{\text{pen}}) \approx 60$. From the graph, it is also clear that the value of $\mathcal{G}$ is not highly sensitive w.r.t. the choice of λ, in the sense that $\mathcal{G}$ is very similar for values between 10 and 100. [Ramsay et al., 2009] mention that in this case, it is unnecessary to lead investigations with high resources to accurately and precisely locate the minimal value, and solely a rough approximation is enough to have reliable results.

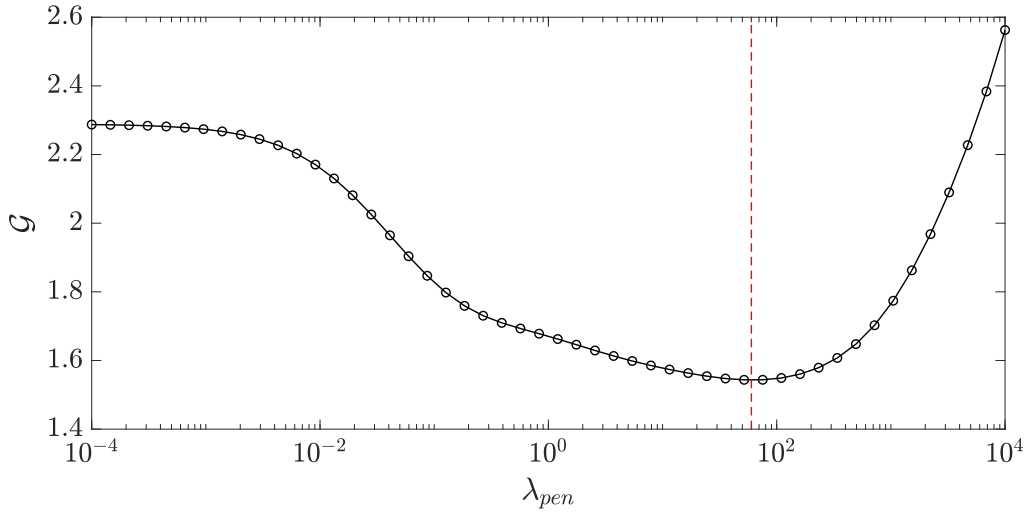

Figure D.2: Generalised cross-validation.

APPENDIX E

Developed GUI for GB-SAR processing

This appendix presents the developed toolbox as an important part of the work realised for the DAMAST project. The presentation is not exhaustive and aims to provide a visualisation of the implemented software package.

The software can be divided into two main graphical user interface (GUI), both developed using the *App designer* of *Matlab*. The first software is dedicated to the preprocessing of the data and is designed to solve the following task:

- Read the raw data and focus the GB-SAR images
- Check the quality of the data
- Lead the first coarse pixel selection to reduce the amount of data
- P-RaySAR multiple signal reflection analysis
- P-RaySAR image simulation from given external parameters
- Tomographic processing from corresponding data
- Correction of offsets according to Chapter 3
- Geocoding according to Chapter 4
- Analysis of corner reflectors position and offset

No interferometric processing is lead, and it enables firstly to reduce the amount of data and to lead an accurate geocoding. A visualisation of the preprocessing tab is available in Figure E.1. The software was designed such that the user can influence (almost) all the parameter values. For the preprocessing, the user can change the size of the windowing functions for the focusing and the parameters for the pixel selection. Figure E.2 gives a visualisation of the geocoding tab. Several parameters can be adjusted, with different possibilities depending on the presence of corner reflectors in the scenario or the availability of TomoSAR data.

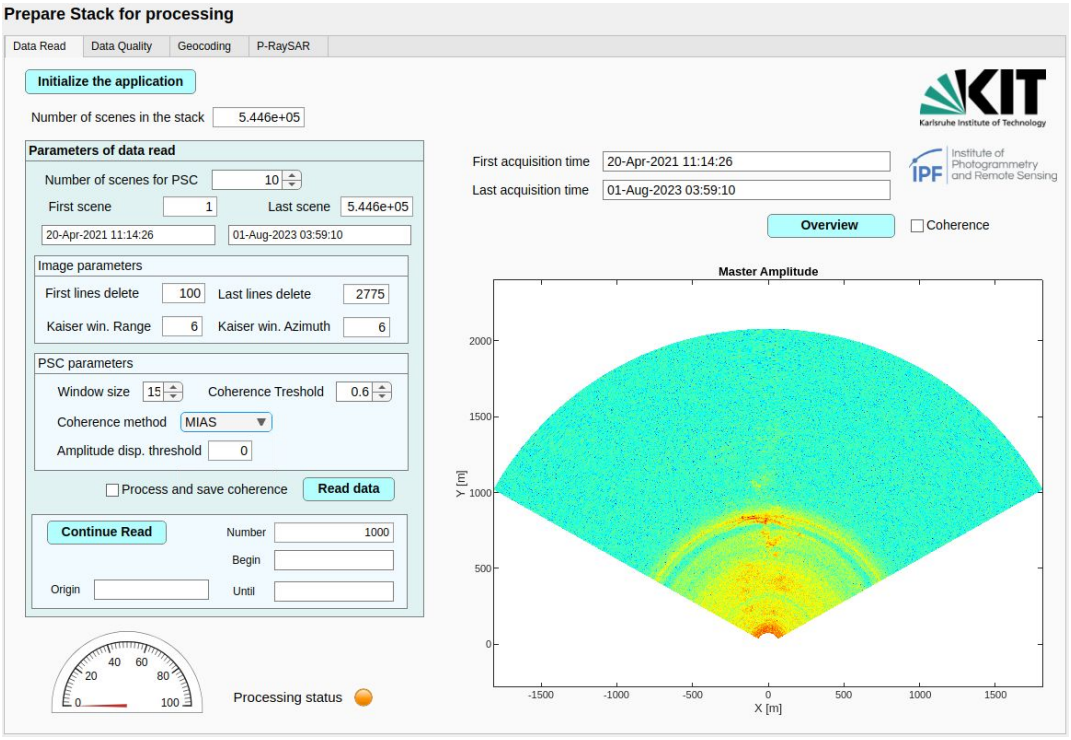

Figure E.1: Panel for the preprocessing of GB-SAR data.

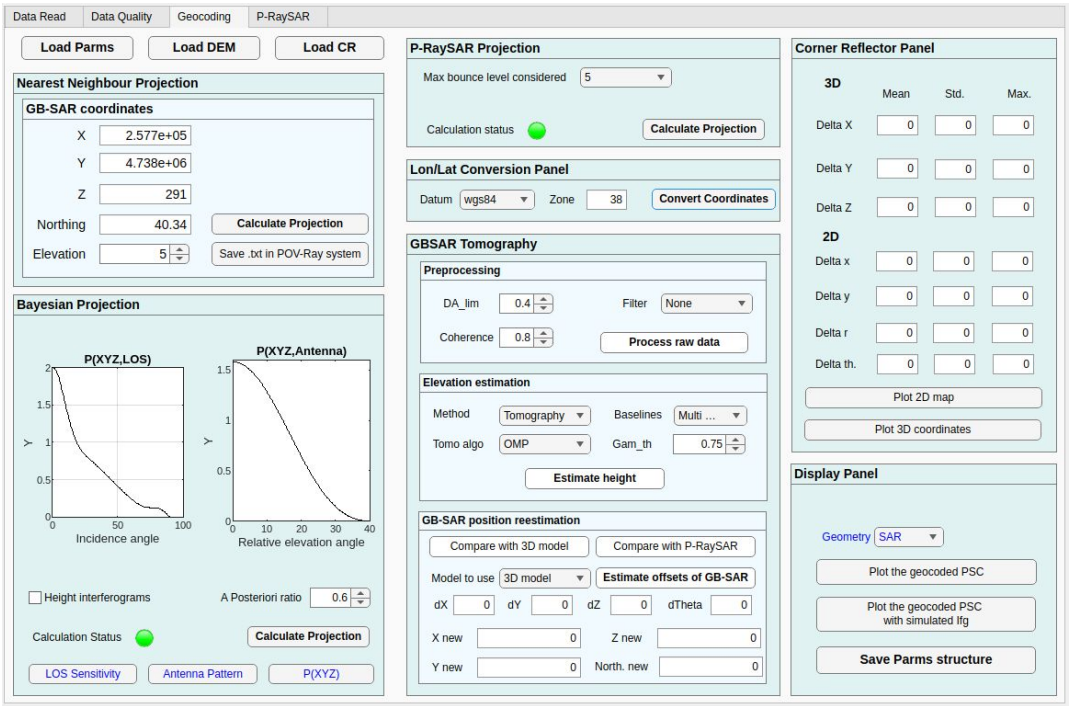

Figure E.2: Panel for the geocoding of the GB-SAR data.

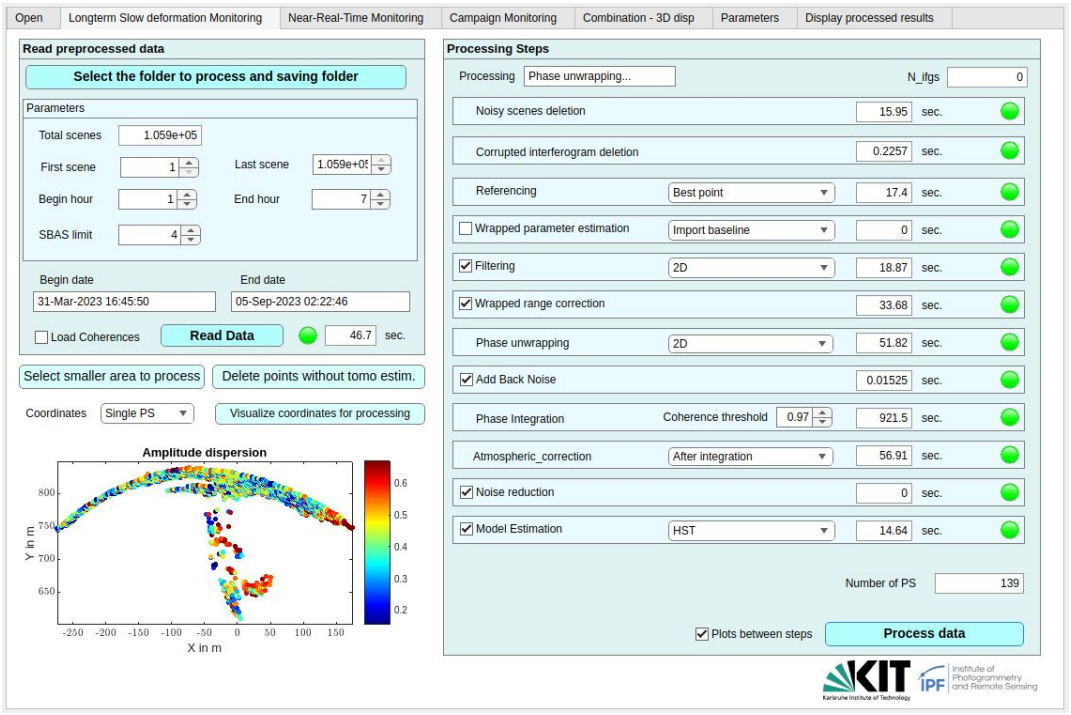

Figure E.3: Panel for the long-term continuous deformation monitoring with GB-SAR data

The second software is dedicated to the interferometric processing with three main different possibilities:

- Long-term geodetic analysis
- Near real-time monitoring
- Epoch-wise monitoring

Figure E.3 is an overview of the panel dedicated to long-term and continuous slow deformation monitoring. The main steps are presented with different lamps, informing the user which action is currently processing and how much time is required to process it. All the parameters corresponding to these steps are grouped in a single panel. The software is not designed for quick usage based on a black box but such that each parameter implemented on the software can be modified. The user does not need to be an expert in InSAR processing, but some basics are required. An overview of the PSC and their amplitude dispersion over the whole stack helps the user select the reference point for the phase unwrapping.

APPENDIX F

List of publications

Publications in peer-reviewed journal

REBMEISTER, M., AUER, S., SCHENK, A., HINZ, S., 2022. Geocoding of Ground-based SAR data using Maximum A Posteriori Estimation and Ray-tracing. *International Journal of Photogrammetry and Remote Sensing*, 189:110–127

REBMEISTER, M., SCHENK, A., HINZ, S., 2023. Phase unwrapping in GB-SAR infrastructure monitoring with optimal PCA geometry *Submitted to the Geoscience and Remote Sensing Letters*

Publications presented in international conferences

REBMEISTER, M., SCHENK, A., BRADLEY, P.-E., HINZ, S., 2021. OCLeaS – A tomographic PSI Algorithm using Orthogonal Matching Pursuit and Complex Least Squares. *Procedia Computer Sciences*

REBMEISTER, M., SCHENK, A., HINZ, S., 2022. Comparison and Evaluation of Different Approaches for Efficient Processing of Long Ground-Based SAR Times Series. *The International Archives of Photogrammetry, Remote Sensing and Spatial Information Sciences*

REBMEISTER, M., SCHENK, A., HINZ, S., ANDRIAN, F., VONIE, M. 2023. High dam monitoring with Ground-based SAR: Opportunities and Challenges. 2023. *91st Annual ICOLD Meeting*

Other contributions

OTTENBURGER SS., TRYBUSHNYI, R., DUJARDIN, R., REBMEISTER, M., KARAM ZADEH TOULAROUD, N., QUANDT, D., MÖHRLE, S., ÜNAL, O., BOSCH, J., MÜLLER, T., HALLER,

C., SCHENK, A., KRON, A., MÜLLER, B., 2023. AI-assisted correlation analysis of dam deformation vs environmental parameters *91st Annual ICOLD Meting*

WEISGERBER, J., REBMEISTER, 2022. Deformationsmonitoring an der Enguri-Staumauer im Kaukasusgebirge, Georgien. *DVW Baden Württemberg e.V., Heft 1/2022, ISSN 0940-2942*

List of Figures

List of Tables

Bibliography

[AccuTrans, 2021] AccuTrans (2021). Accutrans 3d. `http://www.micromouse.ca`. Accessed on 15.09.2023.

[Adamo et al., 2020] Adamo, N., Al-Ansari, N., Sissakian, V., Laue, J., and Knutsson, S. (2020). Dam safety: General considerations. Journal of Earth Sciences and Geotechnical Engineering, 10(6):1–21.

[Adamo et al., 2021] Adamo, N., Al-Ansari, N., Sissakian, V., Laue, J., and Knutsson, S. (2021). Dam safety: Use of seismic monitoring instrumentation in dams. Journal of Earth Sciences and Geotechnical Engineering, 11(1):203–247.

[Alba et al., 2008] Alba, M., Bernardini, G., Giussani, A., Ricci, P., Roncoroni, F., Scaioni, M., Valgoi, P., Zhang, K., et al. (2008). Measurement of dam deformations by terrestrial interferometric techniques. Int. Arch. Photogramm. Remote Sens. Spat. Inf. Sci, 37(B1):133–139.

[Amemiya, 1982] Amemiya, T. (1982). Two stage least absolute deviations estimators. Econometrica: Journal of the Econometric Society, pages 689–711.

[Auer, 2011] Auer, S. (2011). 3D Synthetic Aperture Radar Simulation for Interpreting Complex Urban Reflection Scenarios. PhD thesis, TU München.

[Auer et al., 2016] Auer, S., Bamler, R., and Reinartz, P. (2016). Raysar - 3d sar simulator: Now open source. 2016 IEEE International Geoscience and Remote Sensing Symposium (IGARSS), pages 6730–6733.

[Auer et al., 2011] Auer, S., Gernhardt, S., and Bamler, R. (2011). Ghost persistent scatterers related to signal reflections between adjacent buildings. In 2011 IEEE International Geoscience and Remote Sensing Symposium, pages 1485–1488. IEEE.

[Balz et al., 2015] Balz, T., Hammer, H., and Auer, S. (2015). Potentials and limitations of sar image simulators - a comparative study of three simulation approaches. ISPRS Journal of Photogrammetry and Remote Sensing, 101:102–109.

[Bamler and Hartl, 1998] Bamler, R. and Hartl, P. (1998). Synthetic aperture radar interferometry. Inverse problems, 14(4):R1.

[Barton, 2013] Barton, D. K. (2013). Radar equations for modern radar. Artech House.

[Baumann et al., 2023] Baumann, A., Butt, J. A., and Wieser, A. (2023). Estimating 3d displacement vectors from line-of-sight observations with application to mimo-sar. Journal of Applied Geodesy, (0).

[Berardino et al., 2002] Berardino, P., Fornaro, G., Lanari, R., and Sansosti, E. (2002). A new algorithm for surface deformation monitoring based on small baseline differential sar interferograms. IEEE Transactions on geoscience and remote sensing, 40(11):2375–2383.

[Besl and McKay, 1992] Besl, P. J. and McKay, N. D. (1992). Method for registration of 3-d shapes. In Sensor fusion IV: control paradigms and data structures, volume 1611, pages 586–606. Spie.

[Bourdarot and Robbe, 2012] Bourdarot, E. and Robbe, E. (2012). Prise en compte des résultats de l'auscultation dans la modélisation des barrages en béton. CFBR, Chambéry.

[Budillon et al., 2009] Budillon, A., Evangelista, A., and Schirinzi, G. (2009). Sar tomography from sparse samples. In 2009 IEEE international geoscience and remote sensing symposium, volume 4, pages IV–865. IEEE.

[Caduff et al., 2013] Caduff, R., Kos, A., Schlunegger, F., McArdell, B. W., and Wiesmann, A. (2013). Terrestrial radar interferometric measurement of hillslope deformation and atmospheric disturbances in the illgraben debris-flow catchment, switzerland. IEEE geoscience and remote sensing letters, 11(2):434–438.

[Caduff and Rieke-Zapp, 2014] Caduff, R. and Rieke-Zapp, D. (2014). Registration and visualisation of deformation maps from terrestrial radar interferometry using photogrammetry and structure from motion. The Photogrammetric Record, 29(146):167–186.

[Caduff et al., 2015] Caduff, R., Schlunegger, F., Kos, A., and Wiesmann, A. (2015). A review of terrestrial radar interferometry for measuring surface change in the geosciences. Earth Surface Processes and Landforms, 40(2):208–228.

[Cai et al., 2021] Cai, J., Jia, H., Liu, G., Zhang, B., Liu, Q., Fu, Y., Wang, X., and Zhang, R. (2021). An accurate geocoding method for gb-sar images based on solution space search and its application in landslide monitoring. Remote Sensing, 13(5):832.

[Carballo and Fieguth, 2000] Carballo, G. and Fieguth, P. (2000). Probabilistic cost functions for network flow phase unwrapping. IEEE Transactions on Geoscience and Remote Sensing, 38(5):2192–2201.

[CFBR, 2021] CFBR (2021). French Recommendations for Arch Dams. Guidelines.

[Chan and Hansen, 1990] Chan, T. F. and Hansen, P. C. (1990). Computing truncated singular value decomposition least squares solutions by rank revealing qr-factorizations. SIAM Journal on Scientific and Statistical Computing, 11(3):519–530.

[Chao et al., 2019] Chao, B., Zhang, D., Huang, H., et al. (2019). An overview of atmospheric correction for gb-sar. In 2019 IEEE 19th International Conference on Communication Technology (ICCT), pages 1062–1072. IEEE.

[Chelidze et al., 2021] Chelidze, T., Matcharashvili, T., Abashidze, V., Dovgal, N., Mepharidze, E., and Chelidze, L. (2021). Time series analysis of fault strain accumulation around large dam: The case of enguri dam, greater caucasus. In Building Knowledge for Geohazard Assessment and Management in the Caucasus and other Orogenic Regions, pages 185–204. Springer.

[Chen, 2001] Chen, C. W. (2001). Statistical-cost network-flow approaches to two-dimensional phase unwrapping for radar interferometry. Stanford University.

[Chen and Zebker, 2001] Chen, C. W. and Zebker, H. A. (2001). Two-dimensional phase unwrapping with use of statistical models for cost functions in nonlinear optimization. JOSA A, 18(2):338–351.

[Chen et al., 2001] Chen, S. S., Donoho, D. L., and Saunders, M. A. (2001). Atomic decomposition by basis pursuit. SIAM review, 43(1):129–159.

[Chen and Medioni, 1992] Chen, Y. and Medioni, G. (1992). Object modelling by registration of multiple range images. Image and vision computing, 10(3):145–155.

[Chouinard and Roy, 2006] Chouinard, L. and Roy, V. (2006). Performance of statistical models for dam monitoring data. In Joint international conference on computing and decision making in civil and building engineering, Montreal, pages 14–16.

[Chrzanowski et al., 2011] Chrzanowski, A., Szostak, A., and Steeves, R. (2011). Reliability and efficiency of dam deformation monitoring schemes. In Proceedings of the 2011 Annual Conference of Canadian Dam Association (CDA/ACB), Fredericton, NB, Canada, volume 15.

[Cigna et al., 2014] Cigna, F., Bateson, L. B., Jordan, C. J., and Dashwood, C. (2014). Simulating sar geometric distortions and predicting persistent scatterer densities for ers-1/2 and envisat c-band sar and insar applications: Nationwide feasibility assessment to monitor the landmass of great britain with sar imagery. Remote Sensing of Environment, 152:441–466.

[Costantini, 1998] Costantini, M. (1998). A novel phase unwrapping method based on network programming. IEEE Transactions on geoscience and remote sensing, 36(3):813–821.

[Costantini et al., 2002] Costantini, M., Malvarosa, F., Minati, F., Pietranera, L., and Milillo, G. (2002). A three-dimensional phase unwrapping algorithm for processing of multitemporal sar interferometric measurements. In IEEE International Geoscience and Remote Sensing Symposium, volume 3, pages 1741–1743. IEEE.

[Crosetto et al., 2013] Crosetto, M., Monserrat, O., Luzi, G., Cuevas-González, M., and Devanthéry, N. (2013). A noninterferometric procedure for deformation measurement using gb-sar imagery. IEEE Geoscience and Remote Sensing Letters, 11(1):34–38.

[Crosetto et al., 2014] Crosetto, M., Monserrat, O., Luzi, G., Cuevas-González, M., and Devanthéry, N. (2014). Discontinuous gbsar deformation monitoring. ISPRS journal of photogrammetry and remote sensing, 93:136–141.

[Crosetto et al., 2017] Crosetto, M., Monserrat, O., Luzi, G., Devanthéry, N., Cuevas-González, M., and Barra, A. (2017). Data processing and analysis tool based on ground-based synthetic aperture radar imagery. The International Archives of the Photogrammetry, Remote Sensing and Spatial Information Sciences, XLII-2/W7:593–596.

[Cumming and Wong, 2005] Cumming, I. G. and Wong, F. H. (2005). Digital processing of synthetic aperture radar data. Artech house.

[Curlander and McDonough, 1991] Curlander, J. C. and McDonough, R. N. (1991). Synthetic aperture radar, volume 11. Wiley, New York.

[De Boor, 1978] De Boor, C. (1978). A practical guide to splines, volume 27. springer-verlag New York.

[Deledalle et al., 2010] Deledalle, C.-A., Denis, L., and Tupin, F. (2010). Nl-insar: Nonlocal interferogram estimation. IEEE Transactions on Geoscience and Remote Sensing, 49(4):1441–1452.

[Dematteis et al., 2018] Dematteis, N., Giordan, D., Zucca, F., Luzi, G., and Allasia, P. (2018). 4d surface kinematics monitoring through terrestrial radar interferometry and image cross-correlation coupling. ISPRS Journal of Photogrammetry and Remote Sensing, 142:38–50.

[Dematteis et al., 2017] Dematteis, N., Luzi, G., Giordan, D., Zucca, F., and Allasia, P. (2017). Monitoring alpine glacier surface deformations with gb-sar. Remote Sensing Letters, 8(10):947–956.

[Deng et al., 2022] Deng, Y., Hu, C., Tian, W., and Zhao, Z. (2022). A grid partition method for atmospheric phase compensation in gb-sar. IEEE Transactions on Geoscience and Remote Sensing, 60:1–13.

[Deng et al., 2021] Deng, Y., Tian, W., Xiao, T., Hu, C., and Yang, H. (2021). High-quality pixel selection applied for natural scenes in gb-sar interferometry. Remote Sensing, 13(9):1617.

[Di Pasquale et al., 2013] Di Pasquale, A., Corsetti, M., Guccione, P., Lugli, A., Nicoletti, M., Nico, G., and Zonno, M. (2013). Ground-based sar interferometry as a supporting tool in natural and man-made disasters. In Proceedings of the 33rd EARSel Symposium, Matera, Italy, pages 3–6.

[Dörr et al., 2022a] Dörr, N., Schenk, A., and Hinz, S. (2022a). Fully integrated temporary persistent scatterer interferometry. IEEE Transactions on Geoscience and Remote Sensing, 60:1–15.

[Dörr et al., 2022b] Dörr, N., Schenk, A., and Hinz, S. (2022b). On the relevance of temporary persistent scatterers for long-term ps-insar monitoring. In EUSAR 2022; 14th European Conference on Synthetic Aperture Radar, pages 1–6. VDE.

[Ershov, 2019] Ershov, S. (2019). B-splines and bernstein basis polynomials. Physics of Particles and Nuclei Letters, 16:593–601.

[Ester et al., 1996] Ester, M., Kriegel, H.-P., Sander, J., Xu, X., et al. (1996). A density-based algorithm for discovering clusters in large spatial databases with noise. In kdd, volume 96, pages 226–231.

[Falabella et al., 2021] Falabella, F., Perrone, A., Stabile, T. A., and Pepe, A. (2021). Atmospheric phase screen compensation on wrapped ground-based sar interferograms. IEEE Transactions on Geoscience and Remote Sensing, 60:1–15.

[Ferretti et al., 2011] Ferretti, A., Fumagalli, A., Novali, F., Prati, C., Rocca, F., and Rucci, A. (2011). A new algorithm for processing interferometric data-stacks: Squeesar. IEEE transactions on geoscience and remote sensing, 49(9):3460–3470.

[Ferretti et al., 2001] Ferretti, A., Prati, C., and Rocca, F. (2001). Permanent scatterers in sar interferometry. IEEE Transactions on geoscience and remote sensing, 39(1):8–20.

[Ferro-Famil et al., 2014] Ferro-Famil, L., Tebaldini, S., Davy, M., Leconte, C., and Boutet, F. (2014). Very high-resolution three-dimensional imaging of natural environments using a tomographic ground-based sar system. In The 8th European Conference on Antennas and Propagation (EuCAP 2014), pages 3221–3224. IEEE.

[Flores-Anderson et al., 2019] Flores-Anderson, A. I., Herndon, K. E., Thapa, R. B., and Cherrington, E. (2019). The sar handbook: comprehensive methodologies for forest monitoring and biomass estimation. Technical report.

[Fornaro et al., 2005] Fornaro, G., Lombardini, F., and Serafino, F. (2005). Three-dimensional multipass sar focusing: Experiments with long-term spaceborne data. IEEE Transactions on Geoscience and Remote Sensing, 43(4):702–714.

[Foucart and Rauhut, 2013] Foucart, S. and Rauhut, H. (2013). A Mathematical Introduction to Compressive Sensing. Applied and Numerical Harmonic Analysis. Springer New York.

[Ghanaat, 1993] Ghanaat, Y. (1993). Theoretical manual for analysis of arch dams. Technical report, US Army Corps of Engineers.

[Ghiglia and Romero, 1994] Ghiglia, D. C. and Romero, L. A. (1994). Robust two-dimensional weighted and unweighted phase unwrapping that uses fast transforms and iterative methods. J. Opt. Soc. Am. A, 11(1):107–117.

[Ghiglia and Romero, 1996] Ghiglia, D. C. and Romero, L. A. (1996). Minimum lp-norm two-dimensional phase unwrapping. JOSA A, 13(10):1999–2013.

[Gini et al., 2002] Gini, F., Lombardini, F., and Montanari, M. (2002). Layover solution in multibaseline sar interferometry. IEEE Transactions on Aerospace and Electronic Systems, 38(4):1344–1356.

[Goel and Adam, 2012] Goel, K. and Adam, N. (2012). An advanced algorithm for deformation estimation in non-urban areas. ISPRS Journal of Photogrammetry and Remote Sensing, 73:100–110. Innovative Applications of SAR Interferometry from modern Satellite Sensors.

[Goering et al., 1995] Goering, D., Chen, H., Hinzman, L., and Kane, D. (1995). Removal of terrain effects from sar satellite imagery of arctic tundra. IEEE Transactions on Geoscience and Remote Sensing, 33(1):185–194.

[Goldstein and Werner, 1998] Goldstein, R. M. and Werner, C. L. (1998). Radar interferogram filtering for geophysical applications. Geophysical research letters, 25(21):4035–4038.

[Goldstein et al., 1988] Goldstein, R. M., Zebker, H. A., and Werner, C. L. (1988). Satellite radar interferometry: Two-dimensional phase unwrapping. Radio science, 23(4):713–720.

[Gonzalez and Woods, 2018] Gonzalez, R. and Woods, R. (2018). Digital Image Processing. Pearson.

[Goodman, 1963] Goodman, N. R. (1963). Statistical Analysis Based on a Certain Multivariate Complex Gaussian Distribution (An Introduction). The Annals of Mathematical Statistics, 34(1):152 – 177.

[Graham, 1974] Graham, L. C. (1974). Synthetic interferometer radar for topographic mapping. Proceedings of the IEEE, 62(6):763–768.

[Grant and Boyd, 2014] Grant, M. and Boyd, S. (2014). CVX: Matlab software for disciplined convex programming, version 2.1. http://cvxr.com/cvx. Accesed on 15.09.2023.

[Griffiths et al., 2019] Griffiths, H., Knott, P., and Koch, W. (2019). Christian hülsmeyer: Invention and demonstration of radar, 1904. IEEE Aerospace and Electronic Systems Magazine, 34(9):56–60.

[Hanssen, 2001] Hanssen, R. F. (2001). Radar interferometry: data interpretation and error analysis, volume 2. Springer Science & Business Media.

[Hassan et al., 2018] Hassan, A., Xu, J., Zhang, L., Liu, G., Schmitt, A., Xing, C., Xu, Y., Ouyang, C., and Schwieger, V. (2018). Towards integration of gnss and gb-sar measurements: Exemplary monitoring of a rock fall at the yangtze river in china. In Proceedings of the Embracing Our Smart World Where the Continents Connect: Enhancing the Geospatial Maturity of Societies, Proceedings of the FIG Congress.

[Hein, 2010] Hein, A. (2010). Processing of SAR Data: Fundamentals, Signal Processing, Interferometry. Signals and Communication Technology. Springer Berlin Heidelberg.

[Hooper et al., 2007] Hooper, A., Segall, P., and Zebker, H. (2007). Persistent scatterer interferometric synthetic aperture radar for crustal deformation analysis, with application to volcán alcedo, galápagos. Journal of Geophysical Research: Solid Earth, 112(B7).

[Hooper et al., 2010] Hooper, A., Spaans, K., Bekaert, D., Cuenca, M. C., Arıkan, M., and Oyen, A. (2010). Stamps/mti manual. Delft Institute of Earth Observation and Space Systems Delft University of Technology, Kluyverweg, 1:2629.

[Hooper et al., 2004] Hooper, A., Zebker, H., Segall, P., and Kampes, B. (2004). A new method for measuring deformation on volcanoes and other natural terrains using insar persistent scatterers. Geophysical research letters, 31(23).

[Hooper and Zebker, 2007] Hooper, A. and Zebker, H. A. (2007). Phase unwrapping in three dimensions with application to insar time series. JOSA A, 24(9):2737–2747.

[Hu et al., 2021] Hu, C., Zhu, J., Deng, Y., Tian, W., and Yin, P. (2021). Repositioning error compensation in discontinuous ground-based sar monitoring. Remote Sensing, 13(13):2461.

[Iannini and Guarnieri, 2010] Iannini, L. and Guarnieri, A. M. (2010). Atmospheric phase screen in ground-based radar: Statistics and compensation. IEEE Geoscience and Remote Sensing Letters, 8(3):537–541.

[ICOLD, 2020] ICOLD (2020). International commission on large dams. https://www.icold-cigb.org/GB/world_register/general_synthesis.asp. Accessed on 26.09.2023.

[IDS-Georadar, 2022] IDS-Georadar (2022). IBIS-FM Manual. IDS Georadar.

[IEA, 2019] IEA (2019). International energy agency. https://www.iea.org/data-and-statistics/charts/world-gross-electricity-production-by-source-2019. Accessed on 26.09.2023.

[Iglesias et al., 2013] Iglesias, R., Fabregas, X., Aguasca, A., Mallorqui, J. J., López-Martínez, C., Gili, J. A., and Corominas, J. (2013). Atmospheric phase screen compensation in ground-based sar with a multiple-regression model over mountainous regions. IEEE transactions on geoscience and remote sensing, 52(5):2436–2449.

[Illner, 2008] Illner, M. (2008). Konzept und ergebnisse von deformationsmessungen an der linachtalsperre. ZfV-Zeitschrift für Geodäsie, Geoinformation und Landmanagement, (zfv 5/2008).

[Izumi et al., 2020] Izumi, Y., Zou, L., Kikuta, K., and Sato, M. (2020). Iterative atmospheric phase screen compensation for near-real-time ground-based insar measurements over a mountainous slope. IEEE Transactions on Geoscience and Remote Sensing, 58(8):5955–5968.

[Jacquemart and Meier, 2014] Jacquemart, M. and Meier, L. (2014). Deformationsmessungen an talsperren und in deren alpiner umgebung mittels radarinterferometrie. Wasser Energie Luft, 106:105–111.

[Jenkins et al., 2012] Jenkins, W., Rosenblad, B., Gomez, F., Legarsky, J., and Loehr, E. (2012). Deformation measurements of earth dams using a ground based interferometric radar. In Proceedings of the 2012 ASDSO Annual Conference on Dam Safety, page 15. (GBIR) Association of State Dam Safety Officials-Dam Safety.

[Ji et al., 2014] Ji, Y., Han, H., and Lee, H. (2014). Construction and application of tomographic sar system based on gb-sar system. In 2014 IEEE Geoscience and Remote Sensing Symposium, pages 1891–1894. IEEE.

[Just and Bamler, 1994] Just, D. and Bamler, R. (1994). Phase statistics of interferograms with applications to synthetic aperture radar. Applied optics, 33(20):4361–4368.

[Knott et al., 2004] Knott, E. F., Schaeffer, J. F., and Tulley, M. T. (2004). Radar cross section. SciTech Publishing.

[Lauknes et al., 2010] Lauknes, T. R., Zebker, H. A., and Larsen, Y. (2010). Insar deformation time series using an l_1-norm small-baseline approach. IEEE transactions on geoscience and remote sensing, 49(1):536–546.

[Lee et al., 1994] Lee, J.-S., Hoppel, K. W., Mango, S. A., and Miller, A. R. (1994). Intensity and phase statistics of multilook polarimetric and interferometric sar imagery. IEEE Transactions on Geoscience and Remote Sensing, 32(5):1017–1028.

[Lewis, 1995] Lewis, J. P. (1995). Fast template matching. In Vision interface, volume 95, pages 15–19. Quebec City, QC, Canada.

[Li et al., 2022] Li, S., Xu, W., and Li, Z. (2022). Review of the sbas insar time-series algorithms, applications, and challenges. Geodesy and Geodynamics, 13(2):114–126.

[Li et al., 2008] Li, Z., Bethel, J., et al. (2008). Image coregistration in sar interferometry. The International Archives of the Photogrammetry, Remote Sensing and Spatial Information Sciences, 37:433–438.

[Liebe, 1981] Liebe, H. J. (1981). Modeling attenuation and phase of radio waves in air at frequencies below 100 ghz. Radio Science, 16(06):1183–1199.

[Lin et al., 2016] Lin, P., Zhu, X., Li, Q., Liu, H., and Yu, Y. (2016). Study on optimal grouting timing for controlling uplift deformation of a super high arch dam. Rock mechanics and rock engineering, 49:115–142.

[Lingua et al., 2008] Lingua, A., Piatti, D., and Rinaudo, F. (2008). Remote monitoring of a landslide using an integration of gb-insar and lidar techniques. Int. Arch. Photogramm. Remote Sens. Spat. Inf. Sci, 37:133–139.

[Liu et al., 2021] Liu, J., Yang, H., Xu, L., and Li, T. (2021). Novel model-based approaches for non-homogenous atmospheric compensation of gb-insar in the azimuth and horizontal directions. Remote Sensing, 13(11):2153.

[Liu et al., 2011] Liu, S., Hanssen, R., Samiei-Esfahany, S., Hooper, A., and Van Leijen, F. (2011). Separating non-linear deformation and atmospheric phase screen (aps) for insar time series analysis using least-squares collocation. In Proceedings of the Advances in the Science and Applications of SAR Interferometry, ESA Fringe 2009, Workshop ESA.

[Loève, 2017] Loève, M. (2017). Probability theory. Courier Dover Publications.

[Lombardi et al., 2008] Lombardi, G., Amberg, F., and Darbre, G. (2008). Algorithm for the prediction of functional delays in the behaviour of concrete dams. The international journal on hydropower & dams, 15(3):111.

[Lucas et al., 2017] Lucas, C., Leinss, S., Bühler, Y., Marino, A., and Hajnsek, I. (2017). Multipath interferences in ground-based radar data: A case study. Remote Sensing, 9.

[Luzi et al., 2004] Luzi, G., Pieraccini, M., Mecatti, D., Noferini, L., Guidi, G., Moia, F., and Atzeni, C. (2004). Ground-based radar interferometry for landslides monitoring: atmospheric and instrumental decorrelation sources on experimental data. IEEE transactions on geoscience and remote sensing, 42(11):2454–2466.

[Maeso and Dominguez, 1993] Maeso, O. and Dominguez, J. (1993). Earthquake analysis of arch dams. i: Dam-foundation interaction. Journal of engineering mechanics, 119(3):496–512.

[Magnard et al., 2021] Magnard, C., Wegmüller, U., and Werner, C. (2021). Persistent scatterer interferometry in mountainous areas: advantages of working in map geometry. Procedia Computer Science, 181:198–205.

[Marambio et al., 2009] Marambio, A., Pucci, B., Jungner, A., Núnez, M., and Buill, F. (2009). Terrestrial laser scanner, terrestrial synthetic aperture radar, and topographic data: An integration proposal. Proc. 8th International Geomatics Week, Barcelona.

[Mardia et al., 2000] Mardia, K. V., Jupp, P. E., and Mardia, K. (2000). Directional statistics, volume 2. Wiley Online Library.

[Martinez-Vazquez and Fortuny-Guasch, 2008] Martinez-Vazquez, A. and Fortuny-Guasch, J. (2008). Averaging and formulation impact on gb-sar topographic mapping. IEEE Geoscience and Remote Sensing Letters, 5(4):635–639.

[Mascolo et al., 2014] Mascolo, L., Nico, G., Di Pasquale, A., and Pitullo, A. (2014). Use of advanced sar monitoring techniques for the assessment of the behaviour of old embankment dams. In Earth Resources and Environmental Remote Sensing/GIS Applications V, volume 9245, pages 122–131. SPIE.

[Méric et al., 2009] Méric, S., Fayard, F., Pottier, É., et al. (2009). Radargrammetric sar image processing. Geoscience and remote sensing, pages 421–454.

[Michelini et al., 2019] Michelini, A., Viviani, F., and Mayer, L. (2019). Introduction to ibis-arcsar: a circular scanning gb-sar system for deformation monitoring. In Proceedings of the 4th Joint International Symposium on Deformation Monitoring (JISDM), pages 15–17.

[Mittermayer et al., 2012] Mittermayer, J., Wollstadt, S., Prats, P., Scheiber, R., and Koppe, W. (2012). Staring spotlight imaging with terrasar-x. In 2012 IEEE International Geoscience and Remote Sensing Symposium, pages 1606–1609.

[Monserrat et al., 2009] Monserrat, O., Crosetto, M., Iglesias, R., Rossi, G., Calcagni, L., and Crippa, B. (2009). A tool for 2+ 1d phase unwrapping: application examples. In Proc. Fringe 2009 Workshop.

[Monserrat et al., 2014] Monserrat, O., Crosetto, M., and Luzi, G. (2014). A review of ground-based sar interferometry for deformation measurement. ISPRS Journal of Photogrammetry and Remote Sensing, 93:40–48.

[Monserrat Hernández, 2012] Monserrat Hernández, O. (2012). Deformation measurement and monitoring with Ground-Based SAR. PhD thesis, Universitat Politècnica de Catalunya.

[Mueller and Strauss, 2019] Mueller, B. and Strauss, B. (2019). Damast web site. `https://www.damast-caucasus.de/68.php`. Accessed on 2023.08.12.

[Narula and Wellington, 1982] Narula, S. C. and Wellington, J. F. (1982). The minimum sum of absolute errors regression: A state of the art survey. International Statistical Review/Revue Internationale de Statistique, pages 317–326.

[Nico et al., 2004] Nico, G., Leva, D., Antonello, G., and Tarchi, D. (2004). Ground-based sar interferometry for terrain mapping: Theory and sensitivity analysis. IEEE Transactions on Geoscience and Remote Sensing, 42(6):1344–1350.

[Niemeier, 2008] Niemeier, W. (2008). Ausgleichungsrechnung: statistische Auswertemethoden. De Gruyter Lehrbuch. De Gruyter.

[Noferini et al., 2009] Noferini, L., Mecatti, D., Macaluso, G., Pieraccini, M., and Atzeni, C. (2009). Monitoring of belvedere glacier using a wide angle gb-sar interferometer. Journal of Applied Geophysics, 68(2):289–293.

[Noferini et al., 2005] Noferini, L., Pieraccini, M., Mecatti, D., Luzi, G., Atzeni, C., Tamburini, A., and Broccolato, M. (2005). Permanent scatterers analysis for atmospheric correction in ground-based sar interferometry. IEEE Transactions on Geoscience and Remote Sensing, 43(7):1459–1471.

[Noferini et al., 2007] Noferini, L., Pieraccini, M., Mecatti, D., Macaluso, G., Luzi, G., and Atzeni, C. (2007). Dem by ground-based sar interferometry. IEEE Geoscience and Remote Sensing Letters, 4(4):659–663.

[Noferini et al., 2008] Noferini, L., Takayama, T., Pieraccini, M., Mecatti, D., Macaluso, G., Luzi, G., and Atzeni, C. (2008). Analysis of ground-based sar data with diverse temporal baselines. IEEE Transactions on Geoscience and Remote Sensing, 46(6):1614–1623.

[Oliver and Quegan, 2004] Oliver, C. and Quegan, S. (2004). Understanding synthetic aperture radar images. SciTech Publishing.

[Ottenburger et al., 2023] Ottenburger, S., Trybushnyi, D., Rebmeister, M., Karam Zadeh Toularoud, N., Quandt, D., Mohrle, S., Ünal, O., Bosch, J., Mueller, T., Haller, C., Schenk, A., Kron, A., and Mueller, B. (2023). Ai-assisted analysis of correlations of dam deformation, seismic events, meteorology, and water level changes. In ICOLD 2023: 91st ICOLD Annual Meeting.

[Pang et al., 2023] Pang, L., Liu, D., Li, C., and Zhang, F. (2023). Automatic registration of homogeneous and cross-source tomosar point clouds in urban areas. Sensors, 23(2):852.

[Perner and Obernhuber, 2010] Perner, F. and Obernhuber, P. (2010). Analysis of arch dam deformations. Frontiers of Architecture and Civil Engineering in China, 4:102–108.

[Pettinari et al., 2023] Pettinari, A., Telleschi, G., and Twardzik, M. (2023). Use of ground-based interferometric radars (gb-inra) for remote real-time monitoring of critical infrastructures. In International Conference on Experimental Vibration Analysis for Civil Engineering Structures, pages 758–767. Springer.

[Pieraccini et al., 2001] Pieraccini, M., Luzi, G., and Atzeni, C. (2001). Terrain mapping by ground-based interferometric radar. IEEE Transactions on Geoscience and Remote Sensing, 39(10):2176–2181.

[Pieraccini and Miccinesi, 2019] Pieraccini, M. and Miccinesi, L. (2019). Ground-based radar interferometry: A bibliographic review. Remote Sensing, 11(9):1029.

[Qian et al., 2022] Qian, K., Wang, Y., Jung, P., Shi, Y., and Zhu, X. X. (2022). Basis pursuit denoising via recurrent neural network applied to super-resolving sar tomography. IEEE Transactions on Geoscience and Remote Sensing, 60:1–15.

[Qiu et al., 2020] Qiu, Z., Jiao, M., Jiang, T., and Zhou, L. (2020). Dam structure deformation monitoring by gb-insar approach. IEEE Access, 8:123287–123296.

[Ralph, 2012] Ralph, J. F. (2012). Avionics aero230 (lecture note. Univeristy of Liverpool.

[Ramsay, 1991] Ramsay, J. (1991). Some tools for functional data analysis. Journal of the Royal Statistical Society: Series B (Methodological), 53(3):539–561.

[Ramsay et al., 2009] Ramsay, J. O., Hooker, G., and Graves, S. (2009). Functional Data Analysis with R and MATLAB. Springer Publishing Company, Incorporated, 1st edition.

[Rebmeister et al., 2022a] Rebmeister, M., Auer, S., Schenk, A., and Hinz, S. (2022a). Geocoding of ground-based sar data for infrastructure objects using the maximum a posteriori estimation and ray-tracing. ISPRS Journal of Photogrammetry and Remote Sensing, 189:110–127.

[Rebmeister et al., 2021] Rebmeister, M., Schenk, A., Bradley, P. E., Dörr, N., and Hinz, S. (2021). Ocleas–a tomographic psi algorithm using orthogonal matching pursuit and complex least squares. Procedia Computer Science, 181:220–230.

[Rebmeister et al., 2022b] Rebmeister, M., Schenk, A., and Hinz, S. (2022b). Comparison and evaluation of different approaches for efficient processing of long ground-based sar times series. The International Archives of the Photogrammetry, Remote Sensing and Spatial Information Sciences, 43:341–348.

[Rebmeister et al., 2023] Rebmeister, M., Schenk, A., Hinz, S., Andrian, F., and Vonie, M. (2023). High dam monitoring with ground-based sar: Opportunities and challenges. In ICOLD 2023: 91st ICOLD Annual Meeting.

[Reigber and Moreira, 2000] Reigber, A. and Moreira, A. (2000). First demonstration of airborne sar tomography using multibaseline l-band data. IEEE Transactions on Geoscience and Remote Sensing, 38(5):2142–2152.

[Rödelsperger, 2011] Rödelsperger, S. (2011). Real-time processing of ground based synthetic aperture radar (GB-SAR) measurements. Number 33. Technische Universität Darmstadt, Fachbereich Bauingenieurwesen und Geodäsie.

[Rödelsperger et al., 2012] Rödelsperger, S., Coccia, A., Vicente, D., and Meta, A. (2012). Introduction to the new metasensing ground-based sar: Technical description and data analysis. In 2012 IEEE International Geoscience and Remote Sensing Symposium, pages 4790–4792. IEEE.

[Rudolf et al., 1999] Rudolf, H., Leva, D., Tarchi, D., and Sieber, A. (1999). A mobile and versatile sar system. In IEEE 1999 International Geoscience and Remote Sensing Symposium. IGARSS'99 (Cat. No. 99CH36293), volume 1, pages 592–594. IEEE.

[Salazar et al., 2017] Salazar, F., Morán, R., Toledo, M. Á., and Oñate, E. (2017). Data-based models for the prediction of dam behaviour: a review and some methodological considerations. Archives of computational methods in engineering, 24:1–21.

[Sarabandi and Chiu, 1996] Sarabandi, K. and Chiu, T.-C. (1996). Optimum corner reflectors for calibration of imaging radars. Antennas and Propagation, IEEE Transactions on, 44:1348 – 1361.

[Scaioni et al., 2018] Scaioni, M., Marsella, M., Crosetto, M., Tornatore, V., and Wang, J. (2018). Geodetic and remote-sensing sensors for dam deformation monitoring. Sensors, 18(11).

[Schenk, 2015] Schenk, A. (2015). PS-Interferometrie in urbanen Räumen - Optimierte Schätzung von Oberflächenbewegungen mittels Multi-SBAS Verfahren. PhD thesis, KIT.

[Schmutz and Moog, 2018] Schmutz, S. and Moog, O. (2018). Dams: ecological impacts and management. Riverine ecosystem management: Science for governing towards a sustainable future, pages 111–127.

[Simpson et al., 1988] Simpson, D. W., Leith, W., and Scholz, C. (1988). Two types of reservoir-induced seismicity. Bulletin of the Seismological Society of America, 78(6):2025–2040.

[Skolnik, 2008] Skolnik, M. I. (2008). Radar handbook. McGraw-Hill Education.

[Strozzi et al., 2011] Strozzi, T., Werner, C., Wiesmann, A., and Wegmuller, U. (2011). Topography mapping with a portable real-aperture radar interferometer. IEEE Geoscience and Remote Sensing Letters, 9(2):277–281.

[Su et al., 2022] Su, Y., Yang, H., Peng, J., Liu, Y., Zhao, B., and Shi, M. (2022). A novel near-real-time gb-insar slope deformation monitoring method. Remote Sensing, 14(21):5585.

[Talich, 2016] Talich, M. (2016). The deformation monitoring of dams by the ground-based insar technique-case study of concrete hydropower dam orlík. Int J Adv Agric Environ Eng, 3(1):192–197.

[Tapete et al., 2013] Tapete, D., Casagli, N., Luzi, G., Fanti, R., Gigli, G., and Leva, D. (2013). Integrating radar and laser-based remote sensing techniques for monitoring structural deformation of archaeological monuments. Journal of Archaeological Science, 40(1):176–189.

[Tarchi et al., 1999] Tarchi, D., Rudolf, H., Luzi, G., Chiarantini, L., Coppo, P., and Sieber, A. J. (1999). Sar interferometry for structural changes detection: A demonstration test on a dam. In IEEE 1999 International Geoscience and Remote Sensing Symposium. IGARSS'99 (Cat. No. 99CH36293), volume 3, pages 1522–1524. IEEE.

[Tian et al., 2019] Tian, W., Zhao, Z., Hu, C., Wang, J., and Zeng, T. (2019). Gb-insar-based dem generation method and precision analysis. Remote Sensing, 11(9):997.

[Tillmann and Pfetsch, 2013] Tillmann, A. M. and Pfetsch, M. E. (2013). The computational complexity of the restricted isometry property, the nullspace property, and related concepts in compressed sensing. IEEE Transactions on Information Theory, 60(2):1248–1259.

[Tribolet, 1977] Tribolet, J. (1977). A new phase unwrapping algorithm. IEEE Transactions on Acoustics, Speech, and Signal Processing, 25(2):170–177.

[Tropp and Gilbert, 2007] Tropp, J. A. and Gilbert, A. C. (2007). Signal recovery from random measurements via orthogonal matching pursuit. IEEE Transactions on information theory, 53(12):4655–4666.

[Wang et al., 2020a] Wang, P., Xing, C., and Pan, X. (2020a). Reservoir dam surface deformation monitoring by differential gb-insar based on image subsets. Sensors, 20(2).

[Wang et al., 2021] Wang, P., Xing, C., Pan, X., Zhou, X., and Shi, B. (2021). Microdeformation monitoring by permanent scatterer gb-sar interferometry based on image subset series with short temporal baselines: The geheyan dam case study. Measurement, 184:109944.

[Wang et al., 2020b] Wang, Y., Hong, W., Zhang, Y., Lin, Y., Li, Y., Bai, Z., Zhang, Q., Lv, S., Liu, H., and Song, Y. (2020b). Ground-based differential interferometry sar: A review. IEEE Geoscience and Remote Sensing Magazine, 8(1):43–70.

[Wang et al., 2020c] Wang, Y., Wang, G., Wang, L., and Ogden, R. T. (2020c). Simultaneous confidence corridors for mean functions in functional data analysis of imaging data. Biometrics, 76(2):427–437.

[Wang, 2019] Wang, Z. (2019). Ground-based synthetic aperture radar (GBSAR) interferometry for deformation monitoring. PhD thesis, Newcastle University.

[Wang et al., 2019a] Wang, Z., Li, Z., Liu, Y., Peng, J., Long, S., and Mills, J. (2019a). A new processing chain for real-time ground-based sar (rt-gbsar) deformation monitoring. Remote Sensing, 11(20):2437.

[Wang et al., 2018a] Wang, Z., Li, Z., and Mills, J. (2018a). A new approach to selecting coherent pixels for ground-based sar deformation monitoring. ISPRS journal of photogrammetry and remote sensing, 144:412–422.

[Wang et al., 2019b] Wang, Z., Li, Z., and Mills, J. (2019b). Modelling of instrument repositioning errors in discontinuous multi-campaign ground-based sar (mc-gbsar) deformation monitoring. ISPRS Journal of Photogrammetry and Remote Sensing, 157:26–40.

[Wang et al., 2018b] Wang, Z., Li, Z., and Mills, J. P. (2018b). A new nonlocal method for ground-based synthetic aperture radar deformation monitoring. IEEE Journal of Selected Topics in Applied Earth Observations and Remote Sensing, 11(10):3769–3781.

[Weinmann et al., 2015] Weinmann, M., Jutzi, B., Hinz, S., and Mallet, C. (2015). Semantic point cloud interpretation based on optimal neighborhoods, relevant features and efficient classifiers. ISPRS Journal of Photogrammetry and Remote Sensing, 105:286–304.

[Wieland and Kirchen, 2012] Wieland, M. and Kirchen, G. (2012). Long-term dam safety monitoring of punt dal gall arch dam in switzerland. Frontiers of Structural and Civil Engineering, 6(1):76–83.

[Wieser et al., 2020] Wieser, A., Condamin, S., Barras, V., Schmid, L., and Butt, J. (2020). Staumauerüberwachung–vergleich dreier technologien für epochenweise deformationsmessungen. Ingenieurvermessung 20. Beiträge zum 19. Internationalen Ingenieurvermessungskurs München, 2020, pages 437–449.

[Wiley, 1985] Wiley, C. A. (1985). Synthetic aperture radars. IEEE Transactions on Aerospace and Electronic Systems, (3):440–443.

[Willm and Beaujoint, 1967] Willm, G. and Beaujoint, N. (1967). Les méthodes de surveillance des barrages au service de la production hydraulique d'Électricité de france. problèmes anciens et solutions nouvelles. IXe Congrès CIGB, Istanbul.

[Xiang et al., 2019] Xiang, X., Chen, J., Wang, H., Pei, L., and Wu, Z. (2019). Ps selection method for and application to gb-sar monitoring of dam deformation. Advances in Civil Engineering, 2019.

[Yang et al., 2020] Yang, H., Liu, J., Peng, J., Wang, J., Zhao, B., and Zhang, B. (2020). A method for gb-insar temporal analysis considering the atmospheric correlation in time series. Natural Hazards, 104(2):1465–1480.

[Yigit et al., 2016] Yigit, C. O., Alcay, S., and Ceylan, A. (2016). Displacement response of a concrete arch dam to seasonal temperature fluctuations and reservoir level rise during the first filling period: evidence from geodetic data. Geomatics, Natural Hazards and Risk, 7(4):1489–1505.

[Yu et al., 2019] Yu, H., Lan, Y., Yuan, Z., Xu, J., and Lee, H. (2019). Phase unwrapping in insar : A review. IEEE Geoscience and Remote Sensing Magazine, 7(1):40–58.

[Yunjun et al., 2019] Yunjun, Z., Fattahi, H., and Amelung, F. (2019). Small baseline insar time series analysis: Unwrapping error correction and noise reduction. Computers & Geosciences, 133:104331.

[Zebker et al., 1997] Zebker, H. A., Rosen, P. A., and Hensley, S. (1997). Atmospheric effects in interferometric synthetic aperture radar surface deformation and topographic maps. Journal of Geophysical Research: Solid Earth, 102(B4):7547–7563.

[Zebker et al., 1992] Zebker, H. A., Villasenor, J., et al. (1992). Decorrelation in interferometric radar echoes. IEEE Transactions on geoscience and remote sensing, 30(5):950–959.

[Zhu et al., 2009] Zhu, X. X., Adam, N., Brcic, R., and Bamler, R. (2009). Space-borne high resolution sar tomography: experiments in urban environment using ts-x data. In 2009 Joint Urban Remote Sensing Event, pages 1–8. IEEE.

[Zhu and Bamler, 2010] Zhu, X. X. and Bamler, R. (2010). Tomographic sar inversion by l_1-norm regularization—the compressive sensing approach. IEEE transactions on Geoscience and Remote Sensing, 48(10):3839–3846.

[Zhu and Bamler, 2011a] Zhu, X. X. and Bamler, R. (2011a). Let's do the time warp: Multicomponent nonlinear motion estimation in differential sar tomography. IEEE Geoscience and Remote Sensing Letters, 8(4):735–739.

[Zhu and Bamler, 2011b] Zhu, X. X. and Bamler, R. (2011b). Super-resolution power and robustness of compressive sensing for spectral estimation with application to spaceborne tomographic sar. IEEE Transactions on Geoscience and Remote Sensing, 50(1):247–258.

Acknowledgements

These acknowledgements close the thesis and an entire chapter in my life. The long path of the PhD. thesis is challenging and requires a strong personal investment to be successful. However, nothing would have been achievable without the involvement of different persons, which I want to acknowledge with the following few words!

My first thanks go to my main referent, Prof. Dr.-Ing. Stefan Hinz for his trust and his help during the whole thesis. He was always available for discussion and sharing his immense knowledge and valuable advice. My thanks to him are applicable before the PhD period, as he was always here to support and help me during my studies and my master thesis at the KIT. With all the (challenging !) opportunities he gave me, I could grow from a scientific point of view, but also from a personal point of view. Danke Stefan!

My second thanks go to the second advisor of this PhD thesis: Prof. Dr. Michael Eineder, who kindly agreed to read and evaluate the proposed work. I also kindly thank the members completing the jury, Prof. Dr.-Ing. Hansjörg Kutterer and Prof. Dr.-Ing Boris Jutzi, for the interest they brought in the work achieved in this thesis.

My PhD thesis was only so pleasant with my supervisor and friend, Dr.-Ing. Andreas Schenk. From the beginning of my master studies, where I worked with him as a "Hiwi", through my master thesis and until the end of my PhD studies, he was always here to have valuable and very interesting discussions. We had a lot of good times during the measurements and the workshops in Georgia, making each campaign measurement a pleasure. So, like you would say in your preferred language: Merci Andreas, c'était formidable à tes cotés!

For the very interesting collaborative work we did on the ray-tracing part, I want to thank Dr.-Ing. Stefan Auer from the *German Aerospace Center*. He gave me very helpful advice and shared a lot of knowledge with me. In a couple of meetings, he could very clearly explain to me the potential of what he did in his PhD. and ideas to apply it on terrestrial radar. Moreover, his advice on writing this manuscript enhanced its construction significantly.

During this thesis, I had the opportunity to visit *IDS Georadar* headquarters in Pisa. I want to thank Dr. Alberto Michelini for the invitation and also for the exciting discussions about the instrument and the processing strategies. His investment and knowledge in the domain of terrestrial radar monitoring are rare, and I am very grateful he allowed me to work with him. I also thank Nicola Dal Santo for the collaborative work lead and data sharing.

During the field trips in Georgia, we could always count on Dr. David Svanadze, who supported us many times, to organise car rental and hotel booking and also the communication with security guards at the Enguri Dam. I also want to thank Dr. Birgit Müller, for her impeccable organisation of each Georgian field trip. For the data collection, I acknowledge Dr.-Ing. Nils Dörr for installing the stations and corner reflectors at Enguri dam. On the same topic, I am grateful to Marinus Vogl for acquiring the photogrammetric data.

For a deeper understanding of the deformation processes in dam structures, I acknowledge Frédéric Andrian and Maxime Vonié from the company *Artelia*. Their work at Enguri Dam was precious for the validation of the presented results in the thesis. Their wish to share their knowledge was also a strong motivation for me to have a wider field of view, by trying to understand several mechanical processes of dam deformation and not only remaining in the signal processing of radar data.

For the fast and efficient processing of the GNSS data during the last week of writing this thesis, I want to thank Dr. Malte Westerhaus from the *Geodetic Institute Karlsruhe*. The possibility of comparing the GB-SAR results with independent sensors was a precious value for validating the proposed methodologies.

I want to thank Dr. Michele Crosetto and Dr. Oriol Montserrat for my three months visit in the *Centre Technològic de Telecomunicacion de Catalunya*. Their experience in the domain was very helpful, and they shared interesting directions for the last year of my PhD research. During this period in Barcelona, I also met a lot of other PhD students who made this time there a unique experience. A particular thank goes to Jorge for his friendship that made my stay memorable. I also want to thank the Graduiertenschule *GRACE* for the funding of this scholarship.

My friend Donatien is another important person in the long path of this PhD thesis. He gave me a taste for mathematics, and we had a lot of exciting discussions about statistics, integration, Bayesian inference and the wonderful Cédric.

Finally, my thanks go to my family and friends, who supported me during this challenging period. Tout d'abord, je tiens à remercier mes parents, Cathy et Jean-Louis. Leur soutien infaillible ainsi que leurs encouragements ont fondé le pillier central sur lequel j'ai pu m'appuyer. Je remercie également ma soeur Virginie pour la joie qu'elle me transmet à chaque fois que je la vois. Sans ordre de préférence, je remercie mes amis les plus proches: Gauthier, Grégoire, Mathieu, Pépin (malgré le fait que tu habites dans une pomme), Thierry, Valentin et Vincent. Enfin, je tiens à remercier Clara pour avoir été à mes cotés tout le long de cette thèse. Merci à vous tous!